Adaptive Fabrication of Biofunctional Decellularized Extracellular Matrix *Niche* Towards Complex Engineered Tissues

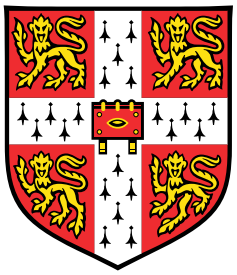

Zhaoying Li

Department of Engineering
University of Cambridge

This dissertation is submitted for the degree of
Doctor of Philosophy

Murray Edwards College

November 2017

I would like to dedicate this thesis to my loving parents.

Declaration

I hereby declare that except where specific reference is made to the work of others, the contents of this dissertation are original and have not been submitted in whole or in part for consideration for any other degree or qualification in this, or any other university. This dissertation is my own work and contains nothing which is the outcome of work done in collaboration with others, except as specified in the text and Acknowledgements. The Enzyme-Linked ImmunoSorbent Assay was performed by Chuan Chen, Wenzhou Medical University, China. The Atomic Force Microscopy measurement was performed by Dr Francesco Simone Ruggeri, Department of Chemistry, University of Cambridge. The glomerular cell culture experiments were done in collaboration with Bristol Academic Renal Unit, School of Clinical Sciences, University of Bristol. This dissertation contains fewer than 65,000 words including appendices, bibliography, footnotes, tables and equations and has fewer than 150 figures.

Zhaoying Li
November 2017

Acknowledgements

I would like to express my sincere gratitude to my supervisor Dr Yan Yan Shery Huang for the continuous support of my Ph.D study, for her patience, motivation, and immense knowledge. Her guidance helped my in all the time of research. She has always been there for me. This thesis would not have been possible without her enormous help.

My sincere thanks also goes to my collaborators for their insightful comments, encouragements, and spiritual and technical support. In particular, I thank Dr Luai Huleihel (University of Pittsburgh, USA) for providing the decellularized extracellular materials, Dr Simon Butler (University of Cambridge, UK) for assisting me with the rheology measurement, Mr Chuan Chen and Dr Jin Mei (Wenzhou Medical University, China) for conducting the Enzyme-Linked ImmunoSorbent Assay, Dr Francesco Simone Ruggeri (University of Cambridge, UK) for conducting the Atomic Force Microscopy measurements, and Mrs Lan Ni, Mr Jack Tuffin, Prof Moin Saleem and Dr Simon Satchell (Univeristy of Bristol, UK) for providing the glomerulus cells and helping me with cell cultures.

I thank my fellow colleagues for the stimulating discussions, and for all the fun we had. My special thanks goes to Xia Li, who worked with me on many early mornings, and enlightened me with so many brilliant ideas. I cannot imagine a better colleague than him.

I would also like to thank my family: my parents, my grandma and my partner for all the sacrifices that you have made on my behalf. You made me believe in myself and sustained me thus far.

Last but not least, I would like to acknowledge EPSRC for providing me with a DTA studentship.

Abstract

Recreating organ-specific microenvironments of the extracellular matrix (ECM) *in vitro* has been an ongoing challenge in biofabrication. In this study, I present a biofunctional ECM-mimicking protein scaffold with tunable biochemical, mechanical and topographical properties. This scaffold, formed by microfibres, displays three favorable characteristics as a cell culture platform: high-loading of key ECM proteins, single-layered mesh membrane with controllable mesh size, and flexibility for supporting a range of cell culture configurations. Decellularized extracellular matrix (dECM) powder was used to fabricate this protein scaffold, as a close replicate of the chemical composition of physiological ECM. The highest dECM concentration in the solidified protein scaffold was 50 wt%, with gelatin consisting the rest. In practice, a high density of dECM-laden nano- to microfibres was directly patterned on a variety of substrates to form a single layer of mesh membrane, using the low-voltage electrospinning patterning (LEP) method. The smallest fibre diameter was measured at 450 nm, the smallest mesh size of the membrane was below 1 μm, and the thickness of the membrane was estimated to be less than 2 μm. This fabrication method demonstrated a good preservation of the key ECM proteins and growth factors, including collagen IV, laminin, fibronectin, VEGF and b-FGF. The integrated fibrous mesh exhibited robust mechanical properties, with tunable fibril Young's modulus for over two orders of magnitude in the physiological range (depending on the dECM concentration). Combining this mesh membrane with 3D printing, a cell culture device was constructed. Co-culture of human glomerulus endothelial cells and podocytes was performed on this device, to simulate the blood-to-urine interface *in vitro*. Good cell attachment and viability were demonstrated, and specific cell differentiation and fibronectin secretion were observed. This dECM-laden protein scaffold sees the potential to be incorporated into a glomerulus-on-chip model, to further improve the physiological relevance of *in vitro* pathological models.

Table of contents

List of figures

List of tables

Nomenclature

Greek symbols

δ	phase shift
η	Newtonian viscosity
η^*	complex viscosity
η_e	effective viscosity
γ	shear strain
ω	angular frequency
ϕ	volume fraction
ϕ^*	overlap volume fraction
ρ	density
σ	normal stress
τ	shear stress
ε	normal strain

Roman symbols

$\triangle L$	change in fibre length
A	cross-sectional area
c	mass concentration
c^*	overlap concentration

d deflection

E Young's modulus

F force

G storage modulus

G' storage modulus

G'' loss modulus

I the area moment of inertia

K flow consistency index

L beam length

M_{mon} molar mass of the monomer

N_{Av} Avogadro's number

r cross-sectional radius

t time

V pervaded volume

v_{mon} occupied volume of a single chemical monomer

W weight

x displacement

Composition symbols

$G(11)$ 11 wt% gelatin concentration

$G(13)$ 13 wt% gelatin concentration

$G(16)$ 16 wt% gelatin concentration

$G(19)$ 19 wt% gelatin concentration

$G(22)$ 22 wt% gelatin concentration

$S(1)$ 0.19 wt% dSIS – 18.81 wt% gelatin solution (1 wt% dSIS in protein dry mass)

$S(10)$ 1.9 wt% dSIS – 18.1 wt% gelatin solution (10 wt% dSIS in protein dry mass)

$S(50)$ 9.5 wt% dSIS – 9.5 wt% gelatin solution (50 wt% dSIS in protein dry mass)

$U(1)$ 0.19 wt% dUBM – 18.81 wt% gelatin solution (1 wt% dUBM in protein dry mass)

$U(10)$ 1.9 wt% dUBM – 18.1 wt% gelatin solution (10 wt% dUBM in protein dry mass)

$U(50)$ 9.5 wt% dUBM – 9.5 wt% gelatin solution (50 wt% dUBM in protein dry mass)

Chapter 1

Introduction

1.1 Motivation

Drug development is a long and expensive process. The typical time span of developing a drug is twelve years, from the initial discovery stage to reaching the market[1]. According to the Association of the British Pharmaceutical Industry, the average cost of development per drug is £1.15bn[2]. Advances in drug testing approaches are needed in order to reduce the cost and time, while maintaining a high product standard. Traditional approaches to pathophysiology include pre-clinical testing using *in vivo* (animal) models and *in vitro* (petri-dish) models[3]. Both models for drug research are continuously advancing. However, for animal models, there are many shortfalls that arise from the differences in genes and complications in the biologic system[4, 5]. This leads to low accuracy in predicting drug effectiveness and dose quantity. On the other hand, the petri-dish-based two-dimensional (2D) culture system cannot capture many of the physiological microenvironments known to influence cell activity[6, 7]. Hence cell behaviour *in vitro* can deviate from the physiological conditions. In order to improve the standardization and accuracy of biological models, three-dimensional (3D) *in vitro* models have attracted intense interest as potential candidates for bridging the gaps between pre-clinical and clinical models in the drug development pipeline. These models include organoid[8] and organ-on-chips[9]. The biological complexity of the models can be tailored to fit specific research purposes. Comparing to animal models, using isolated human cells and engineered biomaterials eliminates the complications caused by species difference. However, current 3D biological models still experience limitations, including maintaining high cell viability and specialised phenotypes over the long term. One possible way to overcome this limitation is to better mimic the physiological microenvironment through biofabrication.

One of the main aims of biofabrication is to recreate certain physiological aspects of the extracellular matrix (ECM), such as the physical dimensions, mechanical properties and chemical compositions. The ECM is highly organ-specific and dynamically remodelled through aging and diseases[10, 11]. The ECM is structurally and chemically complex. Broadly, the ECM can be categorised into two phases – fibril architecture and interstitial gel. In biofabrication, the fibril and gel components can be mimicked by electrospun fibres and hydrogel, respectively. In particular, electrospinning is a robust technique for fabricating nano- to microfibres from a wide range of polymer solutions, including both natural and synthetic polymers. The dimensions of these fibres are comparable to the ECM fibril component. Hence the electrospun fibres have been used in cell cultures to facilitate structural support and guide cell fate. However, there are a few limitations to the conventional electrospinning technique, including high voltage requirements, patterning controllability, limited protein loading and protein denaturation. The high voltage requirement restricts the processability of voltage-sensitive materials. The low patterning controllability is caused by bending instability during the electrospinning process. Modifications to the experimental configuration are required to improve this. Synthetic polymers, such as polycaprolactone (PCL) and polyethylene oxide (PEO), have been used as carrier polymers to facilitate protein electrospinning. In this way, the concentration of the incorporated protein is likely to be low. This constrains its biochemical activity in biological applications. Additionally, protein denaturation can be a significant disadvantage based on the particular sensitivity of cells to biochemical signalling. In this thesis, I propose a method to achieve controllable patterning of high-loading ECM-mimicking microfibres, which have not previously been demonstrated using conventional electrospinning techniques. By retaining key ECM proteins in the low-voltage electrospinning patterning procedure, I aim to improve the controllability of patterns, biochemical activity and biophysical compatibility of the microfibre mesh, in the hope of contributing towards directing and maintaining highly specialised cell functions *in vitro*.

1.2 Importance of replicating ECM microenvironments

The ECM plays a crucial role in providing biochemical cues for cell attachment and growth. It is also known to provide mechanical support and hydration to surrounding cells in two-dimensional (2D) and three-dimensional (3D) microenvironments [12–16]. Features in the hierarchical architecture of ECM span over seven orders of magnitude, from the sub-nanometre scale of molecular sequences to the millimetre scale of tissue layers[17–19]. The ECM structure is highly heterogeneous and exhibits organ-specific morphological, physical, chemical and biological properties[20]. The diversity in properties and functionalities of the

ECM is based on two phases, the fibril network and non-fibril interstitial gel[21], as illustrated in Fig 1.1. The fibril network mediates tensile strength for structural support, as well as providing topographic and biochemical cues to regulate cell adhesion and migration, and guide tissue formation. One representative example is collagen I fibrils[10]. The interstitial gel maintains cell hydration while resisting compressive stress[22]. More importantly, the interstitial gel is rich in proteoglycans and soluble factors[23]. This acts as a chemokine reservoir to influence cell growth, differentiation, and functional behaviour[24–26]. The ECM is secreted by residential cells from embryonic development and, in turn, defines subsequent cell fate and behaviour[26]. Fundamental cell-matrix interactions occur at the molecular level. Cells attach to the ECM and other substrates through focal adhesions and mechano-sensing, which act as communicative dialogues between cells and the matrix[27–29]. Different adhesion molecules interact with specific ligands from the substrates[30–32]. Depending on the nature of the substrates (peptide sequences, topographic features and stiffness), the focal adhesions influence the organisation of cytoskeletons in the cells[33]. This influences the morphology which cells adopt, and subsequently the cell's motility, proliferation and differentiation. After the initial pulling of the focal adhesion and sensing the elastic resistance of the substrate, cell sensing subsequently occurs via signalling from mechanical transducers which communicate the amount of energy required to deform the substrate for attachment[34, 35]. Thus cell migration can also be directed by changes in substrate stiffness. Based on the mechanism of cell-matrix interactions, it is not surprising that the nano- to microscale features of the substrate have paramount importance in governing cellular response. At the nanoscale, cellular protrusion sensing interacts with nanotopographical features, through which gene expression is mediated[36]. At the microscale, the organisation of microfibres can direct cell alignment and orientation[37]. This changes the apparent mechanical properties of the cell population, which can translate to tissue-level functions. Therefore, the biochemical, topographical and mechanical properties of the substrate play a critical role in regulating cell behaviour.

Decellularized extracellular matrix (dECM) is one of the closest replicates of the native ECM structure. It is derived from native tissues which are processed to eliminate materials associated with the inhabiting cells, while maximally retaining the insoluble ECM components[38]. Since the main insoluble components of ECM, such as collagen, fibronectin and laminin, are largely conserved across multiple species, dECM scaffolds fabricated from readily available xenogeneic ECM sources offer potentially compatible biological signals across multiple species, including humans[39]. Thus even dECM from animal sources may act as an appropriate *in vitro* scaffold *niche* for maintaining human cell functions. Whilst whole organ decellularization shows tremendous potential for tissue engineering and xeno-

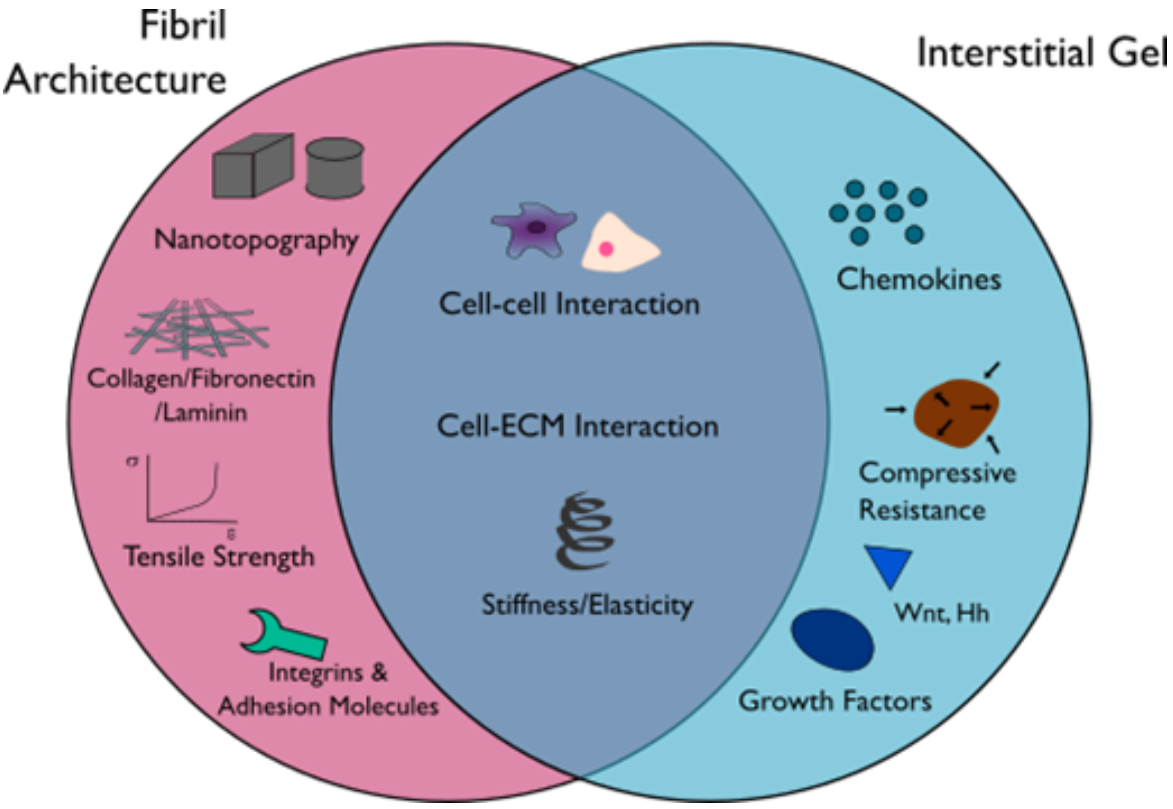

Fig. 1.1 Two phases of the ECM. Adapted from[22].

geneic transplantation, dECM materials used for *in vitro* culture models are normally reduced to the forms of coating, hydrogels or fibre mats of low dECM contents. The inability to tailor the biochemistry, topography and ultrastructures of the fibrous matrix presents a technology gap for fabricating more complex tissue model *in vitro*.

1.3 Biofabrication techniques for microphysiological devices

In order to replicate the multi-scale features of the ECM, biofabrication can potentially offer cross-scale fabrication methods to mimic specific biological aspects. A length scale comparison between the resolution of biofabrication techniques and biological features (ECM components and cells) is shown in Fig 1.2. The range of techniques leads to the establishment of *in vitro* models, which tailor micro-geometry and material properties to obtain the desired cell-matrix interaction[40, 41]. This also enables the control of cell arrangement and assembly in a 3D environment, further mimicking the physiological context[42]. The physiological relevance of these *in vitro* models closely depends on the ability of material fabrication to mimic the properties of biological tissue. Fig 1.3 (adapted from[22]) shows the microenvironmental cues which the main biofabrication methods currently focus on. The gel and fibril components of the ECM are often mimicked using 3D bioprinting and electrospinning, respectively. Soft-lithography-based microfluidics are used to deliver flow and chemical gradient. In order to provide a comprehensive review of biofabrication techniques, this section briefly introduces the 3D bioprinting and soft-lithography methods specifically for organ-on-chip devices. The electrospinning technique, on which this thesis focuses, is more thoroughly explained in the following section.

1.3.1 3D bioprinting

3D bioprinting is a versatile technique in biofabrication, particular in fabricating macroscopic tissue/organ scaffolds. This is based on its major advantages in vast material library, design flexibility, rapid prototyping and multi-material printing. In bioprinting, organ-specific properties can be replicated with the appropriate material selection. In past decades, this technology has paved the way to bioprint cells[50], tissues[51], organ models[52] and organ-on-chip devices[53]. Typically a spatial resolution of 100 μm is achieved in bioprinting and 5 μm in non-biological printing[47]. Bioprinting provides a tool for replicating the biochemical and mechanical properties of the ECM microenvironment, hence providing a matrix for cell encapsulation, cell binding and a reservoir for growth factor release. Biocompatible hydrogel, such as alginate or agarose, is extruded to create blood vessels or for cell encapsulation[54].

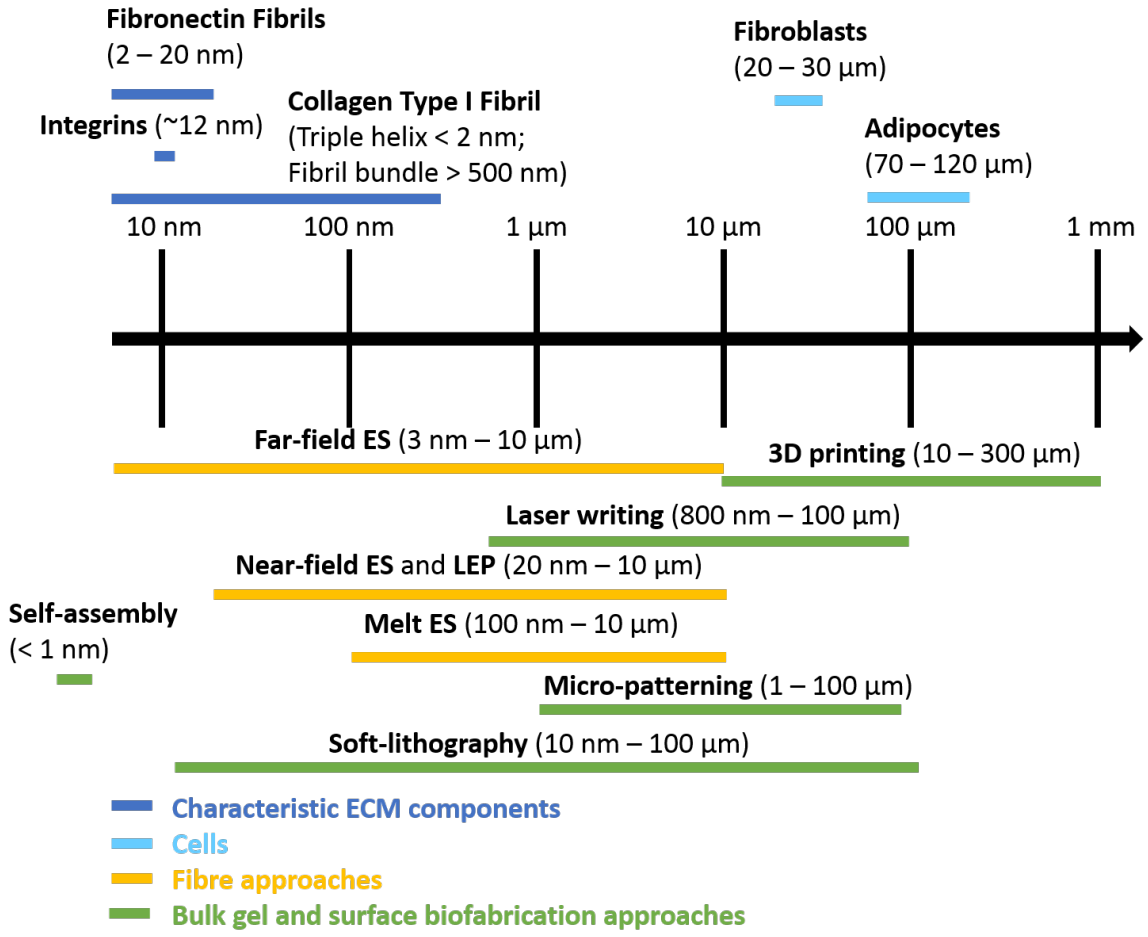

Fig. 1.2 A length scale bar contrasting tissue architectural features to the resolution of current biofabrication techniques[43–49]. ES stands for electrospinning and LEP stands for low-voltage electrospinning patterning. Adapted from[22].

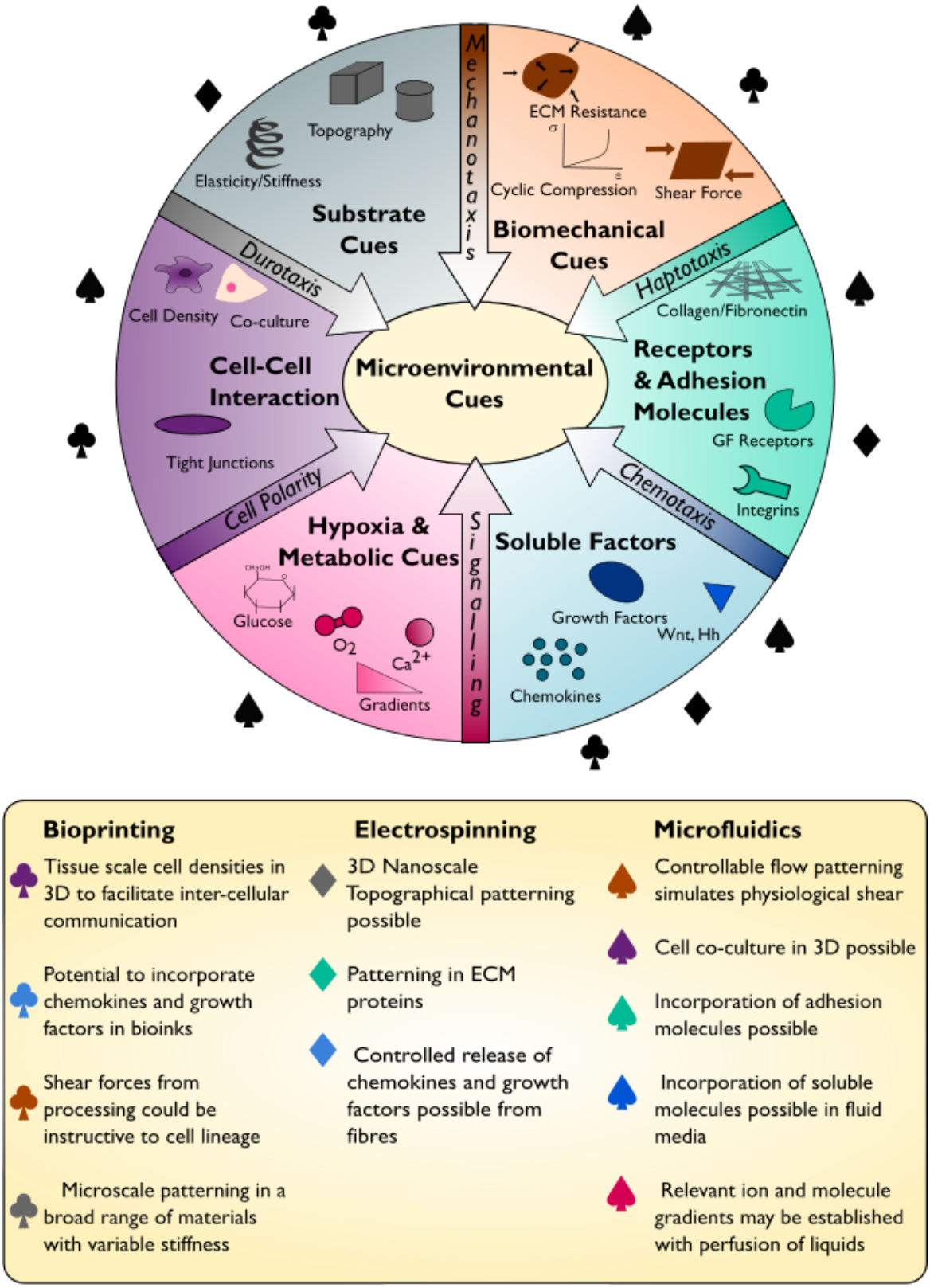

Fig. 1.3 Biofabrication methods targeting microenvironmental cues which dictate cell fate[22].

These types of hydrogel may not provide cell adhesion to promote cell attachment and differentiation. Tissue-derived hydrogel, such as collagen I, Matrigel and dECM, can provide chemical cues for cell adhesion and growth[53]. An important aspect of 3D printing is the ability of direct cell patterning. Cell-laden bioink is formed by a homogeneous mixture of cell suspension and hydrogel. This bioink can be sculpted into a desired 3D structure with controlled cell density and spatial arrangement[55]. By directly patterning bioink, the process of creating tissue/vasculature models is simplified and disruption to cells is reduced. In particular, several organ-specific cell-encapsulated dECM bioinks have been printed into 3D structures by Pati et al.[56]. In this study, polycaprolactone (PCL) was used as a supporting structure to the soft dECM gel. These constructs revealed high levels of cell viability, differential lineage commitment and ECM formation. This opens up the potential of tissue printing. Moreover, cells can be loaded into small carriers with different geometries and porous architectures, recognised as micro-carriers[57]. Commercially available micro-carriers are made with glass, gelatin and collagen. Micro-carriers are particularly useful in the scale-up tissue printing process using hard polymers to address the lack of diffusion issue in hard polymers. A porous micro-carrier can promote cell proliferation and improve cell viability within hard polymers. The current limitation of printing micro-carriers lies in the 3D assembly, degradation-induced toxicity and nozzle clogging. Scaffold-free cell aggregates can also be sculpted into 3D scaffolds[58]. This gives the highest cell density among other bioinks, resulting in better cellular interactions, greater ECM secretion, quick tissue formation and long-term phenotype stability. The disadvantage of cell aggregates includes their weak mechanical stiffness, high cell number requirements and hypoxia induced by limited oxygen diffusion.

1.3.2 Soft-lithography and microfluidics

Soft-lithography is a template-based fabrication method that has been widely used for applications such as semiconductors, energy storage, optical storage media and biomedical devices[59, 60]. Its main advantages include cost effectiveness, high reproducibility and high lateral resolution. Polydimethylsiloxane (PDMS) is the most common material used as it can make reversible conformal contact with substrates with complex geometries. In general, soft PDMS can replicate minimum features of >100 nm[61]. Taking advantages of its deformability, PDMS has been cast to form pillars, valves and stretchable membranes, and assembled into microfluidic devices[62]. When used for tissue or organ models, these microfluidic devices are used to confine the spatial arrangement of cells to establish cell patterning and introducing flow to mimic the physiological shear stress[63–65]. This is especially useful for replicating both the geometry, mechanical stimuli and dynamics of a

physiological environment. This leads to the development of organ-on-chip models[66, 67]. Organ-on-chip models use human cells to replicate the key functional unit that provides an organ-level response *in vitro*. Alongside other techniques, such as synthetic biology and imaging microscopy, these models can provide new insight into the fundamental mechanism of cell behaviour. To date, many organ-on-chip models have been developed to simulate different organ functions, including lung[9], heart[62], liver[68], intestine[69], kidney[70], brain[71] and bone[72]. Considering the kidney in specific, the complex hierarchical structures are replicated by specific microfluidic models. Firstly, the glomerulus-on-chip model, developed by Zhou et al., recreated a glomerular filtration interface[73]. By recreating the glomerular filtration barrier in a microfluidic device and introducing mechanical stretching and medium flow, a disease model of glomerular hypertension was established. This model allows real-time monitoring of cell morphology and protein expression instead of relying on end-point analysis. Secondly, a human kidney proximal tubule-on-chip was built by Jang et al. to replicate molecular reabsorption and ammonium secretion[70]. Distal tubule-on-chip models were constructed, to different extents, in a few studies. Baudoin et al. developed a renal microchip to study cell differentiation under mechanical stimuli[74]. Ramello et al. established a model to study the mass transfer kinetics and response to nephrotoxicity[75]. In order to gain a better understanding of the renal epithelial cell, Ferrell et al. developed a renal microchip which enables the measurement of transepithelial electrical resistance (TEER) *in vitro*[76]. Two collecting-duct-on-chip models were developed by Jang[77, 78]. Other representative organ-on-chip models are displayed in Fig 1.4. The advantages of organ-on-chip models include: long culture periods (can be up to 30 days), small volume requirements, image-assisted real-time study, and high reproducibility. These models demonstrate correlative results to animal models and open up tremendous potential in the field of drug testing. Nevertheless, one of the intrinsic shortfalls in organ-on-chip models is their lack of matrix diversity. A PDMS membrane is physically and chemically different from the ECM matrix. A single type of protein coating cannot replicate the diversity of chemical compositions in ECM. On the other hand, encapsulating fibrous matrix requires multiple fabrication processes[79]. Hence, improving the matrix diversity in microfluidic devices still remains challenging.

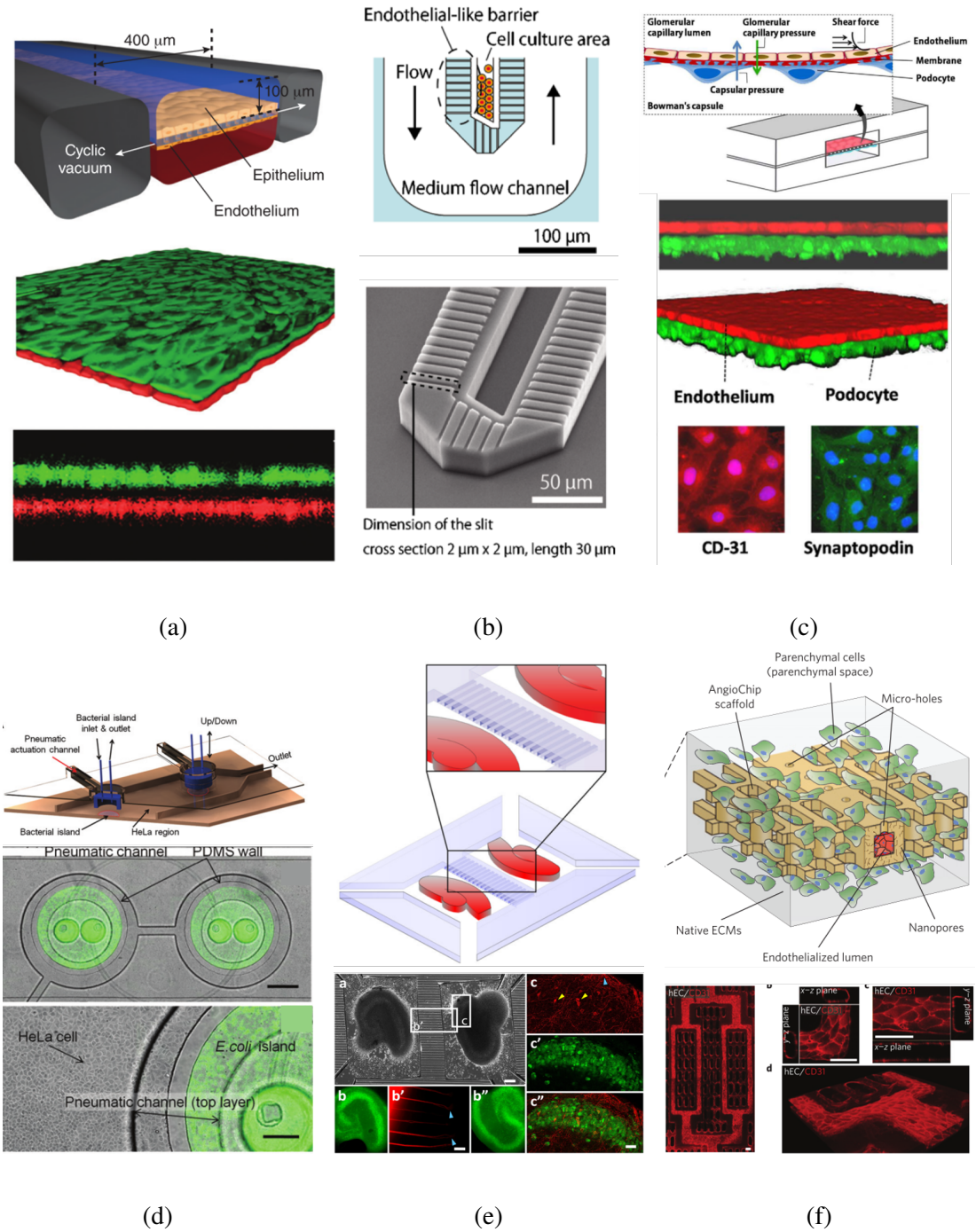

Fig. 1.4 Examples of organ-on-chip models. (a) Lung-on-chip which replicates the alveolar-capillary interface. Human alveolar epithelium (green) and the endothelium (red) were co-cultured on the porous PDMS membrane[9]. (b) Liver-on-chip model mimicking the structure of a hepatic cord[68]. (c) Glomerulus-on-chip model comprising both mice glomerular endothelium and mice podocytes monolayer, recreating the blood-to-urine barrier[73]. (d) Intestine-on-chip model, establishing co-culture of HeLa cells and bacteria[69]. (e) Brain-on-chip model[71] and (f) biodegradable vasculature-on-chip model[80].

1.4 Mimicking the fibril architecture using electrospinning

Fibril structure is a crucial component of the ECM. Nano- and microfibril bundles, such as collagen I, mediate structural support to surrounding cells[10]. Electrospinning enables bio-mimicry of the fibrillar structure by processing a wide range of materials into nano- and microfibres[81]. Polymer materials, ranging from synthetic to natural, can be processed into fibres with defined dimensions using electrospinning. There are three main types of electrospinning that are widely used by researchers over the world: far-field electrospinning (solution based), near-field electrospinning (solution based) and melt electrospinning. Fig 1.5 shows the schematic diagram of each electrospinning technique.

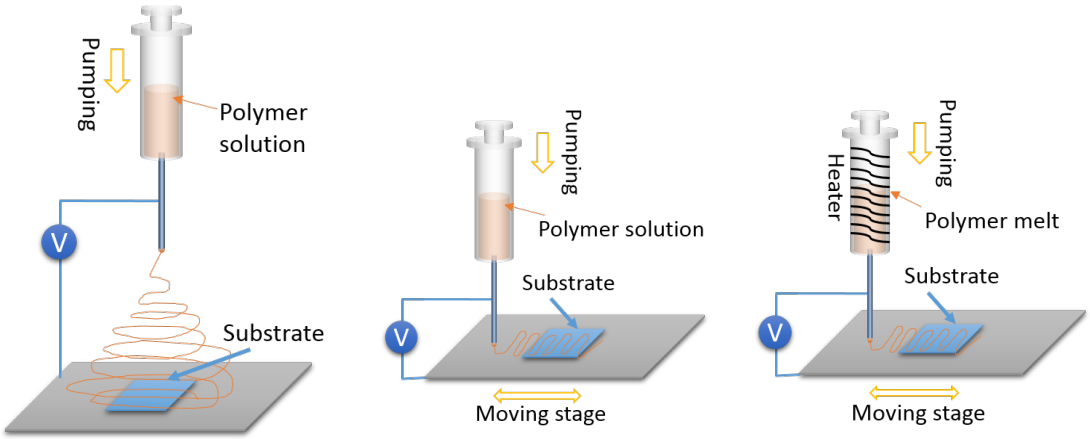

(a) (b) (c)

Fig. 1.5 Schematic diagram of electrospinning techniques. (a) Conventional far-field electrospinning; (b) near-field electrospinning and (c) melt electrospinning.

1.4.1 Far-field electrospinning

Far-field electrospinning was the first conventional electrospinning technique developed. Formhals Anton first patented electrospinning as a fabrication technique for textile yarns in the 1930s[82]. Despite the establishment of the electrospinning technique, however the phenomenon was not fully understood for another 30 years. In 1964, Sir Geoffrey Taylor described the driving mechanism of fibre formation in electrospinning[83]. Hence the deformation of the droplet which initialises the electrospinning process is called the Taylor cone. Since then, numerous studies have been done to extend the understanding of the electrospinning mechanism as well as to improve this fabrication technique[44, 84, 85]. The conventional setup of far-field electrospinning includes a high voltage source, a pump-

controlled reservoir of polymer solution (usually a syringe) with a metallic tip and a collecting stage, as shown in Fig 1.5a. The voltage source is connected to a polymer solution to introduce charge injection and solution discharge. Upon the application of a high voltage, the electric field strength is used to overcome the surface tension of a suspended polymer droplet. Once the voltage exceeds the critical value, the droplet deforms into a Taylor cone and propels a fine stream of polymer jet towards the collecting substrate which has a low electric potential. This polymer jet then solidifies to form nano- to microfibres. As the polymer jet travels from the suspended droplet towards the collecting substrate, several forces influence the trajectory of the jet. These include tensile force induced by the flow, gravitational force, aerodynamic force from the atmosphere, intrinsic rheological and Coulomb force[86]. This leads to chaotic bending instabilities in the polymer jet path, fibre thinning, and solvent evaporation[87]. As a result, the nano- and microfibres created by far-field electrospinning have random orientations. The fundamental mechanism of the bending instability was believed due to a few contributing factors, such as the Coulomb repulsion within the polymer jet and the increase in charge density during fibre thinning. Later study revealed that a whipping instability caused this bending process[87, 88]. Occasionally, splitting of the polymer jet occurs during this path, giving rise to fibres with even smaller diameters. Ultra fine fibres with diameters from <3 nm to over 1 μm have been fabricated using the far-field electrospinning technique[89]. During the development of electrospinning, a range of polymer materials and fabrication configurations have been optimised to improve the versatility of this technique. Fig 1.6 shows some examples of the morphology range obtained using far-field electrospinning. These are achieved by tuning fabrication parameters, including intrinsic solution properties and extrinsic operating configurations.

Influencing parameters

Far-field electrospinning is a solution-based fabrication method. The transformation from polymer solution to solid nano- and microfibres is influenced by a number of parameters. These parameters can be characterised into three categories: intrinsic polymer solution properties, extrinsic operating parameters and ambient factors[89].

1. **Intrinsic polymer solution properties:**
   The intrinsic solution properties play a crucial role in determining the voltage requirement, fibre continuity and fibre morphology. Typical solution properties include viscoelasticity, volatility, conductivity and surface tension. These parameters are the macroscopic representation of the molecular weight, molecular arrangement and entanglement in the solution. The polymer concentration influences both viscosity and surface tension. Surface tension favours minimising the surface area by driving the

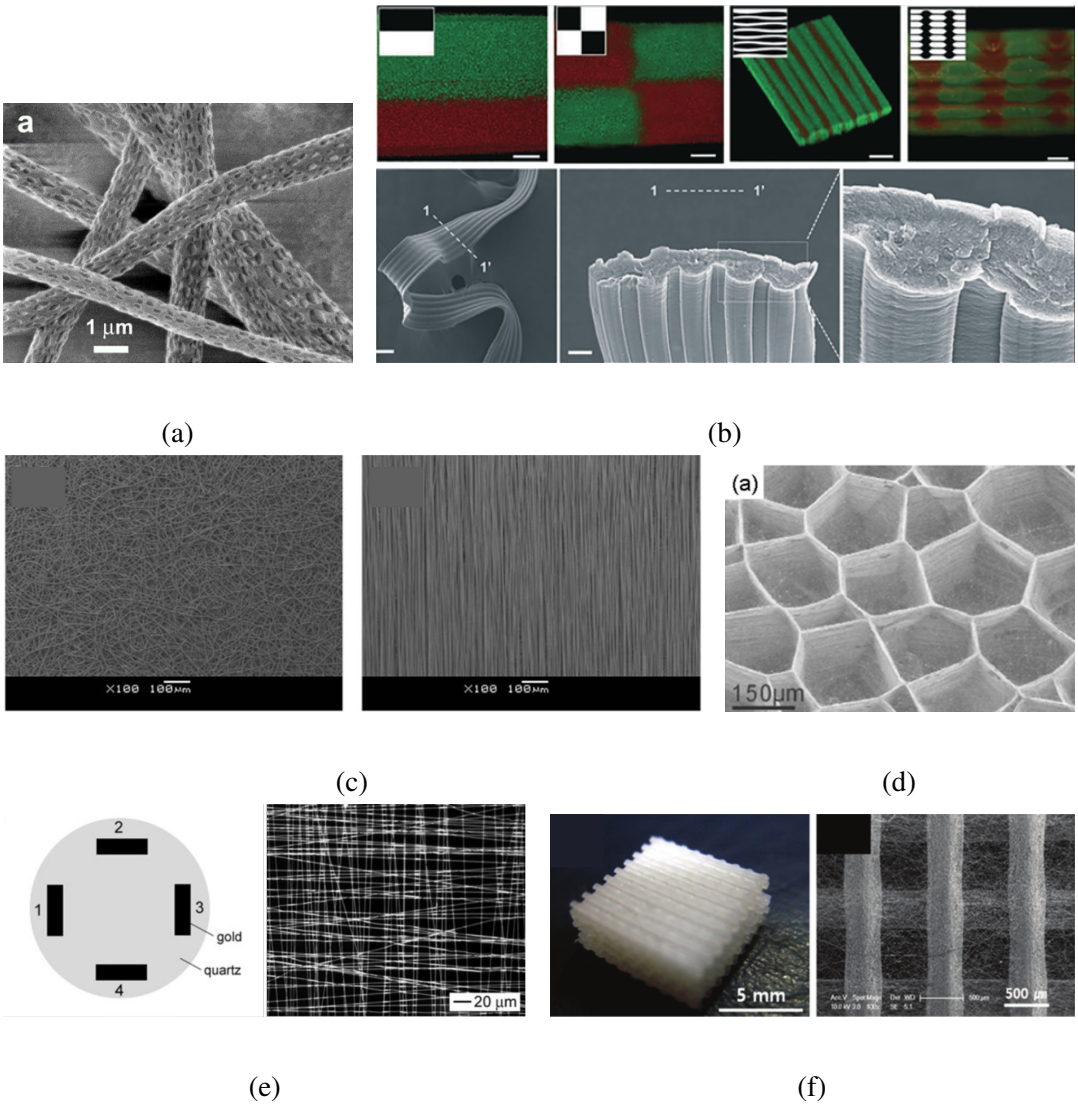

Fig. 1.6 Microfibre fabrication using far-field electrospinning. (a) PLLA fibres with porous morphology[90]; (b) alginate fibres with grooves[91, 92]; (c) controlling PLGA fibre alignment by using rotating drums[93]; (d) controlling fibre alignment by self-assembly, with honeycomb structure formed by PEO fibres[94]; (e) controlling fibre pattern by collector geometry[95] and (f) hybrid structure combining electrospinning and 3D printing[96].

polymer into droplets. Viscosity tends to resist rapid changes in shape and maintains a smooth surface. At lower concentration, the viscosity effect is lower than the surface tension, resulting in beaded morphology on the fibres. As the concentration increases and the molecular entanglement increases, the viscosity effect dominates over the surface tension. In this condition, smooth and defect-free fibres can be fabricated[97]. Increase in viscosity also leads to an increase in fibre diameter. The elasticity is determined by the nature of the polymer chain. Higher elasticity aids the production of continuous fibres[98]. However, this is not a necessary condition for continuous fibre production. The volatility of the solvent is critical to determining fibre formation and surface porosity at the single fibre level. In far-field electrospinning, volatile solvents are used to achieve sufficient solvent evaporation between the tip and the substrate, ensuring that fibres are fabricated with a circular cross-section. Highly volatile solvents can be used to induce phase separation during fibre solidification[90]. In this way, porous structures can be introduced at the fibre surface, further increasing the surface-to-volume ratio of the as-spun fibres (shown in Fig 1.6a). This porous morphology is particularly useful in filtration and drug delivery, as small particles can be trapped within the nano-pores. The conductivity of the polymer solution determines the density of charge carried along the polymer jet. In general, the electrospinnability increases with increasing solution conductivity. This can further influence the fibre thickness and morphology[99]. Solutions with higher electric conductivity experience higher tensile force within an applied electric field. This force stretches the polymer jet and decreases the fibre diameter[100]. In addition, the electrostatic repulsion from high charge density along the fibres tends to maximise the surface area and favours the formation of a smooth fibre.

2. **Extrinsic operating parameters:**
   The extrinsic operating parameters include the applied voltage, electric field distribution, working distance and the solution flow rate controlled by the pump. The applied electric field strength exhibits direct influence on fibre morphology and diameter by changing the density of charge and the magnitude of the Coulomb force. A critical electric field strength is required to initiate fibre formation. The specific value of the corresponding voltage is related to the particular polymer solution and working distance. Suboptimal field strengths provide low charge density and lead to bead formation[89]. Increase in electric field strength gives rise to production of smooth fibres of increasing diameters. The distribution of the electric field can influence fibre orientation as it determines the direction of external force of the polymer jet. The spatial distribution of the electric field can be altered by using auxiliary electrodes[101]

or magnetic fields[102], as well as by changing the geometric design of the collecting substrate[85]. In addition, the polymer flow rate also affects the fibre size as well as the fibre shape[103]. A diminishing flow rate cannot sustain continuous fibre patterning, whereas an excess flow rate results in thick fibres and even bead-defect formation. For the fabrication of an as-spun fibre mat, both the fibre thickness and the porosity between fibres increase with increasing flow rate[104]. Therefore, an optimal flow rate should be controlled complementary to the applied voltage and working distance. The working distance is the distance between the tip and the collecting substrate. This working distance contributes to the electric field strength and thus can also influence the fibre diameter. When the working distance is small, electrospraying can occur instead of electrospinning.

3. **Ambient factors:**
   The ambient factors include solution temperature, humidity and air velocity. These atmospheric parameters strongly influence the polymer jets and resulting electrospun materials. The temperature is closely linked to the volatility of the solvent and the viscosity of the polymer solution[105]. This effect is complicated as rising temperature increases the volatility but decreases the viscosity. The combined effect is different for each polymer solution. Humidity reflects the water content in the atmosphere. Some inorganic polymer solutions are immiscible in water. Therefore a higher water content can cause phase separation of the polymer jet and hinder the continuous fibre production[106]. Far-field electrospinning setups are enclosed within a chamber for safety as well as to maintain a stable environment. The air flow within the chamber can alter the solvent evaporation rate as well as the fibre pattern[107].

In order to fabricate functional fibrous scaffolds, several requirements should be addressed. Firstly, the average fibre diameter should be consistent and controllable. Secondly, the fibre surface should be defect-free or defect-controllable. In general, smooth fibres are desirable. For other applications, such as drug delivery, porous or bead structures can be favoured. The exact fabrication conditions for different fibre morphologies should be well understood. Thirdly, continuous, sustainable and reproducible fabrication is desired. The exact fabrication parameters to meet these three criteria depends on the specific polymer solution and the purpose of the study. Hence, each parameter should be optimised to achieve high throughput stable nano- and microfibre production.

Patterning control

Due to bending instability, the fibres collected are inevitably randomly distributed. This intrinsic nature of far-field electrospinning imposes limitations when used for geometrically dependent purposes, such as the fabrication of electronic devices, energy storage devices, and biological devices. In order to control the pattern of the as-spun fibres, the collector configuration was modified. To date, a number of collector configurations have been developed, including a stationary plate[108], rotating drum/disk[109] and coagulation bath[110]. The stationary plate is the most conventional collector configuration, in which either a conductive or non-conductive plate is used for fibre collection. With a flat plate, disordered fibres are uniformly deposited onto the plate. The porosity of the fibre mat can be tuned by increasing the duration of electrospinning. Using parallel conducting plates with a gap in between, disordered fibres are collected on either plate while parallel arrays of fibres are formed across the gap[95] (shown in Fig 1.6c). This approach is elegant, but has limitations when it comes to scaling up and controlling the stacking density of parallel fibres. The fibre pattern can be further refined by modifying the geometry of the collecting aperture. Another method of obtaining aligned fibres is to collect them with rotating drums[109]. The degree of fibre alignment is closely dependent on the angular velocity of the rotating drum. This method allows the creation of a cylindrical structure made of nanofibres. This is particularly useful for vascular graft applications. Another collecting method is to use an aqueous bath[110]. By choosing the type of liquid according to the polymer solution, this method can be used to leech out the solvent, crosslinking the polymer or inducing phase separation to modify the surface morphology of the fibres. Besides modifying collector configurations, nanofibre self-assembly can be used by tuning the polymer solution properties, fabrication conditions and electric field[111]. Self-assembled 3D honeycomb structures were fabricated using polyacrylonitrile (PAN), poly(vinyl alcohol) (PVA) and PEO at a relatively low polymer concentrations[94] (shown in Fig 1.6d). This phenomenon is observed at low humidity within a narrow range of polymer concentration. The mechanism of this self-assembly is based on the surface tension and electrostatic forces between the incomplete solidified fibres. Centimetres-long twisted yarns were self-assembled vertically upwards from a grounded collector[112]. This is because of the high electrical conductivity of the polymer solution. Once a yarn is formed and connected to adjacent fibres, subsequent fibre deposition may occur preferably on the yarn. However, once the high electric field is removed, the yarn structure may collapse, which restricts their practical uses. Self-assembled 3D fibrous stacks can be formed due to electrostatic repulsion between the nanofibres[113]. This fibrous stack can be built into the macroscopic lengthscale, made from randomly-packed nanofibres in all x-y-z dimensions. This structure is sensitive to the collecting substrate and can only be built

on conductive plates. If the collector is insulating, the electrostatic repulsion is reduced and a 2D film is formed instead.

Biological applications

Electrospun microfibres have been used for tissue regeneration and directing cell fate as a synthetic ECM fibrous *niche*[114, 81]. Due to its ability to form aligned scaffolds for anisotropic mechanical and biological properties, electrospinning has been used for engineering a number of tissues, including vasculature[115, 116], bone[117], neural[118, 119] and tendon/ligment[120]. A vasculature graft made of tubular nanofibre scaffold was developed to facilitate cell attachment and vascularisation[121]. Inoguchi et al. fabricated a compliant vascular graft using electrospun poly(L-lactide-co-e-caprolactone) *niche*[122]. The porosity of the graft enables nutrient permeability while being resilient to pulsatile flow. Cell attachment and growth was demonstrated under directional flow. Another biological application of electrospinning is in bone engineering. It was discovered that the scaffold stiffness changes according to fibre alignment[117]. Based on their tunable mechanical properties and degradation rate of polymers such as polycaprolactone (PCL) and poly(lactic-co-glycolic acid) (PLGA), nanofibre scaffolds have been used for bone regeneration[123] and skin tissue engineering[124]. When transplanted, the PCL scaffold supported mineralized tissue formation, which can be potentially useful for the treatment of bone defects[125]. The fibres obtained through electrospinning can improve cell attachment and spreading due to their surface nanotopography[126]. This has been used for guiding cell outgrowth for nerve regeneration[127]. Electrospinning has also been used with stem cell culture to guide cell differentiation through topographical cues. Christopherson et al. discovered that neural stem/progenitor cell differentiation is particularly sensitive to electrospun fibre diameter[128]. Neuronal differentiation can be achieved by culturing human embryonic stem cells on electrospun polyurethane scaffolds[129]. These studies mainly used synthetic polymers to mimic the topographical and physical structure of fibrous ECM. Natural proteins can also be processed with electrospinning. This includes collagen[108], gelatin[130], silk[131] and polysaccharide/protein composites[132]. However, it has been reported that the electrospinning process can cause degradation of collagen[133]. Processing complex protein composites without altering their chemical structure still remains challenging in electrospinning.

In summary, far-field electrospinning is a robust technique for nano- and microfibre fabrication. By modifying the experimental configuration, random, ordered and 3D complex nanofibrous assemblies can be obtained for a range of polymers. The wide processable

polymer library contains a number of both natural and synthetic polymers. The main advantages of electrospinning are its cost-effectiveness, high-throughput and material flexibility. However, there are several limitations to far-field electrospinning which restrict its further potential for use. Firstly, although the global fibre orientation can be controlled, one cannot pattern the nano- and microfibres in far-field electrospinning. The lack of localised deposition and patterning hinders its use for sensors where accurate geometric design is important. Secondly, the high electric field and solution preparation can irreversibly damage the molecular structures of proteins. This causes loss of protein function and affects the biological application. Thirdly, the charge density causes electrostatic repulsion between adjacent fibres. This imposes a minimum threshold on the pore size of the fibrous mesh. As a result, the pore size is usually controlled by a prolonged electrospinning period which spontaneously increases the thickness of the mesh. Some of these challenges have been overcome by other electrospinning techniques such as near-field and melt electrospinning.

1.4.2 Near-field electrospinning

Near-field electrospinning has been developed particularly to fulfill the precise printing requirements unmet by far-field electrospinning. In the near-field electrospinning protocol, the distance between the tip and collector is reduced to between 0.5 mm and 3 mm[134]. This is a significant change in distance compared to a typical working distance of 10 cm in far-field electrospinning. The reduction in working distance avoids bending instability formation. In this way, straight polymer jets can be collected on the substrate. The collector can move and the moving path is controlled by a computer program, such as LabView. By moving the collector during polymer jet projection, the fibres are printed onto the collecting substrate following the path of the collector. Fig 1.7 shows some examples of near-field electrospinning. Along with the decreased working distance, the applied voltage is reduced from tens of kilovolts to below 1 kV. The lowest voltage reported in near-field electrospinning is 200 V[135]. This is because, with the short working distance, the voltage requirement to maintain the same electric field strength is lower than that of far-field electrospinning. However, occasionally the reduced voltage is insufficient to initialise polymer jet formation. In this case, an array of sharp tips can be used to disrupt the droplets[136]. The mechanical disruption breaks the surface tension and initialises the formation of the polymer jet. In a nutshell, apart from the change in working distance, the fundamental mechanisms of near-field and far-field electrospinning are the same. Hence, theoretically, all polymer materials that are processable using far-field electrospinning could be patterned using near-field electrospinning. In practice, polyethylene oxide (PEO)[137], PCL[138], polystyrene (PS), inorganic materials[139], carbon nanotube composite[140] and co-shell fibres[141]

have been patterned using near-field electrospinning. On the other hand, it is important to note some disadvantages of near-field electrospinning. Firstly, the short working distance reduces the travel time of the polymer jet between the tip and the collector. This causes incomplete solvent evaporation, which mean that the fibres are still wet when attaching to the substrate. Hence a flattened cross-section is obtained instead of the circular cross-section obtained in far-field electrospinning[142]. The short working distance also restricts fibre thinning by axial stretching and solvent evaporation. As a combined result, the minimum fibre diameter is 100 nm. This problem is addressed by reducing the diameter of the tip. Sun et al. demonstrated the patterning of nanofibres with diameters of 50 – 500 nm by using a tip with 25 μm diameter[134]. This is compensated by the increase in cost and limitations in patterning viscous solutions. The thinnest fibre is reported by Bisht et al., which had a diameter of 16.2 nm[143]. Yet this is not continuously patternable. Secondly, the close distance between the polymer droplet to the substrate can cause electric sparking which damages the voltage source as well as causing fire. The suspended droplet needs to be manually refreshed regularly to prevent excess accumulation. Thirdly, the fibre production rate of near-field electrospinning is lower than that of far-field electrospinning. The reduction in throughput also leads to drying of the droplet. Once the droplet has dried, the electrospinning process stops as no polymer jet can form. This hinders the continuity of near-field electrospinning.

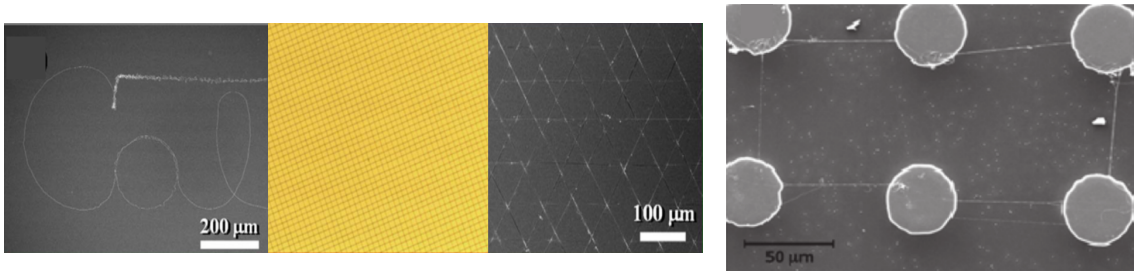

(a) (b)

Fig. 1.7 Near-field electrospinning (a) by continuous and precise deposition[137] and (b) on 3D substrate[135].

1.4.3 Melt electrospinning

Melt electrospinning is another novel technique used to fabricate nano- and microfibres. Melt electrospinning enables both precise and continuous patterning of fibres with fine diameters[144]. In melt electrospinning, a heated spinneret is used to melt and extrude the polymer. A voltage ranging between 700 V to 60 kV is applied between the spinneret and the

movable collector to initialise formation of the jet[145]. Similar to near-field electrospinning, straight fibres can be accurately printed by moving the collector in a designed pattern and at a speed higher than the deposition rate. The polymer is first heated till melted, extruded, formed into fine polymer streams and rapidly cooled to room temperature as the jet leaves the spinneret. The rapid annealing, together with the axial stretching force imposed by the electric field strength, causes fibre thinning. As a result, melt-electrospinning can consistently produce microfibres in the 5 to 40 μm range[146]. Sub-micron fibres, as low as 270 nm in diameter, are also reported[147]. Some examples of melt electrospinning are shown in Fig 1.8.

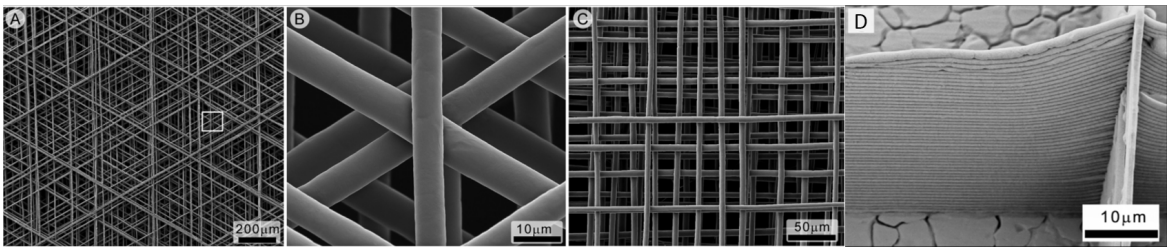

Fig. 1.8 Melt electrospinning. (a) – (c) Precise patterning of fibre arrays[43] and (d) fibre stacking in 3D[148]

Based on the precise printing ability, melt electrospinning is similar to the additive manufacturing method mentioned in the earlier section, but at a scale of several orders of magnitude lower. Similar to extrusion-based 3D printing, melt electrospinning can be used to stack microfibres layer-by-layer into a 3D structure. This highly ordered micro-architecture is not achievable using any conventional electrospinning techniques. Such a structure can be used as a backbone to reinforce a hydrogel. One major difference between this micro-structure to that fabricated using a 3D printer is that the intrafibre spacing relative to the fibre diameter is much higher in melt electrospinning. The capability of printing regular lattice structures at the microscale opens up new applications in biological engineering, such as in bone regeneration. In addition, melt electrospinning can be applied in conjunction with far-field electrospinning to fabricate a bimodal scaffold containing both regular microfibrous and random nanofibrous elements[149]. By maintaining a high temperature at the spinneret, melt electrospinning enables continuous and accurate printing of microfibres into flexible designs. This compensates for the drawbacks of both far-field and near-field electrospinning. However, there are two major disadvantages of melt electrospinning: cost and material selection. The cost of melt electrospinning is higher than near-field electrospinning due to the heating requirement and precise stage control. Melt electrospinning also has limited material selection. Because of the heating requirement, thermoplastics are the main focus

of melt electrospinning. Polymers including polypropylene (PP), PLA and PCL have been widely used in melt electrospinning studies. A mixture of glass and polymer has also been patterned using melt electrospinning. These thermoplastics yield hard polymers which limits the biological applications. Advancing research is ongoing to expand the applications of electrospinning techniques as well as to overcome their shortfalls.

1.5 Research aim and contribution

Since cells are particularly sensitive to the biochemical, mechanical and topographical properties of the surrounding substrate, it is hypothesised that the cells would exhibit a more physiological behaviour when subjected to a closer replication of the native ECM microenvironment. To test this hypothesis, I aim to fabricate a microfibre mesh membrane, which mimics the biochemical, mechanical and topographical properties of the glomerular microenvironment. The tissue-specific biochemical complexity was recreated with high-loading of urinary bladder dECM. The mechanical and microtopographical features were replicated by creating a microfibre mesh structure. However, there are limitations in the existing techniques when mimicking the fibrous microenvironment of the native ECM:

1. In a biochemical aspect, the solvent system can cause protein to denature. This significantly reduces the effective amount of protein incorporated in the microfibres. Since cells are particularly sensitive to the chemical cues of the surrounding microenvironment, the low-loading of proteins may cause deviations in cell activities.

2. In a physical aspect, conventional electrospinning techniques do not allow the construction of a micron-thickness mesh membrane using proteins. Far-field electrospinning offers high throughput and wide material library. However, the mesh size is limited due to electrostatic repulsion[150]. Reducing the mesh size comes at a cost of increasing mesh thickness. This hinders the cross-talk of cells across the membrane. Near-field electrospinning has not demonstrated rapid patterning of closely-packed fibres. Melt-electrospinning enables precise patterning of fibres to the micrometre resolution but with limited processable material.

3. There is a growing demand in combining biofabrication techniques to achieve cross-scale and multi-material fabrication. To date, a few studies have demonstrated the combination of 3D printing with electrospinning, and soft-lithography with electrospinning[79, 151]. However, both require multiple-step fabrications. Hence, a high throughput functional device with simplified fabrication processing is still to be established.

In this research, I aim to address these three problem using the low-voltage electrospinning patterning (LEP). LEP was developed by a former research student, Dr Xia Li who was a PhD student in Dr Yan Yan Shery Huang's group. He established rapid microfibre-patterning of a range of polymers, including polystyrene, polycaprolactone and silver-polyethylene oxide co-shell fibres. LEP is a modern modification of near-field electrospinning. This allows continuous microfibre patterning at a low voltage (typically $<$250 V). The material selection is potentially as wide as conventional electrospinning. I adapted LEP for protein microfibre fabrication. To achieve high-loading of dECM protein composite, gelatin was chosen to facilitate microfibre production and solvent was carefully selected to ensure minimum adverse effect on proteins. With controllable patterning and low working voltage, the microfibres were packed into high density without increasing the mesh thickness. The substrate flexibility is significantly improved comparing to other electrospinning methods. Insulating materials, including PDMS and hydrogel, can be used as the collecting substrate. This enables simplified cross-scale fabrication as the microfibres can be easily incorporated with 3D printing and microfluidics.

This study presents the fabrication of a biofunctional ECM-mimicking protein membrane. This membrane contains high-loading of the key ECM protein composites, including collagen IV, laminin and fibronectin. The protein membrane can be flexibly incorporated into well-established biofabrication techniques. Furthermore, the topography of the membrane has not been previously demonstrated. Fig 1.9 shows a summary of the existing membrane-based cell culture systems. The ECM protein membrane, formed by a single layer of densely packed microfibres, has micron-thickness and can be suspended over complex geometries. The tunable mechanical and dimensional properties provides additional freedom to the current biofabrication techniques.

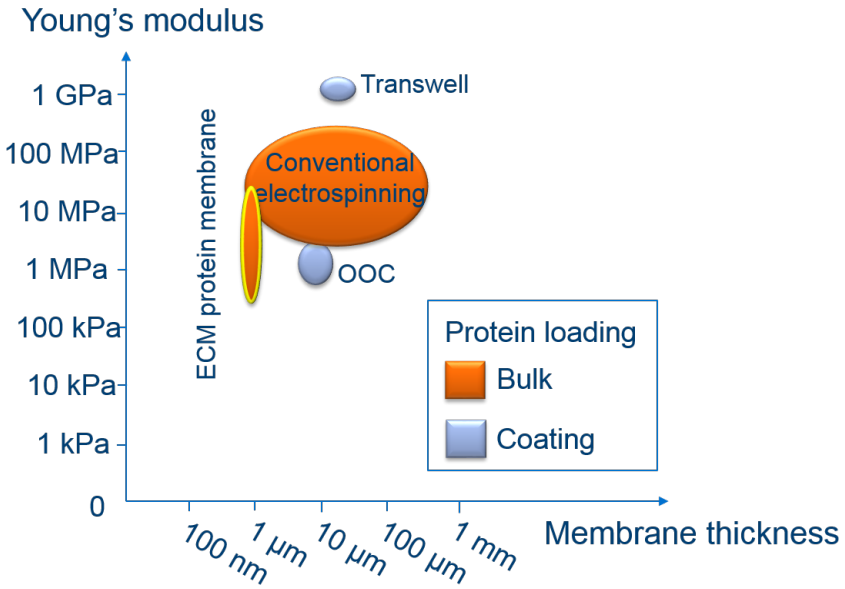

Fig. 1.9 An overview of the physical and chemical properties of the existing membrane-based cell culture system. OOC stands for organ-on-chips. The properties of the ECM protein membrane presented in this study are highlighted in yellow. Based on the tunable Young's modulus and micron-thickness, it widens the mechanical and dimensional resolution of biofabrication techniques.

1.6 Thesis layout

This thesis follows the fabrication process of an integrated cell culture device. The thesis structure is shown in Fig 1.10. A more detailed introduction is given in each chapter. The methodology of patterning dECM-laden fibres using low-voltage electrospinning patterning (LEP) is explained in **Chapter 2**. In this chapter, the relationship between the viscoelastic property of dECM-laden gelatin solution and the resulting LEP fibre morphology is investigated, and the optimum processing condition is determined. The patterning of fibrous networks on an insulating substrate with intrinsic geometry is investigated, to explore the configuration of a cell culture device. Based on the relative precise patterning ability of LEP, the fibre density can be controlled. Membranes can be fabricated, from distinct fibre grids to a non-woven mesh. Based on the low voltage requirement of LEP, the patterned fibres can be suspended over complex geometries, providing a free-standing layer for cell cultures. **Chapter 3** analyses the chemical and mechanical characterisation of the dECM-laden gelatin microfibres. The chemical integrity of the dECM material is measured using complementary methods, including Immunofluorescent Staining, Fourier Transform Infrared Spectroscopy and Enzyme-Linked ImmunoSorbent Assay. Using LEP, the dECM-laden material can be fabricated into microfibres while maintaining the major chemical diversity and structures. The mechanical characterisation includes the stiffness of a single microfibre and its swelling characteristics. This integrated cell culture system is then used in the co-culture of glomerular endothelial cells and podocytes, as explained in **Chapter 4**. These are two types of highly differentiated cells in a glomerulus which forms the blood-to-urine barrier. In this study, the cell morphology and phenotype are investigated. Fibronectin distribution is measured as an indication of ECM secretion. The conclusions are discussed in **Chapter 5**. Future perspectives and outlooks are outlined in **Chapter 6**.

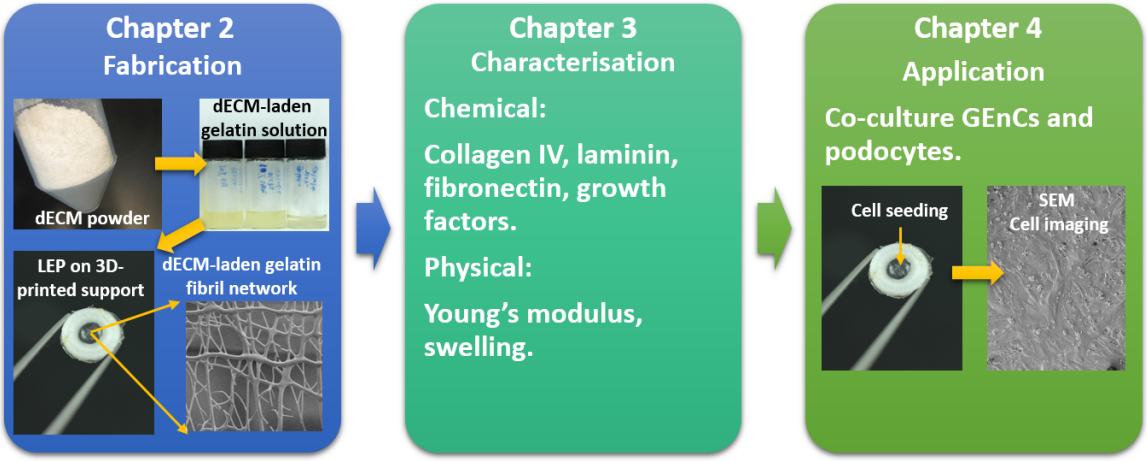

Fig. 1.10 The structure of this thesis. Chapter 2 describes the fabrication process of dECM-laden gelatin fibril structure, Chapter 3 describes the chemical and physical characterisations of the microfibres, and Chapter 4 describes the application of the dECM-laden microfibres in human kidney cell culture. Chapter 1 (introduction), Chapter 5 (conclusion) and Chapter 6 (future work) are not shown here.

Chapter 2

Structuring high-loading dECM-laden microfibres with LEP

Abstract

Extracellular matrix (ECM) regulates and directs cell fate through biological effects and microenvironmental interactions. The biochemical composition of ECM is complex and organ-specific. Decellularized ECM (dECM) derived from dissected organs shows the possibility of retaining most biochemical ingredients of the ECM whilst eliminating previous residential cell components. However, the ultrastructure of the ECM scaffold is damaged during the decellularization process for non-whole organ decellularization. This chapter demonstrates high resolution patterning of dECM-laden microfibres using the low-voltage electrospinning patterning (LEP) technique. Decellularized urinary bladder matrix (dUBM) and small intestinal submucosa (dSIS) matrix powers were acid dissolved and incorporated into gelatin solutions, and patterned using LEP. The fibre patterning outcome was influenced by the intrinsic polymer solution properties, external operating parameters and ambient factors. Within the influencing factors, the viscoelasticity of dECM-laden gelatin solution and voltage dependence was investigated to optimise the fibre patterning condition. LEP enabled the fabrication of organised microfibres on a variety of substrates, including glass slides, PDMS-based microfluidic channels and 3D-printed PLA supports. When patterning on 3D constructs, the dECM-laden gelatin fibres formed a suspended network. By increasing the patterning density, the morphology of the free-standing network could be tuned from distinct fibres to a non-woven mesh membrane. The smallest spacing between the fibres could reach below 1 μm. With SEM, the fibre diameter was measured to be between 450 nm to 1 μm. Since the membrane was formed by one or two layers of microfibres, the thickness of the membrane was estimated to be less than 2 μm. LEP allows one to engineer high-loading of dECM fibril microenvironments in the physiological fibril length scale.

2.1 Introduction

To date, dECM materials have been derived from a range of organs and tissues, including skin[152, 153], adipose[154, 155], ligaments[156], tendons[157], heart[158], liver[159, 160], small intestinal submucosa (SIS)[161] and urinary bladder matrix (UBM)[162]. Decellu-

larization protocols can be categorised into physical, chemical, and enzymatic methods, or a combination of these three methods[38]. Typical decellularizing processes include using chemical agents and detergents, applying pressure, freezing, and perfusion. Any process adapted to remove the cell content can alter the native 3D architecture of ECM. The degree of preservation of the ultrastructure of the organ/tissue comes at the expenses of the efficacy and ease of the decellularizing process. The protocol that least disrupts the ECM ultrastructure is whole organ perfusion-decellularization[158], which shows tremendous potential in tissue engineering. In this protocol, a whole organ is perfused with chemical reagent to remove the cells. The architecture of the organ is preserved and new cells can be perfused into the organ to partially regain organ functions[163]. This method has been demonstrated with promising results in xenogeneic transplantation. However, this new technique still experiences low throughput and a number of technical difficulties when extended to solid organs of large animals. On the other hand, mechanical abrasion and freeze-thaw processing provide effective decellularization with high throughput. This leads to commercially available dECM products, which often come in a homogenised powder form. In this case, the spatial architecture of the ECM is inevitably lost. These dECM material can be used in *in vitro* cell cultures. To harness the ease of decellularization and high throughput associated with these readily available dECM sources, it is thus important to develop biofabrication techniques which can re-configure the physical structures of the extracellular matrix scaffolds, while preserving the biochemistry of the dECM. Hence, compared to a whole organ decellularized organ scaffold, it is expected that a biofabricated dECM scaffold will provide advantages for simple recellularization, culturing of multiple cell types and quality checks, seeing favourable attributes for applications, and particularly for drug testing platforms.

A number of previous studies have demonstrated different dECM ultrastructure biofabrication techniques. For instance, Mironov et al. demonstrated tubular tissue constructs with micropores in decellularized small intestinal submucosa (dSIS) scaffold[164]. Identical micropores with a diameter of approximately 50 μm were created using laser cutting in the dSIS scaffold. Localised cell seeding can be established in these micropores. This recellularization method is simple and relatively fast. However, this strategy cannot be adapted for complex solid organ structures. Using homogenised dECM powder as a starting material, various studies processed the dECM into hydrogel[165, 166], and further combined the dECM hydrogel with cells (forming a bioink) for 3D printing[56]. High cell viability and dECM-specific differentiation has been demonstrated. Although these hydrated dECM gels capture some essential biochemical factors within the matrix (as proven by the dECM-specific cell differentiation), the spatial resolution of the bioprinted features are greater than tens of micrometres. The fibrous architecture and the biophysical cues of the native ECM are lost.

Considering that the native ECM contains defined structural building blocks, ranging from nano-micro-fibrils, to membranes and gels, I explored the possibility of recreating higher resolution fibril structures of dECMs, typically in the hundreds of nanometres to micrometre range. This 'fibril building block' would span the lengthscale of a mammalian cell, and could be used to mimic the fibril structure in the native ECM. Among the various biofabrication techniques available, electrospinning is known for its ability to fabricate fibril structures with a nanometre to micrometre resolution[167]. Although a few prior studies have reported electrospinning of dECM-incorporated composite fibres, the concentration of dECM loaded within the fibre is low, possibly due to the intrinsic limitation of far-field electrospinning. For example, Baiguera et al. reported the successful incorporation of rat brain dECM into electrospun gelatin scaffold[168]. The incorporated dECM concentration was 1 wt% with respect to gelatin. The authors demonstrated the favourable cellular compatibility of the fibril scaffolds, however, with limited information on the actual chemical characterisation of the fabricated scaffold. In another example, D'Amore et al. incorporated vascular dECM into an electrospun polyurethane (PECUU) scaffold by depositing dECM solution during the electrospinning process [169]. The deposited dECM solution had a concentration of 15 mg/mL, approximately 1.5 wt% and the PECUU polymer concentration was 25 wt%. The ratio of the flow rate between the dECM-deposition and electrospinning polymer was 0.075. This gives an estimated concentration of 0.45% of the final dECM concentration in the as-spun scaffold. The as-spun scaffold was implanted into rats as a cardiac patch and showed the capability of maladaptive remodelling. In a more recent study, Gao et al. demonstrated high loading of decellularized meniscus extracellular matrix (dMECM) in polycaprolactone (PCL)[170]. The highest concentration in the polymer blend was 80 wt%. The composite polymer was fabricated into electrospun nanofibres and applied to meniscus cell culture. Increased tensile moduli and yield stress were identified with increasing dMECM concentration. Direct influence on cell arrangement and gene expression was observed with high dMEMC content. Although this composite fibre strategy shows promises for musculoskeletal applications, the use of PCL polymer (with Young's moduli in the GPa range) as a base means the fibres will have biomechanical properties alien to soft tissues, which have Young's moduli typically below 100 MPa. Since cytotoxic organic solvents such as 1,1,1,3,3,3-Hexafluoro-2-propanol (HPF) are often used to dissolve the polymer mixture, special care should also be taken to eliminate all the solvent residuals which could cause adverse effects on cellular behaviour. In this study, I am interested in the fabrication of bio-mimetic fibrillar networks to replicate the intrinsic nanofibril nature of the ECM. Specifically, LEP was used to fabricate a single-layer of fibrous membrane which can be suspended over microfluidic open channels. This single

step fabrication method enables the patterning of mechanically resilient and simultaneously soft dECM-laden membranes with tunable microscale topography.

2.2 Technology aims of the present studies

To investigate the ability to generate dECM fibrils as a building block for biofabricating soft tissue ultrastructures, I used LEP to achieve high resolution patterning of dECM-laden gelatin fibres. This technique was applied to porcine dECM derived from urinary bladder matrix (dUBM) and small intestinal submucosa (dSIS). They represented two of the most well-established, readily available dECM sources from soft tissues. The compositions of dUBM and dSIS processed by mechanically delaminating methods were measured in the study by Badylak et al.[171]. It was found that dUBM consists of collagen I – VI, proteoglycans, glycosaminoglycans and growth factors. Additionally, similar chemical and mechanical properties of bladder acellular matrix graft between pig and human have been reported[172]. This further supports that dUBM from pigs can potentially be used to reassemble the physiological microenvironment. The aim of this project is to produce highly localised patterning of nano- to microfibres while optimally preserving the biochemical components of the dECMs. In order to achieve this, there are three factors to be considered:

1. How to achieve highly localised patterning?

2. How to obtain fibres in the nano- to microdiameter range so that these fibres can be used as a basic element or building block to construct an ultrastructure of prescribed fibrous patterns?

3. How to optimally preserve the biochemical composition of the native ECMs, and the growth factors entrapped within?

For the first and second factors, I adapted the LEP process which allows for direct patterning of fibril structures, with diameters ranging from hundreds of nanometres to several micrometres, on a variety of substrates. LEP is processed under a low voltage (as low as 50 V) at room temperature. This helps to retain the chemical components of the processed polymer solution. To satisfy the third factor, consideration is required for the material and solvent selection. I used porcine dUBM and dSIS as the source of starting materials, provided by Prof Badylak's group. However, pure dECM cannot be processed using LEP. Based on the previous study by Li et al.[45], gelatin was selected as a carrier polymer to assist the LEP process. This was based on both the electrospinnability and the collagen-mimicking nature of gelatin. In addition to the processing technique, the solvent and crosslinker choices

are also of paramount importance in preserving the chemical structures of the dissolved molecules. Although solvents such as HFP are commonly used for dissolving protein materials to produce an electrospinable solution[170], HFP usually leads to degraded protein structures which are undesirable[173–175]. In my experiments, water-based solvents with a proportion of acetic acid and ethyl acetate were chosen, where both reagents are known to have lower toxicity than HFP (LD_{50} for rats is 3310 mg/kg for acetic acid and 5620 mg/kg for ethyl acetate, in comparison to 1040 mg/kg for HFP). The acidity of the solvent may also cause protein denaturation. Acetic acid is widely used as a denaturant in solubilizing growth factors[176], ECM proteins[177] and nucleic acid[178]. Although this can potentially affect protein folding and bioactivities, it is a necessary solvent to solubilize high concentrations of gelatin and dECM. Ethyl acetate was used to lower the surface tension of the combined solution. Among various methods of crosslinking gelatin and collagen components, glyoxal was chosen in this case as a bio-compatible protein crosslinker. The reason of the crosslinker selection is explained in **Chapter 3**. Therefore, with the dECM containing the chemical components of ECM, gelatin as the carrier polymer together with the growth factor-preserving solvents, I hope to achieve the three design criteria for dECM patterning.

2.3 Theoretical background

2.3.1 Mechanism of low-voltage electrospinning patterning (LEP)

The LEP approach used in this study was primarily developed by Xia Li, a former student in the group. I further optimised the patterning condition for gelatin and dECM-laden solutions. This includes the selection of initiators, processing voltage, solution concentration and ambient environmental control.

In the conventional far-field electrospinning process, the localised electric field charges the polymer solution and causes repulsion between molecular chains. Since the initiation process of electrospinning requires competition between the intrinsic electrostatic repulsion and the surface tension of the polymer droplet, the voltage requirement is typically in the 10 kV to 40 kV (electric field strength $\sim 10^5$ V/m) range. The near-field electrospinning (NFES) technique reduces the voltage requirement by decreasing the distance between the collecting substrate and the polymer droplet. This allows for microfibre patterning at a reduced voltage while maintaining a high electric field strength (0.2 – 2 kV, electric field strength $\sim 10^6$ V/m) compared to conventional electrospinning[137]. The operating voltage of low-voltage electrospinning patterning (LEP) can be as low as 50 V while maintaining a local electric field strength that is comparable to the far-field electrospinning (electric field

strength $\sim 10^5$ V/m)[45]. The low voltage mechanism is based on the combination of the lateral mechanical stretching force and the electrostatic field focusing effects facilitates the initiation of the polymeric jet. In practice, there are two types of LEP configuration: generic and drag-and-pattern. The choice of configuration depends on the viscoelasticity of the processing polymer solution. LEP configurations and the low voltage mechanism are further explained in this section.

Generic LEP configuration

Fig 2.1 shows a photo and a schematic diagram of the experimental setup for LEP. The setup for LEP consists of an x-y-z moving stage holding the collecting platform, a DC voltage source, and a metallic needle tip connected to a syringe for which the extrusion is controlled by a mechanical pump. A Labview program is designed to control the stage movement. The movement of the stage can be controlled along all three orthogonal coordinating axes. The z-axis controls the vertical distance between the needle tip to the collecting platform. The translational stage movement pattern determines the global geometry of fibre deposition. The DC voltage is connected between the metallic needle tip and the stage, with the positive voltage connecting to the needle tip and ground voltage connecting to the stage. The syringe is used as a reservoir for storage of the polymer solution, and the extrusion flow rate can be precisely controlled using the mechanical pump. This extrusion-based polymer dispensing process is suitable for a liquid-like solution because of the constant flow rate and rarity of clogging. In the centre of the collecting platform are held the substrates for fibre collection. Two initiators are positioned on each side of the substrate for initialising polymer jet formation and refreshing the suspended polymer solution. Experimentally, the stage is first set into motion, and polymer solution is extruded through the needle tip at a controlled flow rate. Subsequently a voltage is applied between the needle tip and the stage. As the droplet touches the initiator, the surface of the droplet is mechanically deformed and stretched. The mechanical stretching overcomes the surface tension of the droplet, causing mechanical deformation. The combination of mechanical stretching and electrostatic force initialises fibre formation. As the stage moves in the translational designed pattern, continuous microfibres are patterned on the collecting substrate.

Drag-and-pattern LEP configuration

When the solution contains a high polymer concentration or crosslinking, the polymer solution can exhibit high elasticity (see supporting data later in Section 2.3.2). These solutions have dominating solid-like behaviour and are resistant to flow. When processing

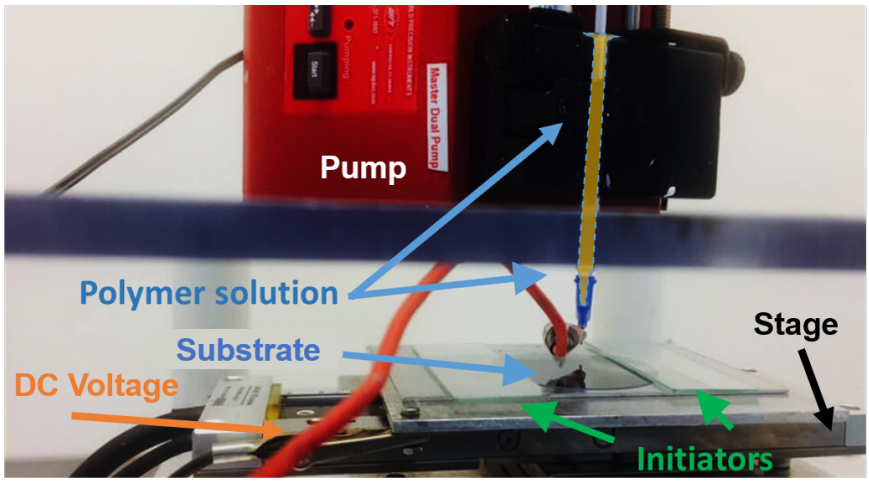

(a)

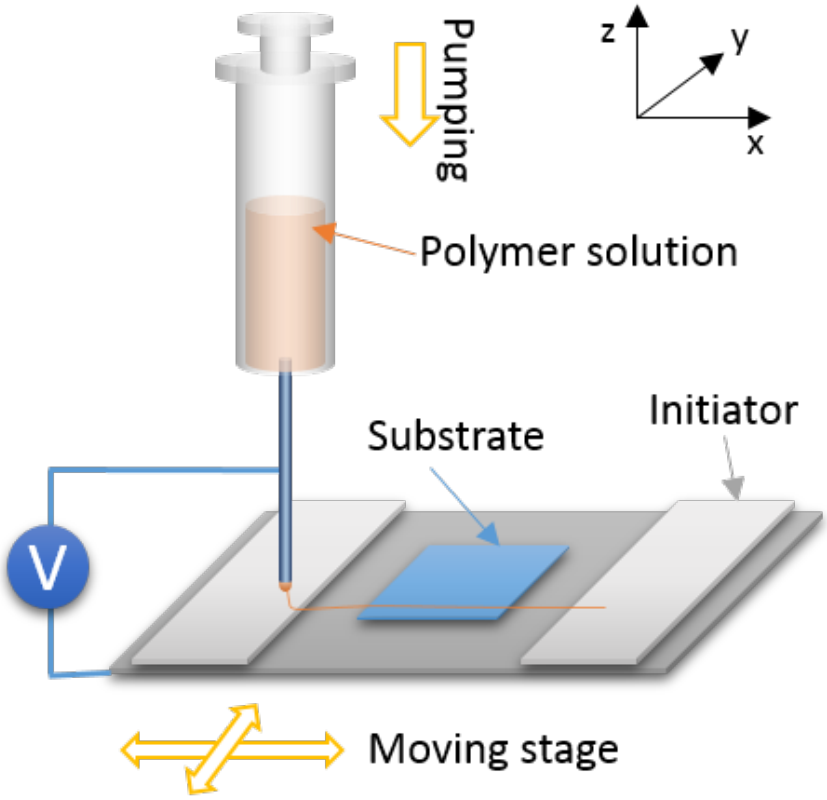

(b)

Fig. 2.1 (a) Photo of the LEP experimental setup. (b) Generic LEP schematic diagram.

such a polymer solution using LEP, extrusion becomes difficult as the solution can cause clogging in the needle tip. This prevents further fibre patterning. In this study, it was discovered that the drag-and-pattern LEP configuration can be adapted to pattern solution with high elasticity. Fig 2.2 shows a schematic diagram of drag-and-pattern LEP. In this configuration, the polymer solution is evenly dispensed on the initiators. As the stage moves with the initiator below the syringe, the needle tip makes contact with the solution. As the stage moves the initiator away from the tip, a shear stress is applied to the solution, causing it to stretch and deform. Upon the application of a voltage, the mechanical deformation of the polymer solution results in polymer jet formation, similar to that described in the LEP process. The polymer jet is subsequently collected on the substrate as microfibres. When the stage moves the other initiator below the syringe, this process repeats and microfibres are continuously patterned on the substrate. However, one shortfall of the drag-and-pattern configuration arises from solution drying. The evaporation of the solution changes its electrospinnability continuously. Hence, the drag-and-pattern configuration can only be used for patterning over small areas, to minimise the effect of solution drying.

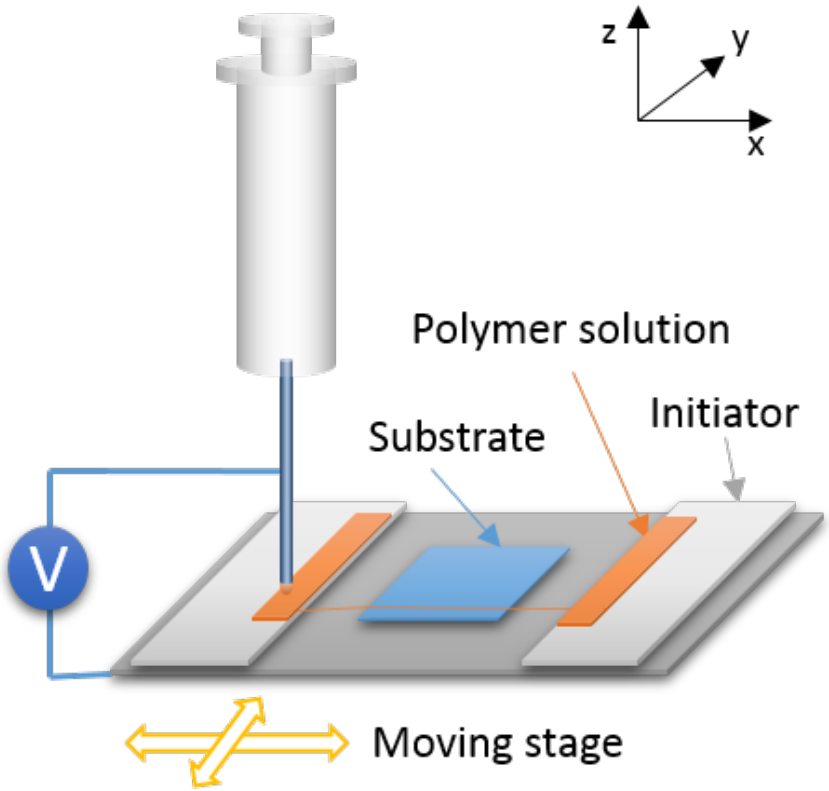

Fig. 2.2 Drag-and-pattern electrospinning schematic diagram. The polymer solution is dispensed on the initiators, instead of being pumped by the syringe.

Low-voltage mechanism for continuous fibre patterning

There are two mechanisms that enable continuous microfibre patterning under low voltage: the lateral mechanical stretching force, in conjunction with an electrostatic focusing effect. Both mechanisms are described in the study by Li et al.[45]. The combined effects are achieved by using initiators on either side of the patterning route. Fig 2.3 illustrates the LEP process. When the initiators move to the position under the extruded droplet, the droplet makes contact with the initiator and is partially removed by it. During this process, the droplet is refreshed and the shape of the droplet is mechanically deformed from a semi-sphere. This process can be categorised into two regimes: the fibre initiation regime and the fibre printing/thinning regime. As the name implies, the initiation regime is for initialising fibre formation. The suspended droplet is stretched longitudinally upon mechanical deformation. The deformed shape is similar to the Taylor cone, which is the critical condition for fibre formation in far-field electrospinning. This enables the formation of a fine polymer jet flowing towards the collecting platform. Upon the application of a voltage, a focused high electric field is introduced at the short distance between the initiator and the needle tip (typically 1–2 mm). Because of the short distance, the localised electric field strength (electric field strength $\sim 2.5 * 10^5$ V/m) is comparable to that of far-field electrospinning. As the initiator moves under the needle tip, the localised electric field steeply increases, changes the charged molecular distribution in the solution, and facilitates polymer jet flow. This is recognised as the electrostatic focusing effect. The two mechanisms significantly lower the voltage requirement for fibre initialisation. The printing regime is for sustaining continuous fibre patterning, at the same time mechanically thinning the fibre by movement of the stage. One of the main obstacles to fabricate continuous fibres in conventional electrospinning is solution drying. Whilst electrospinning often requires a high solution evaporation rate to obtain distinct fibres, drying of the solution at the needle tip can block the tip and hinder the electrospinning process. In the LEP process, the solution is continuously extruded by the pump and refreshed by the initiator. This prevents possible blocking of solidified solution and enables continuous fibre patterning.

The electrostatic focusing effect is also thought to assist in continuous fibre patterning in the drag-and-pattern LEP configuration. The fibre initiation process in the drag-and-pattern configuration is similar to that described in the dry spinning based spinneret based tunable engineered parameter (STEP) technique presented by Nain et al. [179], with the absence of voltage application. In the STEP technique, a glass micropipette spinneret is used to pattern polymer fibres under a mechanical stretching force. The polymer solutions used in this study (polystyrene/xylene and poly(methylacrylate)/chlorobenzene) are highly concentrated. Hence the polymer entanglement is high, which enables immediate fibre patterning. The

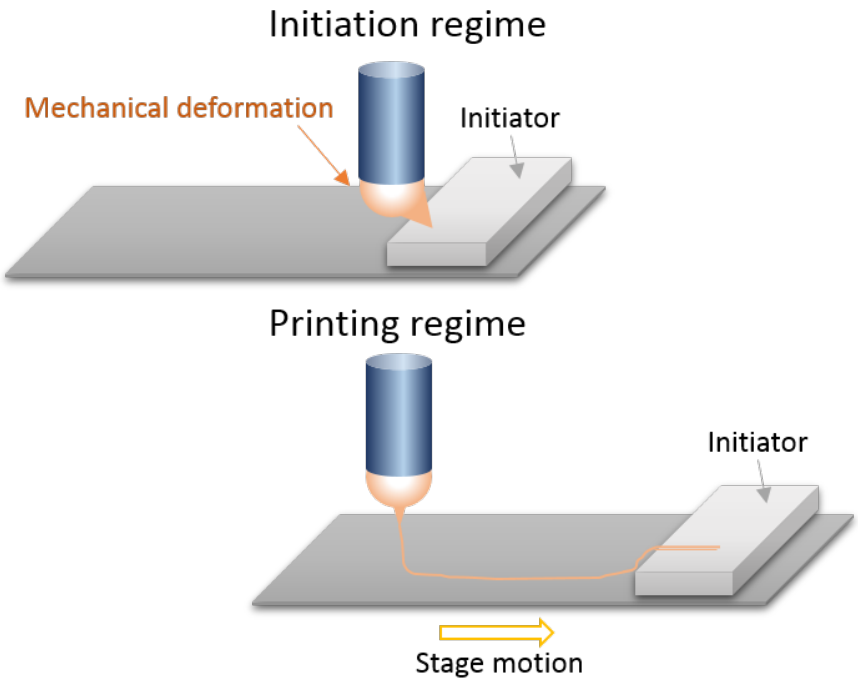

Fig. 2.3 The initiation regime and printing regime during the LEP process. In the initiation regime, the polymer droplet contacts the initiator and is mechanically stretched. This initiates the polymer jet formation. As the stage moves, the polymer jet is sustained by the electric field and forms fibres.

polymer fibre diameter can reach 64 ± 9 nm. In addition, the direct drawing of nano- and microfibres has been demonstrated in a number of studies[180–183]. This technique enables precise patterning of suspended microfibres and can be applied to increase the thermal conductivity of polymer material by increasing the molecular alignment. However, direct fibre drawing requires a high degree of polymer entanglement, and only organic solvent based solutions have been demonstrated. Hence the material selection may be limited, especially for biomaterials which can be sensitive to solvent selection. In the drag-and-pattern configuration, the electric field strength acts as an additional force that initiates and maintains the polymer jet. This aids the patterning of continuous and sustainable fibres. The electrostatic focusing effect of the drag-and-pattern configuration is further studied in Section 2.5.2.

The selection of the initiator is based on the electric conductivity of the polymer solution. For a polymer solution with high electrical conductivity, such as a PEO/water solution, both metallic conducting materials and insulating materials can be used as initiators. However, the applied voltage must be significantly reduced if metallic initiators are employed, to avoid short circuiting. The typical voltage used in this case is less than 100 V. Conducting initiators include silicon wafers, aluminium and steel. The insulating initiators include glass, PDMS

and plastic. For a gelatin aqueous solution, glass slides are often used as initiators. On the other hand, for solutions with low conductivity, such as polystyrene/dimethylformamide solution, only conductive initiators can initialise fibre patterning.

Factors influencing fibre properties

As mentioned in Section 1.4.1, the far-field electrospinning process is influenced by the properties of the polymer solution, governing variables, and ambient parameters[81]. Some of these factors also influence the fibre patterning in LEP. In the following section, the similarities and differences of these effects are discussed:

1. **Intrinsic polymer solution properties:**
   In LEP, the microfibres obtained from the LEP process are affected mainly by polymer entanglement[45]. In the conventional electrospinning process, the formation of a polymer jet is a result of the competition between the Coulomb force and the droplet surface tension. Therefore a significantly high electric field is required. In LEP, the surface of the polymer solution droplet is mechanically disrupted by the initiators. This means that the competition between Coulomb repulsion and surface tension no longer plays the most critical role in the jet formation. The conductivity of the solution mainly determines the selection of initiators (glass or metal) and the threshold of the operating voltage. Therefore, polymer entanglement is the most important factor in maintaining the flow of the polymer jet, in order to achieve continuous microfibre patterning. Viscoelasticity reflects the intra-molecular entanglement in a polymer solution, which is important to achieve sustainable and continuous fibre fabrication. Experimentally, viscosity is closely related to the electrospinnability of a polymer solution and the patterned microfibre morphology[184]. In general, a critical concentration is required for sufficient polymer chain entanglement and stable fibre formation. This critical concentration is different depending on the nature of the polymer, such as molecular weight distribution and molecular structure.

2. **Extrinsic operating parameters:**
   A number of extrinsic operating parameters, including solution flow rate, gap size, applied voltage, and stage speed, can have great influence on the local fibre morphology and/or global fibre patterns. In conventional electrospinning, the solution flow rate is important because virtually all extruded solution is collected as nano- and microfibres. However, in LEP, the excess of extruded solution is collected by the initiators so the changing flow rate does not influence the fibre morphology significantly as long as

more than sufficient flow is delivered for fibre patterning. The gap size between the droplet and the collecting stage is fixed within a small range by the initiator thickness. From the previous study by Li et al.[45], the morphology of fibres is influenced by three forces: the intrinsic surface tension, the Coulomb force acting on the polymer jet, and the lateral aerodynamic disturbance. The Coulomb force is controlled by the operating voltage, which is an important extrinsic operating parameter. The lateral aerodynamic effect, which is from the influence of the ambient air, belongs to the ambient factors. In order to obtain continuous patterning of straight and uniform fibres, the Coulomb force should dominate over the surface tension and lateral aerodynamic effects. This is because the predominating surface tension results in a beaded structure and the aerodynamic disturbance introduces twisting along the fibres. The sufficient operating voltage can also result in a firm attachment of the fibres on the substrate. The minimum voltage threshold for continuous uniform fibre patterning is different for solutions. For example, a PEO/water solution can be patterned with a voltage as low as 50 V, and the minimum voltage required for a gelatin aqueous solution is 100 V. Solutions with higher electric conductivity require a low operating voltage, and *vice versa*. In addition, the stage speed can also influence the fibre morphology, as previously demonstrated in melt electrospinning[43, 185]. A slowly-moving stage can result in tortuous fibre morphology. As the stage speed increases, the fibre morphology becomes straight and uniform. Similar effects are expected in LEP, based on the similarity between the configuration of LEP and melt electrospinning.

3. **Ambient factors:**
   The ambient parameters change the properties of the solution during the short time during which it is exposed to the atmosphere. This includes atmospheric temperature, humidity and air flow velocity. For LEP, although the exposure time is short, the change is non-negligible for a volatile solution. The temperature and humidity influence the solidifying time of the polymer solution, and therefore the patterned fibre morphology. In general, room temperature and humidity can provide suitable fabrication conditions for LEP. Low humidity is preferable to achieve fast solidification in order to obtain distinct fibres. The air flow in the electrospinning chamber gives rise to aerodynamic disturbance. Strong air flow can interfere with fibre deposition and cause disordered fibre alignment. Therefore, minimum air flow is usually adapted for LEP.

Since the solution formulation is the most important factor in determining whether fibre formation is feasible, in the following sections, I will further introduce the theoretical basics of polymer entanglement (Section 2.3.2), and also the measurement technique, based on

rheology, which reflects an important solution property indicator for electrospinnability (Section 2.3.3).

2.3.2 Polymer solution concentration and electrospinnability

As introduced in [186], polymer liquids can be characterised into two states: polymer melts and polymer solutions. Polymer melts are bulk liquid states formed by macromolecules. This type of polymeric liquid exists above the glass transition and melting temperature of the macromolecules. In comparison, polymer solutions are obtained by dissolving a polymer into a solvent. Depending on the polymer concentration, the polymer solution can be classified as dilute, semidilute and concentrated solutions. Fig 2.4 illustrates a schematic diagram of different concentration regimes.

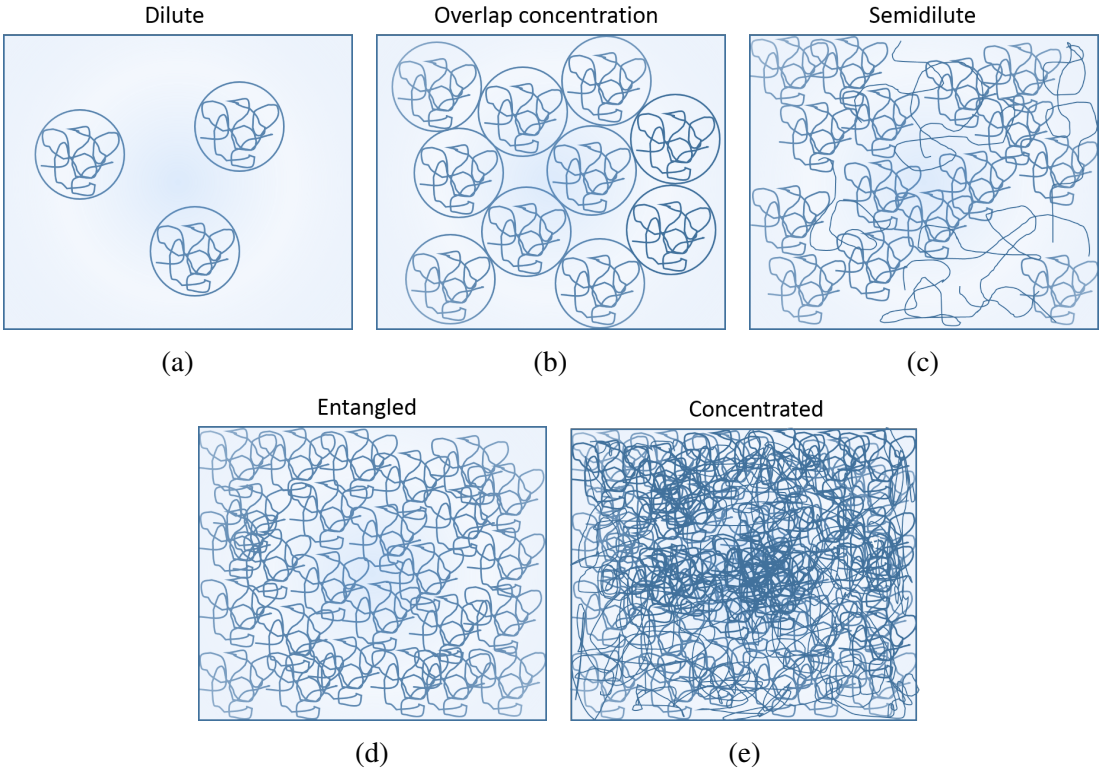

Fig. 2.4 Polymer solution concentration regimes: (a) dilute ($\phi < \phi^*$); (b) overlap concentration/volume fraction ($\phi = \phi^*$); (c) semidilute ($\phi^* < \phi < \phi_{entangled}$); (d) entangled ($\phi > \phi_{entangled}$) and (e) concentrated.

The polymer concentration can be measured as mass concentration, c, or as volume fraction, ϕ. The two concentrations are related through equation 2.1:

$$\phi = \frac{c}{\rho} = c\frac{v_{mon}N_{Av}}{M_{mon}} \tag{2.1}$$

where ρ is the polymer density, v_{mon} is the occupied volume of a single chemical monomer, N_{Av} is Avogadro's number and M_{mon} is the molar mass of the monomer. The pervaded volume (V) is the volume of solution occupied by the polymer chain. This is closely approximated by using the size of the polymer chain (R):

$$V \approx R^3 \tag{2.2}$$

The pervaded volume, V, contains both polymer chains and solvent, hence it is typically orders of magnitude greater than v_{mon}. The volume fraction of a single molecule inside the pervaded volume is the overlap volume fraction (ϕ^*):

$$\phi^* = \frac{Nv_{mon}}{V} \tag{2.3}$$

where N is the number of monomers within the polymer chain. The corresponding overlap concentration, c^*, can be calculated by using equation 2.1. If the volume fraction, ϕ, of the polymer solution is below ϕ^*, the solution is in the **dilute regime** ($\phi < \phi^*$). The polymer coils are surrounded by solvents and the average distance between chains is larger than their size. In this regime, the polymer chains are far away from each other and the interactions between them are weak. As a result, the properties of the solution are dominated by the properties of the solvent, with variation contributed by the polymer. When the polymer volume fraction exceeds the overlap volume fraction ($\phi > \phi^*$), the solution is in the **semidilute regime**. In this case, the polymer chains interact with each other. This becomes the dominating effect to the physical properties of the solution. The physical properties, such as the viscosity, relate to the polymer concentration by a power law. The majority of electrospinning occurs in and beyond the semidilute regime. This is because a high degree of chain interaction is required to form a sustainable polymer stream. As the polymer volume fraction further increases, the solution becomes closer to a polymer melt. In this case, the **concentrated regime** is reached and the chain interactions become increasingly significant.

The dilute and semidilute models assume that the hydrodynamic interactions between polymer chains are screened. More realistically, the presence of neighbouring chains restricts the movement of the primitive polymer chain. This topological constraint limits the chain motion to a tube-like region, called the confining tube. The diameter of the tube is the area within

which the topological constraints by neighbouring chains are screened. This is known as the entanglement of the polymer, which applies to both polymer melts and solutions. In a polymer solution, the entanglement volume fraction occurs when the confining tube diameter equals the chain size. In an entangled polymer solution, the volume defined by the confining tube is smaller than the pervaded volume. Hence, the entanglement volume fraction is higher than the overlap volume fraction. In practice, the overlap and entanglement volume fraction/concentration is highly dependent on the polymer (molecular weight distribution) and the solvent. For gelatin in aqueous solution at 50°C, the overlap concentration is 0.5 wt%[187]. The addition of salt can alter the overlap concentration. Typically, the addition of NaCl can move the overlap and entanglement concentrations from 4.0 wt% to 2.0 wt% and from 14.0 wt% to 12.0 wt%, respectively[188].

2.3.3 Rheology characterisation as an indicator for electrospinnability

The word "rheology" comes from the phrase "to flow" in Greek. Hence, rheology studies the flow and deformation of matter[189]. The deformation of a material is proportional to the applied force, according to Hooke's law:

$$\sigma = E\varepsilon \tag{2.4}$$

where σ is the applied normal stress, defined as the force per unit area, E is the Young's modulus, and ε is the normal strain, defined as the relative change in length. This generally applies to solid materials. Flow is characterised by Newton's law of viscosity, which typically applies to liquid materials:

$$\tau = \eta\dot{\gamma} \tag{2.5}$$

where τ is the applied shear stress, η is the Newtonian viscosity, and γ is the shear strain. There are two types of fluids: Newtonian and non-Newtonian. Newtonian fluids, such as water, are fluids with constant viscosity regardless of the applied shear stress and strain rate. Non-Newtonian fluids exhibit changes in viscosity depending on the shear stress and strain rate. Newtonian fluids are relatively rare, and the majority of fluids are non-Newtonian. Non-Newtonian fluids include shear thinning, shear thickening, Bingham plastic and rheopectic/anti-thixotropic fluids, as shown in Fig 2.5a. Shear thinning (pseudoplastic) fluids have decreasing viscosity with increased stress and shear rate, so that the fluids flows more easily under a higher deformation force or rate of deformation. Examples of shear thinning fluids are paint, nail varnish, whipped cream and blood. It is generally accepted that electrospinning polymer solutions should exhibit shear thinning properties[190]. Shear

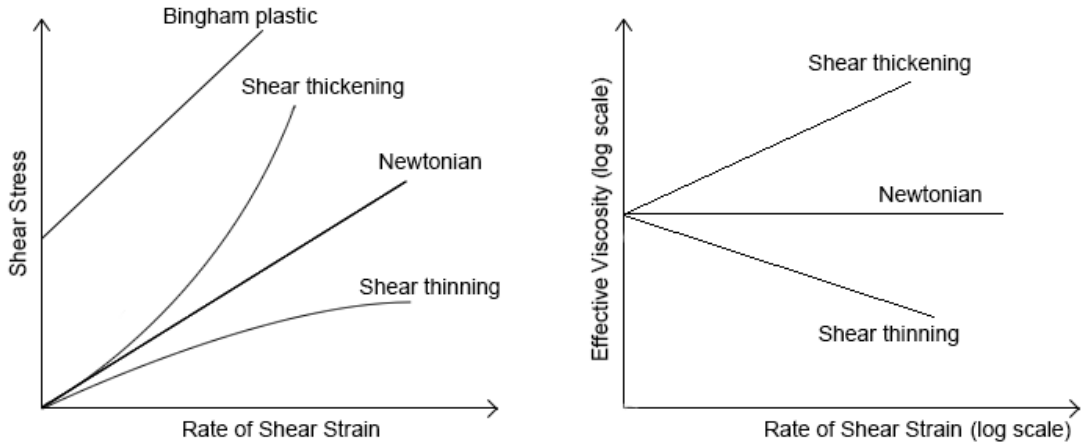

(a) (b)

Fig. 2.5 (a) The behaviour of different fluids under shear deformation. (b) Power-law fluids: the relationship between the effective viscosity and strain rate.

thickening fluids have increasing viscosity with increasing stress and strain rate, an example being corn starch in water. Bingham plastic is a type of fluid which requires a minimum stress in order to flow. Several examples include tooth paste, mayonnaise and mustard. The viscosities of rheopectic and anti-thixotropic fluids are time-dependent. The former has increased viscosity with the duration of stress, and the latter has decreased viscosity. The rheological properties of different non-Newtonian fluids are important in a wide range of fabrication and quality control processes.

Some non-Newtonian fluids can be described using power law, or the Ostwald-de Waele relationship[191]. In this model, the stress is linked to the shear strain rate through the following equation:

$$\tau = K(\dot{\gamma})^n \tag{2.6}$$

where K is the flow consistency index. By combining with equation 2.5, one can identify the effective viscosity η_e:

$$\eta_e = K(\dot{\gamma})^{n-1} \tag{2.7}$$

The effective viscosity is described as a function of the strain rate. Fig 2.5b shows the effective viscosity dependence on strain rate. When n>1, η_e increases with strain rate. The fluid exhibits shear thickening behaviour. When n=1, η_e is independent on strain rate, which indicates Newtonian fluid. When n<1, η_e decreases with increasing strain rate. This fluid is shear thinning.

In general, materials can exhibit both solid-like and liquid-like behaviour. The combination of elastic and viscous properties is described by viscoelasticity. When an external force is applied to a object to cause deformation, a solid elastic material can store the energy and return to its original shape after the force is removed. In contrast, a liquid will continue to flow after the external force is removed. Many polymers exhibit both elastic and viscous behaviour under different stress rates. For example, silly putty is predominantly elastic under a high stress rate and becomes liquid-like over a longer time-scale. Hence, its viscoelastic behaviour is time-dependent and can be characterised with oscillatory shear measurement. In specific, a sinusoidal strain with angular frequency, ω, is applied to a sample material:

$$\varepsilon(t) = \varepsilon_0 sin(\omega t) \tag{2.8}$$

where ε_0 is the amplitude of the applied strain. The elastic component is completely in phase with the applied strain whereas the viscous component is out-of-phase by $\pi/2$. The resulting response of a linear viscoelastic material gives a phase angle, δ, to the strain:

$$\sigma(t) = \sigma_0 sin(\omega t + \delta) \tag{2.9}$$

This can also be expressed as a linear combination of the elastic and viscous components:

$$\sigma(t) = \varepsilon_0 [G'(\omega) sin(\omega t) + G"(\omega) cos(\omega t)] \tag{2.10}$$

where G' is the storage modulus corresponding to elasticity, and G" is the viscous/loss modulus corresponding to the viscous component. The storage modulus, G', measures the amount of energy stored during shear deformation and the viscous modulus, G", measures the amount of energy dissipated. Additionally, the complex shear modulus, G^*, and complex viscosity is defined as:

$$\begin{aligned} G^*(\omega) &= G'(\omega) + iG"(\omega) \\ \eta^* &= \frac{1}{\omega}|G^*| \end{aligned} \tag{2.11}$$

The loss tangent is the ratio of loss and storage modulus, defined in equation 2.12. This measures the relative proportion of the viscous and elastic components of a material.

$$tan\delta = \frac{G"}{G'} \tag{2.12}$$

In a simplistic way, by determining the rheological characteristics of a polymer solution, i.e. G', G" and $\eta*$, one can yield information about whether the solution is in the semi-dilute regime, and the flow properties of the material. This thus will provide guidance on how to

adjust the solution composition, and also the LEP configuration, to tailor the fibre patterning and fibre performance.

2.4 Materials and methods

2.4.1 Materials

Gelatin (from porcine skin) powder was obtained from Sigma-Aldrich G1890 (Lot no. SLBC8470V), glacial acetic acid and ethyl acetates were obtained from Merck Millipore 100063 and 100789, respectively, glyoxal was obtained from Sigma-Aldrich 128465, and decellularized urinary bladder matrix (dUBM) and decellularised small intestinal submucosa (dSIS) were provided by Dr Badylak, University of Pittsburgh, U.S.

2.4.2 Preparation of the dECM/gelatine solutions

Various weight percentages of gelatin powder were dissolved in an aqueous solution combining deionised water, acetic acid and ethyl acetate. The solution was stirred at room temperature until homogeneous. For the dECM-laden solutions, 1 wt%, 10 wt% or 50 wt% gelatin were substituted by dECM powder and the other solvent components were unchanged. The mixed powder was dissolved in the same aqueous solution and stirred at room temperature until homogeneous. 3 wt% glyoxal was added to the solution as crosslinker prior to the electrospinning process.

2.4.3 Low-voltage continuous electrospinning patterning LEP

The polymer solution was dispensed using a 1 mL syringe and pumped at a rate ranging from 5 μL/min. DC voltage of typically 230 V was applied between the syringe tip and a moving stage that held substrates to collect the as-spun fibres. The electrospinning was initialised using a glass slide. By programming the movement of the stage using Labview, the polymer jet could be regularly patterned onto the substrates. The dECM/gelatin fibres were allowed 24 hours to crosslink.

2.4.4 Characterisation of the dECM/gelatin solutions

Dynamic oscillatory rheology measurement was performed using a Controlled Strain Rheometer (TA Instrument ARES), to characterise the dECM/gelatin solution in the process of electrospinning. A parallel plates configuration was adapted. Aluminium rotating discs with

a diameter of 25 mm were placed 600 μm apart. Frequency sweeps and strain sweeps were taken for 0.2 – 100 rad/s and 0.05 – 500%, respectively, for each dECM/gelatin concentration. Due to the high volatility of the polymer solution, limited frequency sweeps (10 – 100 rad/s at 10% strain) were performed at time points during crosslinking, for different gelatin concentrations and dECM concentrations.

2.4.5 Visualising suspended fibres using z-stack

1 wt% fluorescein (F2456 Aldrich) was added to the gelatin solution and mixed with a magnetic stirrer. The solution was used to fabricate fibres across pre-cast PDMS microchannels at voltages of 100 V and 250 V. The samples were imaged using a Leica TCS SP5 microscope. To reconstruct the 3D configuration, a z-stack was acquired over 100 μm with 0.5 μm intervals. The z-stack was converted into 3D using ImageJ.

2.4.6 SEM imaging for fibre morphology

dECM-laden fibres were patterned over a 3D-printed ring holder. The samples were coated with Platinum for 60 seconds. The samples were placed into the FEI Nova NanoSEM. Suspended fibres were selected to perform the EDX measurement. Five points on each fibre were measured at 10.0 kV, as beyond this the fibres were significantly damaged by the electron beam. Ten fibres were measured for each dECM concentration.

2.5 Results and discussion

2.5.1 Intrinsic polymer solution properties controlling the fibre morphologies

The degree of chain interaction and polymer entanglement determines the outcome of electrospinning. The chain interactions between molecules are closely reflected by the physical properties of the polymer solutions. This includes viscoelasticity, surface tension and conductivity. For LEP of gelatin fibres, the minimum electrospinnable concentration was experimentally determined to be 13 wt%, with the minimum operating voltage being 100 V. Here, the change in LEP fibre morphology associated with the dECM-gelatin solution system is presented. In particular, the viscoelastic properties of the dECM-laden gelatin solution are studied through oscillatory rheology measurements.

In this study, the patterned dUBM-laden fibres are used in building a human glomerulus model. This is because the biological origin of the glomerulus is closer to the urinary

bladder during the embryonic development[192]. Hence the protein compositions of dUBM and decellularized kidney are highly similar[19]. In this section, the optimised conditions of dUBM-laden gelatin solution for LEP is characterised. It is important to note that the dSIS-laden gelatin solution can also be patterned in the same LEP configuration.

Selection of rheology measurement geometry

The dECM-laden gelatin solution contains five chemical components: the dECM powder, gelatin powder, glacial acetic acid, ethyl acetate and deionised water. Crosslinker is potentially the sixth component that influences the rheology of the dECM-laden gelatin solution. Since both acetic acid and ethyl acetate are volatile solvents, care was taken when choosing the geometry of the oscillatory rheology measurement (see Table 2.1 for the comparison between different measurement geometries). The drying effect in the cup and bob geometry is the lowest, however it requires a large sample volume which is undesirable for dECM solutions. Both cone-on-plate and parallel plates require small sample volumes but are affected by drying of the solution. The cone and plate geometry holds the advantage of applying a constant strain gradient across the cone. However the disadvantage of its unchangeable gap size makes it less flexible. The parallel plate geometry applies an inhomogeneous strain gradient which must be corrected in the analysis. Its advantage is shown in the flexibility in the gap size as this is insensitive and can be offset in the calculation. Therefore, the parallel plate geometry was chosen for the rheology measurement.

Table 2.1 Oscillatory rheology measurement geometry.

Geometry	Cup and bob	Cone and plate	Parallel plates
Sample volume	13 mL	$<$1 mL	$<$1 mL
Drying effect	Low	High	High

Gelatin concentration dependence

As a measurement of intra-molecular interactions, the viscoelasticity of gelatin solution is closely related to the adapted LEP configuration and fibre morphology. It is hypothesised that the increase in the viscous component (loss modulus) plays a role in the fibre morphology. The ratio between the elastic and viscous component ($\tan(\delta)$) determines the LEP configuration as it affects the ease of extrusion.

The composition of gelatin solution is displayed in Table 2.2. These values were obtained through optimisation processes, which is explained in Appendix A. During the process of

Table 2.2 Gelatin solution composition.

Solution	Gelatin (wt%)	Water (wt%)	AA (wt%)	EA (wt%)
G(11)	11	29	36	25
G(13)	13	28	35	24
G(16)	16	27	34	23
G(19)	19	26	33	22
G(22)	22	25	32	21

AA is Acetic acid and EA is Ethyl acetate.

LEP, polymer solution was extruded at a constant rate of approximately 5 μL/min. By scaling with the needle dimension, this corresponded to a strain rate of roughly 10 rad/s. The translational stage moved at a velocity of 150 mm/s across the needle tip. This corresponded to a strain rate of approximately 100 rad/s. To investigate the relationship between solution viscoelasticity and the gelatin concentration, the complex viscosity, η^*, storage modulus, G', loss modulus, G", and loss tangent, tan(δ), were measured for G(11), G(13), G(16), G(19) and G(22). The polymer solution property was measured over the strain rate, ω, of 10 to 100 rad/s, reflecting the dynamic deformation that occurred to the solution during the extrusion and patterning steps. Fig 2.6 shows the complex viscosity, η^*, of each gelatin concentration over the strain rate range. In general, η^* decreases with increasing strain range, indicating shear thinning behaviour. This was more significant in solutions with higher gelatin concentration. The trends are linear on the logarithmic scale. Fig 2.7 shows a summary of the η^* dependence on gelatin concentration. In general, a linear trend in the logarithmic scale can be identified. This shows that these gelatin solutions were in the semidilute regime. Hence, they are potentially electrospinnable. More specifically, η^* at 10 rad/s (extrusion rate) increases more rapidly than that at 100 rad/s (patterning rate) based on the increasing gradients. This indicates that, as the gelatin concentration increased, the resistance to flow increased to a greater degree during extrusion compared to patterning. This is reflected in LEP, as the G(22) solution was significantly more difficult to extrude than G(19) but both solution can be used to pattern continuous microfibres.

The storage modulus, G', increases as a function of the strain rate, as shown in Fig 2.8. This shows that, at a shorter timescale (higher strain rate), the storage modulus of the viscoelastic material increases. Approximately linear trends can be identified on the logarithm graph, except that the G(11) and G(13) samples contain larger variation. Additionally, the loss modulus, G", shows an increasing trend with increasing strain rate, as shown in Fig 2.9. This shows that the viscous component exhibits greater resistance to flow at shorter

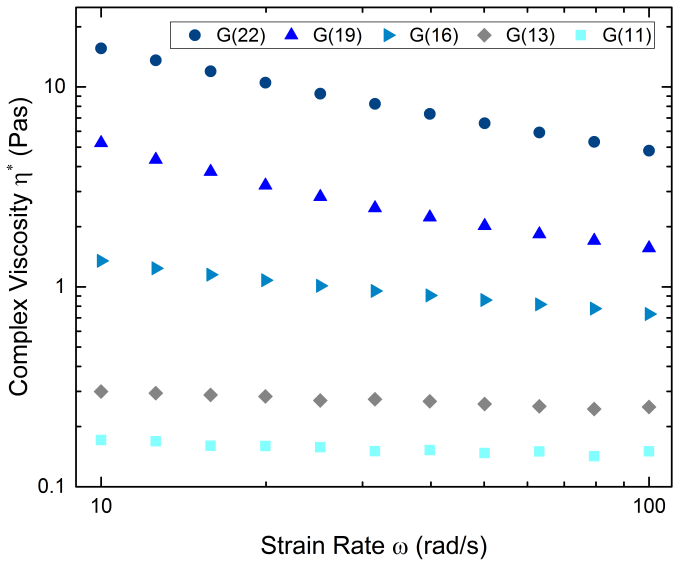

Fig. 2.6 Strain rate measurement for gelatin at different concentrations.

timescales. Fig 2.10 shows a summary of the storage modulus, G', and loss modulus, G", at different gelatin concentrations. Both G' and G" increased with gelatin concentration, with G' increasing faster than G" (indicated by a steeper gradient). This reflects a changing viscoelasticity as gelatin concentration increases in the solution.

The increase in the loss modulus (viscous component) indicates a increasingly entangled solution. In addition, high viscosity tend to retain the shape of the polymer jet[193]. This is reflected in the patterned fibre morphology, as shown in Fig 2.11. More specifically, the G(11) solution, with the lowest G", was sufficient to produce a fibre structure. However, the polymer entanglement was low and only discontinuous and curly fibres were obtained, as shown in Fig 2.11a. Continuous beaded fibre patterning was fabricated from the G(13) solution, as shown in Fig 2.11b. In far-field electrospinning, this beaded structure, as a defect in microfibre patterning, is due to Rayleigh instability which is developed from a polymer jet travelling over distance greater than 1 cm[89, 194–196, 130]. However in LEP, the jet travelling distance is approximately 1 mm. Instead, the beaded structure could be a manifestation of the low viscosity (measured by the loss modulus) and mismatched jet speed and stage speed, which will be discussed under 'Extrinsic operating parameters (Section 2.5.2). As the loss modulus further increased in G(16), straight and continuous fibres were obtained, as shown in Fig 2.11c. This trend held for the G(19) solution, which provided continuous, straight and uniform fibres, as shown in Fig 2.11d. In addition to the uniform

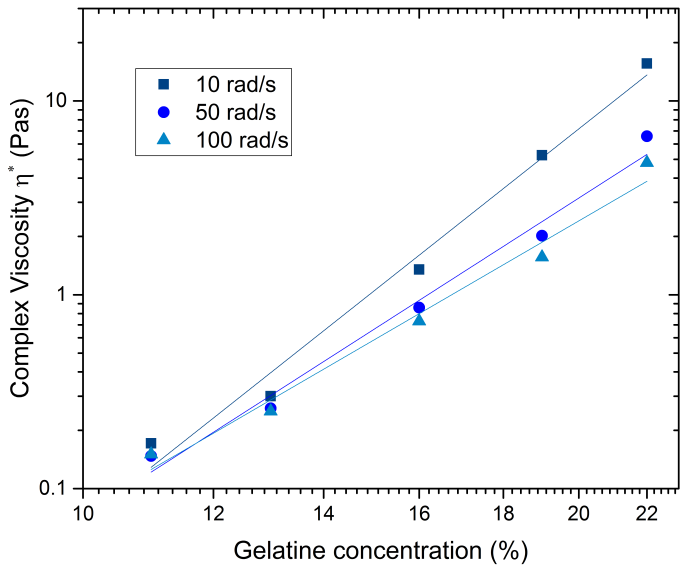

Fig. 2.7 The summary of η^* with different concentrations at characteristic strain rates.

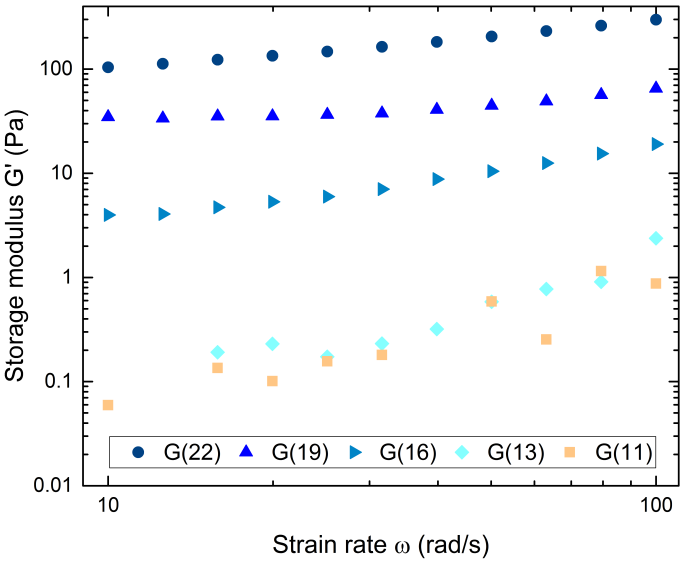

Fig. 2.8 The storage modulus G' of gelatin solution at different strain rates.

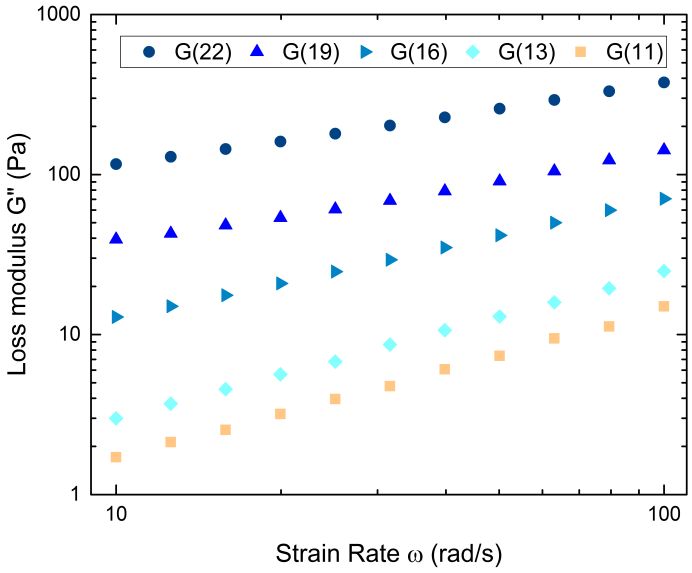

Fig. 2.9 The loss modulus G" of gelatin solution at different strain rates.

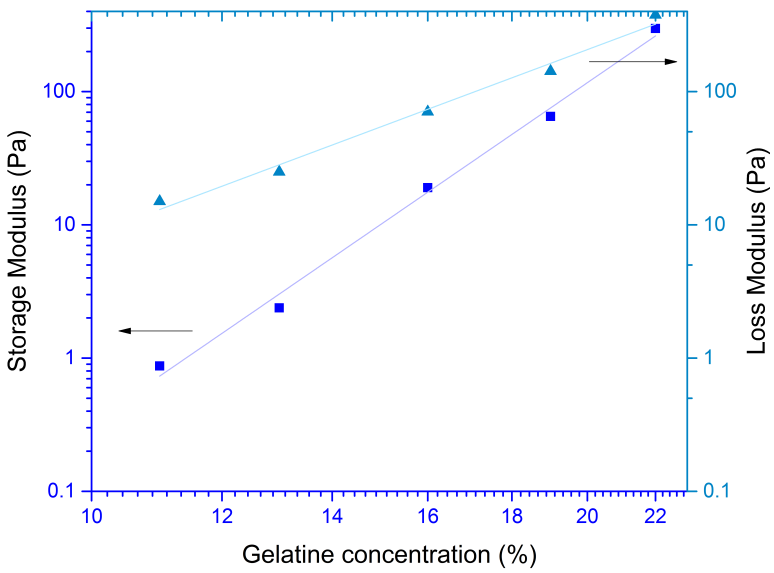

Fig. 2.10 The storage modulus G' and loss modulus G" of gelatin with different concentrations at 100 rad/s, which is the patterning strain rate of LEP.

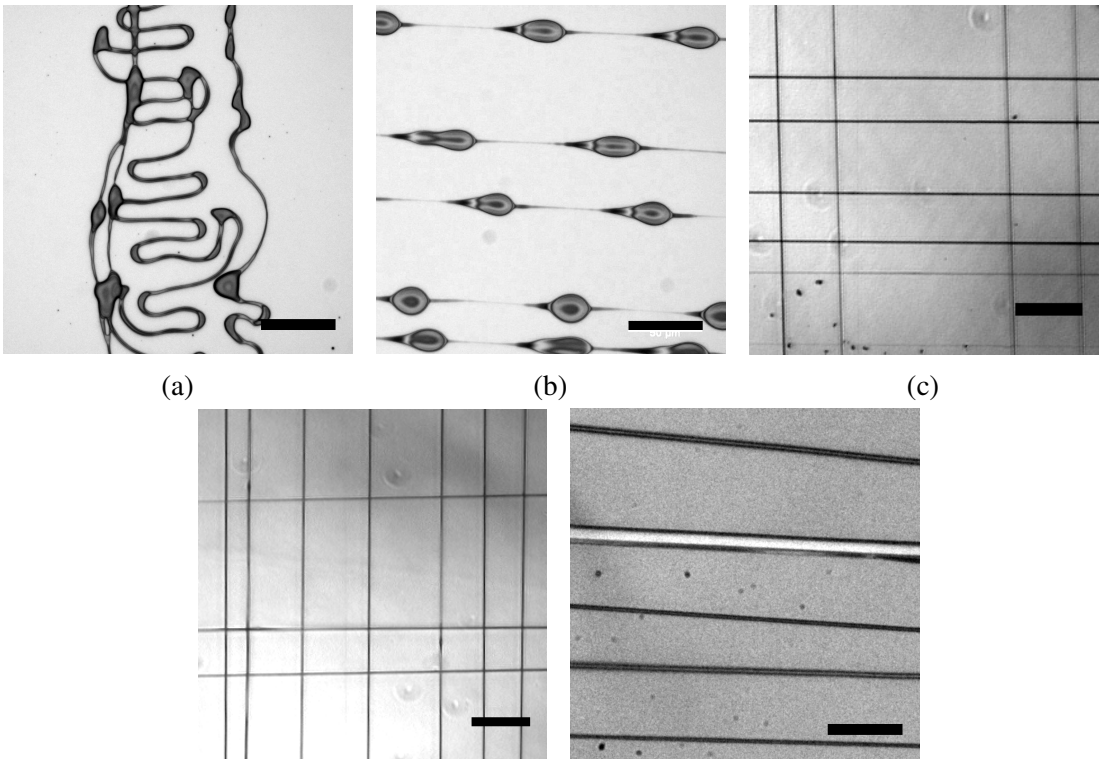

Fig. 2.11 Fibre morphology obtained using LEP with solutions of (a) G(11); (b) G(13); (c) G(16); (d) G(19) and (e) G(22). Scale bars indicate 50 μm.

morphology, these fibres exhibited the ability to be suspended over a complex geometric structure, such as a 3D printed structure, pre-cast PDMS microfluidics and between glass slides[45]. The increase of loss modulus also results in an increase in fibre diameter, as observed in the G(22) samples (Fig 2.11e).

The loss tangent $\tan(\delta)$ measures the relative proportion between the elastic and viscous component in the sample material. As shown in Fig 2.12, where $\tan(\delta)$ of the G(11) and G(13) solutions is greater than 10 and peaks at 11 rad/s. As the storage modulus increases in G(16) and above, $\tan(\delta)$ decreases and becomes weakly dependent on ω. For the G(22) solution, the value of $\tan(\delta)$ is approximately 1. The decrease in $\tan(\delta)$ shows more dominant elastic behaviour. This indicates that, at higher gelatin concentrations, the solution becomes more solid-like than liquid-like. In practice, whilst more liquid-like solutions (up to G(19)) were processed using the generic LEP configuration, and more solid-like solutions (G(22)) were more suitable for the drag-and-pattern configuration due to the difficulty in extrusion.

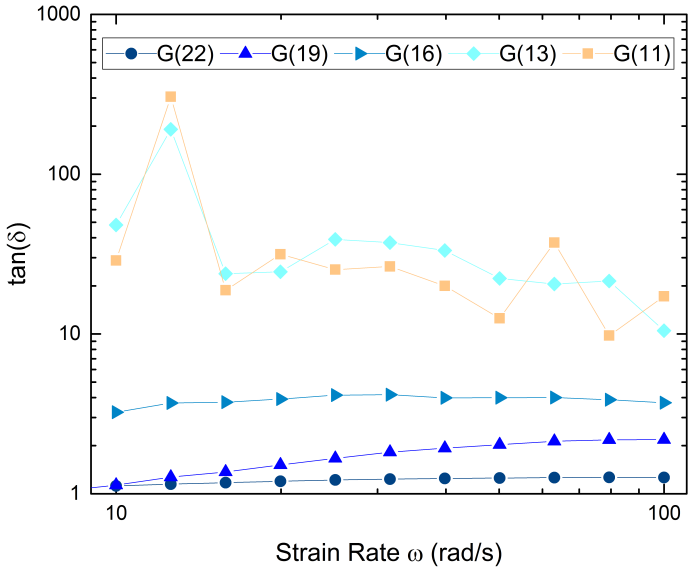

Fig. 2.12 The loss tangent of gelatin solution for strain rate sweep.

dECM concentration dependence

The Atomic Force Microscopy measurements was performed by Dr Francesco Simone Ruggeri, Department of Chemistry, University of Cambridge.

Using dUBM-laden gelatin solution as a guidance, the effect of dECM on the viscosity of the composite solution was investigated. Since the G(19) solution provided the most optimum LEP fibre condition, the overall protein polymer contents (dECM and gelatin) were held at 19 wt% in the composite solution. The solution was prepared by substituting a proportion of gelatin with dECM powder while holding other solvent proportions constant. The composition of dECM-laden gelatin solution is displayed in Table 2.3. With this composition, the prepared solution is shown in Fig 2.13. For U(1) and U(10), the dECM material was not completely dissolved and existed in the solution as a suspension. Hence, the solution appears cloudy. Visually, the texture of the solution was still similar to that of a pure gelatin solution. The highest dECM concentration achieved using this method was 9.5 wt% in the solution (50% in the overall protein and the final solidified fibres). At this concentration, U(50) exhibited a paste-like texture.

Table 2.3 dECM-laden gelatin solution composition.

Solution	dUBM (wt%)	Gelatin (wt%)	Water (wt%)	AA (wt%)	EA (wt%)	Final fibre concentration (wt%)
U(1)	0.19	18.81	26	33	22	1
U(10)	1.9	18.1	26	33	22	10
U(50)	9.5	9.5	26	33	22	50

AA is Acetic acid and EA is Ethyl acetate.

Fig 2.14 shows the complex viscosity, η^*, of the dECM-laden gelatin solution over the strain rate range of 10 rad/s and 100 rad/s. In this case, η^* decreases with increasing strain rate, indicating shear thinning behaviour consist with the pure gelatin solution. Fig 2.15 shows η^* of the dECM-laden solution at 100 rad/s. Since the dECM material was added as a substitution to gelatin, the gelatin concentration in the dECM-laden solutions was 18.9 wt%, 18 wt% and 9.5 wt% for U(1), U(10) and U(50), respectively. In Fig 2.15, the contribution to η^* by gelatin concentration is labelled in dark blue, and the η^* of the composite solution is labelled in light blue. As the dECM concentration increases, η^* increases significantly. As the gelatin contribution decreases with gelatin concentration, the steep increase in η^* is majorally contributed by the dECM component.

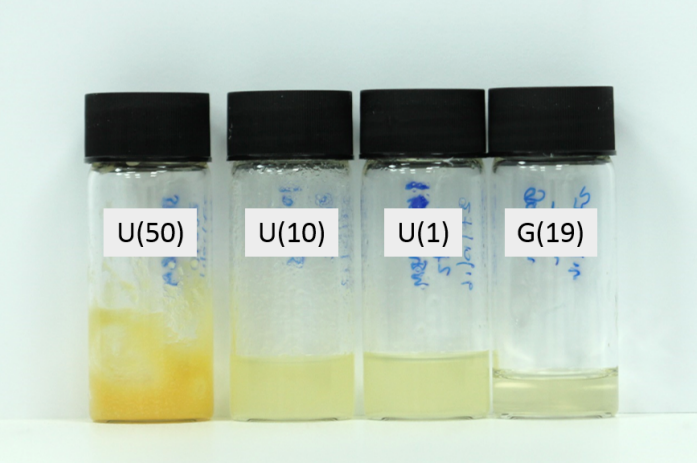

Fig. 2.13 dECM-laden solutions.

The storage modulus, G', increases with the strain rate, indicating an increase in the storage modulus towards a shorter timescale, as shown in Fig 2.16. The loss modulus, G", also increases with the strain rate, reflecting a higher resistance to flow over a shorter timescale (shown in Fig 2.17). Fig 2.18 shows a summary of G' and G" at different dECM concentrations measured at 100 rad/s (patterning rate). As low as 1% dECM is sufficient to give a distinct increase in both G' and G". Whilst G' and G" of U(1) and U(10) solution are similar, the U(50) solution has significantly high G' and G", reflecting its paste-like nature. The increase in G", and possibly the inhomogeneity of the solution, causes slight variations in fibre diameter (Fig 2.20). The relative viscous and elastic components were investigated by measuring $\tan(\delta)$, shown in Fig 2.19. This determines the adapted LEP configuration for processing the dECM-laden solution. Regardless of the dECM concentration, $\tan(\delta)$ exhibits little or no dependence on the strain rate. However, $\tan(\delta)$ decreases with increasing dECM concentration, indicating more solid-like behaviour. Especially for U(50), the value of $\tan(\delta)$ is close to 1, similar to that of the G(22) solution. In practice, the U(50) solution could not be extruded and could only be processed using the drag-and-pattern configuration.

With sufficiently high polymer entanglement (reflected by high loss modulus), all dECM-laden solutions produced straight, uniform and continuous fibres, as shown in Fig 2.20. The fibre diameters increased with the loss modulus. The fibres appeared homogeneous when observed using an optical microscope and no precipitates or phase separation was visible. The smooth morphology was also shown under SEM imaging, as shown in Fig 2.20d. The finer features of fibre morphology were studied using Atomic Force Microscopy (AFM), as shown in Fig 2.21. For the G(19) fibre, the fibre surface was smooth (Fig 2.21d). For the U(10) sample, visually the fibre surface was still smooth (Fig 2.21e) but the root mean square (RMS) roughness increased (Fig 2.21g). As the dECM concentration further increased,

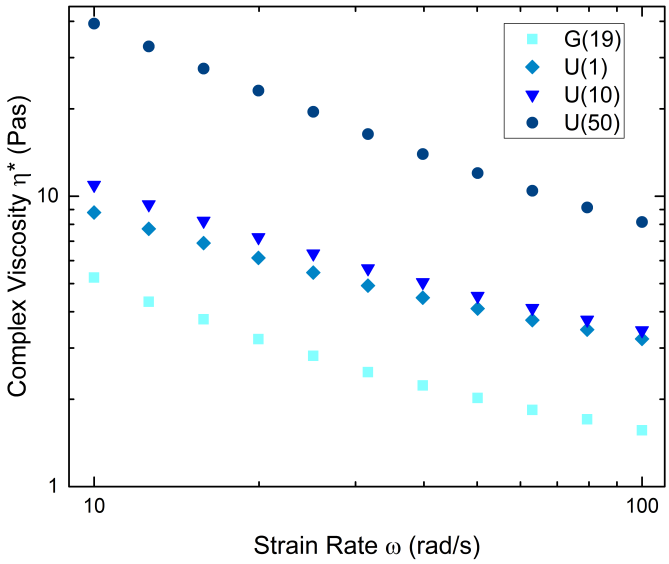

Fig. 2.14 The complex viscosity η^* of the dECM-laden solution over the strain rate range.

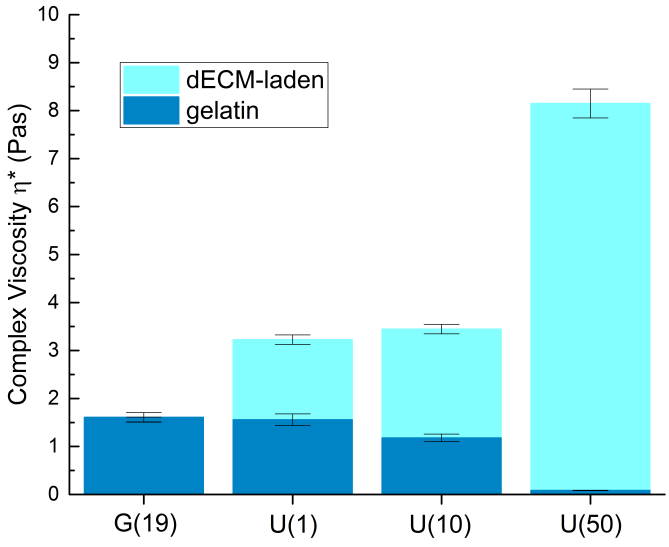

Fig. 2.15 The η^* of dECM-laden solution at different dECM concentrations. The dark blue bars represent the contribution from pure gelatin solution of the specific concentration (18.9 wt%, 18 wt% and 9.5 wt% to the U(1), U(10) and U(50) solution). The light blue bars show η^* of the composite solution. n=3.

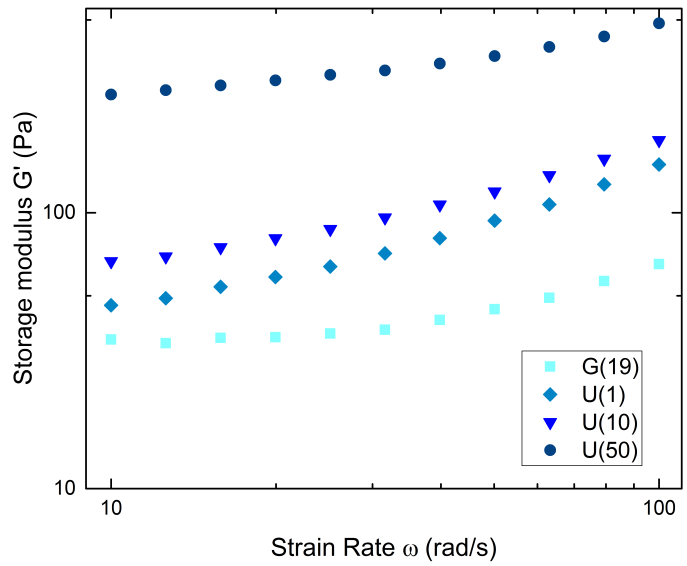

Fig. 2.16 The storage modulus G' of dECM-laden solutions at different strain rates.

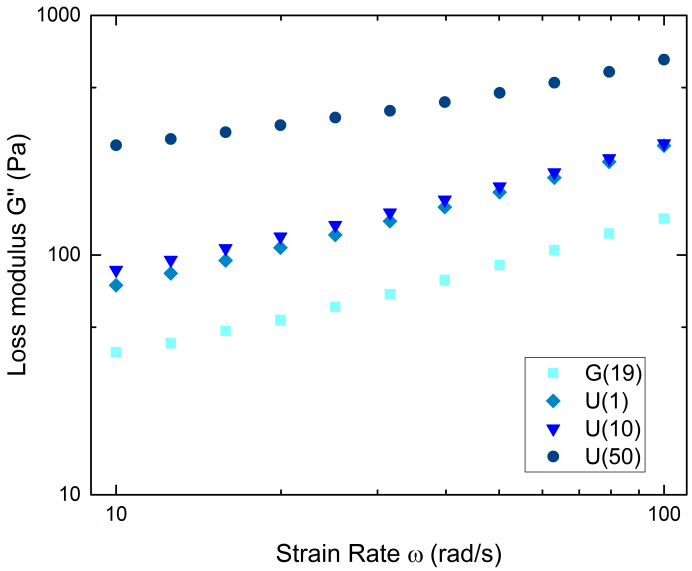

Fig. 2.17 The loss modulus G" of dECM-laden solutions at different strain rates.

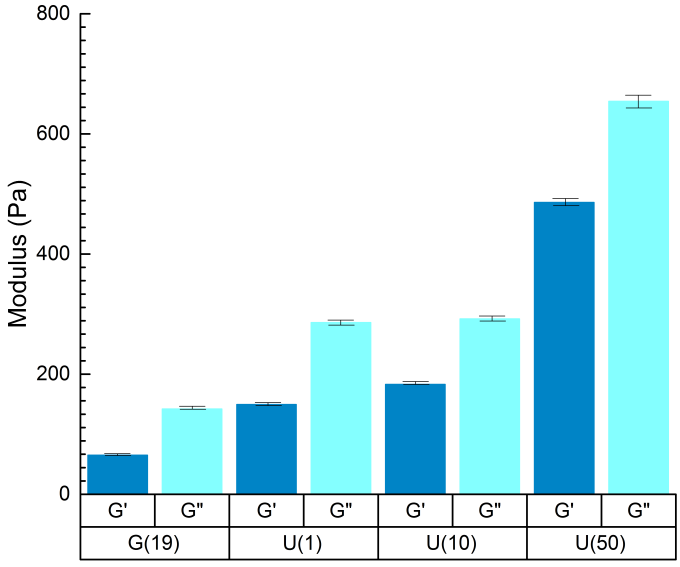

Fig. 2.18 The storage and loss modulus dependence on dECM concentration. n=3.

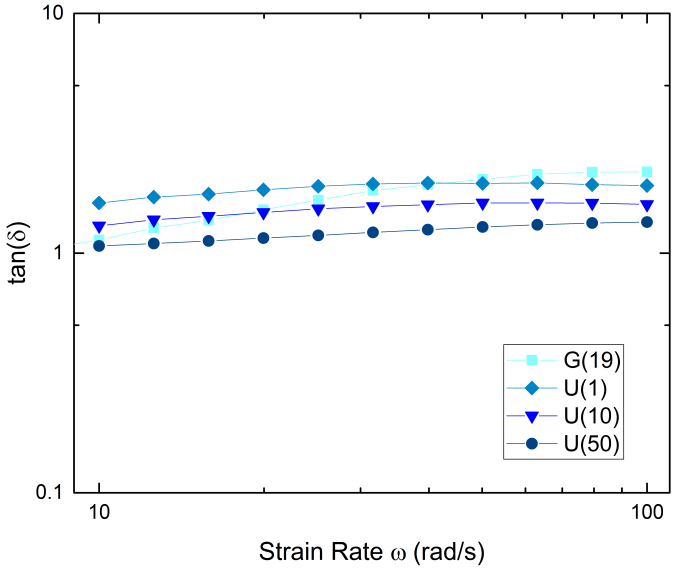

Fig. 2.19 The loss tangent of dECM-laden solutions over the strain rate range.

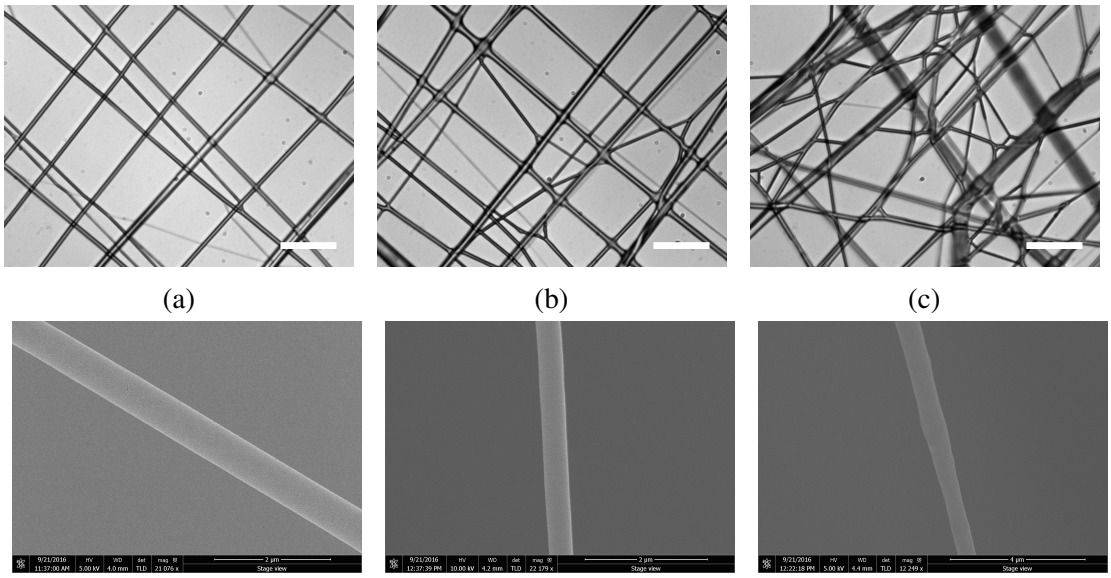

(a) (b) (c)

(d) (e) (f)

Fig. 2.20 Fibre morphology dependence on dECM concentration. (a) and (d) U(1) using optical microscope and SEM respectively; (b) and (e) U(10) in optical microscope and SEM, respectively; (c) and (f) U(50) using optical microscope and SEM, respectively. Scale bars indicate 25 μm.

nano-features on the U(50) fibre became visible (Fig 2.21f). Overall, the roughness of the LEP microfibres increased with dECM concentration.

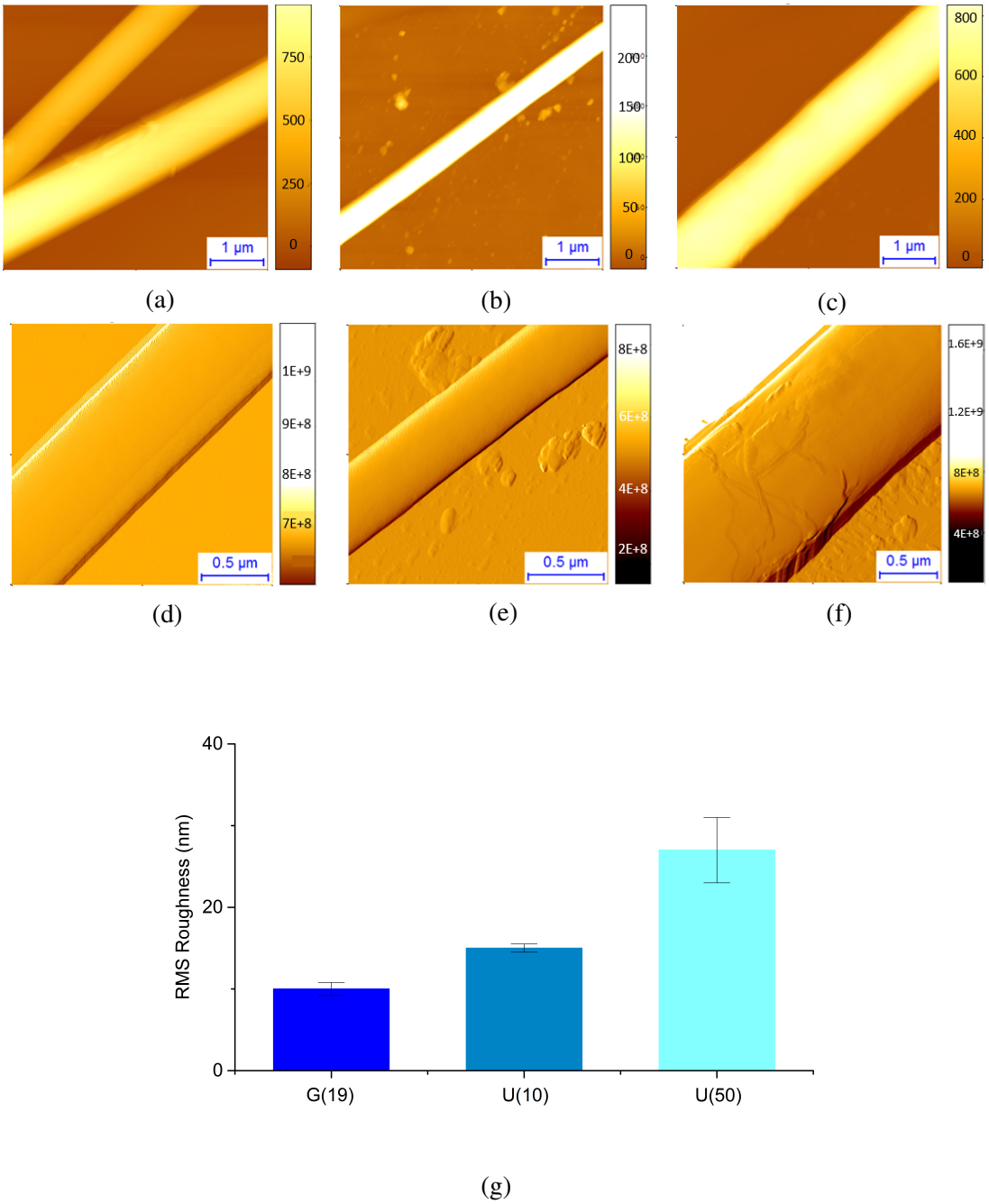

Fig. 2.21 AFM imaging of (a) G(19); (b) U(10) and (c) U(50); and roughness measurement of (d) G(19); (e) U(10) and (f) U(50). (g) The root mean square (RMS) roughness of the dECM-laden gelatin microfibres. n=3.

Crosslinking time dependence

During the LEP process of gelatin, glyoxal was pre-added as a crosslinker and the mixture was loaded in a syringe for microfibre fabrication. The working time of such mixture is up to 4 hours, beyond which the solution was either too viscous for extrusion or drying too fast for continuous processing. Therefore, G(19) solution was mixed with glyoxal and tested over 6 hours, together with a fully crosslinked gelatin gel, to investigate the change of viscoelasticity during LEP working time and beyond. The choice of glyoxal concentration is explained in Appendix B.

The crosslinker was thoroughly mixed with gelatin solution and 1 mL was mounted onto the rheometer at each hour. In addition, a fully crosslinked gel was cast into the cylindrical shape to fit the rheometer dimensions and the rheology data recorded under the same measurement conditions as the solution. Fig 2.22 shows a strain sweep of the G(19) solution and a fully crosslinked hydrogel, ranging from 0.1% to 100% strain. In the solution state, the storage modulus, G', and loss modulus, G", were in the same order of magnitude. Both G' and G" increased with strain, reached a peak at 70% strain and leveled off. In the fully-crosslinked hydrogel state, G' was more than one order of magnitude higher than G". G' was independent of the strain and G" displayed weak dependence on the strain. This shows that, after 24 hours crosslinking, the physical network between molecules was established and the material was solid-like. The hydrogel exhibited more elastic than viscous responses under deformation.

During crosslinking, as shown in Fig 2.23, η^* increased steadily with time over the strain rate range of 10 rad/s (extrusion rate) to 100 rad/s (patterning rate). The same shear thinning behaviour was observed in all crosslinked gelatin solutions. Fig 2.24 shows the complex viscosity was more profoundly influenced at lower strain rate than at higher strain rate. This indicates that, while η^* varied less during fibre patterning, the resistance to flow during extrusion increased more profoundly with crosslinking time. The storage modulus G' increased steadily during crosslinking over the strain rate range, as shown in Fig 2.25. This shows an increase in the storage modulus of the solution when the network of polymer was established. The increase in flow resistance was reflected by the increase in loss modulus G" during crosslinking, as shown in Fig 2.26.

Fig 2.27 displays a summary of the G' and G" at different crosslinking times. Initially during crosslinking, $G' < G$" and the material was more liquid-like. As the crosslinking time increased, G' grew faster than G" and overtook G". The crossover between G' and G" was around 3 – 4 hours which coincided with the working time of LEP after the addition of crosslinker. Both G' and G" continuously increased after the crossover and achieves saturation at full crosslinking. It is important to note that the crossover between G' and G"

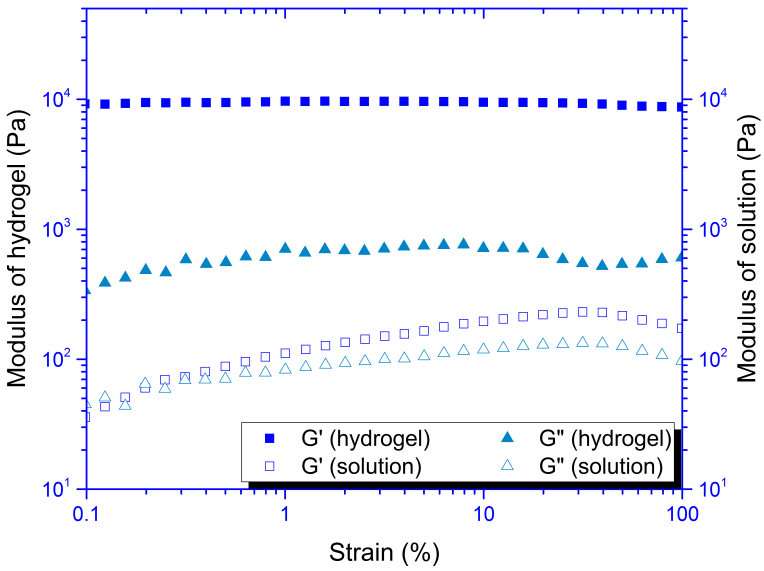

Fig. 2.22 The strain sweep of G(19) solution and hydrogel.

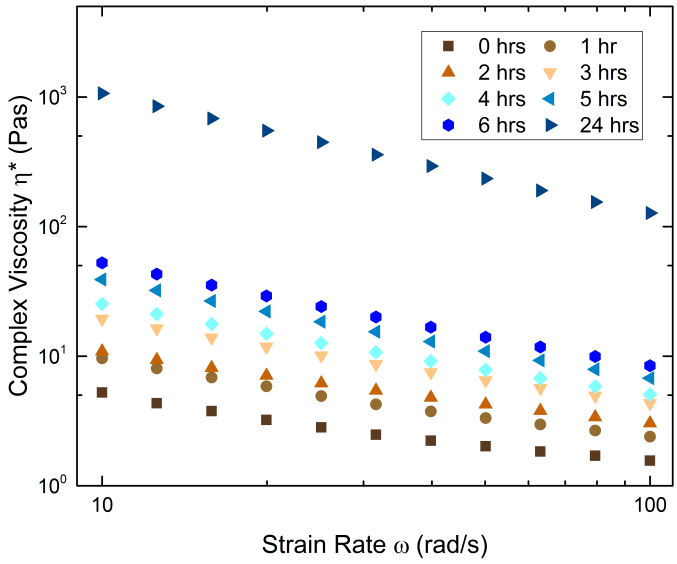

Fig. 2.23 Change in η^* according to crosslinking duration over the strain rate range.

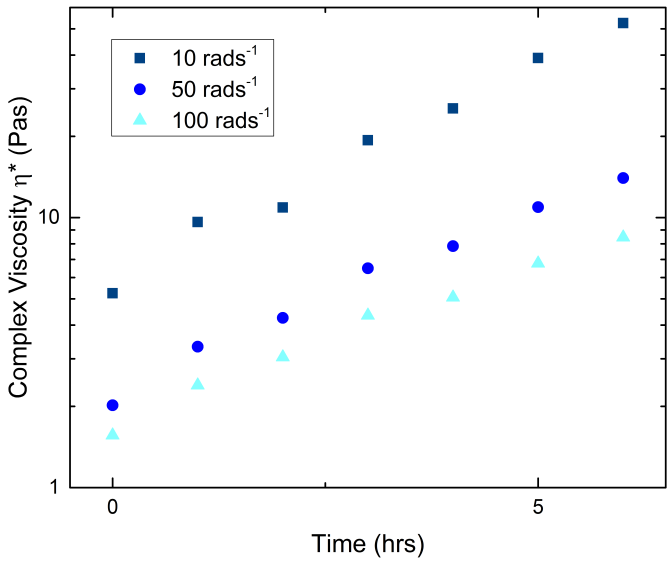

Fig. 2.24 Trend of η^* changes with crosslinking time.

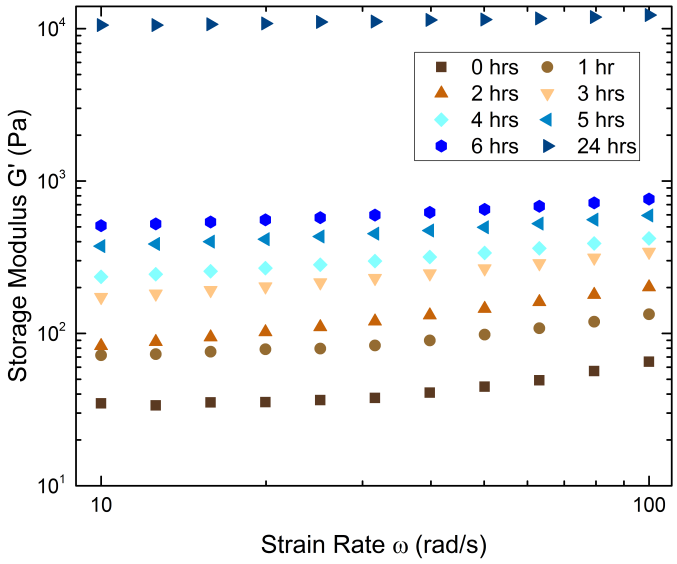

Fig. 2.25 The storage modulus G' of G(19) solution under crosslinking over the strain rate range.

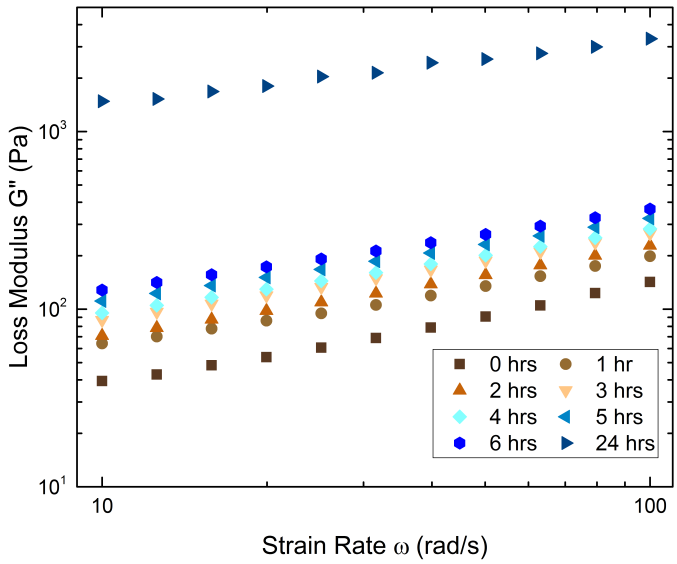

Fig. 2.26 The storage modulus G" of G(19) solution under crosslinking over the strain rate range.

does not necessarily indicate complete crosslinking. The crossover regime can only detect the gel point of crosslinking for some polymers, but not for others[197]. Furthermore, the loss tangent determines the appropriate LEP configuration, shown in Fig 2.28. At first, $\tan(\delta)$ of the gelatin solution at different crosslinking times shows weak dependence on the strain rate. As the crosslinking time increases, $\tan(\delta)$ decreases, indicating more dominant elastic behaviour. At 3 hours of crosslinking, $\tan(\delta)$ decreases to below 1. In practice, this is close to the limit of working time after the addition of crosslinker. At this time, the solution was too viscous to extrude and hence the drag-and-pattern LEP configuration was adopt.

The increase in viscosity (loss modulus) during crosslinking influences the fibre diameter and the network morphology when other experimental parameters remain unchanged. The influence to the morphology of the global fibre network is explained separately in Section 2.5.1. The change in fibre diameter was more observable on agarose hydrogel. Fig 2.29 shows the fibre diameter at 5 minutes, 30 minutes and 60 minutes after adding the crosslinker. Since the agarose gel was moisturised, the water content caused the gelatin fibres to spread more upon attachment to the hydrogel surface. This made the fibre thickening more observable. A continuous increase in fibre diameter can be observed. This thickening effect due to crosslinking is less obvious in suspended fibres. This is because the suspended fibres have

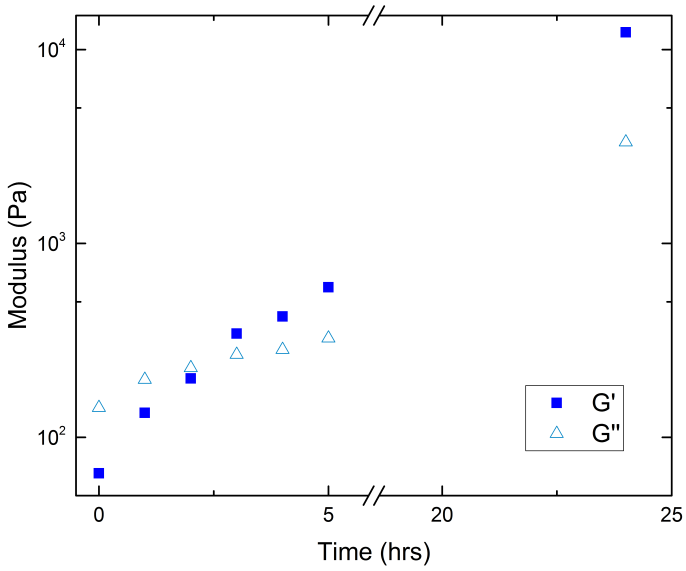

Fig. 2.27 Trend of storage and loss modulus changing with crosslinking time.

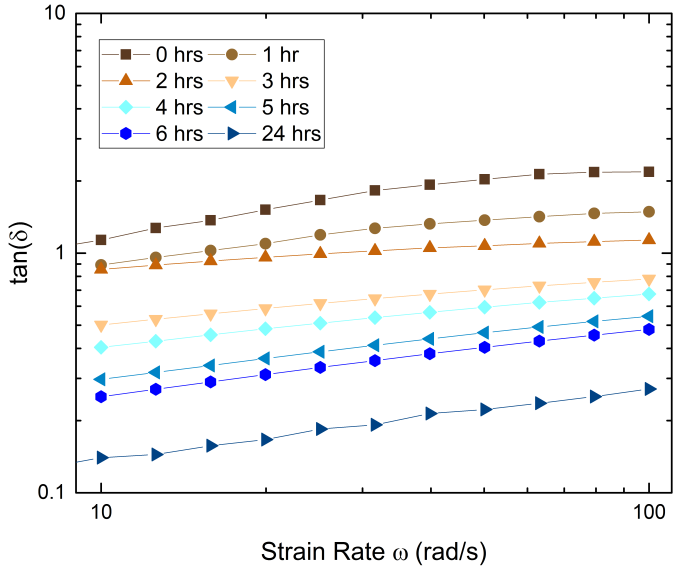

Fig. 2.28 The loss tangent of G(19) solution under crosslinking over the strain rate range.

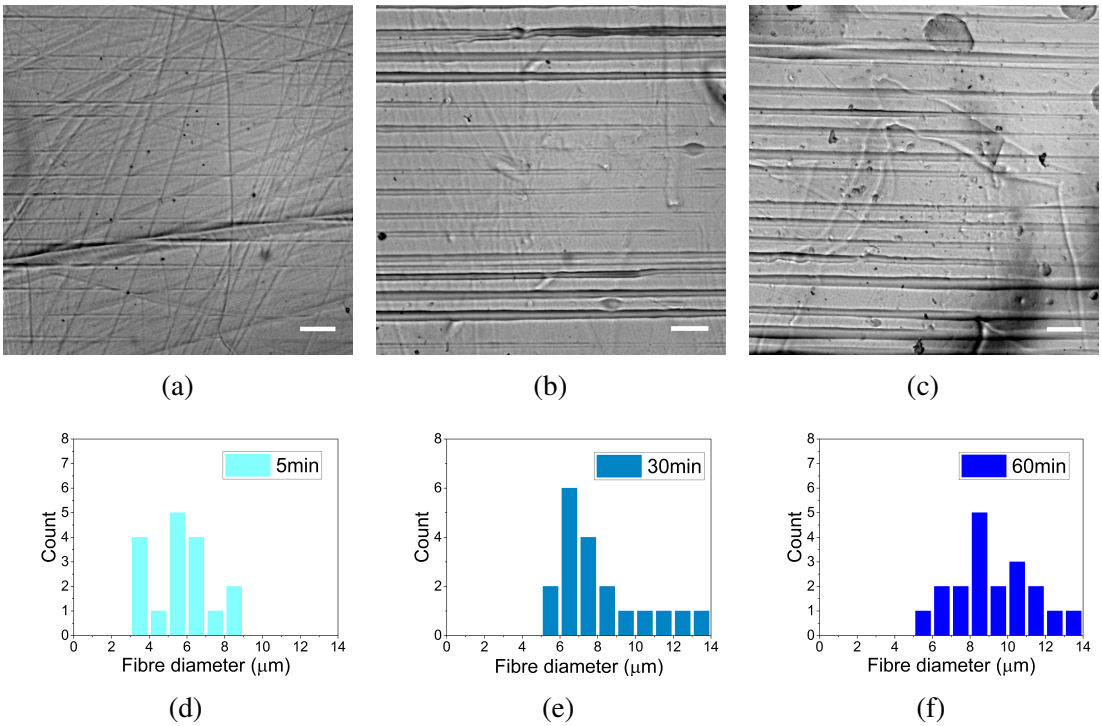

Fig. 2.29 Fibre morphology on agarose gel at (a) 5 min, (b) 30 min and (c) 60 min after adding crosslinker. The statistics of fibre diameter at (d) 5 min: $5.7 \pm 1.6 \mu$m, (e) 30 min: $8.0 \pm 2.3 \mu$m and (f) 60 min: $9.2 \pm 2.1 \mu$m, after adding crosslinker. Scale bars indicate 100 μm.

circular cross section. Fig 2.30 shows the suspended fibres patterned over PDMS-based microfluidic channels and the change of diameter with crosslinking time.

A summary of the fibre morphology and suitable LEP configurations is displayed in Fig 2.31. To summarise, the viscous component, reflected by the loss modulus, G", plays an important role in the fibre morphology. With insufficiently low G", discontinuous fibres or beaded defects was obtained. At the same time, fibre diameter increases with G". The LEP configuration is determined by the loss tangent, which measures the ratio between elastic and viscous component. For $tan(\delta) < 1$, the generic LEP configuration is suitable. For $tan(\delta) \geq 1$, drag-and-patterning LEP configuration should be adapted.

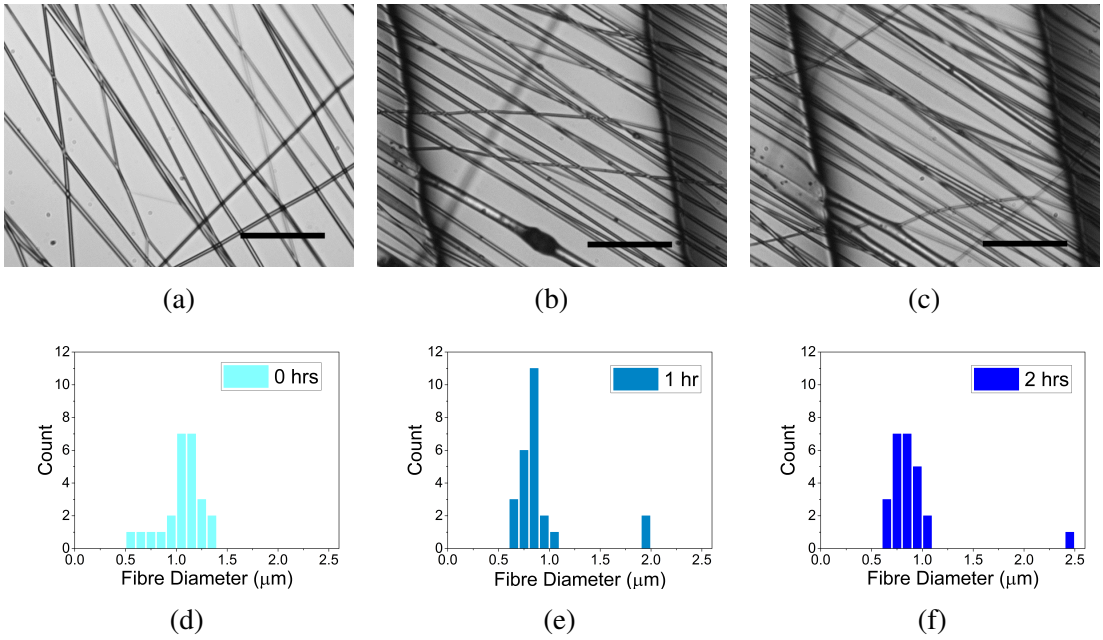

Fig. 2.30 Suspended fibre morphology at (a) 0 hours, (b) 1 hour and (c) 2 hours after adding crosslinker. The statistics of fibre diameter at (d) 0 hours: $0.90 \pm 0.32 \mu$m, (e) 1 hour: $0.90 \pm 0.34 \mu$m and (f) 2 hours: $1.05 \pm 0.19 \mu$m, after adding crosslinker. Scale bars indicate 50 μm.

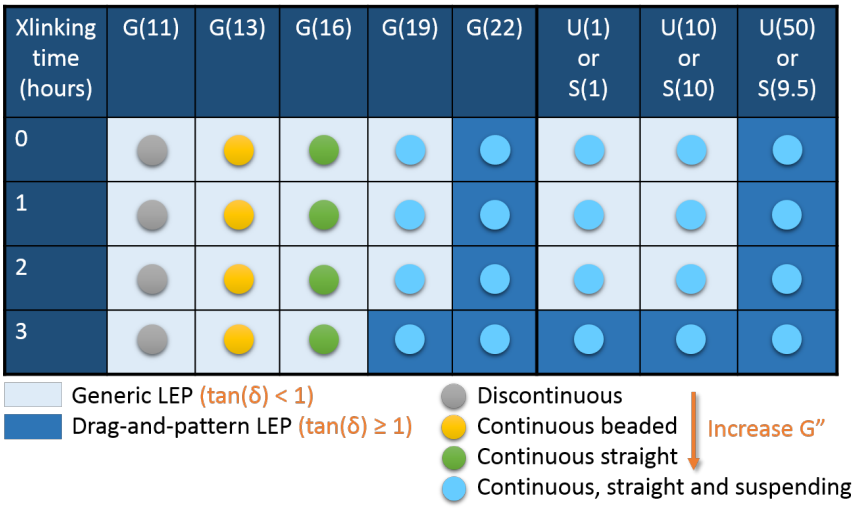

Fig. 2.31 A proposed solution parametric space for fabricating ECM-laden gelatin fibre using LEP.

Woven and non-woven structure

One of the reasons that conventional electrospinning has attracted interests is the capability of producing both woven and non-woven structures. At a high fibre-production rate, the collected fibres fuse together at the junctions[81]. On the other hand, melt electrospinning uses a woven structure to stack the fibres together and obtain a 3D scaffold[148]. With LEP, I have discovered that both woven and non-woven structures can be obtained by carefully tuning the solution properties. For the gelatin and dECM-laden solutions, switching between non-woven and woven structures is most conveniently controlled by the duration of crosslinking. A gradual transition between non-woven to woven was observed as crosslinking established. In the early stage of crosslinking (typically up to 90 minutes after the addition of crosslinker), the polymer chains are minutely crosslinked. The viscosity is relatively low and the solidification rate is slow. Hence fibres can still fuse together and form a non-woven structure. As the polymers become more readily crosslinked, they are more viscous and solidify faster. In this case, they form a woven structure. Fig 2.32 shows the SEM image of a suspended non-woven and woven structures. In the non-woven structure (Fig 2.32a), random fibre orientations and extra fine fibres (diameter $\sim$500 nm) can be identified. This is possibly because the solution was more liquid-like. Hence multiple jets can be formed from a polymer droplet, similar to that observed in far-field electrospinning[198]. In addition, the fibres can change orientation according to the residual charge distribution of the other patterned fibres[199]. Fibres can also merge when they are close to each other. This effect was less observed as the solution crosslinked, and G' increased. Since the fibres fused at the intersections, the non-woven structure is particular useful for fabricating a membrane-like structure. With LEP, one can fabricate a single layer suspended membrane with controllable mesh size. The mesh size of this membrane can be as small as 1 μm in diameter and the membrane thickness can be less than 2 μm, as it is formed by two layers of fibres. Such dimensions are similar to some specific ECM microenvironments *in vivo*[200]. This is not achievable using traditional electrospinning method where the reduction of the mesh size is compromised by adding more fibre layers and therefore increasing the thickness of the membrane. The woven structure is potentially useful in building a 3D scaffold with microfibres. It is interesting to note that the non-woven structure obtained using LEP contains random fibrous orientation. Although the average pore size can be controlled, the orientation of fibres could not be manipulated. In this case, one can only control the average pore size of the membrane rather than the precise position of individual fibres. This is acceptable in tissue engineering because physiological tissues are highly specified but often not perfectly ordered. On the other hand, the woven structure contains a more regular and lattice-like structure. The orientation of the fibres can be controlled more easily and the fabricated

matrix is more ordered. However, it is not possible to control the precise position of each fibre like in melt electrospinning, especially when patterning suspended fibres. This is due to the non-uniform electric field distribution over insulating substrates with complex geometries. This woven structure is still useful for various applications, including fabricating multi-material composites and hydrogel reinforcement. This can also be used to mimic a microfibrous matrix to investigate cell migration through the 3D microenvironment. It is important to note that both woven and non-woven scaffolds of gelatin and dECM-laden gelatin are mechanically robust and resilient. As long as the fibres were not completely dried, one could transfer the sample using a pair of tweezers. However, when the fibres were completely dried, they became brittle and easily damaged when manually handled. When stored in a clean and dry atmosphere, the membrane can be preserved for a few weeks without changing structure or denaturing.

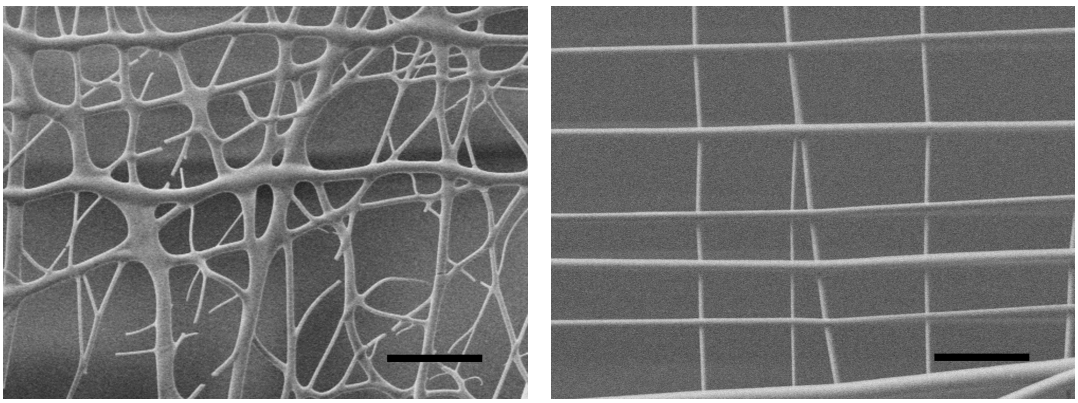

(a) (b)

Fig. 2.32 (a) Non-woven and (b) woven gelatin fibre structures fabricated by controlling the crosslinking time. Scale bars 5 μm.

2.5.2 Extrinsic operating parameters controlling fibre patterning outcomes

As explained in Section 2.3.1, the extrinsic operating parameters that influence LEP fibre morphology include the stage speed and applied voltage. In LEP, altering the stage translation speed is an effective way to tune global patterns, as shown by the work of Li et al. for polystyrene fibres[45]. However in the case of gelatin fibre, I have rarely observed a change of fibre pattern. However, a mismatched stage speed could have given rise to the beaded defects shown in Fig 2.11b for low gelatin concentration. The beads-on-string morphology

obtained in this experiment is particularly similar to that described by N. Bu et al.[201]. By adapting the mechano-electrospinning technique, which has a similar experimental configuration to LEP, different PEO fibre morphologies could be obtained by purely tuning the collecting stage velocity. At relatively low speed, larger beads were obtained. As the stage speed increased, the size of the beads decreased and eventually beads-free fibres were obtained. In this case, the formation of the beads were also a result of the accumulation of deposited solution.

The voltage-induced electrostatic focusing effect aids continuous fibre patterning in the drag-and-pattern LEP configuration. This is illustrated by patterning the G(19) solution, as shown in Fig 2.33. Without voltage, the drag-and-pattern relies only on the mechanical stretching force. In this condition, G(19) solution can not be used for fibre patterning due to its insufficient polymer entanglement. With an applied voltage of 230 V, straight and uniform fibres can be patterned consistently. Therefore, unlike the STEP technique which solely relies on the mechanical stretching of highly entangled polymer solution, voltage is necessary for drag-and-pattern LEP.

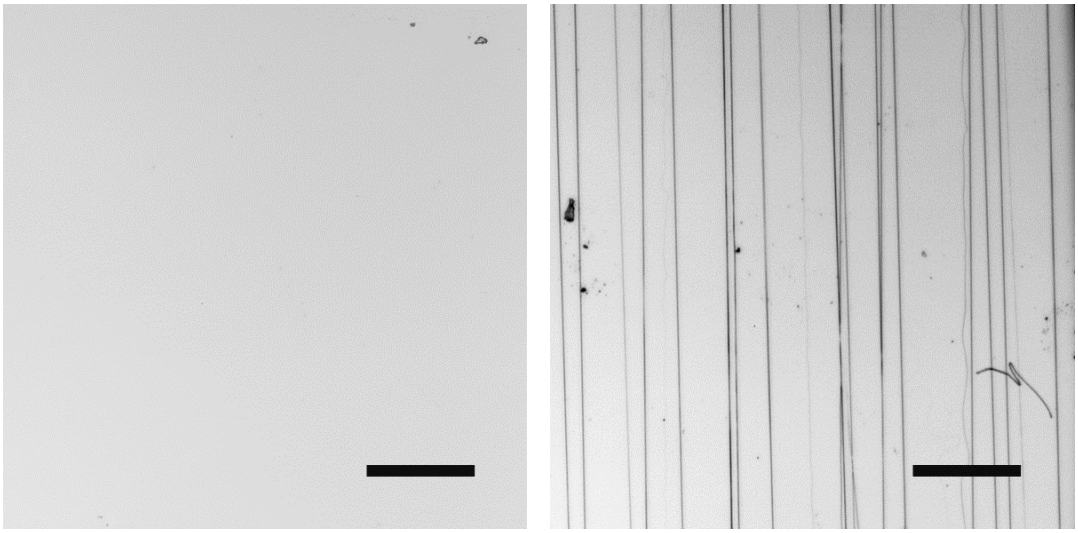

(a) (b)

Fig. 2.33 The voltage effect in the drag-and-pattern electrospinning configuration. Gelatin fibres patterned from 19 wt% solution with (a) no voltage applied and (b) 230 V applied between the needle tip and the collecting substrate. Scale bar 100 μm.

I further investigated the influence on fibre patterns by the applied voltage. In practice, G(19) solution was used to pattern on pre-cast PDMS under 100 V, 230 V and 400 V. This also allowed the investigation of the suspendibility of LEP fibres on complex geometry. Fig 2.34a shows the LEP fibre network patterned under the stated voltage. Under 100 V, the fibres were uniform and straight but not firmly attached to the PDMS substrate. Under 230 V,

uniform straight fibres could be patterned in a regular manner to achieve a high fibre density. As the voltage increased to 400 V, the fibres became thicker and the variation in density was larger. From the statistics of fibre diameters (Fig 2.34b), the spreading of fibre diameter was the lowest at 230 V.

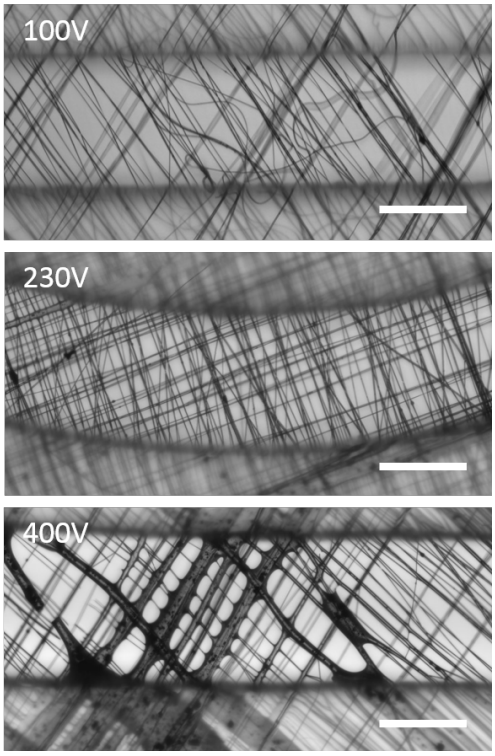

(a)

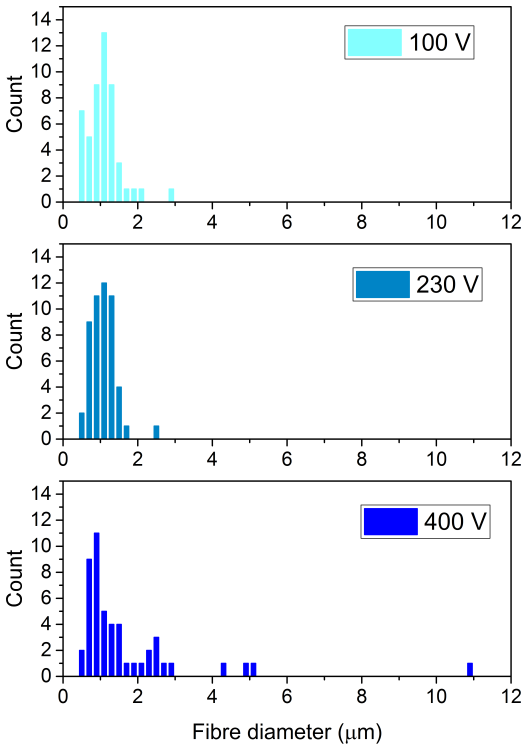

(b)

Fig. 2.34 (a) Fibre networks fabricated under 100 V, 230 V and 400 V. Scale bars 100 μm (b) Statistics of fibre diameters of the corresponding voltage.

Suspended fibres

There are several factors contributing to the suspendibility of patterned fibres: the polymer entanglement, the volatility and evaporation rate of the solvent, and the applied voltage. The polymer entanglement is determined by the molecular weight and solution concentration. Firstly, good polymer entanglements help to maintain the continuous patterning of fibres and improve the inner connectivity within the fibres which makes them harder to break under tension. In this case, I found that the protein concentration (gelatin plus dECM) should be

at least 19 wt% in order to obtain continuous suspended fibres. Secondly, the volatility and solvent evaporation rate should be high so that the fibres solidify fast. Upon solidification, the fibres harden and become plastic-like. This helps to retain the rigidity of the patterned structure and therefore maintain their suspended nature. For the dECM-laden solution, the main solvents are water, acetic acid and ethyl acetate. Both acetic acid and ethyl acetate are highly volatile so the solution solidification rate is high. For less volatile solutions such as Polyethylene oxide (PEO) dissolved in water, a proportion of the patterned fibres buckled and were not able to be suspends in a straight line. Thirdly, the applied voltage imposes an external force to pull the patterned fibres towards the collecting substrate. The voltage should be sufficient to initiate the LEP process and make the fibres attach to the substrate. However it should not be too high as to cause the fibres to collapse. For the dECM-laden solution, the optimum working voltage was 230 V. Fig 2.34 shows the fibre network fabricated under three voltages. At 100 V, the electric field strength was low and the fibres loosely attached to the substrate. This is undesirable for cell culture as the fibres can easily detach from the substrate when immersed in water. At 230 V, regular fibres could be patterned at high density. At 400 V, the high electric field strength caused excess solution flow and fibre collapse. In this case, the fibre diameters were less uniform. In addition, the thick fibres can swell and buckle when immersed in aqueous solution. This brings difficulties when imaging the scaffold for cell studies. Fig 2.35 shows the 3D construction of a suspended gelatin fibre mesh over PDMS channel using a confocal microscope. This was achieved by blending fluorescein (a type of fluorescent molecules) into gelatin solution and processing them using LEP. By imaging the sample layer by layer and stacking them together, a 3D construction could be obtained. Since only the fibres were fluorescent and could be imaged, the channel and the PDMS appeared dark and were manually outlined.

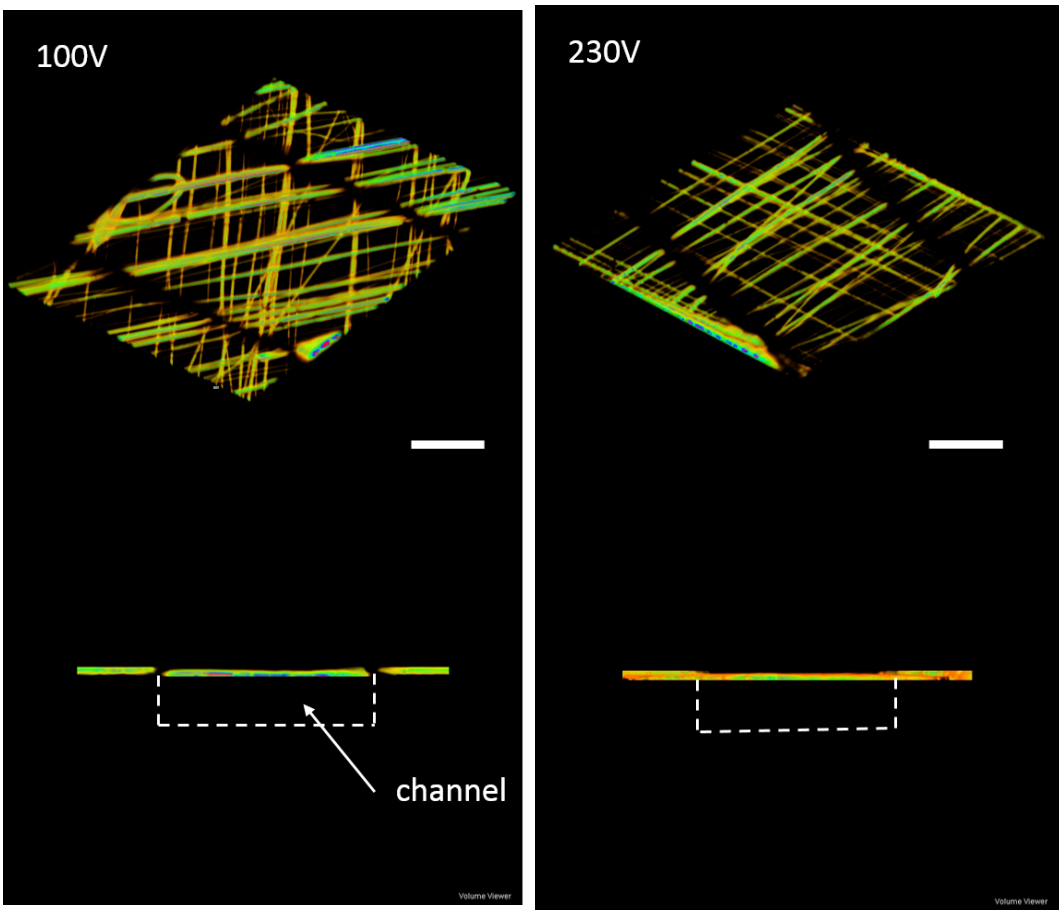

(a) (b)

Fig. 2.35 3D construction of the suspended fibre networks fabricated under (a) 100 V and (b) 230 V, composed from z-stack image sequences. A top-view image and side-view image is shown in each condition. Fibres were visualised by the inclusion of fluorescein, which was blended in the gelatin solution. These fibres were patterned on microfluidic microchannels. Since the microchannels were not labelled with fluorescence, they are manually outlined in the side-view images. Scale bars 100 μm.

2.5.3 Ambient conditions

The ambient parameters that influence LEP outcome include temperature, humidity and air flow velocity in the LEP chamber. In this study, the ambient condition was held unchanged to minimise its impact on fibre patterning. In the case of the gelatin solution, the best electrospinning condition was obtained at 22°C, low humidity and with minimum air flow.

2.6 Conclusion

This chapter demonstrates the precise microfibre patterning with high loading of dECM. The highest dECM concentration incorporated in the solution was 9.5 wt%, which became 50 wt% in the final solidified microfibre. The LEP process enabled a stable and continuous production of nano- to microfibres. As intrinsic polymer solution properties, the loss modulus, G", reflected the fibre morphology; and the loss tangent, tan(δ) determined the LEP configuration to be adopted. These general trends are applied for the effect of gelatin concentration, dECM concentration, and crosslinking time. An optimal gelatin concentration of 19 wt% was identified for fibre patterning. From the extrinsic operating parameters, the voltage affected the attachment between the fibre and PDMS substrate as well as the fibre diameter distribution. The smallest diameter variation was obtained using 230 V, which is adopted in subsequent dECM-laden fibre patterning. To conclude, the individual fibre morphology and network were investigated in this chapter to determine the optimum experimental conditions for dECM-laden gelatin fibre patterning. LEP provides the potential for fabricating robust bio-functional devices for cell culture models. The chemical and physical characterisation of these LEP fibres are explored in **Chapter 3**.

Chapter 3

Chemical and mechanical characterisation of free-standing dECM-laden microfibres

Abstract

Native ECM consists of a complex assembly of proteins, proteoglycans and growth factors. These molecules are secreted by cells during continuous matrix development and remodelling. The specific biochemical composition of ECM is known to play an important role in regulating cell function and behaviour. The dECM, which closely reassembles the native ECM, was chosen to be patterned into nano- and microfibres using methods described in the previous chapter. Since both the biochemical and mechanical properties of the microenvironment play an important role in directing cell fate, some of these properties of the dECM-laden gelatin fibres are characterised in this chapter. It was found that the key dECM components, including collagen IV, laminin and fibronectin, were effectively incorporated within the patterned microfibres. The preservation of vascular endothelial growth factor (VEGF) and basic fibroblast growth factor (b-FGF) were further proven. The dECM-laden gelatin fibre network demonstrated robust mechanical properties and pattern flexibility. As the dECM concentration increased from 0 wt% (G(19)) to 9.5 wt% (U(50)), the Young's modulus of the fibres increased from 607.0±10.0 kPa to 49.0±0.7 MPa, spanning two orders of magnitude. The chemical integrity, mechanical resilience and wide range of mechanical properties can potentially be used to establish cell culture platforms which further resemble the fibrous ECM microenvironments.

3.1 Introduction

The ECM is a complex meshwork consisting of pores, fibres, ridges and other nanoscale features. Depends on the origin of the tissue, the protein composition of the ECM can vary significantly[19]. The protein components include collagens, proteoglycans, ECM-associated glycoproteins and secreted factors. Chemically, the ECM-associated glycoproteins and growth factors, are secreted by cells during continuous matrix development and remodelling. The specific biochemical composition of ECM is known to play an important role in regulating cell function and behaviour[21, 202–204]. Physically, the fibrillar collagens (such as collagen I-III) mediate tensile strength in the ECM. The sheet-forming collagens (collage

IV) contribute to the formation of the basement membranes[20]. Both types of collagen provide a physical scaffold for cell attachment and mechanical cues to guide cell migration and differentiations[205, 206]. The proteoglycans provides hydrations and swelling pressures to withstand compression forces[207]. The differences in collagen and proteoglycan compositions between ECMs from different organs result in a vast range of mechanical properties[19]. Even for the same tissue or organ, the physical properties change between a healthy and a diseased state[208]. Cells are sensitive to the stiffness of the substrate through adhesion complexes and actinmyosin cytoskeleton[209]. The substrate stiffness can influence cell phenotype and differentiation[210, 211]. Therefore, replicating the extremely complex chemical and physical properties of the ECM remains an important task in biofabrication.

In the previous Chapter, the patterning of high-loading dECM-laden gelatin fibres was demonstrated using LEP. This chapter focuses on the chemical and physical characterisations of the LEP fibres. More specifically, the key ECM proteins, such as collagen IV, laminin and fibronectin, were characterised by using Immunofluorescent Staining. The change in molecular structure was further analysed by using Fourier Transform Infrared Spectroscopy (FTIR). The preservation of growth factors was also characterised. In addition, it was hypothesized that cellular processors particularly interact with and locally sense individual microfibres. Therefore, it was of interest to measure the physical properties of an individual suspended fibre. LEP allowed the patterning of suspended fibres on PDMS-based microfluidic channels. Using this suspended configuration, I measured the Young's modulus of the suspended dECM-laden fibres. Aiming to build a cell culture platform, fibre swelling during hydration was measured to clarify the robustness of the suspended fibre *niche* for use in cell culture.

3.2 Theoretical background

3.2.1 Mechanical characterisation using a micropipette cantilever

Inspired by Atomic Force Microscopy (AFM), micropipettes have been used as a cantilever in the characterisation of biological objects. The micropipettes are fabricated by heating and pulling a glass capillary using a capillary puller. The diameter and taper length of the micropipette is strongly dependent on the heating temperature and pulling force of the capillary puller[212]. The aperture size can reach 200 nm in diameter[213]. The end diameter of the cantilever can be tailored according to the purpose of the measurement. For example, the surface friction of living HeLa cells was measured using cantilevers with a diameter of approximately 15 μm[214]. Using this fabrication technique, a thin and flexible micropipette

cantilever can be obtained. The cantilever is calibrated by measuring its deflection under a known force. One method is to add a water droplet to the end of the pipette, as illustrated in Fig 3.1. The water droplet deforms the cantilever under gravitational force. As the volume of the droplet changes, the cantilever deflection changes proportionally to the droplet volume. This process can be modelled as a bending cantilever beam (Fig 3.1). With one end of the beam fixed, the other end is loaded with weight W. Assuming the weight of the beam is negligible compared to the load, the deflection of the end under loading is:

$$d = \frac{WL^3}{3EI} \tag{3.1}$$

where d is the deflection, L is the beam length, E is the Young's modulus, and I is the area moment of inertia of the beam's cross section[215]. From equation 3.1, the deflection, d, is linearly proportional to W by the prefactor $\frac{L^3}{3EI}$, known as the force constant. This prefactor is determined by the geometry of the cantilever. With a shorter length and larger diameter, the cantilever appears stiffer. By tracking the volume of the droplet and the cantilever position, the droplet weight can be plotted as a function of the displacement. The gradient of the force over displacement plot is the force constant of the cantilever. With the force constant calibrated, the cantilever can be used to measure the stiffness of the object of interest. The deformation force can be calculated through the cantilever displacement and force constant.

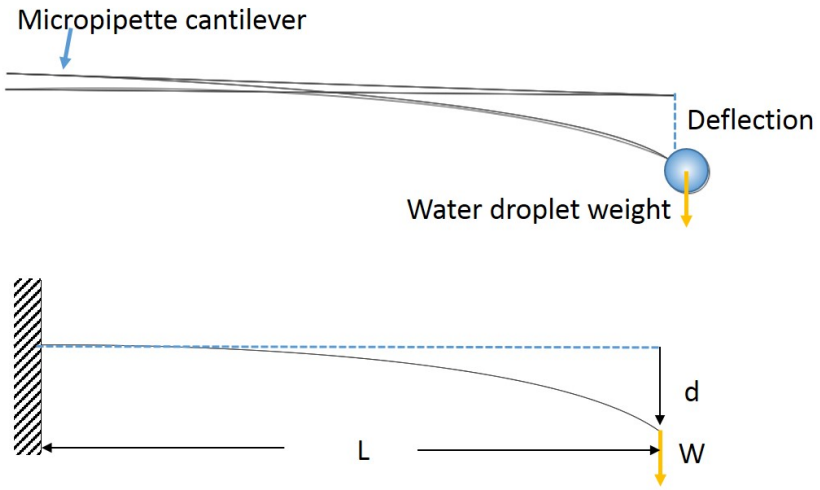

Fig. 3.1 Micropipette cantilever calibration model. L is the cantilever length, W is the weight of the water droplet and d is the deflection displacement.

3.2.2 Protein crosslinking

Proteins are macromolecules which consist of long chains of amino acid residues. The specific sequence of the combinations of 20 types of amino acid results in a vast array of protein functionalities. Despite the complexity of protein structures, only four protein chemical groups are targeted in the majority of crosslinking and chemical modifications. These groups include primary amine, carboxyl, sulfhydryl and carbonyl groups.

- **Primary amine groups (-NH2)** exist at the N-terminus of polypeptide chains (alpha-amine) and the side chains of lysine residues (epsilon-amine). In the physiological environment, the amine groups are positively charged on the outer surface of proteins. Therefore these can be conjugated without denaturing the protein structure.
- **Carboxyl groups (-COOH)** exist at the C-terminus of polypeptide chains and the side chains of aspartic acid and glutamic acid. Similar to primary amines, carboxyls are usually located on protein surfaces and can be easily accessed.
- **Sulfhydryl groups (-SH)** exist in the side chains of cysteine, often as a part of the secondary structure. In order to make them available for conjugation, disulfide bonds (associated with the secondary or tertiary structure) must be reduced.
- **Carbonyl groups (-CHO)** are obtained by oxidizing the polysaccharide in glycoproteins.

Crosslinkers or crosslinking reagents are used to form covalent or ionic bonds between protein molecules to establish a 3D protein network. They have also been used to facilitate the identification of relationships between neighbouring proteins and ligand-receptor interactions, as well as to modify nucleic acids and drugs. Typically, crosslinkers contain two or more chemically reactive groups which bond to the functional groups of protein molecules. There are three types of crosslinkers: homobifunctional, heterobifunctional and photoreactive crosslinkers.

- **Homobifunctional crosslinkers** contain identical reactive groups at either end of the molecules. They are widely used for binding link functional groups, forming intermolecular crosslinks, and preparing polymers from monomers.
- **Heterobifunctional crosslinkers** possess two different reactive groups at either end. Therefore, they can be used to link dissimilar functional groups. These crosslinkers are used with dissimilar biomolecules to produce multiple intermolecular crosslinks and conjugates.

- **Photoreactive crosslinkers** are heterobifunctional crosslinkers which can be activated upon exposure to ultraviolet visible light. Two common chemical groups are aryl-azide and diazirines. These crosslinkers are preferred for non-specific bioconjugation. Typical used include binding nucleic acids.

A specific crosslinker can be selected according to the target functional groups. Some common examples include Carbodiimide (EDC) for carboxyl groups, NHS ester and glutaraldehyde for amine groups, maleimide for sulfhydryl groups, and hydrazide for carbonyl groups. Glyoxal is a homobifunctional crosslinker giving similar reaction characteristics to formaldehyde and glutaraldehyde. The toxicity level of glyoxal is lower than that of formaldehyde and glutaraldehyde (LD_{50} for rat is 640-8979 mg/kg for glyoxal, 600-800 mg/kg for formaldehyde and 246 mg/kg for glutaralderhyde[216–218]). Thus it is more suitable for cell culture purposes. Glyoxal is highly reactive towards alcohols and amides, and is useful for crosslinking a wide range of polymers, including starch[219], chitosan[220] and polyvinyl alcohol[221]. It has been proven to successfully crosslink gelatin[222]. Additionally, there are a few studies proving its crosslinking ability for dECM[223, 224].

In addition to chemical crosslinking using a reagent, the preparation of biological hydrogel relies on physical crosslinking and self-assembly. Physical crosslinking includes changes of temperature to achieve reversible crosslinking. For most biological hydrogels, such as collagen I and dECM, pH balancing and neutralising are crucial steps in hydrogel preparation as well as for cell cultures[165, 153, 225]. The pH neutralisation can induce self-assembly between molecular chains, and hence leads to the formation of a 3D protein network.

3.3 Materials and methods

3.3.1 Immunofluorescent staining of as-spun fibres

Immunofluorescent staining was performed to characterise the distribution of collagen IV, laminin and fibronectin in the as-spun fibres. The antibodies used were anti-transglutaminase 2 (mouse monoclonal, Abcam ab2386), anti-collagen IV (rabbit polyclonal, Abcam ab6586), anti-laminin (mouse monoclonal, Sigma L8271) and anti-fibronectin (rabbit polyclonal, Abcam ab2413). Once the dECM/gelatin fibres were patterned onto a glass coverslip and fully crosslinked, the samples were blocked with 3% BSA/PBS for 1 hour. After washing the sample with PBS (ThermoFisher 10010023), primary antibodies were added and the samples were incubated for 1 hour. Subsequently, the samples were washed again with PBS and incubated with secondary antibodies for 1 hour. After a final wash, the samples were stored in mineral oil and imaged within two days.

3.3.2 Energy-dispersive X-ray spectroscopy EDX

FEI Nova NanoSEM was used for EDX analysis. Suspended dECM-laden fibres were patterned over a 3D-printed holder. As the fibres were free-standing and not attached to any substrate, potential background contamination was eliminated. The fibres were coated with Platinum for 45 seconds. Electronic powder of 10 kV was used in the EDX measurement. Once the fibres were in focus, several points were selected along the centre of the fibre. For each condition, 5 points of interest were taken at different positions along the fibres, several fibres were measured, to obtain statistical data. The elements were identified and their concentrations measured using the EDX program.

3.3.3 Fourier transform infrared spectroscopy FTIR

FT-IR infrared spectrometers (Bruker IFS 113v) was used to measure the molecular structures in the raw dECM, protein references and dECM-laden gelatin fibres. Collagen I and IV, laminin and dECM-laden solutions were deposited on a glass petri-dish and dried for 24 hours. Dry films were obtained and measured. The dECM-laden fibres were patterned onto silicon wafers using LEP. The fibres were removed using a razor blade and collected for measurement.

3.3.4 Enzyme-linked immunoSorbent assay ELISA

ELISA kit (RD Systems, USA) was used to extract the total protein from dUBM and dSIS powder and crosslinked hydrogel. VEGF and b-FGF were assayed with a microplate reader at 450 nm[226].

3.3.5 PDMS microchannel fabrication

The PDMS microchannel device was cast using a silicon mask by standard soft lithography [227]. To fabricate the silicon mask, SU-8 photoresist (MicroChem) was spin-coated onto a silicon wafer to obtain a thickness of 100 μm (2000 rpm). The silicon wafer was pre-baked for 20 minutes at 65°C. The wafer was then covered by a transparency mask printed with the channel outline and exposed under UV light for 15 seconds. After exposure, the wafer was baked for 1 minute at 65°C. Afterwards, the wafer was immersed in photoresistant developer for 15 minutes. The mask was washed using isopropyl alcohol and dried with pressurized nitrogen gas. Sylgard 184 silicone elastomer (Sigma-Aldrich 761036) base and the curing agent were thoroughly mixed in a 10:1 weight ratio. The mixture was poured into the silicon

mask and degassed to remove air bubbles. The PDMS was cured at 60°C for at least 6 hours. Cured PDMS was peeled off the silicon mask, trimmed and ready for fibre patterning.

3.3.6 Fibre patterning on PDMS microchannels

The dECM-laden gelatin solution was prepared as described in the previous chapter. The PDMS microchannel was placed on the stage, in between the initiators. The LEP process was as described in the previous chapter. The dECM-laden gelatin fibres (pre-mixed with crosslinker) were patterned over the microchannel device under 230 V. The fibre sample was stored at room temperature for 24 hours to achieve complete crosslinking.

3.3.7 Capillary pulling and calibration

Sutter P-1000 Micropipette Puller was used to fabricate the micropipette cantilevers. Glass capillaries (1B100-6 OD 1 mm ID 0.58 mm) were mounted onto the Micropipette Puller and fabricated into cantilevers with the following parameters: heat 765, pull 150, velocity 250, time 0 and pressure 200. Afterwards, the pulled capillaries were mounted under a microscope. The end of the cantilever was cut using scissors to obtain an outer diameter of 7.5 – 10 μm. These cantilevers were plasma treated for 10 minutes to obtain a hydrophilic surface which enables the calibration process. For calibration, the thicker end of the cantilever was fixed and distilled water was pushed through with a syringe. Once a droplet formed at the end of the cantilever, the syringe was removed. The evaporation of the droplet was recorded with a camera. The deflection and droplet volume were measured using ImageJ.

3.3.8 Single fibre measurement

Calibrated micropipette cantilevers were fixed onto the arm of an MM3A LMP micromanipulator (Kleindiek Nanotechnik). This was fixed onto the stage of a Zeiss microscope. A speed of c01 was selected for all axes in the micromanipulator with a frequency of 2.7 Hz. The fibre samples were immersed in water for 1 hour. Afterwards the sample was mounted onto the microscope. The suspended fibre was placed in water and the measurement was performed in water. Initially, the cantilever was positioned away from the fibre. The micromanipulator was moved through several steps. The distance the cantilever tip travelled in the microscope view was recorded to calculate the cantilever end displacement corresponding to a single step change in the micromanipulator. Afterwards, the cantilever was made to come into contact with the fibre. As the cantilever deformed the fibre, each position of the micromanipulator was recorded. At the same time, snapshots of the fibre deformation were taken. The cantilever

deflection was calculated by subtracting the tip displacement deforming the fibre from that due to the micromanipulator movement. The fibre deformation was measured in ImageJ.

3.3.9 Bulk film measurement

The dECM-laden gelatin solution was crosslinked and made into films with a width of 10 mm, length of 20 mm and thickness of 1 mm. The film dimensions fluctuated between different samples and were taken into account when calculating the Young's modulus. The films were left to dry and crosslink for 24 hours at room temperature. The fully crosslinked films were immersed in distilled water to rehydrate for at least 1 hour before measurement. The hydrated films were installed on Instron and underwent uniaxial deformation at a deformation rate of 0.6 mm/min.

3.4 Results and discussion

3.4.1 Chemical characterisation of dECM-laden gelatin fibres

Conventional electrospinning requires a high voltage (>3 kV), which limits its use with voltage-sensitive materials. In comparison, LEP requires only several hundreds volts and shows the potential for preserving the chemical structure of proteins during the patterning process. In this section, I investigated the chemical structures and distribution of patterned dECM-laden fibres using immunofluorescent staining, Energy-dispersive X-ray Spectroscopy (EDX) and Fourier Transform Infrared Spectroscopy (FTIR).

Immunofluorescent Staining

Collagen IV, fibronectin and laminin, as the representative proteins in ECM, are known to be present in both dSIS and dUBM[19]. The expression of these proteins was characterised using the immunofluorescent staining method. Measurements were performed on the G(19), U(1). U(10) and U(50) solutions in the form of crosslinked hydrogel films (thickness approximately 100 μm) as well as patterned fibres. A negative control was performed of each protein, to ensure the antibody binding was specific. The negative control was performed by omitting the primary antibody and only using the secondary antibody. The stained gelatin samples are shown in Fig 3.2, together with the negative control result. The fluorescent intensity of the gelatin samples is weak, indicating minor presence of collagen IV, and an absence of fibronectin and laminin proteins. The negative control shows no fluorescent intensity, indicating that the antibodies were specific and an appropriate concentration was applied. The

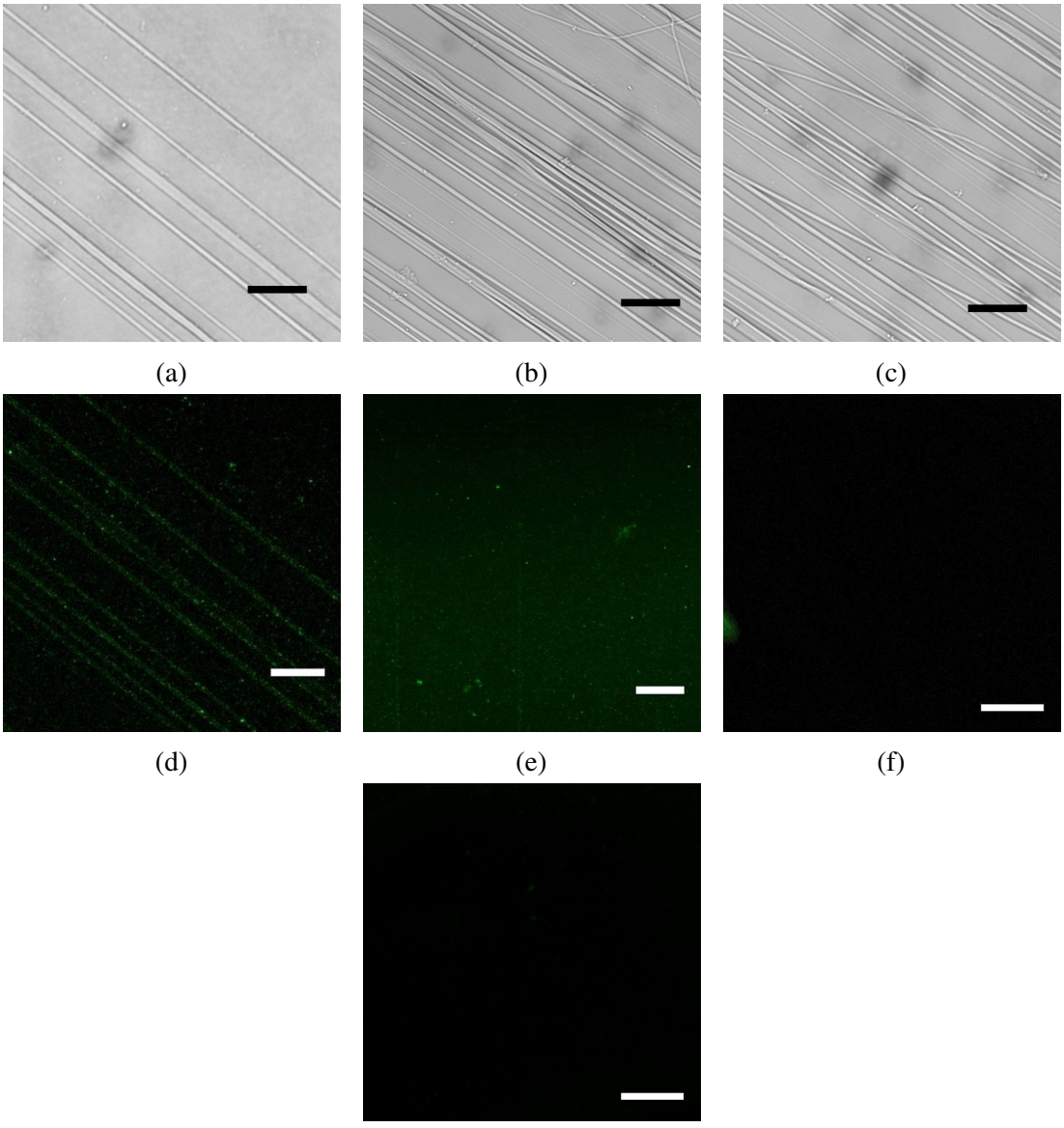

Fig. 3.2 Immunofluorescent staining of gelatin fibres, as a reference, and negative control. (a) and (d) collagen IV bright field and fluorescence; (b) and (e) fibronectin bright field and fluorescence; (c) and (f) laminin bright field and fluorescence and (g) negative control which only contains secondary antibody staining. Scale bars indicate 25 μm.

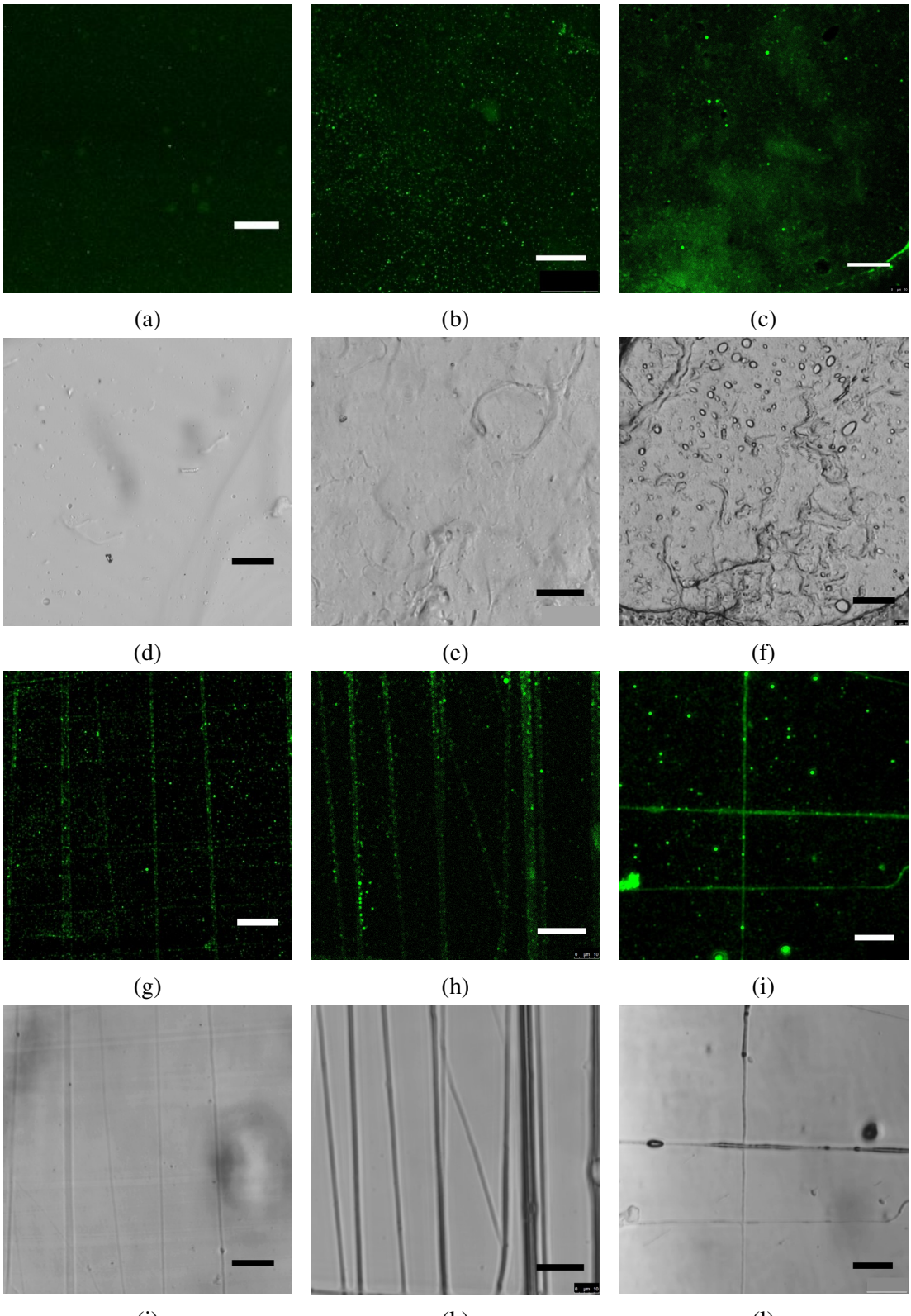

Fig. 3.3 Collagen IV staining of dUBM-laden samples. (a) and (d) U(1) hydrogel fluorescence and bright field; (b) and (e) U(10) hydrogel fluorescence and bright field; (c) and (f) U(50) hydrogel fluorescence and bright field; (g) and (j) U(1) fibre fluorescence and bright field; (h) and (k) U(10) fibre fluorescence and bright field; (i) and (l) U(50) fibre fluorescence and bright field. Scale bar indicate 25 μm.

collagen IV immunostaining of U(1), U(10) and U(50) is shown in Fig 3.3. In the hydrogel, the fluorescent intensity increases with the dECM concentration. High intensity aggregates are observed. This could be clusters of collagen IV. In the patterned fibres, the fluorescent intensity follows the same trend as that of the hydrogel. However, fewer aggregates are observed in the U(1) and U(10) fibres. For U(50) (Fig 3.3i), clusters of collagen IV are visible in the background, as well as along the fibres. This may because of the release of uncrosslinked collagen IV, or due to incomplete washing and sample drying. The fluorescent intensity is quantified in Fig 3.4. The hydrogel intensity is the average of the imaging area. The fibre intensity is the average of the intensity measured on each fibre. For both hydrogel and fibre forms, the fluorescent intensity increases as a function of the dUBM, indicating an increase in collagen IV concentration. The fibre form shows less variation in intensity at each dUBM concentration as the protein is more homogeneously distributed in fibres than in the hydrogel.

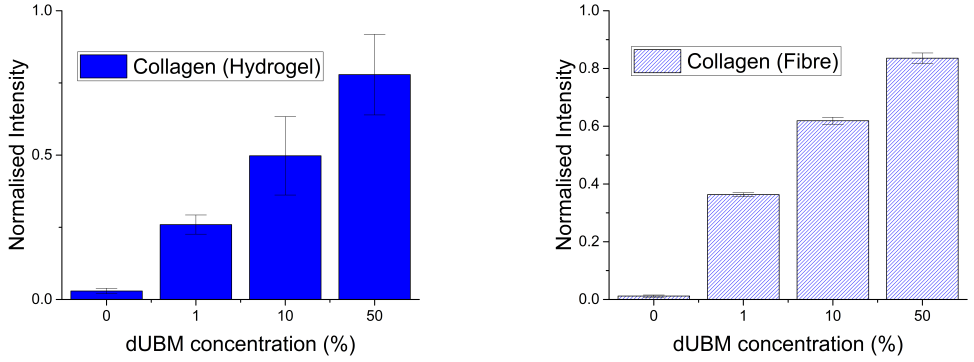

(a) (b)

Fig. 3.4 Fluorescence intensity in the collagen IV staining of (a) hydrogel and (b) fibres. n=5.

Fibronectin has a molecular weight of ∼440 kDa, and binds to the ECM components[228]. Fig 3.5 shows the fibronectin expression in U(1), U(10) and U(50) samples in both hydrogel and fibre form. The fibre visibility in the bright field images varies between samples. This is because mineral oil was used for mounting the samples and they have similar refractive index. When the fibres were fully immersed in the oil, they were not visible (Fig 3.5j and Fig 3.5k). When they were partially or not immersed in oil, they became distinguishable (Fig 3.5l). In hydrogel, the fibronectin intensity increases with the dUBM concentration. Similar to the collagen IV staining results, inhomogeneous fibronectin distribution is observed in the U(50) hydrogel sample. This may be because of the aggregation of fibronectin at high concentration. Fig 3.6 shows the quantification of the intensity trend as a function of dUBM concentration. For both hydrogel and fibre forms, the fluorescent intensity increases with

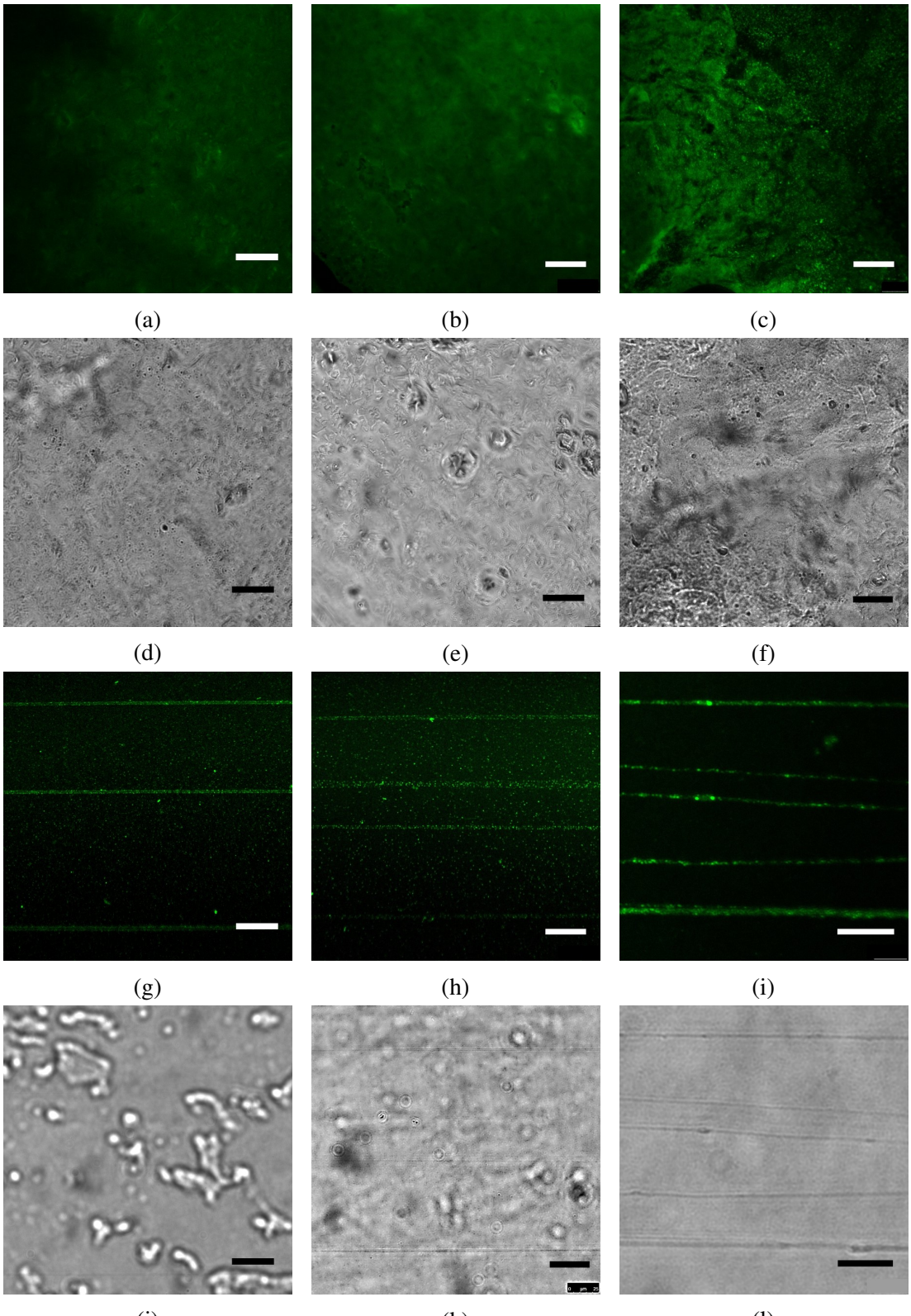

Fig. 3.5 Fibronectin staining of dUBM-laden samples. (a) and (d) U(1) hydrogel fluorescence and bright field; (b) and (e) U(10) hydrogel fluorescence and bright field; (c) and (f) U(50) hydrogel fluorescence and bright field; (g) and (j) U(1) fibre fluorescence and bright field; (h) and (k) U(10) fibre fluorescence and bright field and (i) and (l) U(50) fibre fluorescence and bright field. The fibres in the bright field images (j) and (k) are not visible, because they had similar refractive index to the mineral oil used for mounting. Scale bars indicate 25 μm.

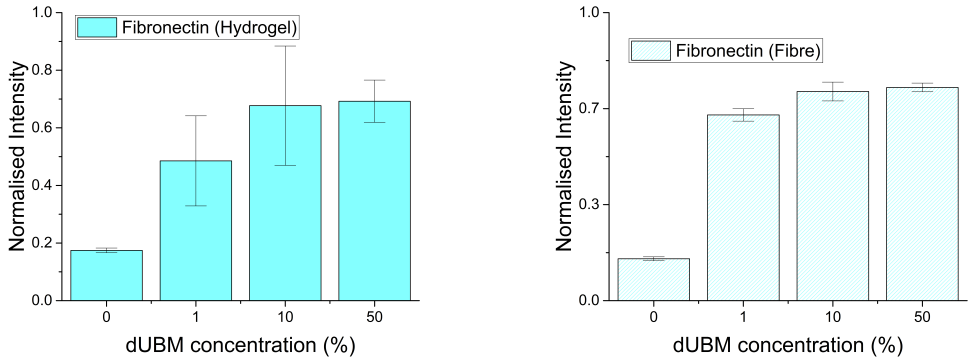

(a) (b)

Fig. 3.6 Fluorescence intensity in the fibronectin staining of (a) hydrogel and (b) fibres. n=5.

the dUBM concentration, indicating an increase in fibronectin concentration. The change in intensity with dUBM concentration is lower in the fibre form. The fibres also demonstrate less variation in intensity. In addition, an interesting difference in the fibronectin molecule distribution compared to collagen IV can be observed in the patterned fibres. In this case, fibronectin molecules, instead of distributing evenly through the fibre, are located towards the surface of the fibre, leaving the centre of the fibre dark, as shown in Fig 3.7. This is mostly observable in the U(50) sample. This interesting phenomenon is evidence of molecule redistribution due to charging of the polymer solution. The applied voltage induces charge repulsion in the polymer solution which leads to the migrations of molecules. Small molecules are easier to move than an integrated collagen network. Following the flow of the polymer jet, the small charged molecules become positioned on the fibre surface.

Laminin has a molecular weight of ∼400 to ∼900 kDa and is associated with collagen IV networks[229]. The laminin distribution in hydrogel and fibre form is shown in Fig 3.8. A general increase in intensity is observed. In the U(50) hydrogel, clusters of laminin are observed, indicated by the bright "dots" in the hydrogel (Fig 3.8c). Fig 3.9 shows the laminin intensity as a function of the dUBM concentration. For both hydrogel and fibre forms, the laminin concentration increases with the dUBM concentration. The fibre form contains less variation in intensity than the hydrogel. It is important to notice that the laminin distribution is towards the surface of the glass slide. Fig 3.10 shows the laminin staining "printed" onto the glass coverslip. I experimentally found that a stronger fluorescent signal could be obtained by removing the fibres than when the fibres were attached. This indicates that laminin molecules are transferred onto the glass during LEP. This gives an insight of different molecule movements due to charge and size in LEP.

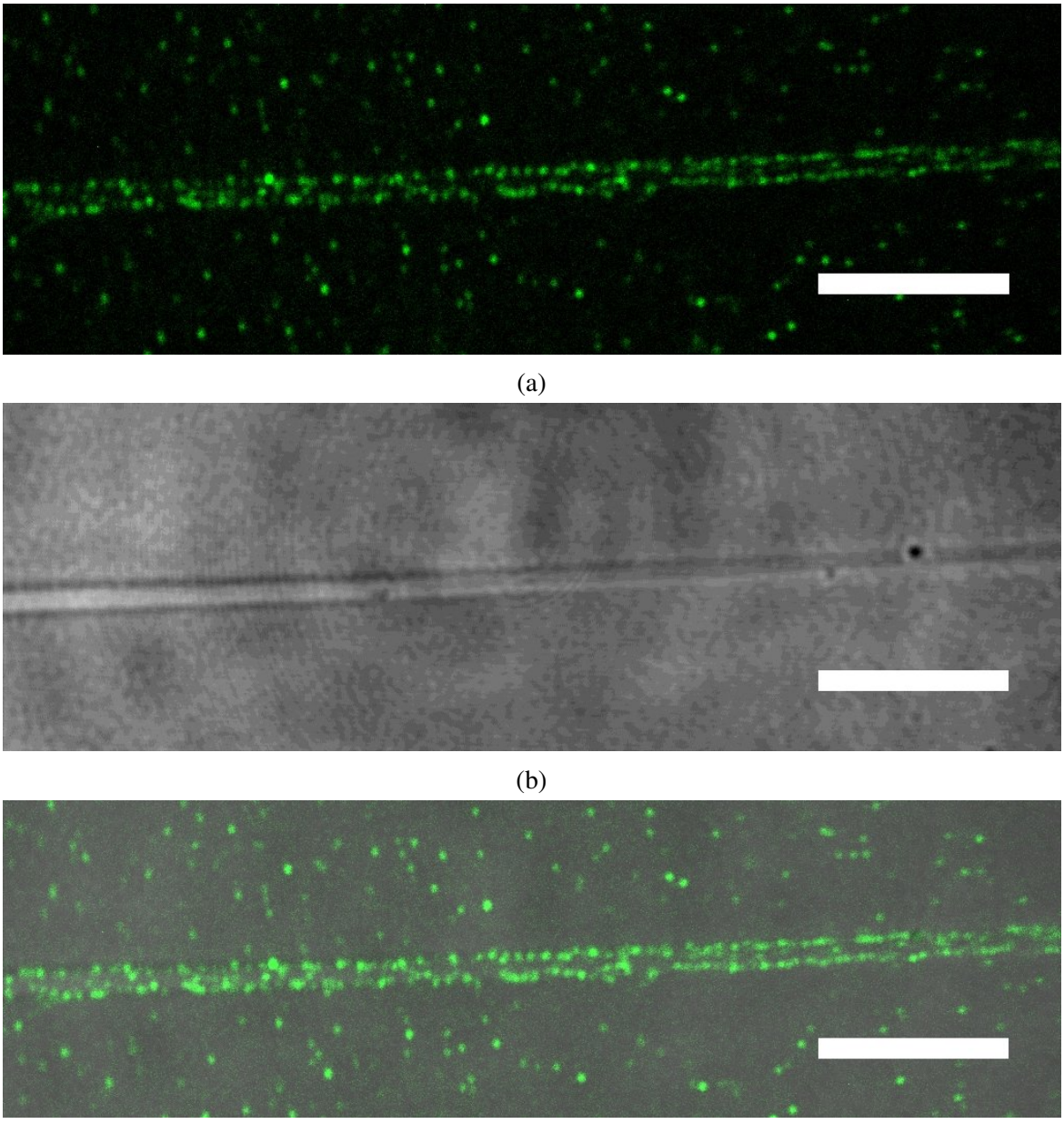

(a)

(b)

(c)

Fig. 3.7 Distribution of fibronectin in U(50) fibres. (a) Fluorescent image; (b) bright field image and (c) merged image.

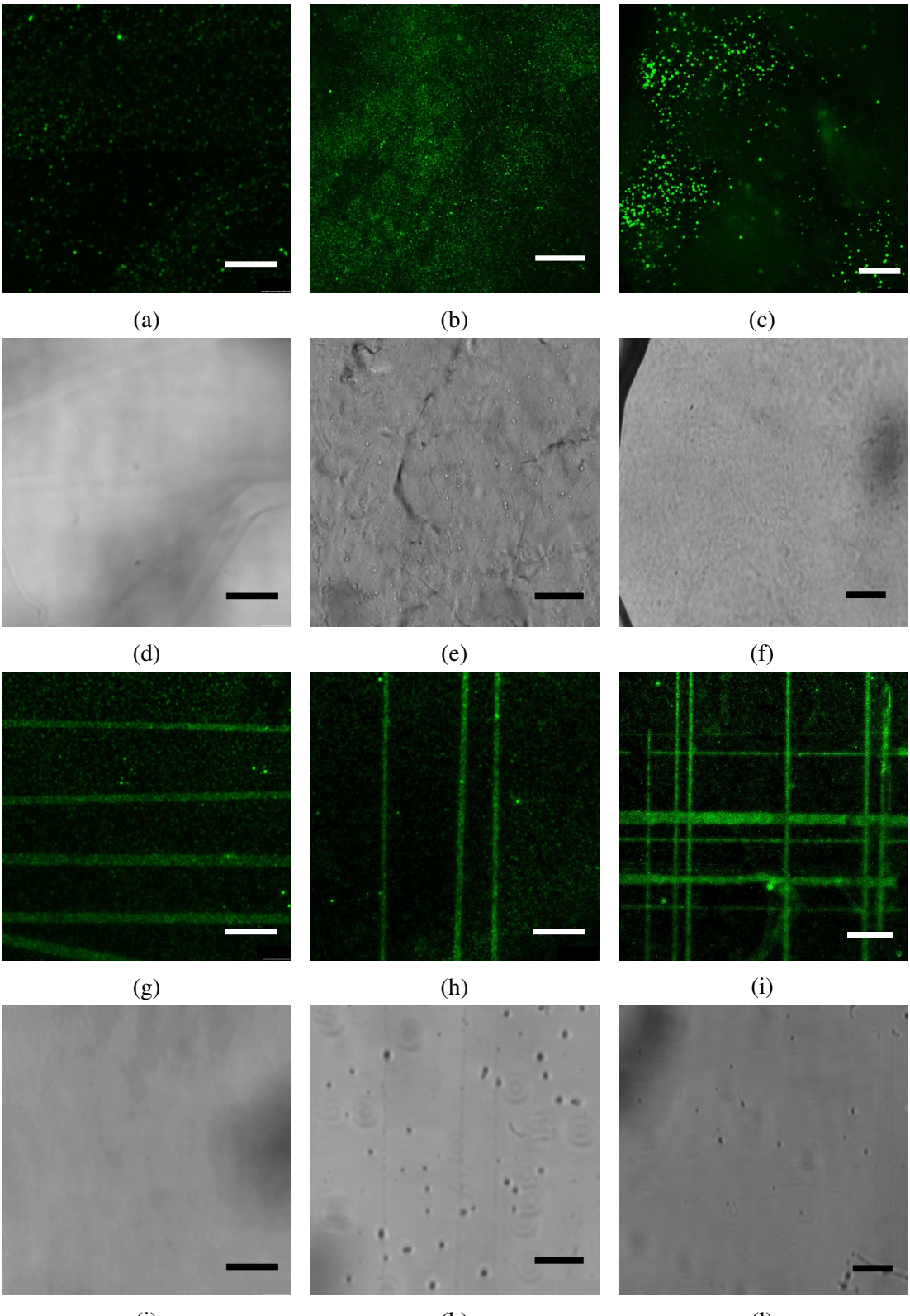

Fig. 3.8 Laminin staining of dUBM-laden samples. (a) and (d) U(1) hydrogel fluorescence and bright field; (b) and (e) U(10) hydrogel fluorescence and bright field; (c) and (f) U(50) hydrogel fluorescence and bright field; (g) and (j) U(1) fibre fluorescence and bright field; (h) and (k) U(10) fibre fluorescence and bright field and (i) and (l) U(50) fibre fluorescence and bright field. The fibres in the bright field images (j), (k) and (l) are not visible, because they removed by washing to show the laminin fluorescence. Scale bars indicate 25 μm.

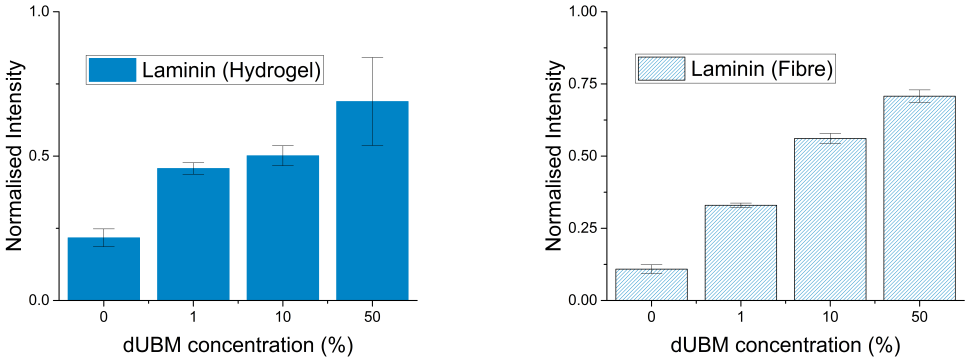

(a) (b)

Fig. 3.9 Fluorescence intensity in the laminin staining of (a) hydrogel and (b) fibres. n=5.

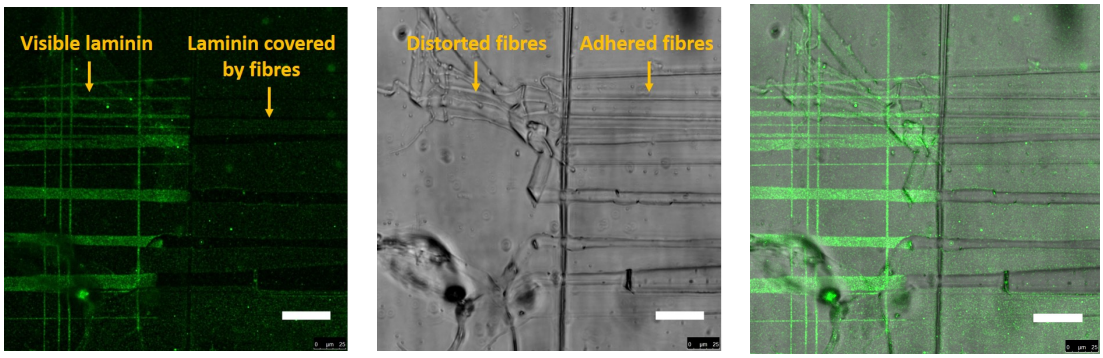

(a) (b) (c)

Fig. 3.10 Printing laminin onto glass coverslip. (a) Shows fluorescent signal; (b) shows the bright field image of the same area and (c) shows the merge of the two images. The presence of laminin is highlighted in green, where the fibres have been removed.

In conclusion, the fluorescent staining results prove that the key ECM components are preserved during LEP. The applied voltage causes molecules redistribution but is not high enough to change the molecular structures. Compared to bulk, LEP allows for precise patterning of dECM proteins which also reduces the aggregation of proteins at high concentration.

Energy-dispersive X-ray Spectroscopy

Energy-dispersive X-ray Spectroscopy (EDX) is a technique used for elemental analysis by detecting the characteristic X-ray emission after colliding the sample with a high-energy electron beam. The high-energy electrons interact and excite the electrons in the sample. Since each element consists of unique atomic structure, when the excited electrons return to the lowest energy state, an X-ray containing a specific energy is released. By analysing the energy level of the emitted X-ray, one can trace the information of the element. Additionally, the emitted X-ray spectrum correlates to the concentration of the element, which allows for quantitative analysis of the elemental composition of the sample material[230]. The sensitivity of the concentration detection is normally 0.1 wt% and the spacial resolution is 1 μm. In this study, I used EDX to obtain a statistical analysis of the dECM-laden fibres.

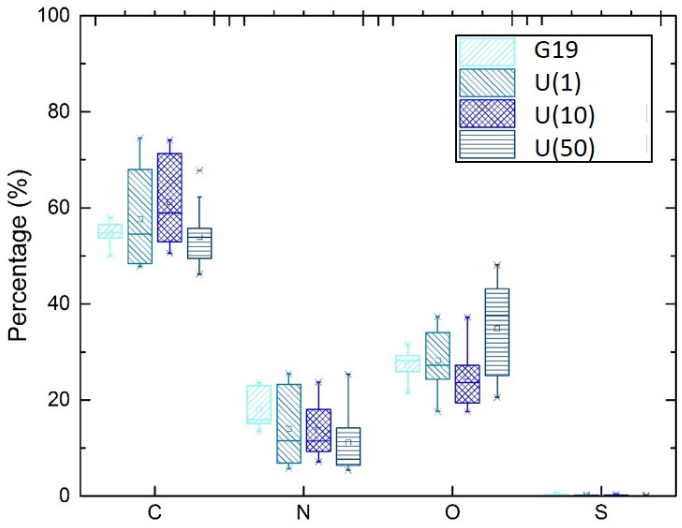

Fig. 3.11 Summary of EDX results for suspended gelatin and dECM-laden fibres. n>5.

ECM is mainly formed from organic compounds containing four elements: hydrogen H, carbon C, oxygen O and nitrogen N. Traces of sulphur S can also be found. Fig 3.11 shows the statistical results of the elements detected (hydrogen is not present) in the fibre

samples with different dECM concentrations. The degree of variation among the fibres was the lowest in pure gelatin. As dECM was incorporated, the variations in C, N and O all increased. This agrees with the observations of immunofluorescent staining where clusters of different proteins were detected. The richness of protein groups can bring variations in the chemical element proportions at the area of measurement.

Fourier Transform Infared Spectroscopy

Fourier Transform Infrared Spectroscopy (FTIR) is a powerful technique used to detect the structures and chemical environments of molecular bonds. FTIR measures the characteristic environments of chemical bonds by measuring the light absorbance at different wavelengths. This takes advantages of how the nature of each bond structure has its own resonance frequency and therefore absorbs infrared light at specific wavelength. In this study, FTIR was used to obtain a comprehensive chemical measurement for the dECM-laden fibres and films in comparison to the reference materials, including gelatin, collagen I, and dECM powder. This helped me to determine whether the LEP process and solution preparation affect the chemical composition of the dECM. The dSIS solutions were prepared in the same manner with the dUBM solution, which is explained in **Chapter 2**.

Fig 3.12 shows the FTIR measurement of the two raw dECM powders (Urinary bladder matrix dUBM and Small intestine submucosa dSIS) compared to reference materials, including collagen type I and IV, gelatin, and laminin. The broad peak at 3000 – 3500 cm^{-1} and the narrow peak at 2360 cm^{-1} are from atmospheric water vapour and CO_2, respectively. The most distinct peaks of the dECM material and reference samples are from the amide bands of proteins. The amide I band, occurring at 1800 – 1600 cm^{-1}, mostly represents C=O stretching (80%), with minor contributions from C−N stretching (10%) and N−H bending (10%)[231]. This was identified in both dUBM and dSIS, as well as in all the reference protein samples. The position of the amide I band was at 1627 cm^{-1} for all samples. The amide II band occured at 1550 – 1450 cm^{-1}, mainly representing N−H bending (60%) with some C−N stretching (40%)[231]. Both amide I and II peaks depend on the secondary structure of molecules, with amide II peaks particularly sensitive to structural denaturation. Amide II bands were identified in all samples with slight variations to the peak position. For collagen I, IV and gelatin, the amide II peak occured at 1526 cm^{-1}, indicating similarity in the secondary structure. In laminin, the amide II position shifted towards a lower wavenumber, whereas in dUBM and dSIS, it shifted to a higher wavenumber. Amide III represents several bonding structures, including C−N stretching (30%), N−H bending (30%), C=O bending (10%) and O=C−N bending (10%). This occurred at 1300 – 1200

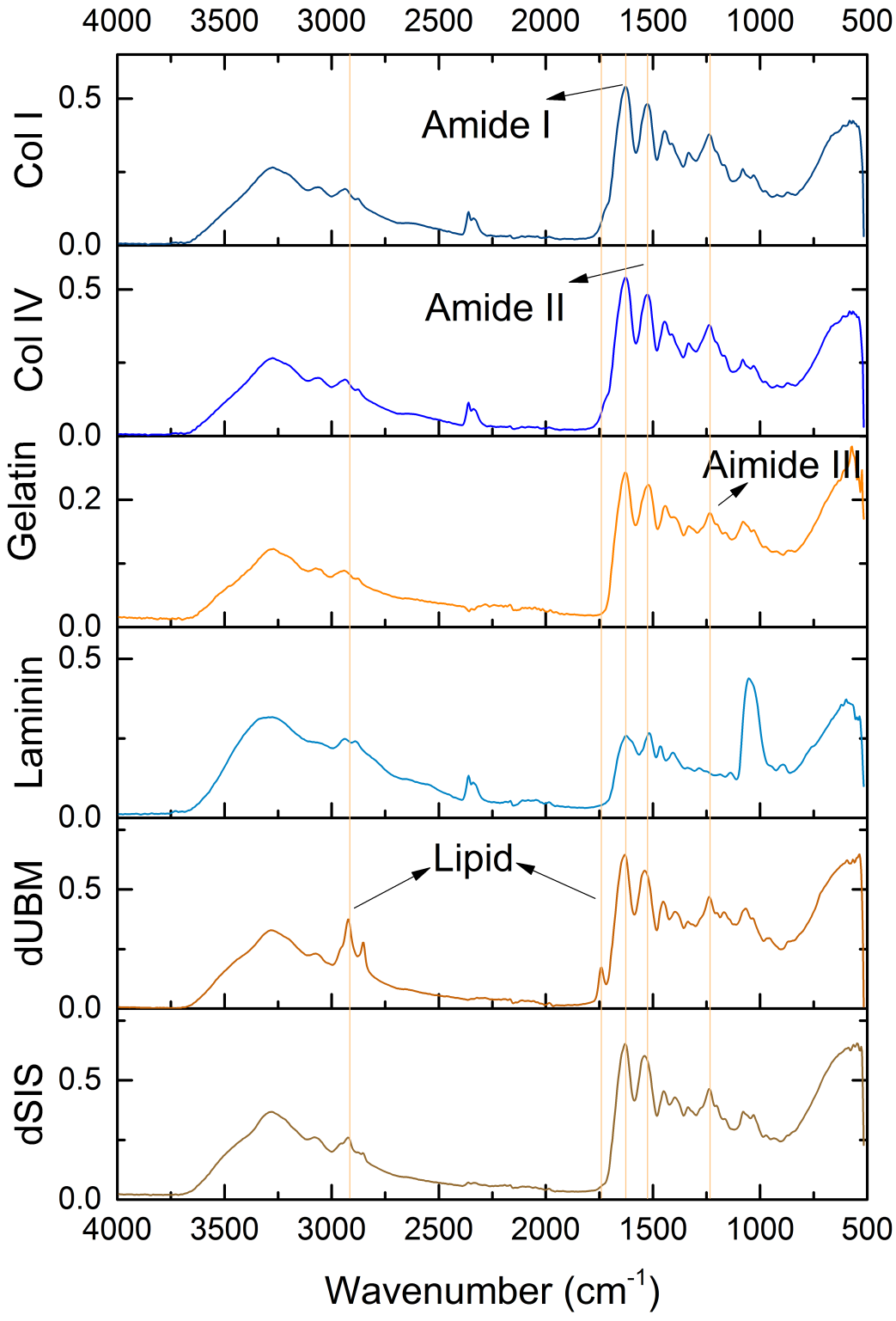

Fig. 3.12 FTIR measurement of dUBM and dSIS with respect to protein references, i.e. collagen I, IV, laminin and gelatin.

cm^{-1}. This was identified in the same position for dUBM, dSIS, collagen I, and collagen IV samples. In gelatin, the amide III position shifted towards the lower wavenumber. The amide III peak is the characteristic difference between collagen I and gelatin as they share similar chemical compositions, but gelatin contains smaller peptides with a wide range of molecular weights. Table 3.1 summarises the position of the amide peaks identified from the FTIR graphs. There are two main distinctive differences between UBM and SIS: the C=O stretching at 1750 cm^{-1} and asymmetric CH_2 at 2920 cm^{-1} were shown in UBM but not SIS. These two peaks are from lipids and their adjacent occurrence confirms the presence of lipid in the dUBM sample.

Table 3.1 Amide absorption peak positions of dECM and reference materials

Sample	Amide I region (cm^{-1})	Amide II region (cm^{-1})	Amide III region (cm^{-1})
Collagen I	1627	1526	1236
Collagen IV	1627	1526	1236
Gelatin	1627	1526	1228
Laminin	1627	1515	N/A
dUBM	1627	1539	1236
dSIS	1627	1539	1236
U(50) film	1627	1532	1236
U(50) fibre	1627	1532	1236
U(10) film	1627	1529	1236
U(10) fibre	1627	1529	1236

In order to investigate the effect of the solvent during LEP solution preparation, G(19), U(10) and U(50) were prepared and measured, as shown in Fig 3.13. The amide I absorption peaked at the same wavenumber among different dUBM concentrations. A slight shift towards a higher wavenumber was observed for both amide II and III peaks are observed with increasing dUBM concentration. More distinctly, the absorption peaks corresponding to lipid structures are not present in the gelatin spectrum. The lipid band appeared in U(10). This became more prominent in U(50). This shows that the bond structure and environment converge towards the dUBM powder form as dUBM concentration increases in the LEP solution. The amide I band is an overtone of various secondary structures, including α-helix, β-structure and random coils[231]. In the FTIR result, the difference between dUBM samples was minor. Therefore this was further investigated in the second derivative spectrum, shown in Fig 3.14. The 1645 – 1640 cm^{-1} region represents the conformation of a random coil. This became more distinct as the dUBM concentration increased. However, the change

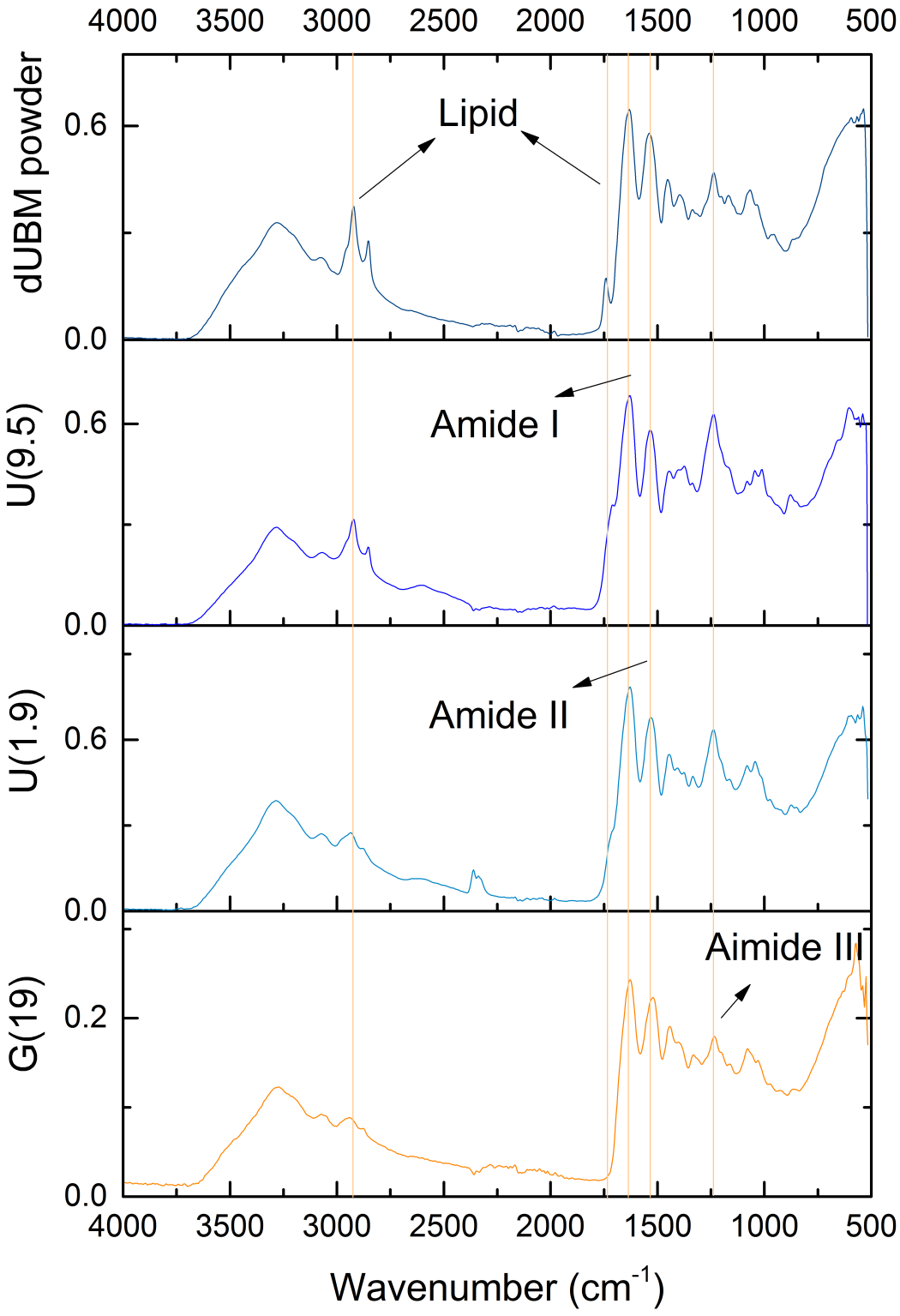

Fig. 3.13 FTIR measurement indicating the concentration dependence of the dECM-laden film.

in the second derivative spectrum is not very significant and may be comparable to the noise level.

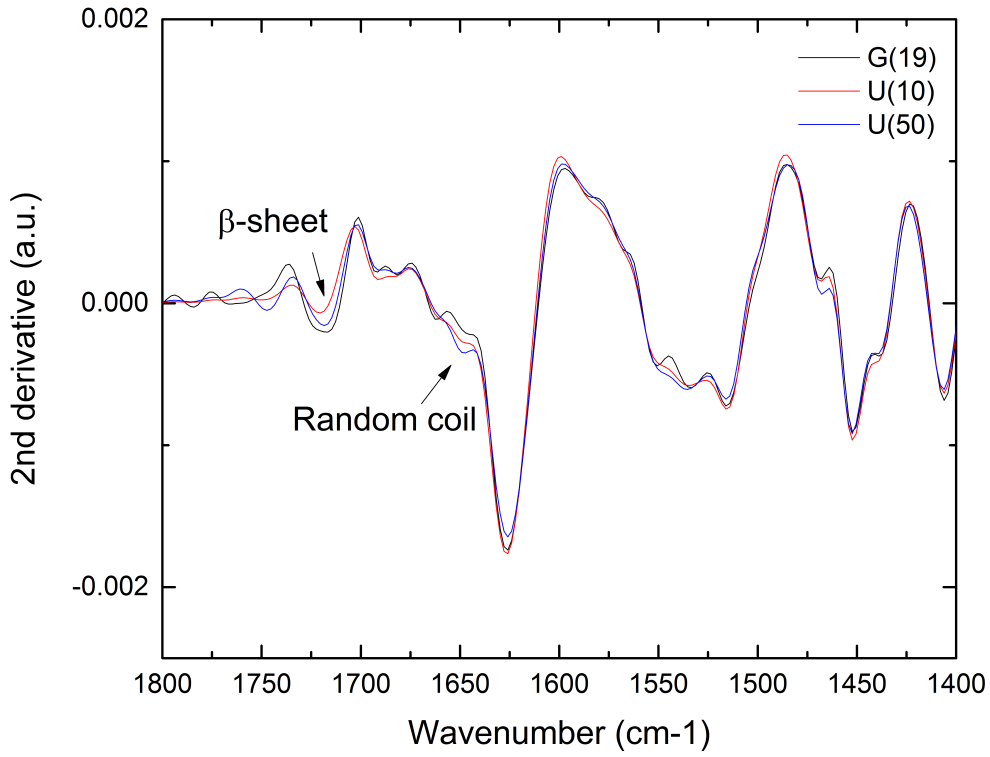

Fig. 3.14 Second derivative of FTIR spectrum, showing the overtone amide I band (1800 – 1600 cm^{-1}).

The effect of the LEP process on chemical structure was also studied. In particular, U(10) was patterned into fibril form using LEP and the fibres were measured using FTIR, as shown in Fig 3.15. The main peaks, including amide I - III and lipid bands, present at identical positions in both the U(10) film and fibre samples. No shift of position or change of relative amplitude was observed. Therefore, the LEP effect on molecular structure is negligible and the secondary structures in the dECM were preserved during solution preparation and fibre patterning.

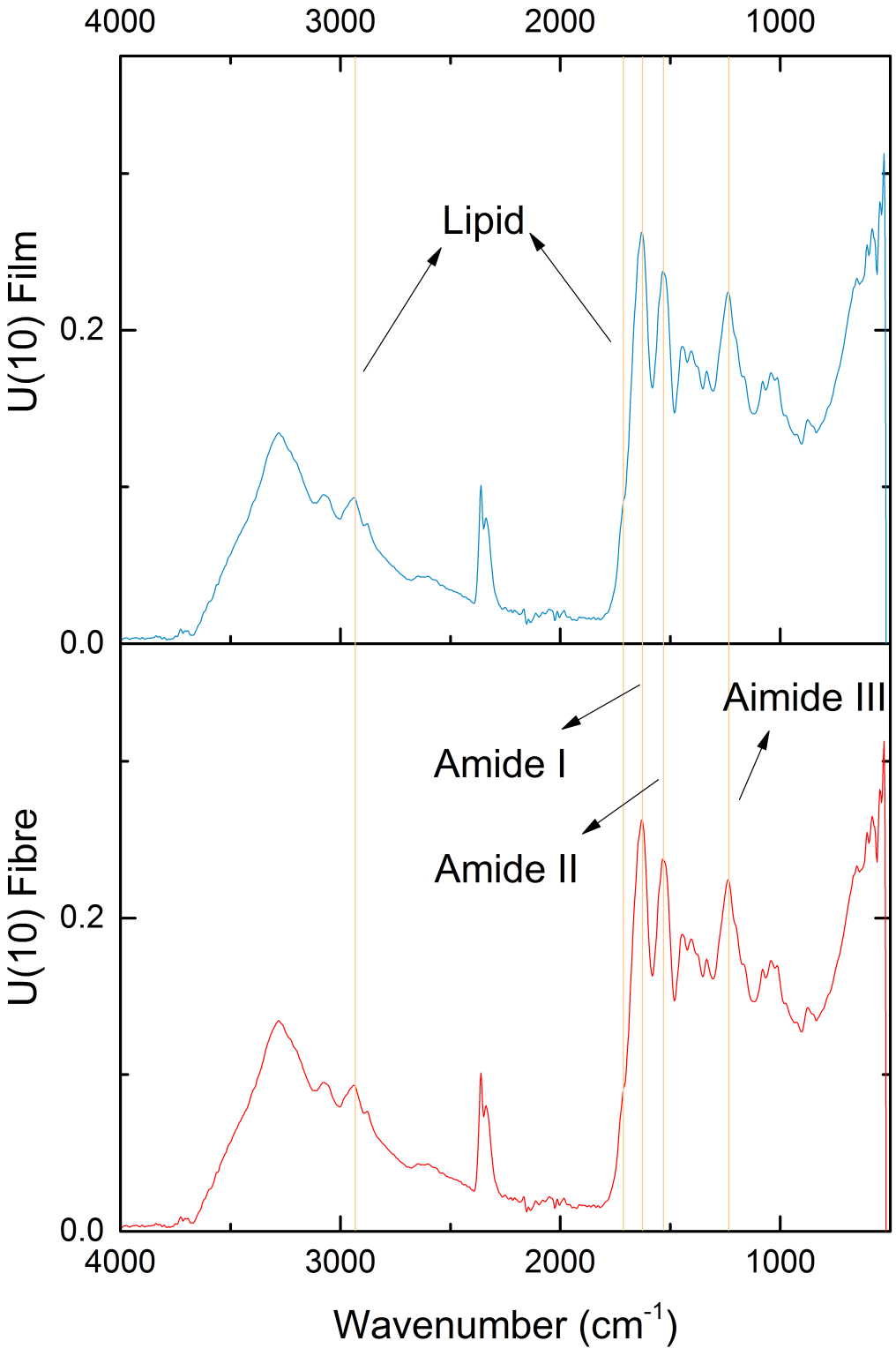

Fig. 3.15 FTIR measurement of U(10) film and U(10) LEP fibres.

Enzyme-Linked ImmunoSorbent Assay

The ELISA measurement was performed by Chuan Chen, Wenzhou Medical University, China.

The Enzyme-Linked ImmunoSorbent Assay (ELISA) measures the growth factor, which is crucial for manipulating cell functions in vitro. Here I aim to investigate whether the acid treatment during solution preparation damages the growth factor protein. Table 3.2 shows a comparison between the growth factors in dUBM, acid-treated dUBM and dUBM material derived by other groups. Depending on the dECM type and the preparation methods, the proportion of preservable growth factor varied[38, 232, 233]. For example, VEGF is more easily preserved than fibroblast growth factor FGF [234]. The growth factor proteins can be sensitive to the pH and solvent. It is important to ensure that the solution preparation does not affect the presence of these proteins. Fig 3.16 and Fig 3.17 show the VEGF and b-FGF concentrations at different dECM concentrations. At 0% dECM, which means the solution was pure gelatin, the concentration of both growth factors was 0. The 100% dECM data shows the growth factor concentration for pure dECM powder. The intermediate concentrations indicate the growth factor concentration in the solutions. A linear trend holds between the growth factor concentration and dECM concentration. This shows that the acidic solvent did not denature the growth factor. Instead, the growth factors purely depend on the amount of dECM incorporated in the solution. This is another confirmation of how much of the active components in the dECM is preserved.

Table 3.2 Growth factor measured in various dECM materials.

Sample	VEGF (pg/g)	b-FGF (pg/g)
dUBM by Badylak	407.52 ± 4.96	3478.8 ± 49.6
Acid-treated dUBM (U(50))	220.60 ± 17.52	1588.48 ± 4.96
dUBM by others	472.5[235]	4.042 ± 0.0075[236]

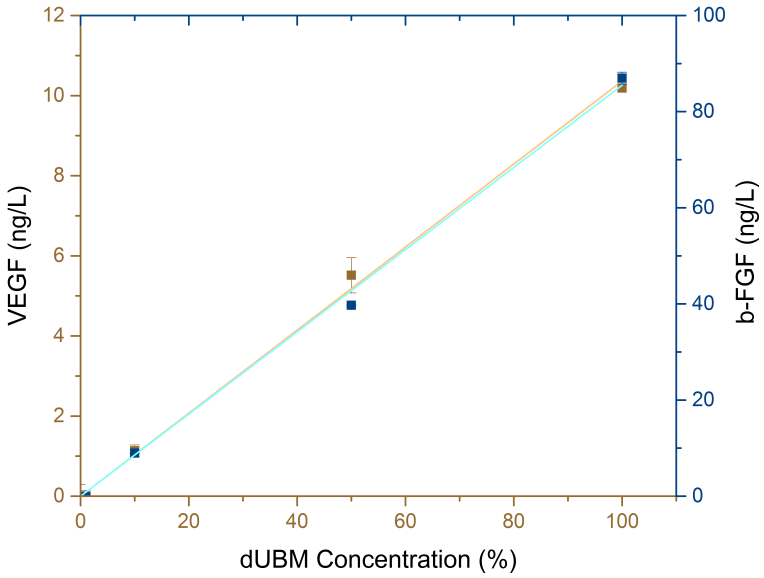

Fig. 3.16 ELISA measurement of UBM. n=3.

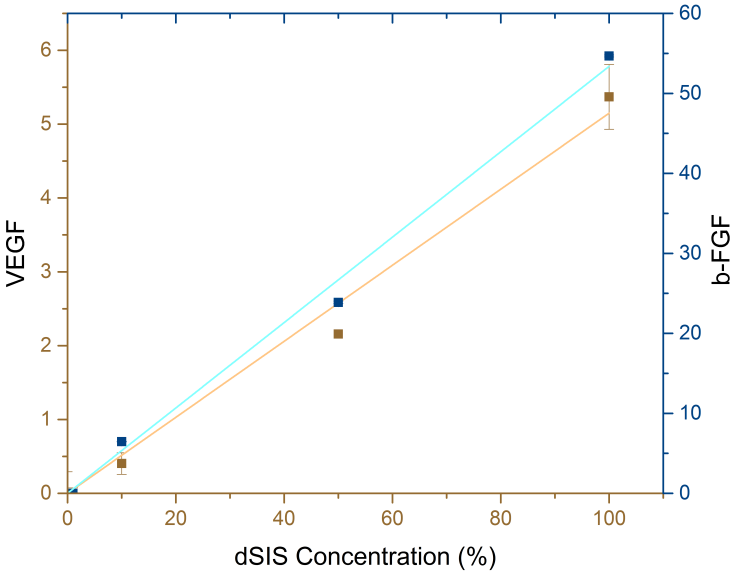

Fig. 3.17 ELISA measurement of SIS. n=3.

3.4.2 Mechanical characterisation of dECM-laden gelatin fibres

Cells are particularly sensitive to the mechanical properties of the substrates. In this section, the Young's modulus of dECM-laden material was measured in both fibril and bulk forms. In order to simulate what cells feel, both mechanical testings were performed in a wet condition. The single fibre measurement was performed in water. The bulk measurement was performed when the samples were fully hydrated.

Single fibre measurement

On average, the diameter of the LEP fibre is less than 1 μm and is soft compared to engineering materials. Hence it is impractical to use conventional mechanical measurement techniques to perform the measurement. In this study, I used a micropipette cantilever to measure the mechanical properties of single dECM-laden gelatin microfibres. As explained in Section 3.2.1, the stiffness of the micropipette cantilever can be tuned by varying the tip diameter. In practice, two cantilever tip diameters, 7.5 μm and 10 μm were fabricated and calibrated. Fig 3.18a shows the calibration process, where a water droplet was used to deform the cantilever. The smaller cantilever tip diameter resulted in a larger deflection when the droplet was attached, indicating a softer cantilever and *vice versa*. Fig 3.18b shows the calibration curves of the two cantilever diameters. In the calibration graph, the displacement is linearly related to the weight of the water droplet. By calculating the gradient, the cantilevers with 7.5 μm and 10 μm tip diameters exhibit a force constant of 4.20 ± 0.05 mN/m and 9.13 ± 0.17 mN/m, respectively. To check the reliability of the cantilever, calibration was performed to each cantilever before and after performing a single fibre measurement. This was to ensure that the measurement process did not cause plastic deformation of the cantilever and the force constant remained valid during the fibre deformation measurement. Compared to the 10 μm cantilevers, the 7.5 μm diameter cantilevers were softer and more comparable to the microfibres. Hence, 7.5 μm diameter cantilevers (with force constant 4.20 ± 0.05 mN/m) were used in the measurement of single fibre deformation and the cantilever deflection, x, can be converted into force, F, through equation 3.2.

$$F = 4.20x \tag{3.2}$$

Fig 3.19a shows a typical set of snapshots when a microfibre was under deformation. A constant strain rate of 0.067%/s was used during the fibre deformation. The cantilever deflection was converted into stress by equation 3.3.

$$\sigma = \frac{F}{A} = \frac{4.2x}{\pi r^2} \tag{3.3}$$

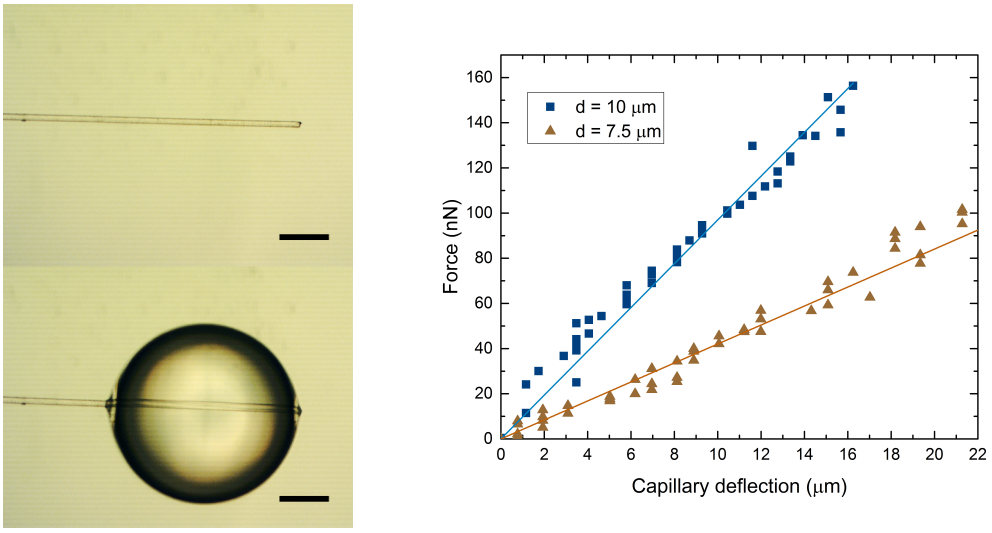

(a) (b)

Fig. 3.18 The calibration method of capillary cantilevers. (a) Snapshots of calibration measurement, scale bar 50 μm; (b) the corresponding force to deflection relationship.

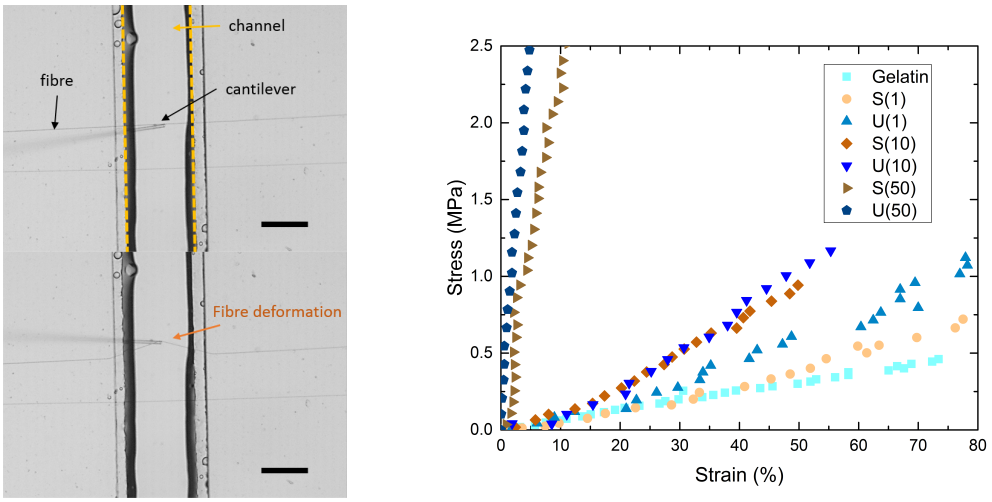

(a) (b)

Fig. 3.19 Single fibre mechanical measurement. (a) Snapshots of single fibre deformation using a capillary cantilever, scale bars 100 μm and (b) summary of the single fibre mechanical measurement.

where A is the cross-section area of the fibre and r is the cross-section radius. The fibre deformation was converted into strain by equation 3.4.

$$\varepsilon = \frac{\triangle L}{L_0} \tag{3.4}$$

where $\triangle L$ is the change in fibre length and L_0 is the original fibre length. By converting the capillary deflection into force and fibre deformation into strain, a stress versus strain graph was plotted as shown in Fig 3.19b. Within the measurement range, the stress was linearly related to the strain for all samples, including pure gelatin and dECM-laden fibres. This indicates the elastic nature of the sample fibres within the deformation range. The gradient of the fitted line corresponds to the Young's modulus (E) of the fibres. Fig 3.19b shows that the gradient became increasingly steeper for samples with increasing dECM concentration. This indicates that E was the lowest for pure gelatin and increased as more dECM material was incorporated in the fibre. Fig 3.20 shows E as a function of the dECM concentration. The stiffening trend with dECM concentration was observed for both dSIS and dUBM. At the same concentration, the dUBM samples exhibited slightly higher E than the dSIS samples. This shows that the physical properties of dECM material are organ-specific. The stiffening of fibres for higher dECM concentration can be caused by physical entanglement of the dECM molecules. If one considers the additional dECM molecules as suspension particles and neglects the charge and molecular interaction, the increase in the volume fraction (concentration) of the dECM provides a linear increase in E [237]. This reinforcement of nanoparticle behaviour has been studied to enhance the mechanical performance of composite materials. In addition to the nanoparticle model, the molecular interaction between dECM molecules can also contribute to the increase in E. This can be explained as the increasing dECM concentration increases the degree of entanglement between molecules, making them more closely packed. Therefore a higher force is required to deform the highly entangled molecular network, resulting in a stiffer material.

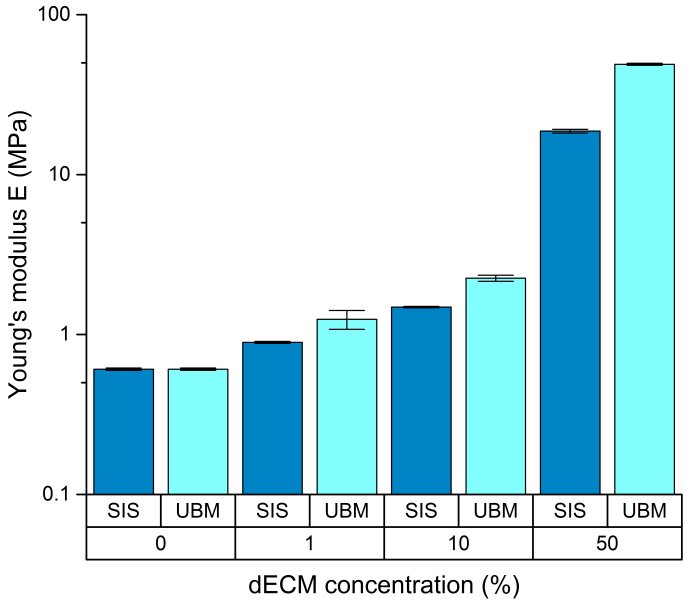

Fig. 3.20 Young's modulus of dECM-laden microfibres. n=3.

Bulk hydrogel measurement

Along with the single fibre measurement, the mechanical properties of bulk hydrogel were characterised. The mechanical responses of the dECM-laden gelatin films with dSIS or dUBM concentration as described, were measured by uniaxial deformation using an Instron. The films were cast using gelatin, S(1), U(1), S(10), and U(10) films were uniform and smooth. Mechanical tests could be reliably performed on these samples. However, the S(50) and U(50) films were inhomogeneous and could not be measured. The original (clamped) length of the films were roughly 15 mm. The films were stretched at a constant rate until failure. For pure gelatin film, the curve was initially straight before curving up. This indicates the transition from the elastic regime to yielding. After the initial yielding, the force increased approximately linearly before fracture. As the dECM concentration increased, the material became more brittle and broke at lower strain. In addition, the dECM-laden samples did not show significant yielding, and instead the force curve was roughly linear, indicating its elastic character. The stress and strain relationship can be obtained by taking the film dimensions into account. Fig 3.21 shows the stress as a function of strain in the elastic deformation regime. As the dECM concentration increased, the gradient became steeper, indicating an increase in E. This is similar to the mechanical properties of a single fibre. Table 3.3 shows the value of E and the associated standard deviation for the dECM-laden material in fibre and film configuration. In both configurations, material stiffening was observed with increase in dECM concentration. Overall, E increased by two orders of magnitude from pure gelatin to U(50) fibre. The positive correlation between E and dECM particle concentration has been observed in other composite materials[238–241].

At each dECM concentration, the fibre and film configurations show similar stiffness, as shown in Table 3.3. Within the same order of magnitude, the films are slightly stiffer than the fibres. It is hypothesised that the film form contains dECM particles of various sizes, whereas in the fibre form, the upper limit of particle size distribution is constrained to the fibre diameter. The larger particle size may contribute to the stiffening of the sample material. As illustrated in the study by Feng et al., the larger particle size hinders the deformation of surrounding polymer chains[242]. The influence of particle size on material stiffness is further explored in the study by Fu et al.[237], indicating a close relationship between the Young's modulus with both particle size and volume fraction. However, due to the complexity in particle shape and size distribution, the quantitative relationship of E and particle size has not been further explored. In biological applications, stiffening due to the incorporation of dECM can improve the robustness of the material. This is widely observed in dECM-based materials. According to the research performed by Rosario et al., native bladder tissue has a Young's modulus of 0.04 MPa[243]. The decellularization and sterilisation process causes

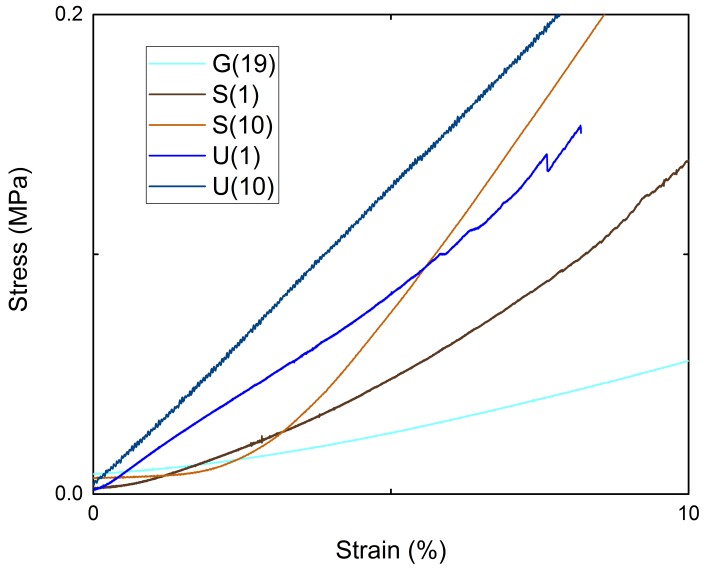

Fig. 3.21 Stress vs strain relation of dECM-laden film.

a significant increase in the mechanical stiffness of UBM, giving a Young's modulus of roughly 2 MPa. In addition, Farhat et al. reported an increase in the Young's modulus after decellularization (from 0.20 MPa for native bladder to 0.65 MPa for decellularised bladder matrix)[244]. This is further confirmed in the study by Beachley et al.[19]. As reported, the elastic moduli of dried dECM tissue spots were two orders of magnitude higher than that of fresh hydrated tissue. Although dECM material is organ-specific, the variation in stiffness between tissue types is less in dry tissues than fresh hydrated tissues. The stiffening result of incorporating dECM material can lead to deviation from physiological parameters. The mechanical stiffness of matrix influences cell fate and behaviour through cell-matrix interactions. Here, I was concerned about the abnormal increase in the stiffness of dUBM-laden fibres compared to that of the native tissue. Therefore, U(10) gelatin fibres were used in the cell culture study. This aimed to provide chemical signaling while maintaining a mechanical stiffness similar to that of native tissue.

Table 3.3 Young's modulus and failure strain of dECM-laden gelatin fibres and hydrogel.

Material	E(fibre) (MPa)	failure strain (fibre) (%)	E(film) (MPa)	failure strain (film) (%)
Gelatin	0.61 ± 0.01	73.4 ± 3.5	0.59 ± 0.02	120.0 ± 2.5
S(1)	0.89 ± 0.01	80.6 ± 4.2	1.35 ± 0.18	100.0 ± 1.0
U(1)	1.25 ± 0.17	63.7 ± 4.4	1.57 ± 0.15	83.3 ± 1.3
S(10)	1.49 ± 0.14	60.0 ± 5.7	2.62 ± 0.15	33.3 ± 1.6
U(10)	2.25 ± 0.10	55.3 ± 3.4	3.19 ± 0.16	26.7 ± 1.4
S(50)	18.7 ± 0.5	>13	N/A	N/A
U(50)	49.0 ± 0.7	>6.2	N/A	N/A

Swelling

The fabrication process of a dECM-laden microfibre network involves LEP, drying to eliminate solvents and rehydration in a medium to neutralise the pH. Both gelatin and dECM material can absorb water during rehydration, as reported in [245]. This causes swelling in the patterned fibres, resulting in diameter increase and even buckling. To obtain a robust and reproducible device for bioengineering purposes, one needs to control the amount of swelling to ensure the least variation in the final product. In this section, the swelling effect is studied for G(19) and U(10) fibres with different diameters. These two fibre compositions were selected because they were applied in cell culture, as described in **Chapter 4**. Other fibre compositions (e.g. U(1) and U(50)) can be characterised using the same method. Suspended G(19) and U(10) fibres were patterned over PDMS channels. The diameter of the fibres was measured before and after immersing in water for 1 hour. An example of fibre buckling is shown in Fig 3.22. Fig 3.23 shows the histograms of the fibre diameter distribution in dry and wet samples. For G(19) the diameter and variation increased after rehydration. A similar trend held for U(10). The variation in diameter before and after swelling was similar for the G(19) and U(10) samples. In addition, fibres that swelled to greater than 5 μm buckled and therefore imposed negative effects on the functionality of the fibre network.

I consider the shape of the fibres to be cylindrical and the volume of the cylinders to be:

$$V = \pi r^2 * L \tag{3.5}$$

where V is the fibre volume, r is the radius of the cross-section and L is the length of the fibre. Since the fibre length was much larger than the cross-section diameter, a small change in the volume is more obviously shown by an increase in diameter than in length. From equation 3.5, the change in fibre volume should be linearly dependent on the square of change in diameter. Fig 3.24 shows the amount of swelling in relation to the square of fibre diameter. Deviating from the predicted trend this data was scattered with no clear relationship between the variables. One could not identify a clear numerical relationship. The amount of swelling seemed random. Interestingly, a proportion of fibres did not appear to swell at all (the change in fibre volume was close to 0, indicated towards the bottom of the graph). This might because the LEP process increased the tendency for the polymer chain orientation to align and therefore there was less intermolecular space to intake water molecules.

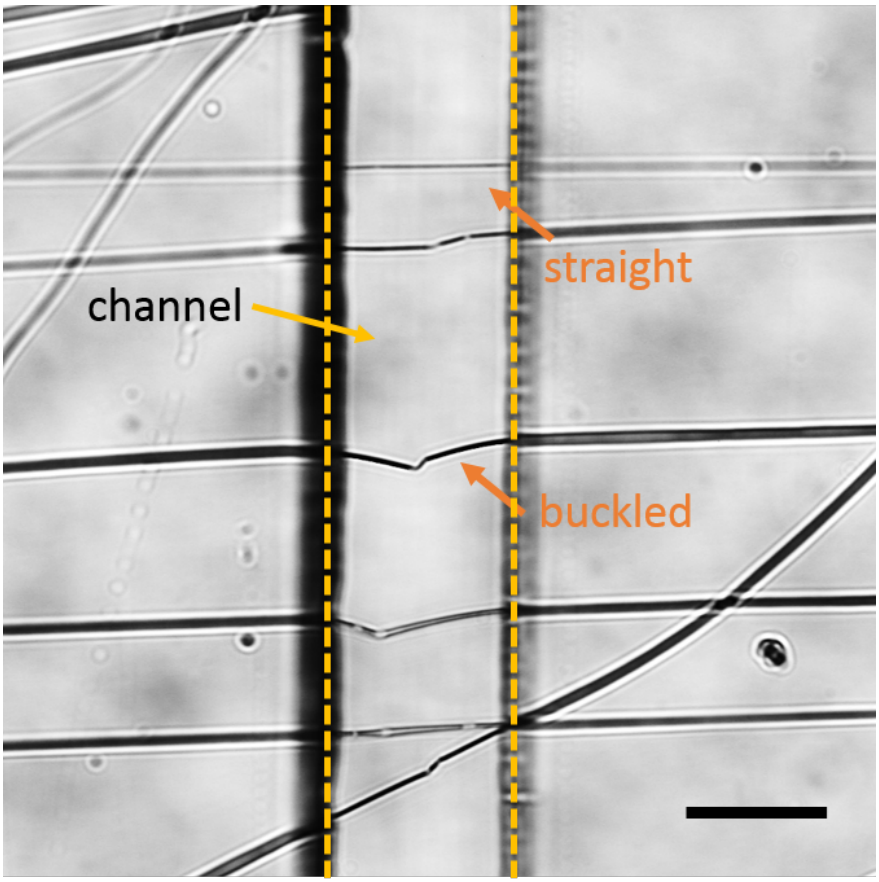

Fig. 3.22 Snapshot of the buckled fibres when immersed in water. The channel is indicated with dotted yellow lines; straight and buckled fibre indicated with orange arrows. Scale bar 100 μm.

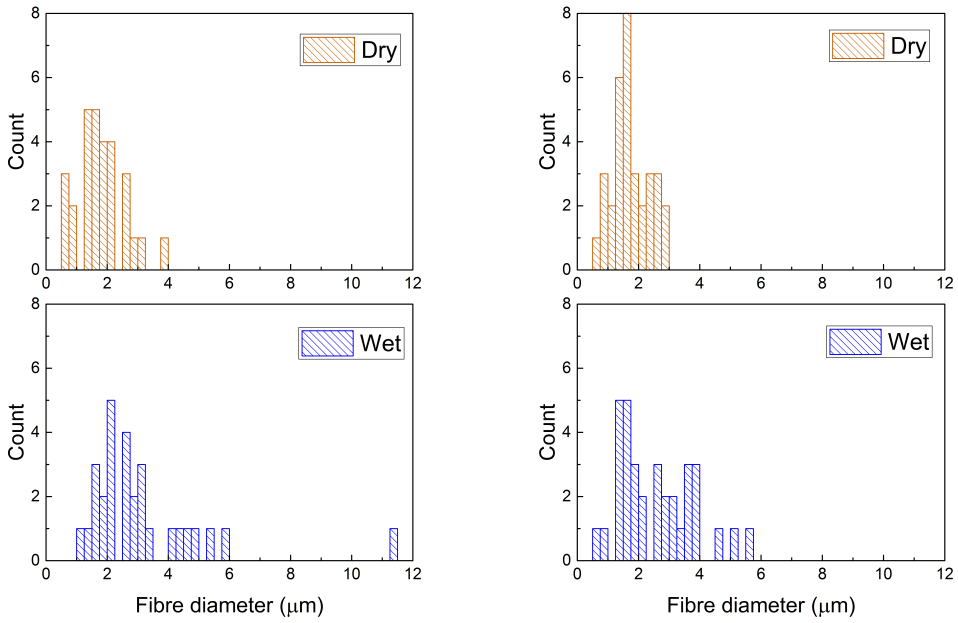

(a) (b)

Fig. 3.23 Histograms of the fibre dimensions before and after rehydration. (a) The average G(19) fibre diameter was $1.8 \pm 0.8 \mu$m when dried and became $3.1 \pm 2.0 \mu$m when hydrated, and (b) the average U(10) fibre diameter was $1.7 \pm 0.6 \mu$m when dried and became $2.6 \pm 1.2 \mu$m when hydrated.

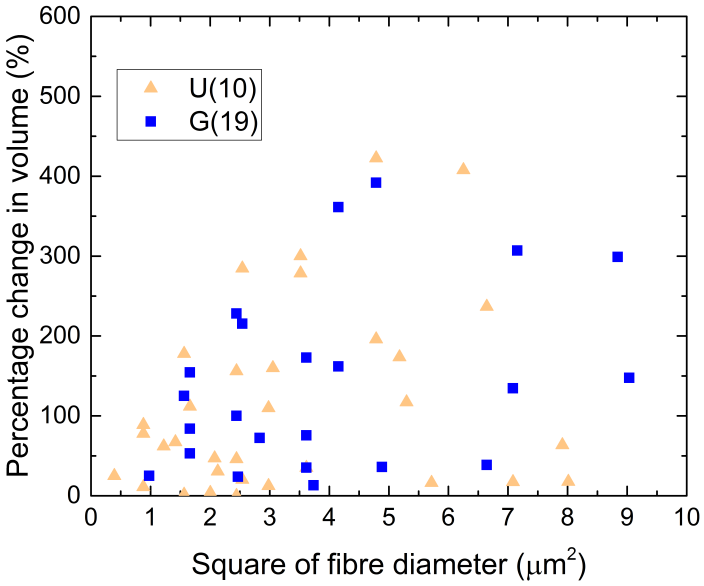

Fig. 3.24 Percentage increase in fibre volume with increasing dry fibre diameter.

3.5 Conclusion

In this study, the chemical and mechanical properties of LEP dECM-laden fibres were measured. At a low working voltage of 230 V, the key molecules in the ECM (including collagen IV, laminin and fibronectin) were preserved, although there was some redistribution of laminin and fibronectin. This demonstrates fine patterning of multi-proteins. On a molecular level, the secondary and tertiary structures of the collagen contained in a fibre were indifferent before and after LEP processing. Two growth factor proteins, VEGF and b-FGF, were measured in the raw material and in acidic solution to show that the growth factor concentration was not influenced by the solvent. The Young's moduli of gelatin and dECM-laden fibres and films were measured to investigate the influence of LEP on the mechanical properties. For the same dECM concentration, the fibres and film exhibited similar values of Young's modulus. As the dECM concentration increased from 0% (G(19)) to 50% (U(50)), Young's modulus increased accordingly. This indicated that the increase in stiffness in the LEP patterned fibres is contributed by the dECM components. It is important to note that the Young's modulus of an individual dECM-laden microfibre was higher than that of bladder tissues *in vivo*. It has been reported that the decellularization process caused the dECM material to become stiffer than the original native tissue. In order to incorporate ECM chemical signaling while minimising the impact of stiffening, U(10) fibres were used for a subsequent cell culture study. The swelling of fibres in water was also investigated. As a result of swelling, there was a wider distribution of fibre diameters when the fibres were in water than when they were dry, and there was an general increase in fibre diameter. Overall, LEP allows for the preservation of proteins and growth factors of dECM material. This can potentially contribute to building a more physiologically relevant cell culture platform. However, the incorporation of dECM causes material stiffening, which leads to deviation from the stiffness of native tissue. Hence there needs to be compensation between biochemical integrity and mechanical stiffening.

Chapter 4

Applications towards a glomerulus-on-chip model

Abstract

Kidney toxicity is one of the most common adverse reactions reported during drug development. This can lead to serious terminal conditions as damage to kidney function is often non-reversible. *In vitro* models have limitations in recreating the ECM-like biochemical and topographical *niche*. In this study, I fabricated a dUBM-laden gelatin membrane (U(10)) using LEP and explored its use for human cell culture. As demonstrated in previous chapters, this membrane consists of ECM-derived biochemical composite, including collagen IV, laminin and growth factors. Topographically, a membrane with tunable mesh size is formed by the close packing of microfibres. With a preliminary test, EAhy926 cultured on the membrane exhibited different morphology according to the mesh size. When the mesh size was significantly greater than the cell size (length typically >70 μm), the cells exhibited bi-polar morphology along the fibre direction. As the mesh size decreased, the cell morphology became increasingly polygon-like. For mesh sizes less than 5 μm in diameter, the cells formed an integrated confluent layer instead of orientating along each fibre. To investigate the possibility of maintaining differentiated cell phenotypes, single and co-cultures of human glomerular endothelial cells (GEnCs) and podocytes were performed on the G(19) and U(10) membrane for seven days. Cellular differentiation was monitored by the expression of VE-cadherin and podocin in GEnCs and podocytes, respectively. Single cell type cultures showed a tendency to form a confluent cell sheet on the membrane, whereas the co-culture exhibited preferential reorganisation. In addition, SEM images of the cell layer showed interesting foot processes. These preliminary studies demonstrate the feasibility of cell culture using the dECM-laden gelatin fibrous membrane structure and proved the possibility of manipulating cellular phenotype by tuning the membrane properties. This U(10) membrane can potentially be incorporated into a glomerulus-on-chip model to further improve its biological relevance.

4.1 Introduction

The kidney is the basic functional unit for blood filtration and maintaining ion concentrations in the body. It plays a crucial role in removing waste, retaining water, maintaining blood

pressure, and regulating pH and the balance of ions[246]. Renal pathology has always been an intensively studied area because many kidney-associated diseases can become terminal illnesses, including Chronic Kidney Disease[247–250]. The kidney contains around 1 million nephrons (the fundamental unit of a kidney) and 20 distinct cell types[192]. Each nephron consists of complex hierarchical structures, which perform unique functions. A number of kidney-on-chip models have been developed to synthesise specific nephron components. This includes the models of a glomerulus[73], proximal tubule[70], distal tubule[74–76], and collecting duct[77, 78]. Recently, two glomerulus-on-chip models were reported by Zhou et al.[73] and Musah et al. [251]. Both studies used PDMS-based microfluidic systems to introduce mechanical stimuli, either by mechanical stretching or medium flow. Either a polycarbonate membrane or a porous PDMS membrane was used to co-culture the glomerulus endothelial cells and podocytes, and to simulate the blood-to-urine barrier in a glomerulus. These models could be used as a disease model to study the dynamic cell response, which was monitored by live cell imaging. With the progress above, the PDMS-based microfluidic systems are still accompanied by limitations in mimicking the biochemical and topographical ECM microenvironment *in vivo*. Lacking these physiological cues can hinder cell differentiation into the specific phenotype required[252]. Therefore, the cell response and behaviour can deviate from the physiological condition.

The hypothesis is that by providing the appropriate bio-chemical signalling and structural support of an ECM, one can achieve highly differentiated cell phenotypes and maintain cell functions. Fibrous *niches* are fabricated for a multitude of tissue and biological model applications, and mediate mechanical and biochemical cues to promote cell proliferation, differentiation and self-assembly. Specific differentiation of GEnCs and podocytes has been demonstrated on a porous membrane fabricated by electrospinning[253]. The main disadvantage of the electrospun fibrous membrane, fabricated by conventional far-field technique, is that the effective membrane mesh size and permeability is tuned by increasing the membrane thickness. Thus the microtopographical cues sensed by the cells and the crosstalk between cells across the membrane are different from the *in vivo* conditions. For example, to obtain a sufficiently small mesh size, the electrospun membrane thickness can be 35 μm, which is much higher than the physiological layer thickness (<400 nm)[200]. Additionally, incorporating fibrous membranes into microfluidic devices have traditionally been a multi-step process[79, 151]. This increases the technical difficulty for scale-up applications.

The dUBM-laden gelatin membrane (U(10)) fabricated using LEP is a potential candidate to address the above mentioned technical difficulties, and to better mimic the glomerular microenvironment. From a biochemical aspect, the protein composition of dUBM is closer to

the kidney than other organs[19]. The choice of dUBM is further supported by the fact that, during embryonic development, both the kidney and the urinary bladder develop from the mesonephros[192]. There are similarities in the bio-chemical and functional link between the two organs. Since large quantity production of kidney dECM remains challenging, dUBM was used in the preliminary study. Topographically, LEP provides a single layer of the U(10) membrane with tunable mesh size, while maintaining a thin suspended structure. In this study, I explored the feasibility of using U(10) membrane for glomerular cell culture. The fabrication and cell seeding condition on the free-standing U(10) membrane was first optimised using EAhy926 cells. Having determined the suitable membrane mesh size, G(19) and U(10) membranes were fabricated and cultured with human glomerular endothelial cells (GEnCs) and podocytes. Protein expression of VE-cadherin and podocin was visualised with immunofluorescent staining, as indicators for cell differentiation. Similar characterisation was also performed for the fibronectin secretion. This is a proof-of-concept study that could potentially lead to a functional glomerulus-on-chip device with improved physiological relevance.

4.2 Design principles

With LEP, a high concentration of dECM-laden nano- to microfibres can be patterned on a variety of substrates with complex geometries. This gives us the main advantage over the membrane-fabrication methods in other organ-on-chip models. In mainstream organ-on-chip development, cells are cultured on a protein-coated PDMS membrane. The PDMS membrane acts as a physical barrier and is typically 10 μm thick with pores of diameter 10 μm[254]. The coated proteins are typically collagen and laminin to assist initial cell attachment[255–257]. Such a microfabricated membrane structure is mechanically and chemically different from the basement membrane in glomerulus, which has a thickness of hundreds of nanometres and contains a variety of extracellular matrix components with encapsulated growth factors. The LEP technique allows one to better mimic this structure, and I aim to apply this to cell culture study.
To obtain the optimum cell culture conditions, the following criteria should be satisfied:

1. The substrate should be biocompatible. The material used in the device should not release chemicals over time which may harm the viability of the cells or affect the cell functions and phenotypes.

2. The device should be easily handled, transported and operated. For primary cell study, the cell seeding procedure should be gentle and straightforward, to avoid damage to the cells.

3. The device should allow live-cell analysis. As one of the advantages offered by organ-on-chip models, one can study cell behaviour in real time. I aim to create devices which enable live-cell imaging as well as quantitative analysis.

In order to meet these criteria, I combined 3D-printing and LEP, based on its wide material selection and design flexibility. PLA was adopted in the 3D printing because of its biocompatibility. To achieve a user-friendly design for preliminary drug testing purposes, the trans-well configuration was adopted, in which the cylindrical supporting structure is 3D-printed and the top is covered with LEP-patterned dECM-laden membrane. This allows easy access for cell culturing on both sides of the membrane.

In order to model the glomerulus structure, an endothelial to podocyte interface must be created. I reduced the mesh sizes in the fibrous membrane to prevent cell infiltration. By seeding endothelial cells on one side of the membrane and podocytes on the other, the interface between the cells could be created. In this way, the two cell types are spatially localised on each side of the membrane whilst cross-talk between the cells could be achieved through the mesh. The bio-active molecules in the dECM fibres provide chemical cues to the cells, and the cells can secrete protein as they grow and differentiate. This protocol allows one to optimise the cell culture conditions on the fibrous membrane and analyse cellular behaviour.

4.3 Background

4.3.1 Membrane-based cell culture platforms

Membranes consisting of nano- and micropores have been used as cell growth substrates. This was firstly used by Grobstein in 1953[259] and has subsequently been adapted to a variety of cell types. This membrane-based cell culture system has been developed into Transwell assays, which has been widely applied in various biological studies such as cell migration[260–262]. The advantage of porous membrane over solid, impermeable substrate is the ability to support cell growth in a polarized state under more natural conditions[263].

Table 4.1 Membrane thickness and pore size comparison between cell culture devices

Model	Material	Membrane thickness	Pore size
Transwell[258]	Polyester or Polycarbonate	$10\mu m - 50\mu m$	$0.4\mu m - 8.0\mu m$
Lung-on-chip[9]	PDMS	$10\mu m$	$10\mu m$
Glomerulus-on-chip[73]	Polycarbonate	$10\mu m$	$10\mu m$
Proximal tubule-on-chip[70]	PDMS	$10\mu m$	$0.4\mu m$
Distal tubule-on-chip[75]	Polyethersulfone	$100\mu m$	$0.4\mu m$
Electrospun membrane[151]	Polyurethane	$5\mu m$	N/A

Moreover, cells are influenced by the biological molecules from the substrates and surrounding medium that promote cell adhesion and cell migration. The chemical properties of free-standing membrane structures can be modified to influence cell behaviour. By tuning the permeability of the membrane, chemical gradients can be temporarily established across the membrane. The commercially available Transwell membrane can be made of polyester and polycarbonate[258]. Collagen can be used to coat the surface of the membrane substrate to improve cell adhesion and viability. In addition to the Transwell system, Polydimethylsiloxane (PDMS) membrane has been used in cell culture and biological models because of low cost and flexibility. The PDMS membrane can be easily bound to other PDMS or glass by plasma treatment. The bulk stiffness of PDMS can be tuned in the range of 0.1 kPa – 2.3 MPa by varying the base-to-crosslinker ratio[264]. This better mimics the biological condition and is the main advantage over the plastic-based Tanswell membrane system. Moreover, PDMS is optically transparent which enables real-time imaging-assisted cell studies[265]. It is also gas-permeable which enables Oxygen exchange to improve cell viability[266]. More importantly, the geometric design of microfluidics is highly reproducible with lithography technique[267]. The design can be flexible by changing the lithography design. However, PDMS is hydrophobic and bio-inert. This can be overcome by modifying the surface chemistry using plasma treatment and coating the surface with various proteins. Yet, the protein coating cannot replicate the complexity of the native ECM. Comparing to the polymeric membrane-based system, electrospun fibre matrix closely recapitulates the fibrous nature in the ECM. The typical pore size of an electrospun fibrous mesh is about 0.5 – 5 μm[268]. This pore size can be tuned by controlling the electrospinning duration. In particular, small pore size (in the range of 300 nm) can be fabricated[269]. Incorporation of electrospun membrane into microfluidics has been demonstrated by combining with photolithography[151] or

by introducing electrolyte solution[79]. Currently, both techniques still require multi-step processing. A summary of the membrane-based cell culture system is displayed in Table 4.1.

4.3.2 Cell morphology and behaviour

Cell morphology refers to the appearance, shape and structure of a cell. This is the most direct characterisation of the state of a cell *in vitro* and is closely linked to cell functions, such as migration and differentiation. The change in cell shape is associated with a number of cell biological processes, including cell polarization, the formation of cell protrusions, cell division and apoptosis[270]. There are four main categories of mammalian cells based on their morphology[271], shown in Fig 4.1:

1. **Fibroblast-like cells** grow attached to a substrate. They exhibit elongated bi-polar or multi-polar shapes. Fibroblast cells are involved in the secretion of ECM proteins, including collagen, fibronectin and laminin. These cells play an important role in the tissue repair process.

2. **Epithelial-like cells** grow attached to a substrate in patches. They exhibit polygon shapes *in vitro* and become squamous (flat, square-like), cuboidal (same height and width) and columnar (height greater than width) *in vivo*. As epithelial cells develop into sheet structures, they contribute to the formation of a tissue-tissue interface. In cell culture, these cells have flattened morphology and form a contiguous monolayer.

3. **Lymphoblast-like cells** grow without attaching to a substrate. They exhibit spherical shapes. These cells are mostly found in blood, responsible for oxygen delivery (red blood cells) and immune response (white blood cells).

4. **Neuronal cells** exhibit different sizes and shapes. The two categories of neuronal cells are type I which contain long axons and type II which are without axons.

The control of cell shape relies on intercellular mechanics and cell-matrix interactions. The intrinsic forces affecting cell shapes are imposed by the cytoskeleton[273], polarisation of actins[274] and osmosis pressure[275]. The external forces are contributed by environmental adhesion and cell-cell interactions. These factors are not independent, but closely coupled together to actively regulate cell morphologies. From an Engineering perspective, I considered the external force provided by cell culture substrates. The relationship between cell morphology and substrate stiffness has been addressed in a number of studies[48, 276]. In general, fibroblast-like cells are flatter, spanning a larger area and change from more rounded to more polygonal shapes when cultured on stiffer substrates[277]. Stiffening of

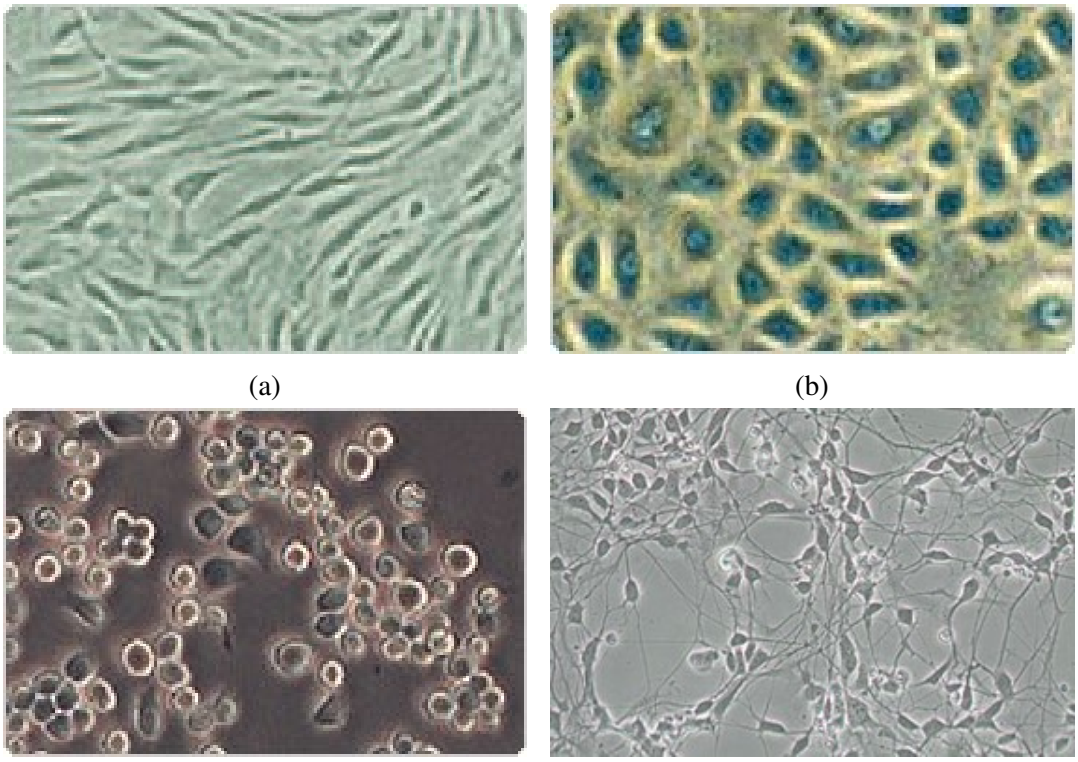

(a) (b)

(c) (d)

Fig. 4.1 Four main categories of cell morphology. (a) Fibroblast-like cells; (b) epithelial-like cells; (c) lymphoblast-like cells[271] and (d) neuronal cells (human IPSC-derived)[272].

F-actin filaments was observed as the substrate stiffness increased. The stiffening of F-actin was also observed when cells intended to make cell-cell contact from an isolated culture. When endothelial cells were cultured at low density, increasing the substrate stiffness caused an increase in protrusion length. This change in morphology became indistinguishable when the cells reached confluence. The change in morphology changes the cell phenotype and can be used to guide stem cell differentiation[34]. In addition, the contrast in cell adhesive surface was demonstrated to affect cell shape[278] and can be used to engineer cell function[279].

Cell fate, including proliferation, specialization, interaction and migration, is closely associated with the physical and biochemical properties of culturing substrates. This correlation especially has been used as the means of directing stem cell fate. There are three methods of probing stem cell differentiation *in vitro*[280]:

1. **Tailoring biochemical properties of the substrate:**
   Sequence and combination of ECM proteins; spatial arrangement and local concentration of ECM components; surface treatment to attach active functional groups and growth factors[281].

2. **Tailoring physical properties of the substrate:**
   Elastic modulus[282]; soluble factor gradient; topography[128] and geometric arrangement[283].

3. **Monitoring cell-cell interactions:**
   Cell seeding density; cross-talk between two cell types in co-culture conditions; feeder cell layer.

For more differentiated cell types, the physical and biochemical properties of culturing substrate are equally important in maintaining cell phenotypes. In this case, a closer replication of the physiological condition is desired. With this, a more physiologically-relevant response can be predicted using the *in vitro* model.

4.3.3 The glomerulus

The nephron is the structural and functional unit of the kidney. Each nephron consists of the Bowman's capsule (containing the glomerulus), proximal convoluted tubule, the loop of Henle (containing the descending limb and ascending limb), distal convoluted tubule and cortical collecting duct. The glomerulus, situated inside the Bowman's capsule, is the primary filtration unit which controls the selective filtration from blood to become urine. It consists of glomerular endothelial cells which line the glomerular capillaries (the filtration barrier) and

the podocytes that cover the outer surface of the filtration barrier, as shown in Fig 4.2. It also contains mesangial cells which fill between the capillaries[284] (not shown in the figure). The glomerular endothelial cells, podocytes, and the glomerular basement membrane together control the selective filtration of molecules[285]. The glomerulus contains fenestrated capillaries which are more porous than those in the circulation system. SEM images of a mouse glomerulus are shown in Fig 4.3. The basement membrane of the fenestrated capillaries filter large proteins and molecules (Fig 4.3c). Podocytes cover the outer surface of the basement membrane. The foot processes of podocytes form the slit membrane which filters the medium size molecules (Fig 4.3b). This leads to the production of glomerular filtrate which is plasma without proteins. The filtrate leaves the Bowman's capsule through the convoluted tubules, and becomes urine after several reabsorption processes.

There are three types of cell in the glomerulus: glomerular endothelial cells (GEnCs), podocytes, and mesangial cells:

- **Glomerular endothelial cells**:
  The GEnCs are specialised endothelial cells that line the inner surface of the capillaries. GEnCs contain porous cell surfaces, and are known as fenestrated endothelial cells. The typical pore size is approximately 50 – 100 nm in diameter. These fenestrations are coated with diaphragms to facilitate the filtration of fluid, plasma solutes and proteins. The GEnCs can be characterised by the expression of cadherin. Cadherin, named for "calcium-dependent adhesion", is a type I transmembrane-protein. The VE-cadherin plays an important role in the cell-cell adhesion for endothelial cells. It maintains the integrity of intercellular junctions and a restrictive endothelial barrier. Hence, the expression of VE-cadherin reflects the formation of an integrated vascular endothelial layer. In this study, the VE-cadherin expression was used to evaluate the differentiation of GEnCs.

- **Podocytes**:
  Podocyte cells are highly specialised epithelial cells which control the filtration in the glomerulus. Podocytes develop long foot processes (also known as pedicles) which wrap around the outer surface of the capillaries and form a layer of filtration slits. The space between adjacent foot processes is spanned by a slit diaphragm formed by proteins, including nephrin and podocin. Due to the negative surface charge and the size restrictions imposed by the filtration slits, only selective molecules from the blood can pass through the slits. Hence, the podocytes and GEnCs together regulate the filtration function in the glomerulus. Podocin is a characteristic protein component localised in the foot processes of podocytes. The expression of podocin reflects the differentiation of podocytes.

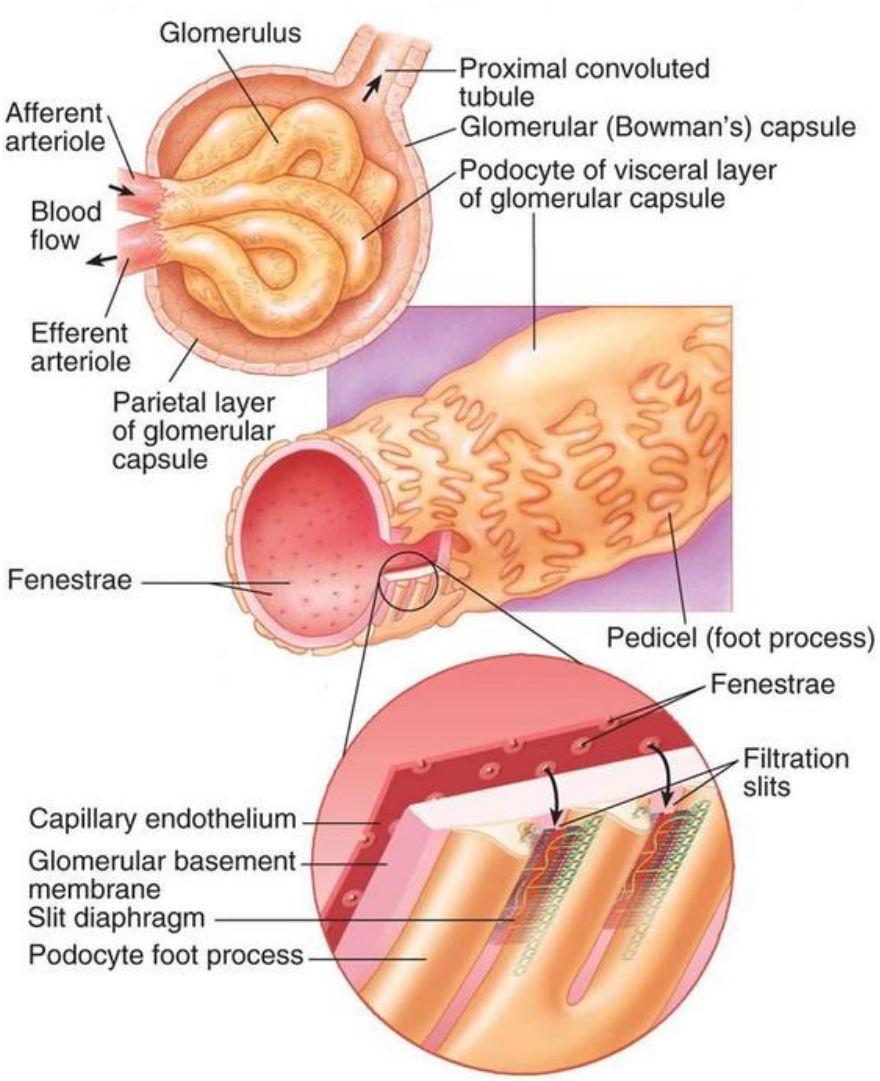

Fig. 4.2 The structure of a glomerulus[286].

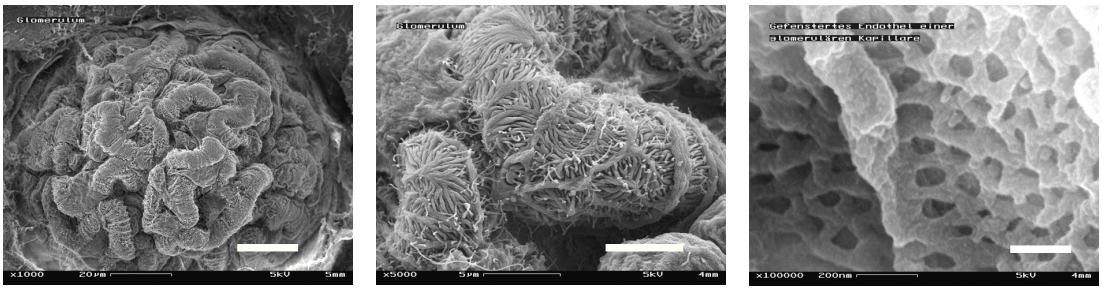

(a) (b) (c)

Fig. 4.3 Mouse glomerulus structure in the SEM (image source *http://www.wikidoc.org/index.php/Glomerulus*). (a) The glomerulus structure, scale bar 20 μm; (b) foot processes of podocytes, embracing the glomerular capillaries, scale bar 5 μm and (c) fenestrated endothelial layer at the inner surface of glomerular capillaries, scale bar 20 nm.

- **Mesangial cells**:
  Intraglomerular mesangial cells are highly specialised pericytes. They are positioned between the glomerular capillaries and actively control the mechanical tension imposed on the glomerular capillaries and the glomerular surface area. This contributes to the control of blood flow in the capillaries.

4.4 Materials and methods

4.4.1 Materials

Human glomerular endothelial cell lines and podocytes cell lines were kindly donated by Dr Simon Satchell, University of Bristol. Collagen IV antibody ab6586 was obtained from Abcam. Laminin antibody L8271 was from Sigma Aldrich. Fibronectin antibody ab2413 was obtained from Abcam. Hoescht 33342 was used for nuclei staining.

4.4.2 Device preparation

PDMS was cast in the mould and cross-linked using a 10:1 volume ratio of a base and curing agent. The PDMS was cured at 60 °C for 24 hours. The cured PDMS was removed from the mould and immersed in absolute ethanol for 24 hours. Then, the PDMS devices were dried and used as a collecting substrate for LEP fibre deposition. The PLA supporting ring was 3D-printed using an Ultimaker 2, and used as a collecting substrate for fibre deposition. G(19) and U(10) solutions were prepared as described in the previous chapter. The solution was loaded in a 1 mL syringe and pumped at 1.3 μL/hr. Glass slides were used as initiators.

In the Labview program, the acceleration was 1500 mm/s^2, speed 150 mm/s, line length 30 mm, line width 30 mm and number of lines 15000. The applied voltage was 230 V. These parameters were held constant when fabricating all the devices.

4.4.3 Endothelial cell culture on dECM-laden membranes

Cell culture medium was prepared by adding 10% v/v fetal bovine serum (Sigma-Aldrich F0804) and 1% v/v penicillin-streptomycin (Sigma-Aldrich P4333) into 500 mL Dulbecco's Modified Eagle Medium (DMEM, Sigma-Aldrich D6429). PDMS devices were immersed in PBS (ThermoFisher 10010023) for 18 hours and in DMEM culture medium for 1 hour before cell seeding. EAhy926 cells were cultured till confluent in a 25 mL flask. For resuspension, the cells were washed with 5 mL PBS. 1 mL trypsin was added to the cells and incubated at 37°C for 5 minutes. The suspended cells were centrifuged at 1000 rpm for 5 minutes. The cell medium was removed and replaced with 500 μL DMEM culture medium. A proportion of the cells were seeded onto the dECM-laden gelatin membrane according to the area of the PDMS device. The cells were cultured at 37°C and 5% CO_2.

4.4.4 Kidney cell culture on dECM-laden membranes

The PLA devices were immersed in DMEM for 1 hour before cell seeding, with the fibrous membrane facing the bottom of the 8-well plate. GEnCs were cultured in a T75 flask at 33°C to reach confluence. The cells were washed with 15 mL PBS. 3 mL trypsin was added to the cells (sufficient to cover the surface) and incubated at 37°C for 5 minutes. The cell medium was removed and replaced with 1 mL new medium. The cell number was counted and 150,000 cells were seeded onto each device. GEnCs were cultured at 37°C for 24 hours. Podocytes were resuspended in the same manner. After resuspension, the devices were flipped using a pair of sterilised tweezers. 150,000 podocyte cells were seeded on top of the membrane and incubated at 37°C for 7 days. In this way, the number of GEnCs and podocytes on each side of the membrane should be similar. The culture medium was changed every two days.

4.4.5 Immunofluorescent staining

For fixation, the medium was replaced using absolute ethanol and incubated at -4°C for 4 hours. After washing 3 times with PBS, the sample was immersed in 3% BSA/PBS solution and stored at room temperature for 1 hour. Afterwards, the sample was washed with TBS-T 3 times. Primary antibody (1/100 for fibronectin and 1/200 for VE-cadherin and podocin)

was added to the sample and stored at room temperature for 1 hour. Then, the sample was washed with TBS-T again and the secondary antibody was added and incubated for 1 hour at room temperature. The sample was washed with TBS-T and hoescht 33342, and left for 30 minutes. Finally, the sample was washed with TBS-T and the sample was preserved in mineral oil. The sample was imaged the next day.

4.4.6 Fluorescent imaging

A confocal microscope Leica TS5 was used for fluorescence imaging. The argon laser power was at 30% and a 633 NeHe laser was used. The visible laser power was between 10% and 25%, with digital gain between 800 and 1000. The same laser power and gain were used for cross comparison of the samples. The images were captured at 10 Hz.

4.4.7 Cell fixation for SEM imaging

The cell fixation and SEM imaging protocol was adopted from [287]. The cells were fixed with glutaldehyde and cacodylate buffer solution for 10–15 minutes. The sample was transferred into pure cacodylate solution for 1 hour. Afterwards, the sample was immersed in a 0.1 M osmium/cacodylate/water solution for 15 minutes. Then the sample was washed in distilled water and immersed in a sequence of ethanol solutions with concentrations of 25%, 50%, 60%, 70%, 80% 90%, and 96% for 10 minutes each. The sample was then immersed in absolute ethanol for 30 minutes, with a change of ethanol every 10 minutes. The sample was loaded in the critical point dryer for 2 hours and underwent gold coating. SEM imaging (FEI Nova NanoSEM) was performed one day after the cell preparation.

4.5 Results and discussion

4.5.1 Fabrication of free-standing dECM-laden membrane towards a functional cell culture platform

LEP shows the potential to fabricate robust bio-functional devices. The suspended dECM-laden fibres provide ECM-mimicking biochemical to topographical cues for cell culture. In this section, I used LEP to precisely pattern U(10) solution into a microfibre mesh with controllable mesh size. With decreasing mesh size, this microfibre network became a membrane structure. Using LEP, this membrane can be suspended on both microfluidic and 3D-printed structures. In order to optimise the membrane morphology, the following problems were encountered and required troubleshooting:

1. **Droplet formation on the membrane:**
   When the solution was not viscous enough and the flow rate during LEP was too high, small droplets could be deposited on the membrane, as shown in Fig 4.4a. The droplets, when rehydrated, could swell and cause the membrane to become uneven. On the other hand, if the flow rate was too low, the fibre patterning was unsustainable. Therefore it is crucial to maintain a steady, low, and sufficient flow rate.

2. **Fibres emerging:**
   When the evaporation rate of the solvent was low, suspended fibres can merge to form a thick one when they were patterned too closely, as shown in Fig 4.4b. This brings difficulty in fabricating membranes with small mesh sizes and reduces the patterning resolution. It was found that the outcome of fibre fabrication was the more optimal at an atmospheric temperature of 22°C . At this temperature, the solution evaporation rate was sufficiently fast to prevent fibre merging. In this way, the mesh size of the single-layer membrane can be less than 5 μm in diameter.

3. **Fibre damage when transferring the structure:**
   When the fabrication of the fibrous membrane was completed, it was transported from the stage to a petri-dish. At this point, the fibres are connected between the initiators and the 3D-printed structure. If the substrates were removed and the fibres broken mechanically, the fibre network could be damaged and the overall integrity is lost, as shown in Fig 4.4c. I found that this could be overcome by using water to dissolve the fibres connected to the initiators. Upon hydrolysation, the dECM-laden fibres became soft. Any uncrosslinked fibres dissolve in the water and readily crosslinked fibres could be cut off with a razor blade. In this way, the integrity of the fibrous membrane could be retained.

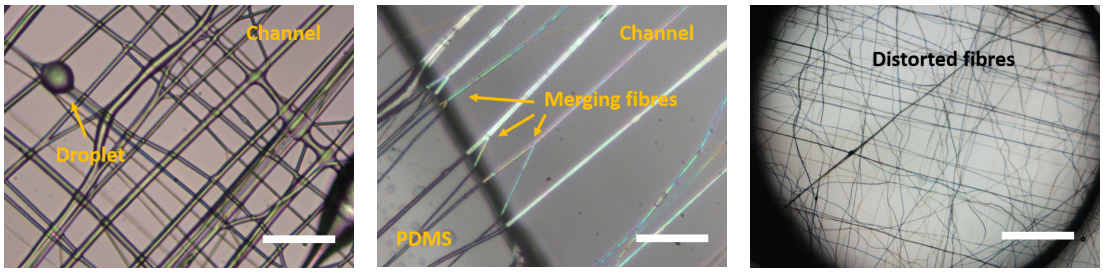

(a) (b) (c)

Fig. 4.4 Troubleshooting of the membrane fabrication. (a) Droplet formation due to high flow rate and low viscosity, scale bar 10 μm; (b) fibre merging due to low evaporation rate, scale bar 10 μm and (c) distorted fibres, scale bar 100 μm.

After troubleshooting and optimisation of the membrane fabrication conditions, I explored the appropriate configuration for a cell culture platform. Two substrate materials were used to achieve this: PDMS-based microfluidics, and a 3D-printed PLA scaffold. First, dECM-laden fibres were directly patterned on the PDMS microchannel. Excess fibres were removed before crosslinking. The fibre-covered PDMS was plasma treated together with another microfluidic and the two parts were subsequently assembled, as shown in Fig 4.5. The assembled device was attempted in cell culture. However, there are several problems associated with the cell seeding procedure. Firstly, PDMS is bio-inert. In order to obtain a confluent sheet of cells in the microfluidic channel, one needs to coat the PDMS surface with proteins to promote cell adhesion. The coating requires thorough washing to remove excess protein solution and rebalance the osmotic pressure. Failing to remove excess solution can results in cell death. However, washing caused irreversible damage to the fibrous membrane. The damage did not necessarily cause the membrane to fracture, but often increased the mesh size of the membrane. As a result, the cells penetrated through the membrane and sediment into the other channel. Many washing methods were evaluated however the optimum method is still to be discovered. Secondly, PDMS is soft and elastic. When transferring the PDMS between the stage and the petri-dish, the fibrous membrane could be damaged as it can be brittle when dried.

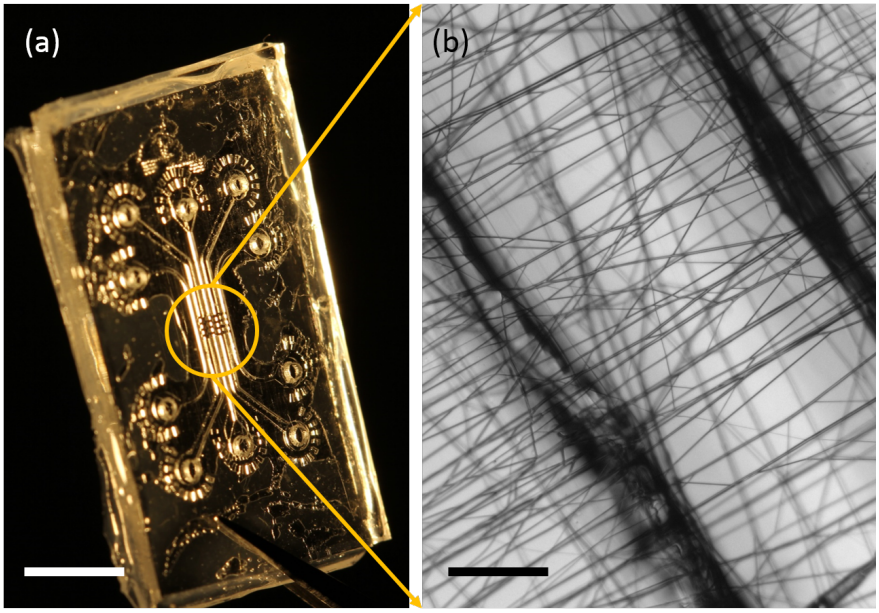

Fig. 4.5 U(10) membrane encapsulated within a microfluidic device made of PDMS. (a) Photo of the device, scale bar 5 mm; and (b) image of the fibrous membrane, scale bar 50 μm.

3D-printed PLA is more bio-compatible and no protein coating is required. One can introduce cell attachment simply by immersing the 3D-printed scaffold in culture medium for a few hours. Using this method, I adapted the trans-well configuration to first investigate the feasibility of using the U(10) membrane for cell culture. A supporting ring structure was printed and suspended U(10) microfibres were patterned on the top surface of the ring, as illustrated in Fig 4.6. The fibre-covered structure was immersed in cell culture medium for one hour before cell culture. The preparation procedure in this case was simpler and the rigid PLA structure improved the robustness of the structure when manually handled. Once the fabricating conditions for the membrane were optimised, one could obtain a final product as shown in Fig 4.6(a). This structure was subsequently used in cell culture studies.

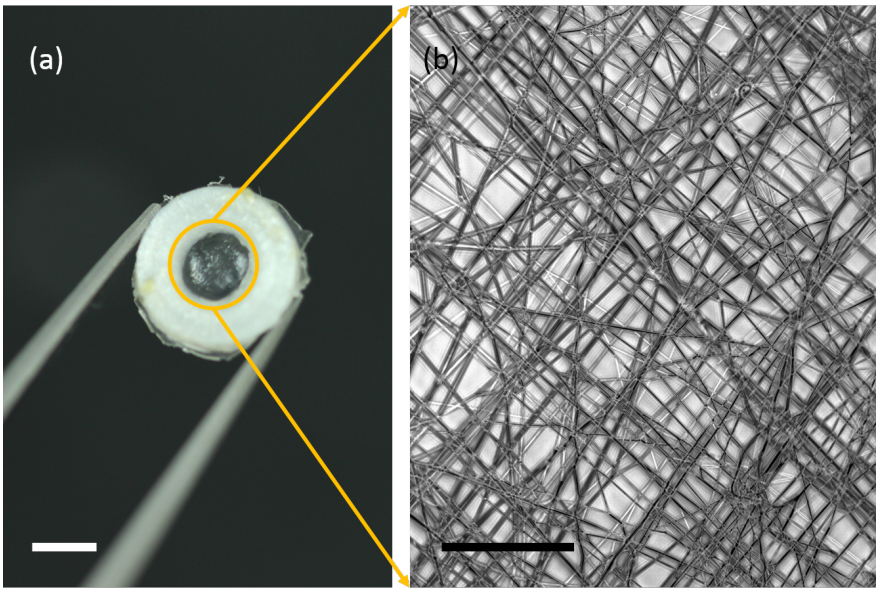

Fig. 4.6 U(10) membrane patterned on a 3D-printed PLA scaffold. (a) Photo of the device, scale bar 1 mm; and (b) image of the fibrous membrane, scale bar 50 μm.

4.5.2 Cell morphology dependence on mesh density

Cells exhibit different morphology and migration behaviour depending on the topography of their scaffold. For example, in quasi-1D, when endothelial cells are attached on one single fibre, they orient themselves along the fibre and migrate under its directional guidance. The migration speed is higher than that observed when cultured in a 2D environment, i.e on a petri-dish[288, 289]. To achieve the most optimum cell culture condition, the mesh size of the membrane must be determined. In this study, human endothelial cell line EAhy926 was cultured on suspended fibrous membranes with different mesh sizes. It was found that the cellular morphology changed accordingly.

Suspended gelatin microfibres were patterned on a PLA scaffold, with a range of densities. The mesh sizes ranged from greater than 100 μm to less than 10 μm in diameter. EAhy926 cells with passage number x+15 were seeded on the membrane, and cultured for 48 hours followed by fixation and staining. Fig 4.7 shows the stained cells on the membrane of four sample: EA1–4. The average mesh size of each sample is displayed in Table 4.2. The mesh size statistics and cell orientations are shown in Fig 4.8. In sample EA1 where the mesh size was the largest (Fig 4.7a), the cells exhibited bi-polar or tri-polar morphology and were oriented along the fibres. This is reflected in the top graph in Fig 4.8, where a higher cell number was distributed towards 90° (the orientation of a number of fibres). In this condition, cells showed a tendency to form cord-like structures along the fibres and polarised networks. Each cell had 2–3 contacting neighbouring cells. This morphology is close to the initial process of vascularisation and capillary formation. In sample EA2 (Fig 4.7b), the cells were still attached along the fibres but they began to form bundles. An alignment between the cells and the fibres can still be identified from Fig 4.8b. The average number of contacts between cells increased. The majority of the cell population still aligned with the fibres. In sample EA3 where the mesh size was comparable to the cell size (Fig 4.7c), some cells spread out and attached within the mesh. In this case, the cell shape changed from a bi-polar to a polygonal morphology. The number of contacts between cells was 3–4. The cell orientation became more random, as shown in Fig 4.8b. In sample EA4 (Fig 4.7d), the cells were larger than the mesh and they attached to the upper surface of the membrane. In this case, the cells were more integrated into a cell sheet and the cell contours became less visible. Polygonal morphology could be identified. Cell orientation was random and independent of the fibre orientation. With decreasing mesh size, the cell organisation changed from a cord-like network to a confluent and integrated cell sheet. This morphology better models the cell-tissue or cell-blood interface.

The suspended nature of the membrane also allows matrix remodelling by the cells as they proliferate and differentiate. In this case, cells were cultured on fibre-patterned

Table 4.2 Mesh size of the membrane samples for EAhy926 cell culture

Sample	Mesh Size (μm)
EA1	72 ± 40
EA2	35 ± 14
EA3	27 ± 7
EA4	3.9 ± 1.1

PDMS channels. This configuration contains both geometries of a flat surface (on PDMS) and a fibrous membrane (LEP fibres). Since the initial cell adhesion was only provided by the gelatin fibres, this allowed one to compare cell behaviour on different substrate geometries. With the same cell type, passage number and culturing conditions, different matrix remodelling depending on the membrane mesh size and chemical composition were discovered. For G(19) membrane, the matrix remodel behaviour of EAhy926 was closely dependent on the mesh size. For membranes with a larger mesh size, cells tended to migrate to pack closer together on suspended fibres. As a result, the mesh size increased and eventually became a cord-like network, as shown in Fig 4.9c. On PDMS, where matrix remodelling was not possible, the cells remained as a confluent cell layer. For membranes with a smaller mesh size, cells were more likely to continue proliferating and maintaining a confluent sheet on the suspended membrane. For U(10) membrane, the cell behaviour was less dependent on the fibre density. Even for a membrane with a large mesh size, cells were more likely to remain as a confluent cell layer than aggregate and remodel the matrix, as shown in Fig 4.9f. This can be a result of both biochemical and mechanical differences between dUBM-laden and pure gelatin membranes.

The glomerulus basement membrane (GBM) provides binding sites for glomerular endothelial cells (GEnCs) and podocytes. GBM acts as the barrier between the two cell types whilst allowing interaction and crosstalk between adjacent cells. To better mimic the GBM structure, I adopted a membrane structure with a smaller mesh size, aiming to create an integrated cell-cell interface. The typical mesh size was smaller than 5 μm in diameter. This was small enough for the cells to form a confluent sheet. This also allowed cells to remodel the matrix and secrete ECM as they differentiated.

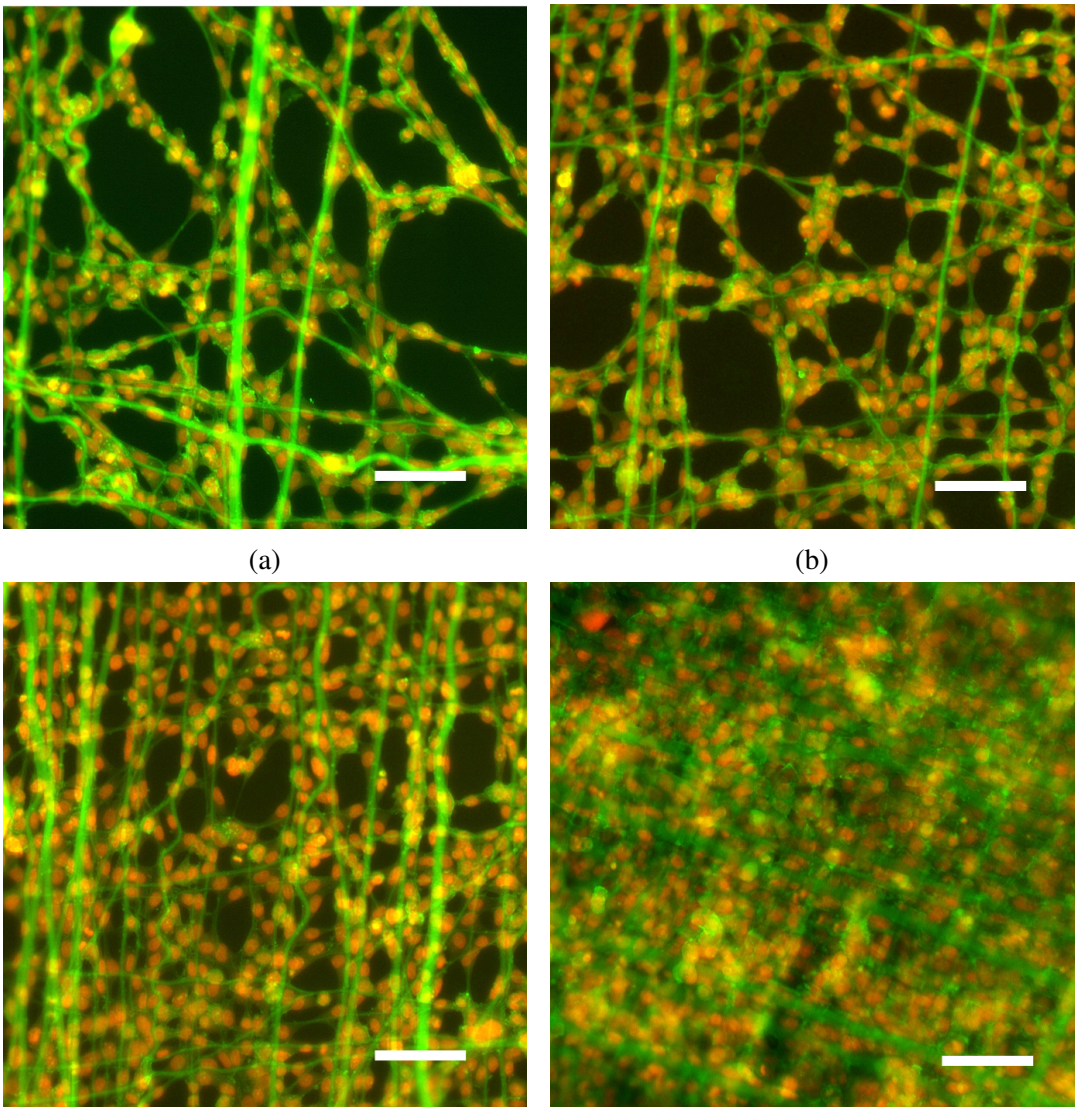

Fig. 4.7 Change in EAhy926 cells according to suspended membrane porosity, with f-actin marked in green and nuclei marked in red. The gelatin fibres also show autofluorescence in green. (a) EA1; (b) EA2; (c) EA3; (d) EA4. Scale bar 75 μm.

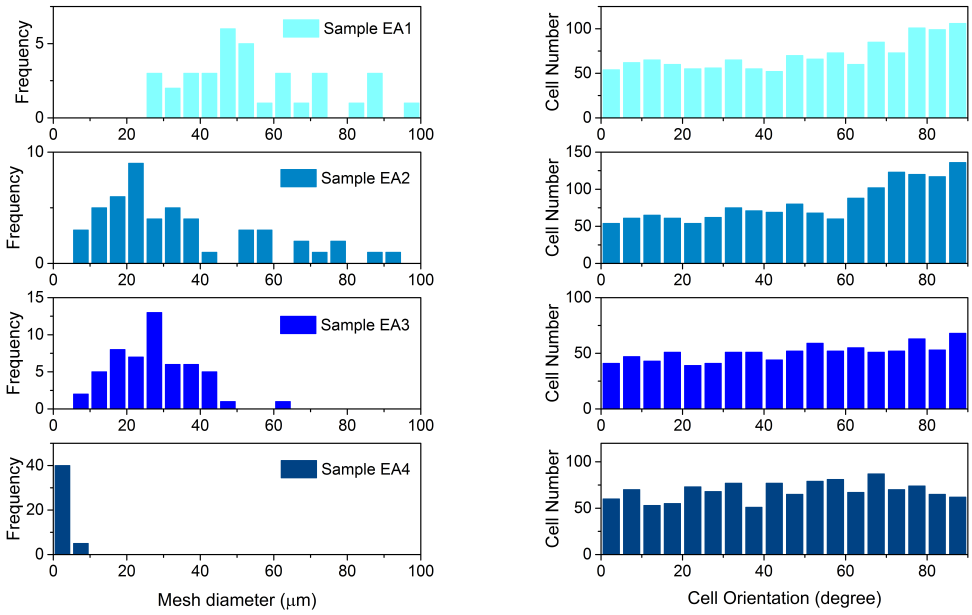

(a) (b)

Fig. 4.8 Statistics of (a) mesh size and (b) the corresponding cell orientation. (a) From top to bottom, the mesh size statistics of EA1 to EA 4. (b) For large mesh sizes (EA1 and EA2), more cells show 90° orientation with respect to the horizontal axis. This shows that the cells mainly aligned with the fibres as a number of fibres are oriented at 90°. For smaller mesh sizes (EA3 and EA4), the cell orientation is evenly distributed in all directions, despite many fibres oriented at 90°. This shows an overall random cell orientation.

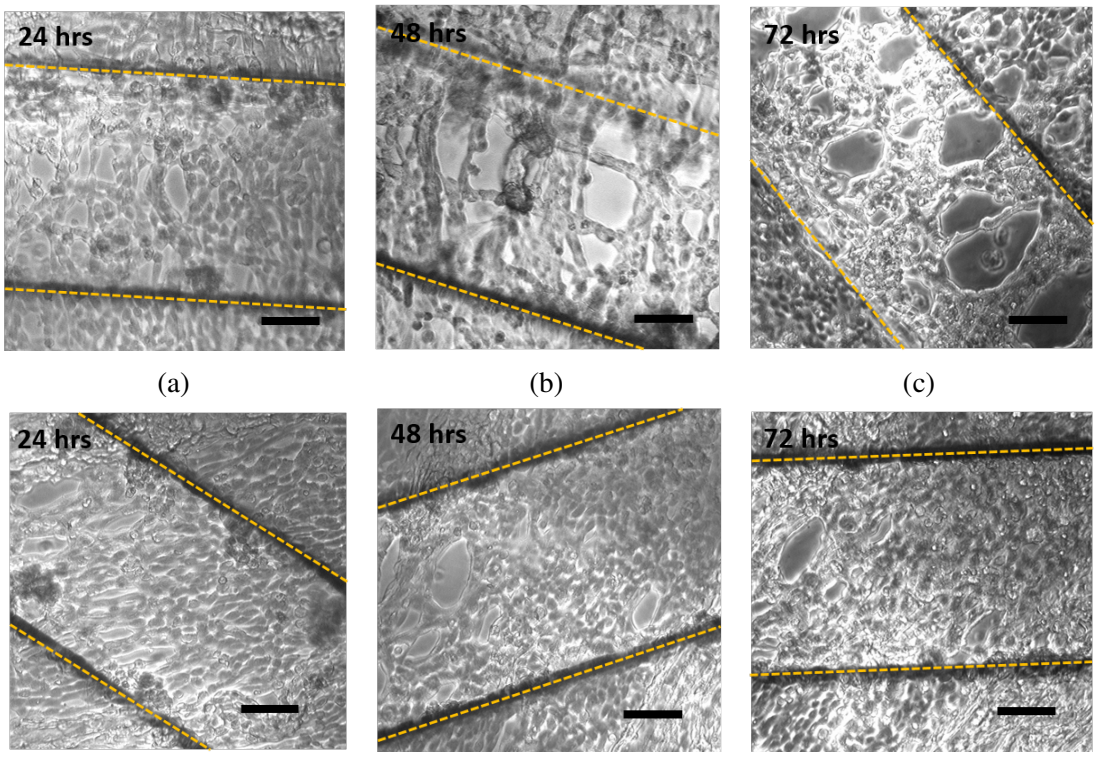

Fig. 4.9 Membrane matrix remodelling by EAhy926 cells (channel outlined in yellow). (a) – (c) G(19) membrane, tendency of cell bundle formation and enlarging the meshes. (d) – (f) U(10) membrane, the matrix geometry being roughly unchanged over 3 days. Scale bar 50 μm.

4.5.3 Glomerular endothelial and podocyte cell culture

The previous section demonstrated the effect of the geometric organisation of the scaffold and its chemical composition on cell behaviour. In this section, I further explore the possibility of creating cell-cell interfaces using the U(10) membrane. Cell culture assays were performed under the following conditions (Fig 4.10):

1. As a proof-of-concept study, human glomerular endothelial cells (GEnCs) and podocytes were individually and co-cultured on suspended membranes made from G(19) and U(10) solutions, as shown in Fig 4.10a. This was to investigate whether the dUBM components affect the cell phenotypes and protein expression.

2. Mono-culture and co-culture of the two cell types were performed on G(19) and U(10) homogeneous film which was made by spreading a droplet of solution in the well-plate, as shown in Fig 4.10b. This offers the chemical composition of dUBM but the organisational configuration of the cells is different from the suspended membranes. Instead of isolating the two cell populations in the co-culture study, GEnCs and podocytes were mixed and cultured on one surface.

3. The same mono- and co-culture condition was performed in a well-plate, as shown in Fig 4.10c. This was the basic reference which lacked both the chemical signalling of dUBM and substrate-remodelling freedom.

The GEnCs and podocyte cells were engineered to proliferate at 33°C and differentiate at 37°C. For cells cultured on a membrane, the confluent cells (previously proliferated at 33°C) were resuspended, counted and seeded onto the membranes. The seeded cells were incubated at 37°C for attachment and differentiation. Proliferation at a reduced rate was still expected for one or two days after the temperature transition. After this, the cells would stop proliferating. Fig 4.11 shows the co-culture on suspended U(10) membrane at days 1, 3 and 7 after the last cell seeding and the cell number at these days. Due to the limitation of the imaging method, the distinct shape of the podocytes (in green) is not clear (the GEnCs were not fluorescence). Nevertheless, the membrane structure was retained and the cells remained attached to the membrane after 7 days of culturing. The cell number grew slightly from day 1 to day 3 after the cell seeding, and remained unchanged after day 3. This was because the rate of proliferation decayed after the thermo-switch from 33°C to 37°C. Hence some proliferation was expected at the first two days after thermo-switch. After day 3, the cells should stop proliferating as they continuously differentiated.

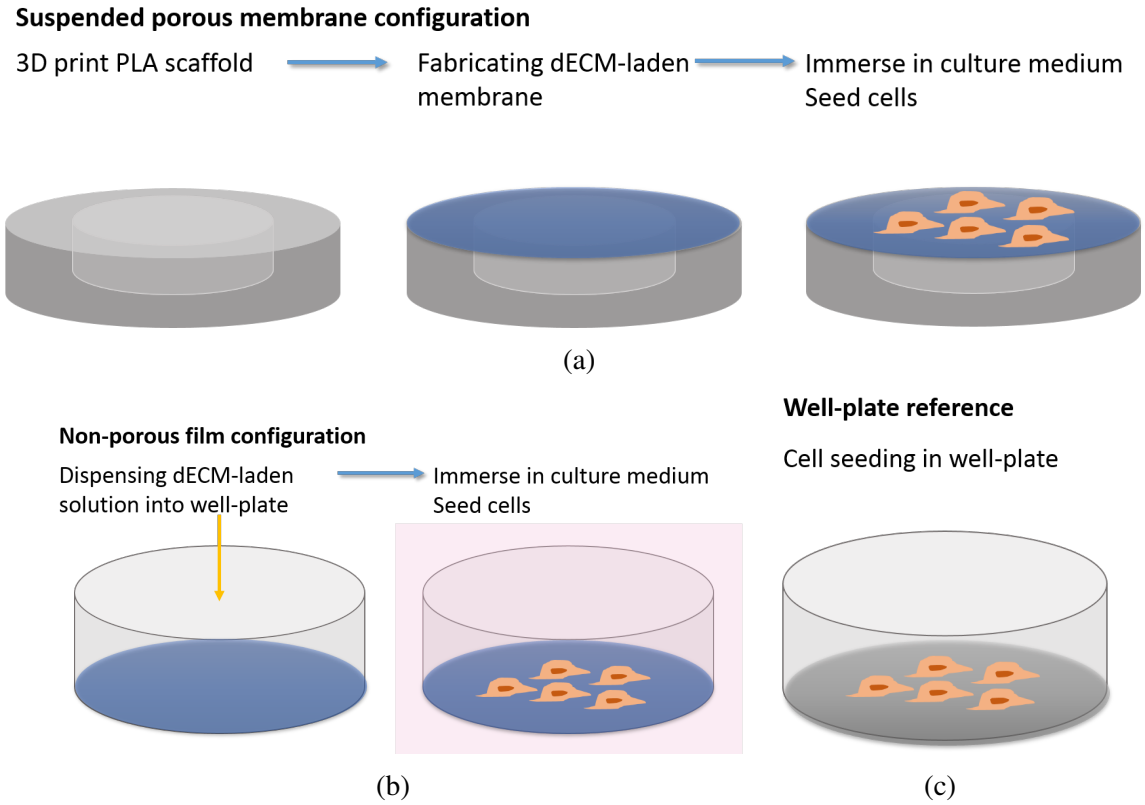

Fig. 4.10 Process of three cell culture configurations. (a) Cell culture on suspended membrane which was fabricated on PLA scaffold. In co-culture conditions, GEnCs and podocytes were seeded on either side of the membrane. In mono-culture conditions, the cells were seeded on top of the membrane. (b) A small amount of U(10) or G(19) solution was dispensed on the bottom of a well-plate to cover the surface and form a membrane. Cells were seeded on top of the non-porous film. (c) Well-plate reference in which cells were directly seeded in the well-plate.

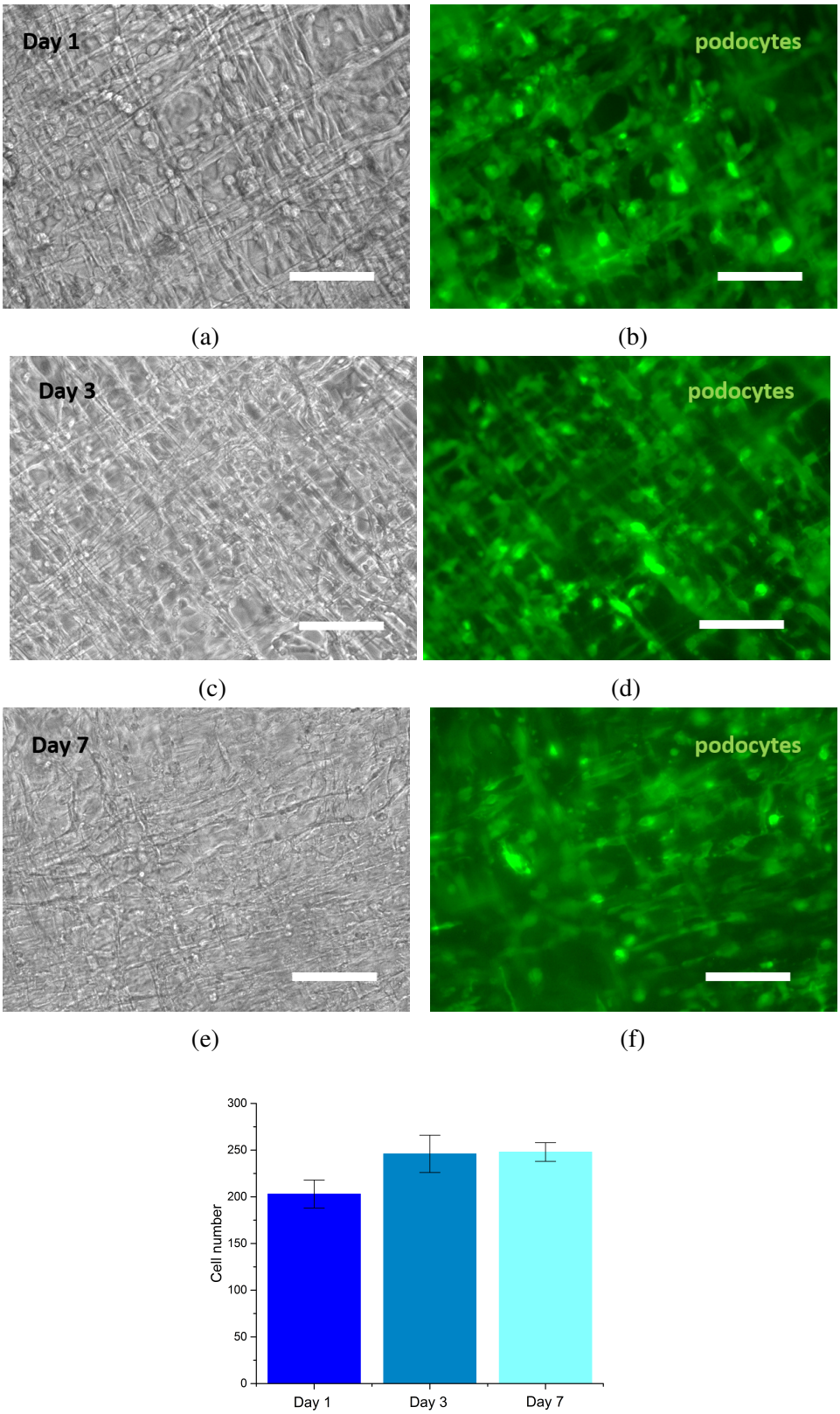

Fig. 4.11 Co-culture of GEnCs and podocytes on suspended U(10) membrane. Podocytes expressing GFP are shown in green. Scale bar 50 μm. (a) and (b) One day after cell seeding, cells attached to the membrane; (c) and (d) three days after cell seeding, cells were allowed to differentiate at 37°; (e) and (f) seven days after cell seeding and differentiation; (g) number of cells counted in the area of imaging (200 x 150 μm^2). n=3.

After seven days of differentiation, the GEnCs were characterised by the expression of VE-cadherin (vascular endothelial cadherin) and podocytes were stained with podocin. Fig 4.12 shows the VE-cadherin and podocin staining for GEnCs and podocytes, respectively. In the co-culture configuration, VE-cadherin was mainly expressed at the cell-cell junctions when the cells were cultured on suspended fibrous membrane, for both G(19) (Fig 4.12a) and U(10) (Fig 4.12g). Interestingly, the level of VE-cadherin expression was not homogeneous throughout the membrane, which may indicate specifically localised growth, migration and differentiation. This was more predominately shown in the G(19) sample than U(10) sample. This may be due to remodelling of the fibrous matrix as GEnCs migrated and preferably grouped together. When the cells were mix co-cultured on one single layer of non-porous film, a reduced level of the VE-cadherin was expressed in the cells, as shown in Fig 4.12d and Fig 4.12j. The G(19) sample gave a higher intercellular VE-cadherin expression than the U(10) sample. In the well-plate reference (Fig 4.13), the overall VE-cadherin expression was lower than the previous configurations, which contained dECM-derived proteins. The intercellular expression of VE-cadherin was observed for a small portion of cells, as shown in Fig 4.13a. This is because only the tight junctions formed between GEnCs expressed VE-cadherin signalling.

When GEnCs were mono-cultured on the suspended fibrous membrane, the VE-cadherin expression was evenly distributed throughout the membrane, as shown in Fig 4.12b for G(19) and Fig 4.12h for U(10). This shows that, without the presence of podocytes, GEnCs did not exhibit preferential reorganisation. Instead, GEnCs formed a homogeneous monolayer on the suspended membrane. No significant matrix remodelling or degradation was observed and the cell layer maintained its integrity. The difference between the G(19) and U(10) samples was not significant. When podocytes were cultured isolated on the suspended fibrous membrane, as shown in Fig 4.12c for G(19) and Fig 4.12i for U(10), podocin was expressed on the cells and at the intercellular junctions, and was homogeneous across the membrane. The cells appeared to be integrated and the boundaries of the cells were not distinct. As a result, the exact location of podocin expression was not clear. There was no observable difference between the G(19) and U(10) samples. When the GEnCs were cultured on non-porous film, a reduced VE-cadherin signal was observed with the cells than those on suspended membranes, as shown in Fig 4.12e for G(19) and Fig 4.12k for U(10). The VE-cadherin expression was more evenly distributed in the G(19) than in the U(10) sample. In the U(10) film, the VE-cadherin expression was higher in a proportion of cells. This may due to the inhomogeneous distribution of certain dUBM proteins in the membrane, as observed in the immunofluorescent staining of bulk dUBM hydrogel (shown in **Chapter 3**). When podocytes were cultured on non-porous films, the podocin expression was more

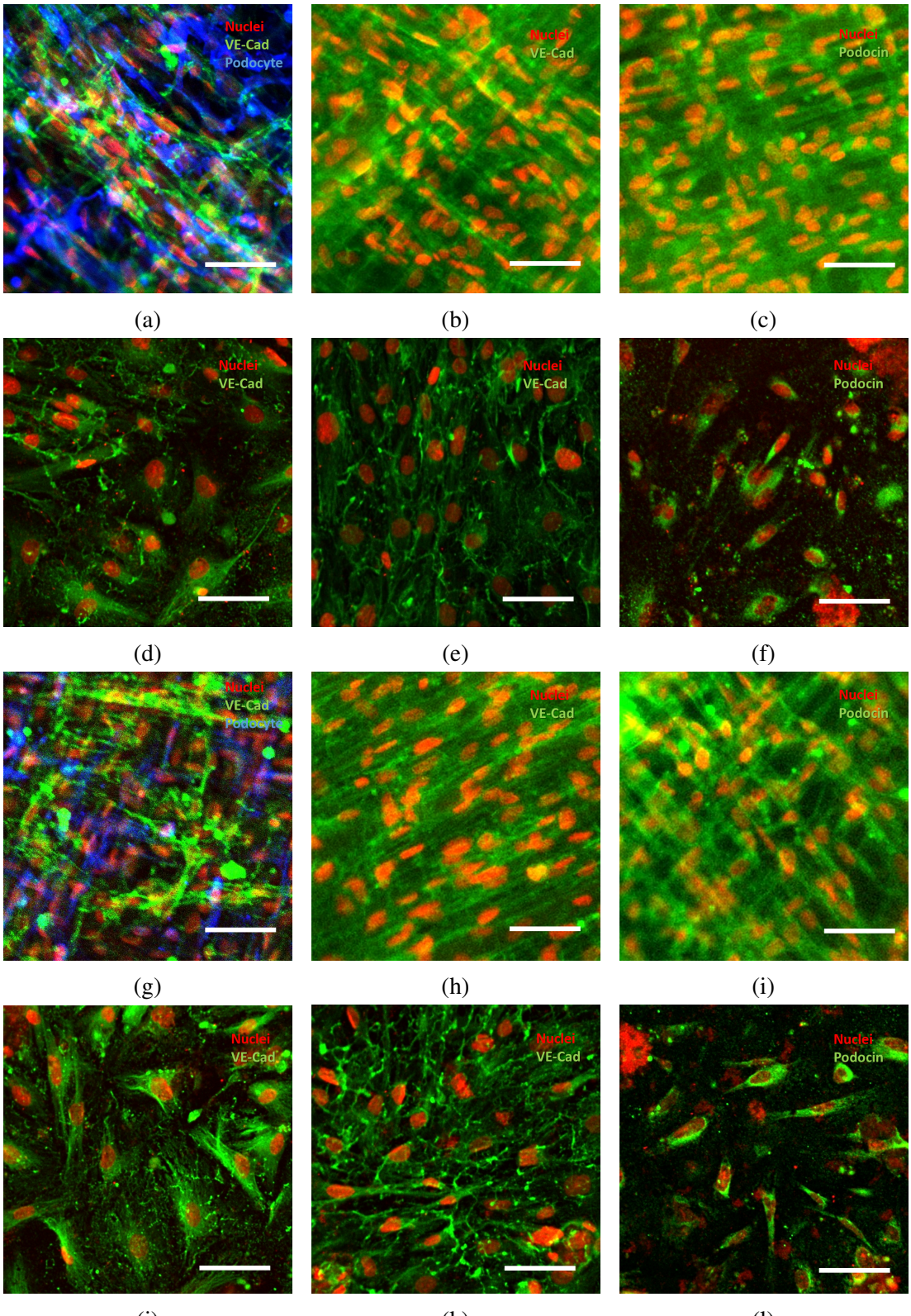

Fig. 4.12 Confocal image of GEnCs and podocytes cell culture on suspended membrane and homogeneous film configurations. Nuclei are marked in red, podocytes in blue, and cell markers in green. Suspended G(19) membrane with (a) co-culture; (b) GEnCs mono-culture; and (c) podocytes mono-culture. Homogeneous G(19) film with (d) co-culture; (e) GEnCs mono-culture; and (f) podocytes mono-culture. Suspended U(10) membrane with (g) co-culture; (h) GEnCs mono-culture; and (i) podocytes mono-culture. Homogeneous U(10) film with (j) co-culture; (k) GEnCs mono-culture; and (l) podocytes mono-culture. Scale bars 25 μm.

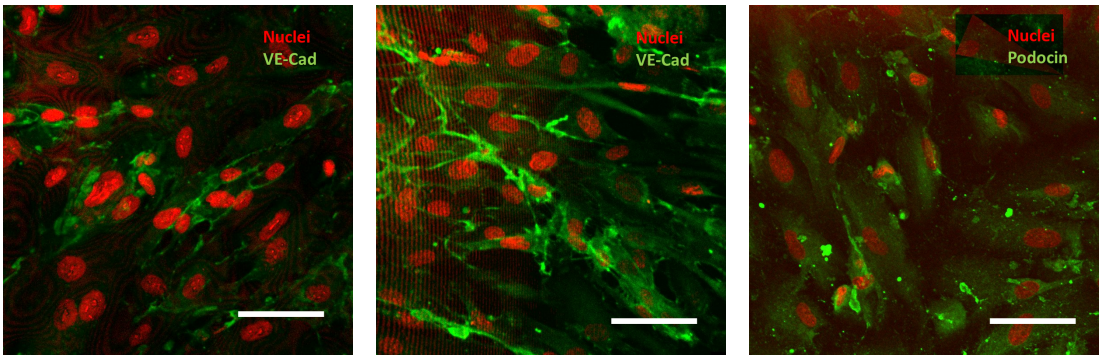

(a) (b) (c)

Fig. 4.13 Reference samples of GEnCs and podocytes cultured in well-plates. (a) Co-culture; (b) GEnCs mono-culture; and (c) Podocytes mono-culture. Scale bars 25 μm.

localised in the cell bodies than between the cells, as shown in Fig 4.12f for G(19) and Fig 4.12l for U(10). This shows that the podocytes differentiated but were less integrated than those cultured on suspended membrane.

The well-plate reference was similar to that of the co-culture, with lower overall and partially localised VE-cadherin expression, as shown in Fig 4.13b. The podocytes cultured on the well-plate references showed a low level of podocin expression, and the staining was mainly localised on the cell bodies. Fig 4.14 shows the normalised global intensity per cell measured for the suspended membrane, non-porous film and well-plates. The level of fluorescence was the highest in U(10) suspended membranes. On average, the VE-cadherin or podocin expression was higher in suspended membrane than non-porous film (structural difference), and higher in U(10) than G(19) (biochemical difference). The lowest cell marker expression was observed in the well-plate references.

In order to investigate the influence of matrix to cell phenotypes, the VE-cadherin distribution across individual GEnCs cell is measured in the mono-culture conditions and shown in Fig 4.15. For GEnCs mono-cultured on suspended fibrous membranes, the VE-cadherin expression was generally high and distributed towards the outskirts of the cell. In the film sample, VE-cadherin expression was more towards the centre of the cells. Although from the fluorescent images, one can see the VE-cadherin expression on the cell outskirts, this is not shown in the intensity measurement. This is possibly because the VE-cadherin on cell edges was distributed like dots and was discrete. When taking the average of a few cells, these signals were overcome by the more homogeneous distribution in the cell body. In the well-plate sample, the VE-cadherin expression was mainly at the outskirts of the cell.

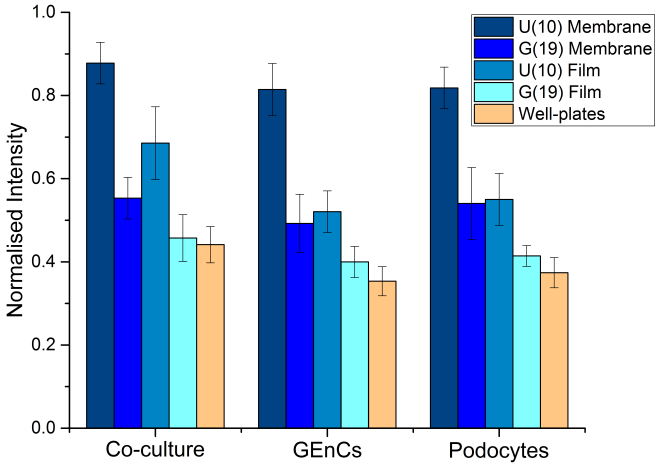

Fig. 4.14 The normalised fluorescent intensity per cell of VE-cadherin for co-culture and GEnCs mono-culture, and podocin for podocytes mono-culture. n=3, each sample contained between 50 – 60 cells.

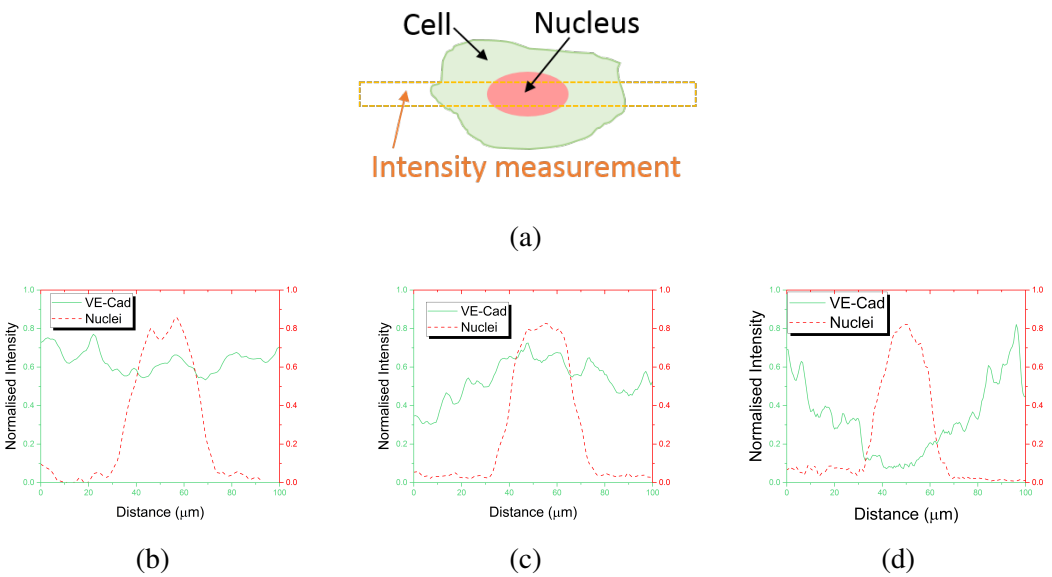

Fig. 4.15 Intensity quantification of mono-cultured GEnCs. (a) The section of intensity measurement of a single cell, with the measured fluorescent intensity shown in (b) for suspended membrane, (c) for non-porous film and (d) for well-plate. The VE-cadherin and nucleus is indicated in green and red, respectively. n=5.

4.5.4 Fibronectin expressions

Having determined the differentiated phenotypes of GEnCs and Podocytes on different substrates, I moved on to investigate the secretion of fibronectin by cells in different culturing configurations. Fibronectin is a key protein component in the ECM of a glomerulus, and is known to bind to extracellular matrix components such as collagen, fibrin, and heparan sulfate proteoglycans[290, 291]. Cell-secreted fibronectin is intensely involved in tissue repair and a number of pathologies[292, 293].

In this study, the podocytes and GEnCs were mono- and co-cultured on suspended membrane and non-porous films for both G(19) and U(10), as shown in Fig 4.16. Well-plate culture was used as a basic reference (Fig 4.17). After 7 days of differentiation, a layer of fibronectin was secreted on the suspended G(19) membrane, as shown in Fig 4.16a. The shaded elliptical areas are the nuclei. On the suspended U(10) membrane (Fig 4.16g), the fibronectin expression distribution was less homogeneous and more fibrous. In both cases, the secreted fibronectin formed a layer attached to the membrane and formed a layer over the mesh, further reducing the overall permeability of the membrane. This shows that, although the mesh size of the fabricated membrane was larger than that of the physiological basement membrane, it provided adhesion sites for the cells and promoted the secretion of ECM proteins. Furthermore, the membrane provided the physical structure while allowing crosstalk between the podocytes and GEnCs.

When the GEnCs were individually cultured on the suspended membrane, a web-like layer of fibronectin was observed. The web-like network bridged between the G(19) or U(10) fibres, as shown in Fig 4.16b for G(19) and Fig 4.16h for U(10). On the other hand, when the podocytes were individually cultured on the suspended membranes, one did not observe the formation of the fibronectin layer. Instead, the fibre structure in the membrane was observed, as shown in Fig 4.16c for G(19) and Fig 4.16i for U(10). This indicates that the podocytes did not secrete much fibronectin in this configuration. The fibronectin expression in the G(19) membrane was less than that in the U(10) membrane.

When the two cell types were co-cultured on G(19) films, fibronectin expression reflected the cell positions and intercellular junctions, as shown in Fig 4.16d for G(19) and Fig 4.16j for U(10). Interestingly, the mono-culture of podocytes on non-porous films also showed fibronectin expression, as shown in Fig 4.16f for G(19) and Fig 4.16l for U(10). The secreted fibronectin was distributed on the cells and not at the intercellular junctions. In comparison, GEnCs secreted more fibronectin at intercellular junctions, as shown in Fig 4.16e for G(19) and Fig 4.16k for U(10). The well-plate reference showed a low intensity of fibronectin secretion, as shown in Fig 4.17.

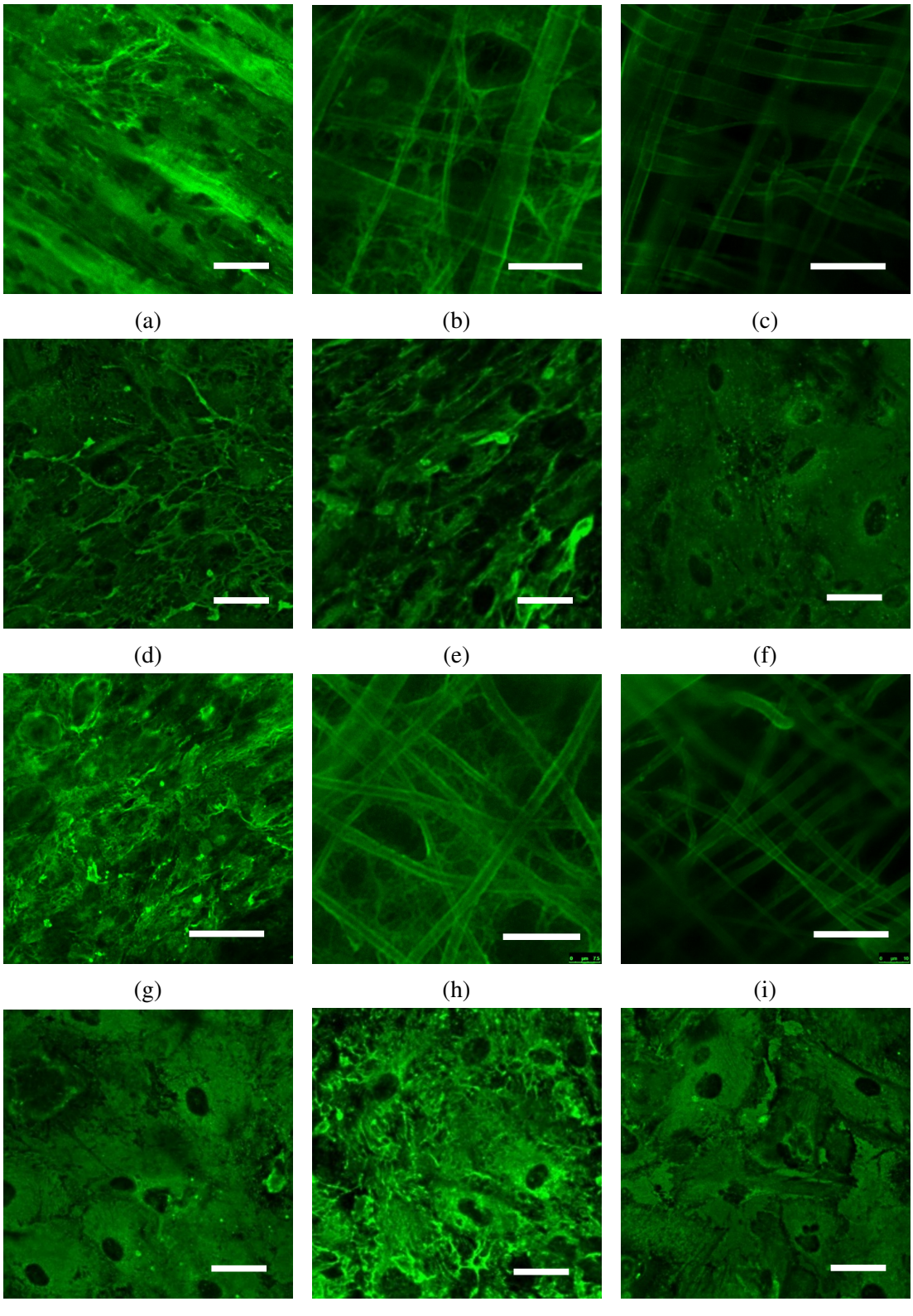

Fig. 4.16 Fibronectin expression by GEnCs and podocytes cultured on suspended membrane and homogeneous film configurations. Suspended G(19) membrane with (a) co-culture; (b) GEnCs mono-culture; and (c) podocytes mono-culture. Homogeneous G(19) film with (d) co-culture; (e) GEnCs mono-culture; and (f) podocytes mono-culture. Suspended U(10) membrane with (g) co-culture; (h) GEnCs mono-culture; and (i) podocytes mono-culture. Homogeneous U(10) film with (j) co-culture; (k) GEnCs mono-culture; and (l) podocytes mono-culture. Scale bars 25 μm.

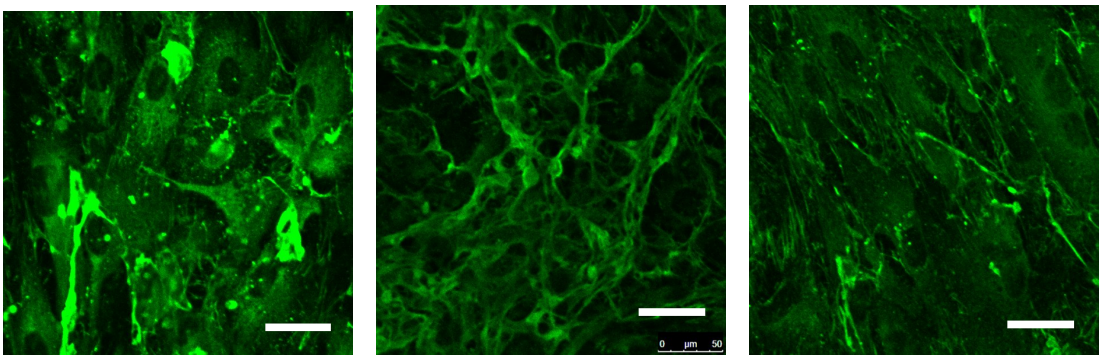

(a) (b) (c)

Fig. 4.17 Reference samples of the fibronectin expression by GEnCs and podocytes cultured in well-plates. (a) Co-culture; (b) GEnCs mono-culture; and (c) podocytes mono-culture. Scale bars 25 μm.

The normalised fibronectin intensity per unit area is shown in Fig 4.18. The highest fibronectin secretion was found in the mono-culture of GEnCs on non-porous G(19) film. The least fibronectin secretion was observed in podocytes cultured on suspended G(19) membrane. It is important to note that, due to autofluorescence of the gelatin fibres, the fibronectin intensity of podocytes cultured on suspended membranes was mainly contributed by the autofluorescence. An interesting observation is that the suspended G(19) co-culture sample induced higher fibronectin intensity than the U(10) sample, despite the original fibronectin content in the U(10) membrane. Nevertheless, the trend in this quantification is unclear. Further investigations on the secretion of other ECM proteins is required.

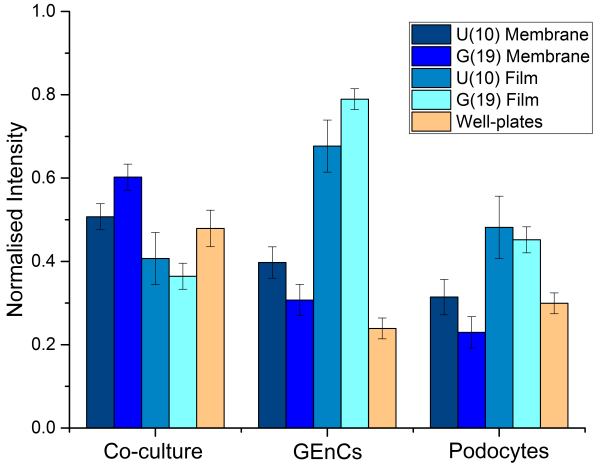

Fig. 4.18 The normalised fluorescent intensity per unit area of fibronectin for co-culture, GEnCs, and podocytes mono-culture. n=3.

4.5.5 SEM

To obtain high resolution imaging, SEM was used to visualise the cell morphology. In this study, the two cell types were co-cultured on a suspended U(10) membrane. The podocytes were seeded on the upper surface and the GEnCs were seeded on the lower surface of the membrane. The cells were allowed to differentiate at 37°C for 7 days before fixation. Fig 4.19 shows global images of the top surface (podocyte layer) obtained using SEM. Based on the topography of the patterned fibres, the cells were either aligned or randomly orientated. Despite the orientation configuration, foot process-like projection structures were observed at cell-cell junctions, as shown in Fig 4.20. Various lengths of the projections were observed, ranging from 1–3 μm to tens of micrometres when the neighbouring cell was far away. Fig 4.20d shows a gap between the podocyte cell layer and the foot process-like projections spread over the GEnCs on the other side of the membrane. This demonstrates the feasibility of direct cross-talk between the two cell types across the membrane. These projections are morphologically more similar to the *in vivo* foot processes (Fig 4.3b) than those formed on petri-dish[294]. Although this demonstrates the relatively successful differentiation of podocytes, noticeable differences were observed in the foot processes compared to those *in vivo*. In the physiology context, the foot processes of podocytes can wrap around the glomerular capillaries and pack closely, as shown in Fig 4.3b. However, the processes in this configuration cannot pack as tightly as those *in vivo*. This may be because of the organisational topography of the cells. In the physiological condition, the glomerular capillaries are vascular structures with small curvature. The diameter of capillaries can be as small as 5 μm. The podocytes wrap around the capillaries and the foot processes tightly embrace the capillary. This is different from my configuration which contains flat cell layers. Therefore, in future study, adjustment of the geometry configuration will be required.

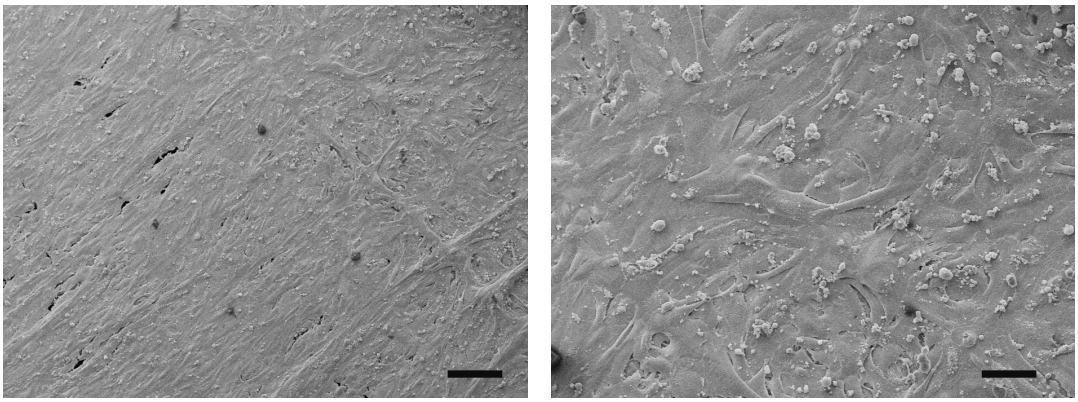

(a) (b)

Fig. 4.19 Global images of the podocyte cell layer by SEM. (a) Homogeneous cell layer covering the fibrous suspended membrane. Scale bar 150 μm; (b) Zoomed in image showing the cell morphology. Scale bar 50 μm.

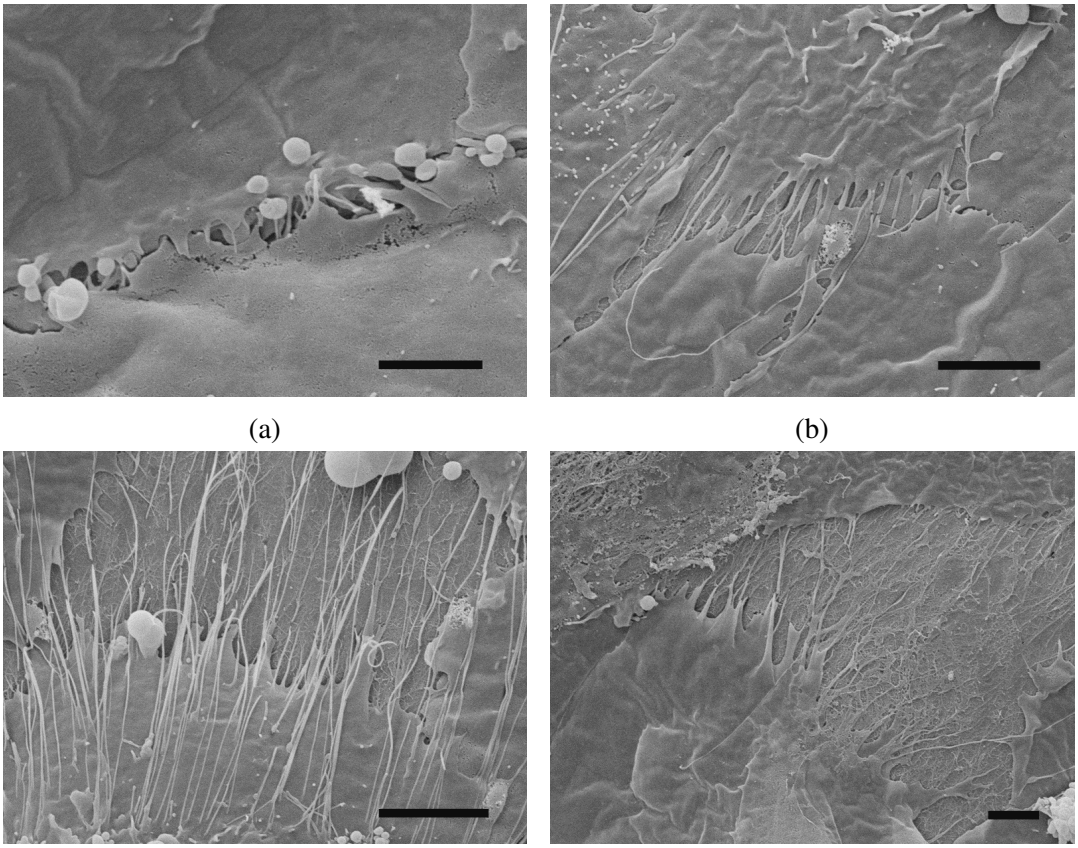

Fig. 4.20 Zoomed-in images of podocyte cells layer by SEM, showing the foot processes between cells. (a) Short foot processes with length approximately 1 μm; (b) medium foot processes with length between 1 – 5 μm; (c) long foot process-like structures with length greater than 10 μm; and (d) spreading of the foot process-like structures over the cells on the other side of the suspended membrane. Scale bars 5 μm.

4.6 Conclusion

In this chapter, I explored the application of the dUBM-laden membrane in cell culture. A cell culture platform was designed, consisting a suspended U(10) membrane on a 3D-printed PLA support. EAhy926 cells were cultured on suspended G(19) membrane with various mesh sizes. From large to small mesh size, the cell morphology changed from bi-polar (elongating along the fibres) to polygonal (forming a confluent cell layer). Both suspended G(19) and U(10) membranes could guide physiological cell differentiation. VE-cadherin and podocin were used to mark the differentiation of GEnCs and podocytes, respectively. In the co-culture condition on suspended membranes, GEnCs migrated aggregately. A homogeneous expression of VE-cadherin was observed in the mono-culture condition when GEnCs were cultured on membranes. A similar trend was observed for the podocin staining of mono-cultured podocytes on suspended membranes. When the cells were cultured on non-porous films, a reduced level of VE-cadherin in GEnCs was observed in either co-culture or mono-culture conditions. The distinct cell marker expression indicates the importance of the geometric configuration of the scaffold and the freedom of matrix remodelling. Furthermore, the distribution of fibronectin secretion was different depending on the scaffold geometry and chemical composition. On suspended G(19) membrane, a uniform layer of fibronectin was secreted in the co-culture condition. In mono-culture, GEnCs secreted fibronectin that formed a web-like network between the membrane mesh, and podocytes did not appear to actively secrete fibronectin. A similar trend was observed for U(10) membrane, except that the fibronectin distribution showed a fibrous morphology on the suspended membrane. The differentiation of podocytes was further confirmed by SEM imaging. In particular, foot process-like projections were observed between podocyte cells. However, these projections did not form tight packing like that found *in vivo*. In conclusion, it seems that the topography of the substrates plays a more predominant role in regulating cell differentiation and migration than the chemical composition. Although the advantage of incorporating dUBM components in cell culture scaffold has been discovered, the topographical design of the cell culture platform needs to be further optimised in order to closely mimic the physiological cell function.

Chapter 5

Conclusion

This thesis explains the fabrication process of a cell cultivation device integrated with dECM-laden fibrous membrane. With optimisations of the fabrication condition, I demonstrated controllable patterning of high-loading dECM microfibres using LEP.

5.1 Flexible dECM-laden microfibre patterning using LEP

High loading of dECM was patterned into microfibres using LEP. The highest dECM concentration incorporated in the solution was 9.5 wt%, which is 50 wt% in the total protein dry mass. The fibre morphology was closely related to the viscous component (loss modulus) of the solution, whilst the LEP operation was determined by the ratio between elastic and viscous components, tan(δ). With an increase in the loss modulus, G", the fibre morphology changed from discontinuous, continuous beaded to continuous uniform fibres. The storage modulus, G', increased with G", resulting a change in tan(δ). When tan(δ) was approximately 1, the drag-and-pattern LEP configuration must be used.

The low processing voltage in LEP enabled the patterning of suspended fibrous structure on complex geometries. A single step fabrication enabled the patterning of suspended dECM-laden fibres on both 3D-printed structures and microfluidic channels. This demonstrated the dECM-laden protein scaffold can be flexibly incorporated into different devices structured for other biological models. By tuning the solution property, both non-woven and woven mesh were fabricated. By modifying the patterning motion, the suspended fibrous structure could be tuned from distinct grids to a mesh membrane.

5.2 Biochemically preserved and mechanically robust fibres

The key chemical compositions in dECM were retained in the microfibre mesh. The immunofluorescent staining identified the spatial distribution of collagen IV, laminin and fibronectin in bulk hydrogel and in fibres. For all proteins, the intensity of expression increased according to the dUBM concentration. More interestingly, the protein distribution in the fibres was different depending on the type of protein. For collagen IV, the distribution was homogeneous throughout the fibres. For fibronectin, the intensity distribution was located towards the surface of all the fibres, leaving the central region dark; with increased dUBM concentrations (U(50)), the fluorescent spots were re-distributed to the surface of the fibres. For laminin, a similar trend was observed as the intensity distributed towards the fibre surface. Furthermore, laminin remained printed on the glass substrate after the fibres were removed. FTIR measurement provided comprehensive information of the molecules bonding. In particular, amide I, II and III absorptions were measured in all fibre samples. These indicate the key bonding vibrations in proteins and reflects the tertiary structure of proteins. The representative biological growth factors (VEGF and b-FGF) were also preserved.

The suspended nature of the LEP dECM-laden fibres allowed for the direct measurement of the mechanical strength of individual microfibres. Glass capillary cantilevers were used to deform the fibres and measure the corresponding force. The Young's modulus, E, of the dECM-laden fibres was higher than that of pure gelatin fibres, and can be tuned from $\sim$600 kPa to $\sim$50 MPa. For the same dECM concentration, the measured E was similar for both LEP microfibres and bulk hydrogel.

5.3 Cell differentiation and functionality on the dECM-laden membrane

Using the patterning ability of LEP, fibres with increasing spatial density were patterned on 3D structures, forming a suspended membrane. This structure was used as an easily accessible cell culture device. The cell morphology changed significantly according to different mesh size, from an elongated bi-polar to a polygonal morphology. Human GEnCs and podocytes were co-cultured on G(19) and U(10) membranes, aiming to mimic the blood-to-urine interface of a glomerulus. In the co-culture on the suspended membranes, preferential cell migration were identified by the heterogeneous VE-cadherin expression at intercellular junctions. The heterogeneity was greater in the G(19) membrane than in the U(10) membrane. Homogeneous intercellular expression of VE-cadherin and podocin was respectively observed for mono-culture of GEnCs and podocytes on membranes. The

cells appeared to be integrated into a monolayer, and the cell markers were not distinct. This can also due to the limited imaging conditions. When the cells were either co-cultured or mono-cultured on non-porous G(19) and U(10) film, both VE-cadherin and podocin expression was more located within the cells than between cells. In the well-plate reference, a low level of VE-cadherin and podocin expression was observed. The secretion of fibronectin was measured as an indicator of cell functions. In the co-culture on suspended membrane, a homogeneous layer of fibronectin was secreted, filling the mesh in the membrane. This was observed for both the G(19) and the U(10) membrane, with a more fibrous morphology in the U(10) sample. The mono-culture of podocytes on suspended membrane did not indicate secretion of fibronectin. The mono-culture of GEnCs on suspended membrane showed web-like fibronectin distribution, without forming a monolayer. When the cells were cultured on non-porous films, fibronectin was secreted at the location of cells and intercellular junctions. Therefore, both the biochemical components of dUBM and the topological cues contributed to the secretion of fibronectin and the protein distribution. In this case, the topological cues showed a more significant influence in the fibronectin distribution.

The degree of cell differentiation was further characterised using SEM imaging. In the U(10) membrane, the development of foot process-like structures was observed. This was a promising result showing that the podocytes were maturely differentiated. However, the foot processes did not form close packing as they do *in vivo*.

Chapter 6

Future work

In this study, I demonstrated a robust technique for incorporating dECM-laden microfibres into 3D-printed structures and microfabricated channels. This cell culture model can effectively promote cell adhesion, and guide cell differentiation and ECM secretion. This model can potentially be incorporated into a glomerulus-on-chip model. However, in order to best mimic the physiological microenvironment of the glomerulus *in vivo*, this model needs to be improved in the aspect of material selection. Because of the embryonic development process, the ECM components are highly organ-specific. Although the urinary bladder and the kidney are developed from the same source, the specific biochemical composition of the ECM is different in each. This small difference can potentially bring significant changes in biochemical signalling to the cells. Subsequently, the cell fate and behaviour may deviate from the *in vivo* condition. This thesis aims to demonstrate a proof-of-concept for high load dECM-laden microstructure fabrication. Hence, due to the limitations in cost and sample availability, the dECM components were obtained from the porcine urinary bladder. In future study, kidney dECM should be used to maximally replicate the biochemical composition of the glomerulus *in vivo*. In addition, quantitative analysis on cell phenotype and ECM secretion is required. This may include the measurement of the secreted protein concentrations, such as collagen IV and fibronectin. These can be compared to the *in vivo* values, to further determine the physiological relevance of the dECM-laden protein scaffold.

References

[1] "Fact sheet: new drug development process," 2013.

[2] P. Corr and D. Williams, "The pathway from idea to regulatory approval: examples for drug development," 2009.

[3] J. P. Hughes, S. S. Rees, S. B. Kalindjian, and K. L. Philpott, "Principles of early drug discovery," *British Journal of Pharmacology*, vol. 162, no. 6, pp. 1239–1249, 2011.

[4] T. Hartung, "Thoughts on limitations of animal models," *Parkinsonism and Related Disorders*, vol. 14, no. SUPPL.2, pp. 83–85, 2008.

[5] A. Terpstra, "Differences between humans and mice in efficacy of the body fat lowering effect of conjugated linoleic acid: role of metabolic rate," *The Journal of nutrition*, vol. 131, no. 7, pp. 2067–2068, 2001.

[6] S. Breslin and L. O'Driscoll, "Three-dimensional cell culture: the missing link in drug discovery," *Drug discovery today*, vol. 18, no. 5, pp. 240–249, 2013.

[7] P. Godoy, N. J. Hewitt, U. Albrecht, M. E. Andersen, N. Ansari, S. Bhattacharya, J. G. Bode, J. Bolleyn, C. Borner, J. Böttger, *et al.*, "Recent advances in 2d and 3d in vitro systems using primary hepatocytes, alternative hepatocyte sources and non-parenchymal liver cells and their use in investigating mechanisms of hepatotoxicity, cell signaling and adme," *Archives of toxicology*, vol. 87, no. 8, pp. 1315–1530, 2013.

[8] T. Sato, R. G. Vries, H. J. Snippert, M. Van de Wetering, N. Barker, D. E. Stange, J. H. Van Es, A. Abo, P. Kujala, P. J. Peters, *et al.*, "Single lgr5 stem cells build crypt villus structures in vitro without a mesenchymal niche," *Nature*, vol. 459, no. 7244, pp. 262–265, 2009.

[9] D. Huh, B. D. Matthews, A. Mammoto, M. Montoya-Zavala, H. Y. Hsin, and D. E. Ingber, "Reconstituting organ-level lung functions on a chip.," *Science (New York, N.Y.)*, vol. 328, no. 5986, pp. 1662–8, 2010.

[10] C. Frantz, K. M. Stewart, and V. M. Weaver, "The extracellular matrix at a glance," *J Cell Sci*, vol. 123, no. 24, pp. 4195–4200, 2010.

[11] B. N. Brown and S. F. Badylak, "Extracellular matrix as an inductive scaffold for functional tissue reconstruction," *Translational Research*, vol. 163, no. 4, pp. 268–285, 2014.

[12] K. R. Johnson, J. L. Leight, and V. M. Weaver, "Demystifying the effects of a three-dimensional microenvironment in tissue morphogenesis," *Methods in cell biology*, vol. 83, pp. 547–583, 2007.

[13] F. Guilak, D. M. Cohen, B. T. Estes, J. M. Gimble, W. Liedtke, and C. S. Chen, "Control of stem cell fate by physical interactions with the extracellular matrix," *Cell stem cell*, vol. 5, no. 1, pp. 17–26, 2009.

[14] S. P. Grogan, X. Chen, S. Sovani, N. Taniguchi, C. W. Colwell Jr, M. K. Lotz, and D. D. D'Lima, "Influence of cartilage extracellular matrix molecules on cell phenotype and neocartilage formation," *Tissue Engineering Part A*, vol. 20, no. 1-2, pp. 264–274, 2013.

[15] J. A. Madri and S. K. Williams, "Capillary endothelial cell cultures: phenotypic modulation by matrix components.," *The Journal of cell biology*, vol. 97, no. 1, pp. 153–165, 1983.

[16] C. Streuli, "Extracellular matrix remodelling and cellular differentiation," *Current Opinion in Cell Biology*, vol. 11, no. 5, pp. 634–640, 1999.

[17] K. K. Parker and D. E. Ingber, "Extracellular matrix, mechanotransduction and structural hierarchies in heart tissue engineering," *Philosophical Transactions of the Royal Society of London B: Biological Sciences*, vol. 362, no. 1484, pp. 1267–1279, 2007.

[18] M. M. Stevens and J. H. George, "Exploring and engineering the cell surface interface," *Science*, vol. 310, no. 5751, pp. 1135–1138, 2005.

[19] V. Z. Beachley, M. T. Wolf, K. Sadtler, S. S. Manda, H. Jacobs, M. R. Blatchley, J. S. Bader, A. Pandey, D. Pardoll, and J. H. Elisseeff, "Tissue matrix arrays for high-throughput screening and systems analysis of cell function," *Nature methods*, 2015.

[20] R. Mecham, *The Extracellular Matrix: an Overview*. Biology of Extracellular Matrix, Springer Berlin Heidelberg, 2011.

[21] E. D. Hay, *Cell biology of extracellular matrix*. Springer Science & Business Media, 2013.

[22] E. L. Gill, Y. Yan, and S. Huang, "Hybridised Biofabrication- Biomimetic Structures of Extracellular Matrices and Soft Tissues via Cell and Biomaterial Printing," pp. 1–34, 2016.

[23] D. Heinegård, A. Björne-Persson, L. Cöster, A. Franzen, S. Gardell, A. Malmström, M. Paulsson, R. Sandfalk, and K. Vogel, "The core proteins of large and small interstitial proteoglycans from various connective tissues form distinct subgroups," *Biochemical Journal*, vol. 230, no. 1, pp. 181–194, 1985.

[24] M. Lutolf and J. Hubbell, "Synthetic biomaterials as instructive extracellular microenvironments for morphogenesis in tissue engineering," *Nature biotechnology*, vol. 23, no. 1, pp. 47–55, 2005.

[25] N. Boudreau, C. J. Sympson, Z. Werb, and M. J. Bissell, "Suppression of ice and apoptosis in mammary epithelial cells by extracellular matrix," *Science (New York, NY)*, vol. 267, no. 5199, p. 891, 1995.

[26] R. O. Hynes, "The extracellular matrix: not just pretty fibrils," *Science*, vol. 326, no. 5957, pp. 1216–1219, 2009.

[27] K. K. Parker, A. L. Brock, C. Brangwynne, R. J. Mannix, N. Wang, E. Ostuni, N. A. Geisse, J. C. Adams, G. M. Whitesides, and D. E. Ingber, "Directional control of lamellipodia extension by constraining cell shape and orienting cell tractional forces," *The FASEB Journal*, vol. 16, no. 10, pp. 1195–1204, 2002.

[28] D. E. Discher, D. J. Mooney, and P. W. Zandstra, "Growth factors, matrices, and forces combine and control stem cells," *Science*, vol. 324, no. 5935, pp. 1673–1677, 2009.

[29] B. Geiger, J. P. Spatz, and A. D. Bershadsky, "Environmental sensing through focal adhesions.," *Nature reviews. Molecular cell biology*, vol. 10, no. 1, pp. 21–33, 2009.

[30] S. M. Albelda and C. A. Buck, "Integrins and other cell adhesion molecules.," *The FASEB Journal*, vol. 4, no. 11, pp. 2868–2880, 1990.

[31] T. M. Carlos and J. M. Harlan, "Leukocyte-endothelial adhesion molecules," *Blood*, vol. 84, no. 7, pp. 2068–2101, 1994.

[32] E. Zamir and B. Geiger, "Molecular complexity and dynamics of cell-matrix adhesions," *Journal of cell science*, vol. 114, no. 20, pp. 3583–3590, 2001.

[33] A. Brock, E. Chang, C.-C. Ho, P. LeDuc, X. Jiang, G. M. Whitesides, and D. E. Ingber, "Geometric determinants of directional cell motility revealed using microcontact printing," *Langmuir*, vol. 19, no. 5, pp. 1611–1617, 2003.

[34] A. J. Engler, S. Sen, H. L. Sweeney, and D. E. Discher, "Matrix elasticity directs stem cell lineage specification," *Cell*, vol. 126, no. 4, pp. 677–689, 2006.

[35] A. Elosegui-Artola, R. Oria, Y. Chen, A. Kosmalska, C. Pérez-González, N. Castro, C. Zhu, X. Trepat, and P. Roca-Cusachs, "Mechanical regulation of a molecular clutch defines force transmission and transduction in response to matrix rigidity," *Nature cell biology*, vol. 18, no. 5, pp. 540–548, 2016.

[36] M. Schvartzman, M. Palma, J. Sable, J. Abramson, X. Hu, M. P. Sheetz, and S. J. Wind, "Nanolithographic control of the spatial organization of cellular adhesion receptors at the single-molecule level," *Nano letters*, vol. 11, no. 3, pp. 1306–1312, 2011.

[37] X. Yang and H. Wang, *Electrospun functional nanofibrous scaffolds for tissue engineering*. INTECH Open Access Publisher, 2010.

[38] T. W. Gilbert, T. L. Sellaro, and S. F. Badylak, "Decellularization of tissues and organs," *Biomaterials*, vol. 27, pp. 3675–3683, 2006.

[39] S. F. Badylak, "Xenogeneic extracellular matrix as a scaffold for tissue reconstruction," *Transplant Immunology*, vol. 12, no. 3-4, pp. 367–377, 2004.

[40] A. Folch and M. Toner, "Microengineering of cellular interactions.," *Annual review of biomedical engineering*, vol. 2, pp. 227–56, 2000.

[41] G. M. Whitesides, E. Ostuni, S. Takayama, X. Jiang, and D. E. Ingber, "Soft lithography in biology and biochemistry," *Annual review of biomedical engineering*, vol. 3, no. 1, pp. 335–373, 2001.

[42] E. R. Shamir and A. J. Ewald, "Three-dimensional organotypic culture: experimental models of mammalian biology and disease," *Nature reviews Molecular cell biology*, vol. 15, no. 10, pp. 647–664, 2014.

[43] T. D. Brown, P. D. Dalton, and D. W. Hutmacher, "Direct writing by way of melt electrospinning," *Advanced Materials*, vol. 23, no. 47, pp. 5651–5657, 2011.

[44] W. S. Khan, R. Asmatulu, M. Ceylan, and A. Jabbarnia, "Recent progress on conventional and non-conventional electrospinning processes," *Fibers and Polymers*, vol. 14, no. 8, pp. 1235–1247, 2013.

[45] X. Li, Z. Li, L. Wang, G. Ma, F. Meng, R. H. Pritchard, E. L. Gill, Y. Liu, and Y. Y. S. Huang, "Low-voltage continuous electrospinning patterning," *ACS Applied Materials & Interfaces*, vol. 8, no. 47, pp. 32120–32131, 2016.

[46] C. Vieu, F. Carcenac, A. Pepin, Y. Chen, M. Mejias, A. Lebib, L. Manin-Ferlazzo, L. Couraud, and H. Launois, "Electron beam lithography: resolution limits and applications," *Applied Surface Science*, vol. 164, no. 1, pp. 111–117, 2000.

[47] C. Mandrycky, Z. Wang, K. Kim, and D. H. Kim, "3D bioprinting for engineering complex tissues," *Biotechnology Advances*, vol. 34, no. 4, pp. 422–434, 2016.

[48] M. Théry, "Micropatterning as a tool to decipher cell morphogenesis and functions," *J Cell Sci*, vol. 123, no. 24, pp. 4201–4213, 2010.

[49] V. Melissinaki, A. Gill, I. Ortega, M. Vamvakaki, A. Ranella, J. Haycock, C. Fotakis, M. Farsari, and F. Claeyssens, "Direct laser writing of 3d scaffolds for neural tissue engineering applications," *Biofabrication*, vol. 3, no. 4, p. 045005, 2011.

[50] L. E. Bertassoni, M. Cecconi, V. Manoharan, M. Nikkhah, J. Hjortnaes, A. L. Cristino, G. Barabaschi, D. Demarchi, M. R. Dokmeci, Y. Yang, *et al.*, "Hydrogel bioprinted microchannel networks for vascularization of tissue engineering constructs," *Lab on a Chip*, vol. 14, no. 13, pp. 2202–2211, 2014.

[51] S. M. Ehsan, K. M. Welch-Reardon, M. L. Waterman, C. C. Hughes, and S. C. George, "A three-dimensional in vitro model of tumor cell intravasation," *Integrative Biology*, vol. 6, no. 6, pp. 603–610, 2014.

[52] F. Marga, K. Jakab, C. Khatiwala, B. Shepherd, S. Dorfman, B. Hubbard, S. Colbert, and F. Gabor, "Toward engineering functional organ modules by additive manufacturing.," *Biofabrication*, vol. 4, no. 2, p. 022001, 2012.

[53] D. B. Kolesky, R. L. Truby, a. S. Gladman, T. a. Busbee, K. a. Homan, and J. a. Lewis, "3D Bioprinting of Vascularized, Heterogeneous Cell-Laden Tissue Constructs," *Advanced Materials*, pp. n/a–n/a, feb 2014.

[54] K. Markstedt, A. Mantas, I. Tournier, H. Martinez Avila, D. Hagg, and P. Gatenholm, "3d bioprinting human chondrocytes with nanocellulose–alginate bioink for cartilage tissue engineering applications," *Biomacromolecules*, vol. 16, no. 5, pp. 1489–1496, 2015.

[55] T. Billiet, E. Gevaert, T. De Schryver, M. Cornelissen, and P. Dubruel, "The 3d printing of gelatin methacrylamide cell-laden tissue-engineered constructs with high cell viability," *Biomaterials*, vol. 35, no. 1, pp. 49–62, 2014.

[56] F. Pati, J. Jang, D.-H. Ha, S. Won Kim, J.-W. Rhie, J.-H. Shim, D.-H. Kim, and D.-W. Cho, "Printing three-dimensional tissue analogues with decellularized extracellular matrix bioink.," *Nature communications*, vol. 5, p. 3935, 2014.

[57] R. Levato, J. Visser, J. A. Planell, E. Engel, J. Malda, and M. A. Mateos-Timoneda, "Biofabrication of tissue constructs by 3d bioprinting of cell-laden microcarriers," *Biofabrication*, vol. 6, no. 3, p. 035020, 2014.

[58] C. Norotte, F. S. Marga, L. E. Niklason, and G. Forgacs, "Scaffold-free vascular tissue engineering using bioprinting," *Biomaterials*, vol. 30, no. 30, pp. 5910–5917, 2009.

[59] Y. Xia and G. M. Whitesides, "Soft lithography," *Annual review of materials science*, vol. 28, no. 1, pp. 153–184, 1998.

[60] D. Qin, Y. Xia, and G. M. Whitesides, "Soft lithography for micro- and nanoscale patterning.," *Nature protocols*, vol. 5, no. 3, pp. 491–502, 2010.

[61] D. J. Lipomi, R. V. Martinez, L. Cademartiri, and G. M. Whitesides, *Soft Lithographic Approaches to Nanofabrication*, vol. 7. Elsevier B.V., 2012.

[62] A. Agarwal, J. A. Goss, A. Cho, M. L. McCain, and K. K. Parker, "Microfluidic heart on a chip for higher throughput pharmacological studies," *Lab Chip*, vol. 13, no. 18, pp. 3599–3608, 2013.

[63] G. M. Whitesides, "The origins and the future of microfluidics.," *Nature*, vol. 442, no. 7101, pp. 368–73, 2006.

[64] T. M. Squires and S. R. Quake, "Microfluidics: Fluid physics at the nanoliter scale," *Reviews of modern physics*, vol. 77, no. 3, p. 977, 2005.

[65] H. A. Stone, A. D. Stroock, and A. Ajdari, "Engineering flows in small devices: microfluidics toward a lab-on-a-chip," *Annu. Rev. Fluid Mech.*, vol. 36, pp. 381–411, 2004.

[66] S. N. Bhatia and D. E. Ingber, "Microfluidic organs-on-chips," *Nature Biotechnology*, vol. 32, no. 8, pp. 760–772, 2014.

[67] M. Baker, "Tissue models: a living system on a chip," *Nature*, vol. 471, no. 7340, pp. 661–665, 2011.

[68] Y. Nakao, H. Kimura, Y. Sakai, and T. Fujii, "Bile canaliculi formation by aligning rat primary hepatocytes in a microfluidic device," *Biomicrofluidics*, vol. 5, no. 2, pp. 1–7, 2011.

[69] J. Kim, M. Hegde, and A. Jayaraman, "Co-culture of epithelial cells and bacteria for investigating host–pathogen interactions," *Lab on a Chip*, vol. 10, no. 1, pp. 43–50, 2010.

[70] K.-J. Jang, A. P. Mehr, G. a. Hamilton, L. a. McPartlin, S. Chung, K.-Y. Suh, and D. E. Ingber, "Human kidney proximal tubule-on-a-chip for drug transport and nephrotoxicity assessment.," *Integrative biology : quantitative biosciences from nano to macro*, vol. 5, no. 9, pp. 1119–29, 2013.

[71] Y. Berdichevsky, "Building and manipulating neural pathways with microfluidics," *Computer*, vol. 144, no. 5, pp. 724–732, 2010.

[72] E. W. Esch, A. Bahinski, and D. Huh, "Organs-on-chips at the frontiers of drug discovery.," *Nature reviews. Drug discovery*, vol. 14, no. 4, pp. 248–260, 2015.

[73] M. Zhou, X. Zhang, X. Wen, T. Wu, W. Wang, M. Yang, J. Wang, M. Fang, B. Lin, and H. Lin, "Development of a Functional Glomerulus at the Organ Level on a Chip to Mimic Hypertensive Nephropathy," *Scientific Reports*, vol. 6, no. 457, p. 31771, 2016.

[74] R. Baudoin, L. Griscom, M. Monge, C. Legallais, and E. Leclerc, "Development of a renal microchip for in vitro distal tubule models," *Biotechnology Progress*, vol. 23, no. 5, pp. 1245–1253, 2007.

[75] C. Ramello, P. Paullier, A. Ould-Dris, M. Monge, C. Legallais, and E. Leclerc, "Investigation into modification of mass transfer kinetics by acrolein in a renal biochip," *Toxicology in Vitro*, vol. 25, no. 5, pp. 1123–1131, 2011.

[76] N. Ferrell, R. R. Desai, A. J. Fleischman, S. Roy, H. D. Humes, and W. H. Fissell, "A microfluidic bioreactor with integrated transepithelial electrical resistance (teer) measurement electrodes for evaluation of renal epithelial cells," *Biotechnology and bioengineering*, vol. 107, no. 4, pp. 707–716, 2010.

[77] K.-J. Jang and K.-Y. Suh, "A multi-layer microfluidic device for efficient culture and analysis of renal tubular cells," *Lab on a Chip*, vol. 10, no. 1, pp. 36–42, 2010.

[78] K.-J. Jang, H. S. Cho, W. G. Bae, T.-H. Kwon, K.-Y. Suh, *et al.*, "Fluid-shear-stress-induced translocation of aquaporin-2 and reorganization of actin cytoskeleton in renal tubular epithelial cells," *Integrative Biology*, vol. 3, no. 2, pp. 134–141, 2011.

[79] S. M. Park and D. S. Kim, "Electrolyte-assisted electrospinning for a self-assembled, free-standing nanofiber membrane on a curved surface," *Advanced Materials*, vol. 27, no. 10, pp. 1682–1687, 2015.

[80] B. Zhang, M. Montgomery, M. D. Chamberlain, S. Ogawa, A. Korolj, A. Pahnke, L. A. Wells, S. Massé, J. Kim, L. Reis, A. Momen, S. S. Nunes, A. R. Wheeler, K. Nanthakumar, G. Keller, M. V. Sefton, and M. Radisic, "Biodegradable scaffold with built-in vasculature for organ-on-a-chip engineering and direct surgical anastomosis," *Nature Materials*, vol. 1, no. March, pp. 1–42, 2016.

[81] J. D. Schiffman and C. L. Schauer, "A Review: Electrospinning of Biopolymer Nanofibers and their Applications," *Polymer Reviews*, vol. 48, no. August, pp. 317–352, 2008.

[82] F. Anton, "Process and apparatus for preparing artificial threads," Oct. 2 1934. US Patent 1,975,504.

[83] G. Taylor, "Disintegration of water drops in an electric field," in *Proceedings of the Royal Society of London A: Mathematical, Physical and Engineering Sciences*, vol. 280, pp. 383–397, The Royal Society, 1964.

[84] S. Agarwal, J. H. Wendorff, and A. Greiner, "Use of electrospinning technique for biomedical applications," *Polymer*, vol. 49, no. 26, pp. 5603–5621, 2008.

[85] D. Li and Y. Xia, "Electrospinning of nanofibers: reinventing the wheel?," *Advanced materials*, vol. 16, no. 14, pp. 1151–1170, 2004.

[86] T. Subbiah, G. S. Bhat, R. W. Tock, S. Parameswaran, and S. S. Ramkumar, "Electrospinning of Nanofibers," 2004.

[87] D. H. Reneker, A. L. Yarin, H. Fong, and S. Koombhongse, "Bending instability of electrically charged liquid jets of polymer solutions in electrospinning," *Journal of Applied physics*, vol. 87, no. 9, pp. 4531–4547, 2000.

[88] C. Luo, S. D. Stoyanov, E. Stride, E. Pelan, and M. Edirisinghe, "Electrospinning versus fibre production methods: from specifics to technological convergence," *Chemical Society Reviews*, vol. 41, no. 13, pp. 4708–4735, 2012.

[89] Z. M. Huang, Y. Z. Zhang, M. Kotaki, and S. Ramakrishna, "A review on polymer nanofibers by electrospinning and their applications in nanocomposites," *Composites Science and Technology*, 2003.

[90] M. Bognitzki, W. Czado, T. Frese, A. Schaper, M. Hellwig, M. Steinhart, A. Greiner, J. H. Wendorff, *et al.*, "Nanostructured fibers via electrospinning," *Advanced Materials*, vol. 13, no. 1, pp. 70–72, 2001.

[91] E. Kang, Y. Y. Choi, S. K. Chae, J. H. Moon, J. Y. Chang, and S. H. Lee, "Microfluidic spinning of flat alginate fibers with grooves for cell-aligning scaffolds," *Advanced Materials*, vol. 24, no. 31, pp. 4271–4277, 2012.

[92] L. Leng, A. McAllister, B. Zhang, M. Radisic, and A. Günther, "Mosaic hydrogels: one-step formation of multiscale soft materials," *Advanced materials*, vol. 24, no. 27, pp. 3650–3658, 2012.

[93] V. Milleret, B. Simona, P. Neuenschwander, and H. Hall, "Tuning electrospinning parameters for production of 3d-fiber-fleeces with increased porosity for soft tissue engineering applications," *Eur Cell Mater*, vol. 21, pp. 286–303, 2011.

[94] G. Yan, J. Yu, Y. Qiu, X. Yi, J. Lu, X. Zhou, and X. Bai, "Self-assembly of electrospun polymer nanofibers: A general phenomenon generating honeycomb-patterned nanofibrous structures," *Langmuir*, vol. 27, no. 8, pp. 4285–4289, 2011.

[95] D. Li, Y. Wang, and Y. Xia, "Electrospinning nanofibers as uniaxially aligned arrays and layer-by-layer stacked films," *Advanced Materials*, vol. 16, no. 4, pp. 361–366, 2004.

[96] S. H. Park, T. G. Kim, H. C. Kim, D.-Y. Yang, and T. G. Park, "Development of dual scale scaffolds via direct polymer melt deposition and electrospinning for applications in tissue regeneration," *Acta Biomaterialia*, vol. 4, no. 5, pp. 1198–1207, 2008.

[97] P. Gupta, C. Elkins, T. E. Long, and G. L. Wilkes, "Electrospinning of linear homopolymers of poly(methyl methacrylate): Exploring relationships between fiber formation, viscosity, molecular weight and concentration in a good solvent," *Polymer*, vol. 46, no. 13, pp. 4799–4810, 2005.

[98] J. H. Yu, S. V. Fridrikh, G. C. Rutledge, *et al.*, "The role of elasticity in the formation of electrospun fibers," *Polymer*, vol. 47, no. 13, pp. 4789–4797, 2006.

[99] H. Fong, I. Chun, and D. Reneker, "Beaded nanofibers formed during electrospinning," *Polymer*, vol. 40, no. 16, pp. 4585–4592, 1999.

[100] I. S. Chronakis, S. Grapenson, and A. Jakob, "Conductive polypyrrole nanofibers via electrospinning: electrical and morphological properties," *Polymer*, vol. 47, no. 5, pp. 1597–1603, 2006.

[101] Y. Wu, L. A. Carnell, and R. L. Clark, "Control of electrospun mat width through the use of parallel auxiliary electrodes," *Polymer*, vol. 48, no. 19, pp. 5653–5661, 2007.

[102] D. Yang, B. Lu, Y. Zhao, and X. Jiang, "Fabrication of aligned fibrous arrays by magnetic electrospinning," *Advanced Materials*, vol. 19, no. 21, pp. 3702–3706, 2007.

[103] D. H. Reneker and I. Chun, "Nanometre diameter fibres of polymer, produced by electrospinning," *Nanotechnology*, vol. 7, no. 3, pp. 216–223, 1996.

[104] S. Megelski, J. S. Stephens, D. B. Chase, and J. F. Rabolt, "Micro-and nanostructured surface morphology on electrospun polymer fibers," *Macromolecules*, vol. 35, no. 22, pp. 8456–8466, 2002.

[105] S. De Vrieze, T. Van Camp, A. Nelvig, B. Hagström, P. Westbroek, and K. De Clerck, "The effect of temperature and humidity on electrospinning," *Journal of materials science*, vol. 44, no. 5, p. 1357, 2009.

[106] C. L. Casper, J. S. Stephens, N. G. Tassi, D. B. Chase, and J. F. Rabolt, "Controlling surface morphology of electrospun polystyrene fibers: effect of humidity and molecular weight in the electrospinning process," *Macromolecules*, vol. 37, no. 2, pp. 573–578, 2004.

[107] M. J. McClure, P. S. Wolfe, D. G. Simpson, S. A. Sell, and G. L. Bowlin, "The use of air-flow impedance to control fiber deposition patterns during electrospinning," *Biomaterials*, vol. 33, no. 3, pp. 771–779, 2012.

[108] J. A. Matthews, G. E. Wnek, D. G. Simpson, and G. L. Bowlin, "Electrospinning of collagen nanofibers," *Biomacromolecules*, vol. 3, no. 2, pp. 232–238, 2002.

[109] P. Katta, M. Alessandro, R. Ramsier, and G. Chase, "Continuous electrospinning of aligned polymer nanofibers onto a wire drum collector," *Nano letters*, vol. 4, no. 11, pp. 2215–2218, 2004.

[110] H. R. Pant, M. P. Neupane, B. Pant, G. Panthi, H.-J. Oh, M. H. Lee, and H. Y. Kim, "Fabrication of highly porous poly (-caprolactone) fibers for novel tissue scaffold via water-bath electrospinning," *Colloids and Surfaces B: Biointerfaces*, vol. 88, no. 2, pp. 587–592, 2011.

[111] B. Sun, Y. Long, H. Zhang, M. Li, J. Duvail, X. Jiang, and H. Yin, "Advances in three-dimensional nanofibrous macrostructures via electrospinning," *Progress in Polymer Science*, vol. 39, no. 5, pp. 862–890, 2014.

[112] H. Okuzaki, T. Takahashi, N. Miyajima, Y. Suzuki, and T. Kuwabara, "Spontaneous formation of poly (p-phenylenevinylene) nanofiber yarns through electrospinning of a precursor," *Macromolecules*, vol. 39, no. 13, pp. 4276–4278, 2006.

[113] B. Sun, Y.-Z. Long, F. Yu, M.-M. Li, H.-D. Zhang, W.-J. Li, and T.-X. Xu, "Self-assembly of a three-dimensional fibrous polymer sponge by electrospinning," *Nanoscale*, vol. 4, no. 6, pp. 2134–2137, 2012.

[114] T. J. Sill and H. A. V. Recum, "Electrospinning : Applications in drug delivery and tissue engineering," vol. 29, 2008.

[115] J. Stitzel, J. Liu, S. J. Lee, M. Komura, J. Berry, S. Soker, G. Lim, M. Van Dyke, R. Czerw, J. J. Yoo, *et al.*, "Controlled fabrication of a biological vascular substitute," *Biomaterials*, vol. 27, no. 7, pp. 1088–1094, 2006.

[116] C. Xu, R. Inai, M. Kotaki, and S. Ramakrishna, "Aligned biodegradable nanofibrous structure: a potential scaffold for blood vessel engineering," *Biomaterials*, vol. 25, no. 5, pp. 877–886, 2004.

[117] V. Thomas, M. V. Jose, S. Chowdhury, J. F. Sullivan, D. R. Dean, and Y. K. Vohra, "Mechano-morphological studies of aligned nanofibrous scaffolds of polycaprolactone fabricated by electrospinning," *Journal of Biomaterials Science, Polymer Edition*, vol. 17, no. 9, pp. 969–984, 2006.

[118] E. Schnell, K. Klinkhammer, S. Balzer, G. Brook, D. Klee, P. Dalton, and J. Mey, "Guidance of glial cell migration and axonal growth on electrospun nanofibers of poly-ε-caprolactone and a collagen/poly-ε-caprolactone blend," *Biomaterials*, vol. 28, no. 19, pp. 3012–3025, 2007.

[119] F. Yang, R. Murugan, S. Wang, and S. Ramakrishna, "Electrospinning of nano/micro scale poly (l-lactic acid) aligned fibers and their potential in neural tissue engineering," *Biomaterials*, vol. 26, no. 15, pp. 2603–2610, 2005.

[120] S. Sahoo, H. Ouyang, J. C.-H. Goh, T. Tay, and S. Toh, "Characterization of a novel polymeric scaffold for potential application in tendon/ligament tissue engineering," *Tissue engineering*, vol. 12, no. 1, pp. 91–99, 2006.

[121] S. J. Lee, J. J. Yoo, G. J. Lim, A. Atala, and J. Stitzel, "In vitro evaluation of electrospun nanofiber scaffolds for vascular graft application," *Journal of biomedical materials research Part A*, vol. 83, no. 4, pp. 999–1008, 2007.

[122] H. Inoguchi, I. K. Kwon, E. Inoue, K. Takamizawa, Y. Maehara, and T. Matsuda, "Mechanical responses of a compliant electrospun poly (l-lactide-co-ε-caprolactone) small-diameter vascular graft," *Biomaterials*, vol. 27, no. 8, pp. 1470–1478, 2006.

[123] A. Schneider, X. Wang, D. Kaplan, J. Garlick, and C. Egles, "Biofunctionalized electrospun silk mats as a topical bioactive dressing for accelerated wound healing," *Acta Biomaterialia*, vol. 5, no. 7, pp. 2570–2578, 2009.

[124] S. G. Kumbar, S. P. Nukavarapu, R. James, L. S. Nair, and C. T. Laurencin, "Electrospun poly (lactic acid-co-glycolic acid) scaffolds for skin tissue engineering," *Biomaterials*, vol. 29, no. 30, pp. 4100–4107, 2008.

[125] H. Yoshimoto, Y. M. Shin, H. Terai, and J. P. Vacanti, "A biodegradable nanofiber scaffold by electrospinning and its potential for bone tissue engineering," *Biomaterials*, vol. 24, no. 12, pp. 2077–2082, 2003.

[126] T. G. Kim and T. G. Park, "Biomimicking extracellular matrix: cell adhesive rgd peptide modified electrospun poly (d, l-lactic-co-glycolic acid) nanofiber mesh," *Tissue engineering*, vol. 12, no. 2, pp. 221–233, 2006.

[127] W. Wang, S. Itoh, K. Konno, T. Kikkawa, S. Ichinose, K. Sakai, T. Ohkuma, and K. Watabe, "Effects of schwann cell alignment along the oriented electrospun chitosan nanofibers on nerve regeneration," *Journal of Biomedical Materials Research Part A*, vol. 91, no. 4, pp. 994–1005, 2009.

[128] G. T. Christopherson, H. Song, and H.-Q. Mao, "The influence of fiber diameter of electrospun substrates on neural stem cell differentiation and proliferation," *Biomaterials*, vol. 30, no. 4, pp. 556–564, 2009.

[129] B. Carlberg, M. Z. Axell, U. Nannmark, J. Liu, and H. G. Kuhn, "Electrospun polyurethane scaffolds for proliferation and neuronal differentiation of human embryonic stem cells.," *Biomedical materials*, vol. 4, no. 4, p. 045004, 2009.

[130] Z. M. Huang, Y. Z. Zhang, S. Ramakrishna, and C. T. Lim, "Electrospinning and mechanical characterization of gelatin nanofibers," *Polymer*, vol. 45, no. 15, pp. 5361–5368, 2004.

[131] S. Zarkoob, D. H. Reneker, D. Ertley, R. Eby, and S. D. Hudson, "Synthetically spun silk nanofibers and a process for making the same," Aug. 29 2000. US Patent 6,110,590.

[132] Z. Chen, X. Mo, and F. Qing, "Electrospinning of collagen–chitosan complex," *Materials Letters*, vol. 61, no. 16, pp. 3490–3494, 2007.

[133] D. I. Zeugolis, S. T. Khew, E. S. Yew, A. K. Ekaputra, Y. W. Tong, L.-Y. L. Yung, D. W. Hutmacher, C. Sheppard, and M. Raghunath, "Electro-spinning of pure collagen nano-fibres–just an expensive way to make gelatin?," *Biomaterials*, vol. 29, no. 15, pp. 2293–2305, 2008.

[134] D. Sun, C. Chang, S. Li, and L. Lin, "Near-field electrospinning," *Nano Letters*, 2006.

[135] G. S. Bisht, G. Canton, A. Mirsepassi, L. Kulinsky, S. Oh, D. Dunn-Rankin, and M. J. Madou, "Controlled continuous patterning of polymeric nanofibers on three-dimensional substrates using low-voltage near-field electrospinning," *Nano letters*, vol. 11, no. 4, pp. 1831–1837, 2011.

[136] A. Haghi and M. Akbari, "Trends in electrospinning of natural nanofibers," *physica status solidi (a)*, vol. 204, no. 6, pp. 1830–1834, 2007.

[137] C. Chang, K. Limkrailassiri, and L. Lin, "Continuous near-field electrospinning for large area deposition of orderly nanofiber patterns," *Applied Physics Letters*, 2008.

[138] T. Padmanabhan, V. Kamaraj, L. Magwood, and B. Starly, "Experimental investigation on the operating variables of a near-field electrospinning process via response surface methodology," *Journal of Manufacturing Processes*, vol. 13, no. 2, pp. 104–112, 2011.

[139] K. Onozuka, B. Ding, Y. Tsuge, T. Naka, M. Yamazaki, S. Sugi, S. Ohno, M. Yoshikawa, and S. Shiratori, "Electrospinning processed nanofibrous tio2 membranes for photovoltaic applications," *Nanotechnology*, vol. 17, no. 4, p. 1026, 2006.

[140] Z. Liu, C. Pan, L. Lin, and H. Lai, "Piezoelectric properties of pvdf/mwcnt nanofiber using near-field electrospinning," *Sensors and Actuators A: Physical*, vol. 193, pp. 13–24, 2013.

[141] F.-L. Zhou, P. L. Hubbard, S. J. Eichhorn, and G. J. Parker, "Jet deposition in near-field electrospinning of patterned polycaprolactone and sugar-polycaprolactone core–shell fibres," *Polymer*, vol. 52, no. 16, pp. 3603–3610, 2011.

[142] N. Xue, X. Li, C. Bertulli, Z. Li, A. Patharagulpong, A. Sadok, and Y. Y. S. Huang, "Rapid patterning of 1-d collagenous topography as an ecm protein fibril platform for image cytometry," *PloS one*, vol. 9, no. 4, p. e93590, 2014.

[143] G. Bisht, S. Nesterenko, L. Kulinsky, and M. Madou, "A computer-controlled near-field electrospinning setup and its graphic user interface for precision patterning of functional nanofibers on 2D and 3D substrates.," *Journal of laboratory automation*, vol. 17, no. 4, pp. 302–8, 2012.

[144] G. Hochleitner, T. Jüngst, T. D. Brown, K. Hahn, C. Moseke, F. Jakob, P. D. Dalton, and J. Groll, "Additive manufacturing of scaffolds with sub-micron filaments via melt electrospinning writing," *Biofabrication*, vol. 7, no. 3, p. 035002, 2015.

[145] R. Deng, Y. Liu, Y. Ding, P. Xie, L. Luo, and W. Yang, "Melt electrospinning of low-density polyethylene having a low-melt flow index," *Journal of Applied Polymer Science*, vol. 114, no. 1, pp. 166–175, 2009.

[146] D. W. Hutmacher and P. D. Dalton, "Melt electrospinning," *Chemistry–An Asian Journal*, vol. 6, no. 1, pp. 44–56, 2011.

[147] P. D. Dalton, D. Grafahrend, K. Klinkhammer, D. Klee, and M. Möller, "Electrospinning of polymer melts: phenomenological observations," *Polymer*, vol. 48, no. 23, pp. 6823–6833, 2007.

[148] G. Hochleitner, T. Jüngst, T. D. Brown, K. Hahn, C. Moseke, F. Jakob, P. D. Dalton, and J. Groll, "Additive manufacturing of scaffolds with sub-micron filaments via melt electrospinning writing," *Biofabrication*, vol. 7, no. 3, p. 035002, 2015.

[149] S. J. Kim, D. H. Jang, W. H. Park, and B.-M. Min, "Fabrication and characterization of 3-dimensional plga nanofiber/microfiber composite scaffolds," *Polymer*, vol. 51, no. 6, pp. 1320–1327, 2010.

[150] J. M. Deitzel, J. Kleinmeyer, D. Harris, and N. B. Tan, "The effect of processing variables on the morphology of electrospun nanofibers and textiles," *Polymer*, vol. 42, no. 1, pp. 261–272, 2001.

[151] P. Wallin, C. Zandén, B. Carlberg, N. Hellström Erkenstam, J. Liu, and J. Gold, "A method to integrate patterned electrospun fibers with microfluidic systems to generate complex microenvironments for cell culture applications," *Biomicrofluidics*, vol. 6, no. 2, pp. 1–18, 2012.

[152] R.-N. Chen, H.-O. Ho, Y.-T. Tsai, and M.-T. Sheu, "Process development of an acellular dermal matrix (ADM) for biomedical applications.," *Biomaterials*, vol. 25, no. 13, pp. 2679–2686, 2004.

[153] M. T. Wolf, K. A. Daly, E. P. Brennan-Pierce, S. A. Johnson, C. A. Carruthers, A. D'Amore, S. P. Nagarkar, S. S. Velankar, and S. F. Badylak, "A hydrogel derived from decellularized dermal extracellular matrix," *Biomaterials*, vol. 33, no. 29, pp. 7028–7038, 2012.

[154] L. Wang, J. A. Johnson, Q. Zhang, and E. K. Beahm, "Combining decellularized human adipose tissue extracellular matrix and adipose-derived stem cells for adipose tissue engineering," *Acta biomaterialia*, vol. 9, no. 11, pp. 8921–8931, 2013.

[155] L. E. Flynn, "The use of decellularized adipose tissue to provide an inductive microenvironment for the adipogenic differentiation of human adipose-derived stem cells," *Biomaterials*, vol. 31, no. 17, pp. 4715–4724, 2010.

[156] T. Woods and P. F. Gratzer, "Effectiveness of three extraction techniques in the development of a decellularized bone-anterior cruciate ligament-bone graft," *Biomaterials*, vol. 26, no. 35, pp. 7339–7349, 2005.

[157] G. Schulze-Tanzil, O. Al-Sadi, W. Ertel, and A. Lohan, "Decellularized tendon extracellular matrix-a valuable approach for tendon reconstruction?," *Cells*, vol. 1, no. 4, pp. 1010–28, 2012.

[158] H. C. Ott, T. S. Matthiesen, S.-K. Goh, L. D. Black, S. M. Kren, T. I. Netoff, and D. a. Taylor, "Perfusion-decellularized matrix: using nature's platform to engineer a bioartificial heart.," *Nature medicine*, vol. 14, no. 2, pp. 213–221, 2008.

[159] P. M. Baptista, M. M. Siddiqui, G. Lozier, S. R. Rodriguez, A. Atala, and S. Soker, "The use of whole organ decellularization for the generation of a vascularized liver organoid," *Hepatology*, vol. 53, no. 2, pp. 604–617, 2011.

[160] B. E. Uygun, A. Soto-Gutierrez, H. Yagi, M.-L. Izamis, M. A. Guzzardi, C. Shulman, J. Milwid, N. Kobayashi, A. Tilles, F. Berthiaume, M. Hertl, Y. Nahmias, M. L. Yarmush, and K. Uygun, "Organ reengineering through development of a transplantable recellularized liver graft using decellularized liver matrix.," *Nature medicine*, vol. 16, no. 7, pp. 814–20, 2010.

[161] S. F. Badylak, G. C. Lantz, A. Coffey, and L. a. Geddes, "Small intestinal submucosa as a large diameter vascular graft in the dog," *The Journal of surgical research*, vol. 47, no. 1, pp. 74–80, 1989.

[162] T. W. Gilbert, D. B. Stolz, F. Biancaniello, A. Simmons-Byrd, and S. F. Badylak, "Production and characterization of ECM powder: Implications for tissue engineering applications," *Biomaterials*, vol. 26, no. 12, pp. 1431–1435, 2005.

[163] J. P. Guyette, S. E. Gilpin, J. M. Charest, L. F. Tapias, X. Ren, and H. C. Ott, "Perfusion decellularization of whole organs," *Nature protocols*, vol. 9, no. 6, pp. 1451–1468, 2014.

[164] V. Mironov, R. P. Visconti, V. Kasyanov, G. Forgacs, C. J. Drake, and R. R. Markwald, "Organ printing: Tissue spheroids as building blocks," *Biomaterials*, vol. 30, no. 12, pp. 2164–2174, 2009.

[165] C. J. Medberry, P. M. Crapo, B. F. Siu, C. A. Carruthers, M. T. Wolf, S. P. Nagarkar, V. Agrawal, K. E. Jones, J. Kelly, S. A. Johnson, S. S. Velankar, S. C. Watkins, M. Modo, and S. F. Badylak, "Hydrogels derived from central nervous system extracellular matrix," *Biomaterials*, vol. 34, no. 4, pp. 1033–1040, 2013.

[166] Y. Hong, A. Huber, K. Takanari, N. J. Amoroso, R. Hashizume, S. F. Badylak, and W. R. Wagner, "Mechanical properties and in vivo behavior of a biodegradable synthetic polymer microfiber-extracellular matrix hydrogel biohybrid scaffold," *Biomaterials*, vol. 32, no. 13, pp. 3387–3394, 2011.

[167] C. P. Barnes, S. A. Sell, E. D. Boland, D. G. Simpson, and G. L. Bowlin, "Nanofiber technology: designing the next generation of tissue engineering scaffolds," *Advanced drug delivery reviews*, vol. 59, no. 14, pp. 1413–1433, 2007.

[168] S. Baiguera, C. Del Gaudio, E. Lucatelli, E. Kuevda, M. Boieri, B. Mazzanti, A. Bianco, and P. Macchiarini, "Electrospun gelatin scaffolds incorporating rat decellularized brain extracellular matrix for neural tissue engineering," *Biomaterials*, vol. 35, no. 4, pp. 1205–1214, 2014.

[169] A. D'Amore, T. Yoshizumi, S. K. Luketich, M. T. Wolf, X. Gu, M. Cammarata, R. Hoff, S. F. Badylak, and W. R. Wagner, "Bi-layered polyurethane - Extracellular matrix cardiac patch improves ischemic ventricular wall remodeling in a rat model," *Biomaterials*, 2016.

[170] S. Gao, W. Guo, M. Chen, Z. Yuan, M. Wang, Y. Zhang, S. Liu, T. Xi, and Q. Guo, "Fabrication and characterization of electrospun nanofibers composed of decellularized meniscus extracellular matrix and polycaprolactone for meniscus tissue engineering," *Journal of Materials Chemistry B*, vol. 5, no. 12, pp. 2273–2285, 2017.

[171] S. Badylak, S. Meurling, M. Chen, A. Spievack, and A. Simmons-Byrd, "Resorbable bioscaffold for esophageal repair in a dog model," *Journal of pediatric surgery*, vol. 35, no. 7, pp. 1097–1103, 2000.

[172] S. Dahms, H. Piechota, R. Dahiya, T. Lue, and E. Tanagho, "Composition and biomechanical properties of the bladder acellular matrix graft: comparative analysis in rat, pig and human," *British journal of urology*, vol. 82, pp. 411–419, 1998.

[173] L. Yang, C. F. Fitie, K. O. van der Werf, M. L. Bennink, P. J. Dijkstra, and J. Feijen, "Mechanical properties of single electrospun collagen type i fibers," *Biomaterials*, vol. 29, no. 8, pp. 955–962, 2008.

[174] P. Qi, Y. Zhou, D. Wang, Z. He, and Z. Li, "A new collagen solution with high concentration and collagen native structure perfectly preserved," *RSC Advances*, vol. 5, no. 106, pp. 87180–87186, 2015.

[175] K. Gast, A. Siemer, D. Zirwer, and G. Damaschun, "Fluoroalcohol-induced structural changes of proteins: some aspects of cosolvent-protein interactions," *European Biophysics Journal*, vol. 30, no. 4, pp. 273–283, 2001.

[176] E. Froesch, H. Bürgi, E. Ramseier, P. Bally, and A. Labhart, "Antibody-suppressible and nonsuppressible insulin-like activities in human serum and their physiologic significance. an insulin assay with adipose tissue of increased precision and specificity," *Journal of Clinical Investigation*, vol. 42, no. 11, p. 1816, 1963.

[177] T. Sampath and A. Reddi, "Homology of bone-inductive proteins from human, monkey, bovine, and rat extracellular matrix," *Proceedings of the National Academy of Sciences*, vol. 80, no. 21, pp. 6591–6595, 1983.

[178] J. P. López-Alonso, M. Bruix, J. Font, M. Ribó, M. Vilanova, M. A. Jimenez, J. Santoro, C. González, and D. V. Laurents, "Nmr spectroscopy reveals that rnase a is chiefly denatured in 40% acetic acid: implications for oligomer formation by 3d domain swapping," *Journal of the American Chemical Society*, vol. 132, no. 5, pp. 1621–1630, 2010.

[179] A. S. Nain, M. Sitti, A. Jacobson, T. Kowalewski, and C. Amon, "Dry spinning based spinneret based tunable engineered parameters (step) technique for controlled and aligned deposition of polymeric nanofibers," *Macromolecular rapid communications*, vol. 30, no. 16, pp. 1406–1412, 2009.

[180] S. Shen, A. Henry, J. Tong, R. Zheng, and G. Chen, "Polyethylene nanofibres with very high thermal conductivities," *Nature nanotechnology*, vol. 5, no. 4, pp. 251–255, 2010.

[181] A. S. Nain, J. C. Wong, C. Amon, and M. Sitti, "Drawing suspended polymer micro-/nanofibers using glass micropipettes," *Applied Physics Letters*, vol. 89, no. 18, p. 183105, 2006.

[182] S. A. Harfenist, S. D. Cambron, E. W. Nelson, S. M. Berry, A. W. Isham, M. M. Crain, K. M. Walsh, R. S. Keynton, and R. W. Cohn, "Direct drawing of suspended filamentary micro-and nanostructures from liquid polymers," *Nano Letters*, vol. 4, no. 10, pp. 1931–1937, 2004.

[183] J. Ma, Q. Zhang, Y. Zhang, L. Zhou, J. Yang, and Z. Ni, "A rapid and simple method to draw polyethylene nanofibers with enhanced thermal conductivity," *Applied Physics Letters*, vol. 109, no. 3, p. 033101, 2016.

[184] M. G. McKee, G. L. Wilkes, R. H. Colby, and T. E. Long, "Correlations of Solution Rheology with Electrospun Fiber Formation of Linear and Branched Polyesters," *Macromolecules*, vol. 37, pp. 1760–1767, 2004.

[185] P. Dalton, T. Jungst, A. Youssef, A. Hrynevich, G. Hochleitner, and J. Groll, "Electrospinning and direct writing: why polymer melts are excellent fluids for 3d printing," *Frontiers in Bioengineering and Biotechnology*, no. 2557.

[186] M. Rubinstein and R. Colby, *Polymer Physics*. OUP Oxford, 2003.

[187] M. Djabourov, K. Nishinari, and S. B. Ross-Murphy, *Physical gels from biological and synthetic polymers*. Cambridge University Press, 2013.

[188] C. Qiao, G. Chen, Y. Li, and T. Li, "Viscosity properties of gelatin in solutions of monovalent and divalent salts," *Korea-Australia Rheology Journal*, vol. 25, no. 4, pp. 227–231, 2013.

[189] C. Macosko, *Rheology: principles, measurements, and applications*. Advances in interfacial engineering series, VCH, 1994.

[190] R. Rošic, J. Pelipenko, P. Kocbek, S. Baumgartner, M. Bešter-Rogač, and J. Kristl, "The role of rheology of polymer solutions in predicting nanofiber formation by electrospinning," *European Polymer Journal*, vol. 48, no. 8, pp. 1374–1384, 2012.

[191] Wikipedia, "Power-law fluid — wikipedia, the free encyclopedia," 2016. [Online; accessed 17-October-2017].

[192] M. Takasato, P. X. Er, H. S. Chiu, B. Maier, G. J. Baillie, C. Ferguson, R. G. Parton, E. J. Wolvetang, M. S. Roost, S. M. Chuva de Sousa Lopes, and M. H. Little, "Kidney organoids from human iPS cells contain multiple lineages and model human nephrogenesis.," *Nature*, vol. 526, pp. 564–8, oct 2015.

[193] J. Eggers and E. Villermaux, "Physics of liquid jets," *Reports on progress in physics*, vol. 71, no. 3, p. 036601, 2008.

[194] N. Bhattarai, Z. Li, D. Edmondson, and M. Zhang, "Alginate-Based Nanofibrous Scaffolds: Structural, Mechanical, and Biological Properties," *Advanced Materials*, vol. 18, no. 11, pp. 1463–1467, 2006.

[195] C. J. Buchko, L. C. Chen, Y. Shen, and D. C. Martin, "Processing and microstructural characterization of porous biocompatible protein polymer thin films," *Polymer*, vol. 40, no. 26, pp. 7397–7407, 1999.

[196] N. Choktaweesap, K. Arayanarakul, D. Aht-Ong, C. Meechaisue, and P. Supaphol, "Electrospun gelatin fibers: effect of solvent system on morphology and fiber diameters," *Polymer journal*, vol. 39, no. 6, p. 622, 2007.

[197] H. Winter, "Can the gel point of a cross-linking polymer be detected by the g–g crossover?," *Polymer Engineering & Science*, vol. 27, no. 22, pp. 1698–1702, 1987.

[198] S. Theron, A. Yarin, E. Zussman, and E. Kroll, "Multiple jets in electrospinning: experiment and modeling," *Polymer*, vol. 46, no. 9, pp. 2889–2899, 2005.

[199] L. H. Catalani, G. Collins, and M. Jaffe, "Evidence for molecular orientation and residual charge in the electrospinning of poly (butylene terephthalate) nanofibers," *Macromolecules*, vol. 40, no. 5, pp. 1693–1697, 2007.

[200] C. Rayat, K. Joshi, V. Sakhuja, and U. Datta, "Glomerular basement membrane thickness in normal adults and its application to the diagnosis of thin basement membrane disease: an indian study.," *Indian journal of pathology & microbiology*, vol. 48, no. 4, pp. 453–458, 2005.

[201] N. Bu, Y. Huang, H. Deng, and Z. Yin, "Tunable bead-on-string microstructures fabricated by mechano-electrospinning," *Journal of Physics D: Applied Physics*, vol. 45, p. 405301, oct 2012.

[202] J. Meredith, B. Fazeli, and M. Schwartz, "The extracellular matrix as a cell survival factor.," *Molecular biology of the cell*, vol. 4, no. 9, pp. 953–961, 1993.

[203] W. G. Stetler-Stevenson, S. Aznavoorian, and L. A. Liotta, "Tumor cell interactions with the extracellular matrix during invasion and metastasis," *Annual review of cell biology*, vol. 9, no. 1, pp. 541–573, 1993.

[204] I. Vlodavsky, J. Folkman, R. Sullivan, R. Fridman, R. Ishai-Michaeli, J. Sasse, and M. Klagsbrun, "Endothelial cell-derived basic fibroblast growth factor: synthesis and deposition into subendothelial extracellular matrix," *Proceedings of the National Academy of Sciences*, vol. 84, no. 8, pp. 2292–2296, 1987.

[205] S. Guido and R. T. Tranquillo, "A methodology for the systematic and quantitative study of cell contact guidance in oriented collagen gels. correlation of fibroblast orientation and gel birefringence," *Journal of Cell Science*, vol. 105, no. 2, pp. 317–331, 1993.

[206] R. B. Dickinson, S. Guido, and R. T. Tranquillo, "Biased cell migration of fibroblasts exhibiting contact guidance in oriented collagen gels," *Annals of biomedical engineering*, vol. 22, no. 4, pp. 342–356, 1994.

[207] M. Yanagishita, "Function of proteoglycans in the extracellular matrix," *Pathology International*, vol. 43, no. 6, pp. 283–293, 1993.

[208] Y.-c. Fung, *Biomechanics: mechanical properties of living tissues*. Springer Science & Business Media, 2013.

[209] D. E. Discher, P. Janmey, and Y.-l. Wang, "Tissue cells feel and respond to the stiffness of their substrate," *Science*, vol. 310, no. 5751, pp. 1139–1143, 2005.

[210] V. Vogel and M. Sheetz, "Local force and geometry sensing regulate cell functions.," *Nature reviews. Molecular cell biology*, vol. 7, pp. 265–75, apr 2006.

[211] Y. S. Pek, A. C. Wan, and J. Y. Ying, "The effect of matrix stiffness on mesenchymal stem cell differentiation in a 3d thixotropic gel," *Biomaterials*, vol. 31, no. 3, pp. 385–391, 2010.

[212] Y. Kawata, S. Urahama, M. Murakami, and F. Iwata, "The use of capillary force for fabricating probe tips for scattering-type near-field scanning optical microscopes," *Applied physics letters*, vol. 82, no. 10, pp. 1598–1600, 2003.

[213] F. Iwata, Y. Sumiya, and A. Sasaki, "Nanometer-scale metal plating using a scanning shear-force microscope with an electrolyte-filled micropipette probe," *Japanese journal of applied physics*, vol. 43, no. 7S, p. 4482, 2004.

[214] B. M.-A. GOULET, J. COLBERT, and K. Dalnoki-Veress, "Friction measurements on living cells," *La Physique au Canada*, p. 129.

[215] Wikipedia, "Deflection (engineering) — wikipedia, the free encyclopedia," 2017. [Online; accessed 22-April-2017].

[216] O. Sids and U. Publications, "Introduction Glyoxal Cas N ° : 107-22-2,"

[217] Organisation for Economic Co-Operation and Development Screening Information Data Sets (OECD SIDS), "Glutaradehyde CAS N°: 111-30-8," pp. 1–83, 2008.

[218] O. Sids and U. Publications, "Formaldehy De," *Unep Publications*, pp. 1–395, 2002.

[219] M.-K. Uslu and S. Polat, "Effects of glyoxal cross-linking on baked starch foam," *Carbohydrate polymers*, vol. 87, no. 3, pp. 1994–1999, 2012.

[220] L. Wang and J. P. Stegemann, "Glyoxal crosslinking of cell-seeded chitosan/collagen hydrogels for bone regeneration," *Acta biomaterialia*, vol. 7, no. 6, pp. 2410–2417, 2011.

[221] J.-Y. Park, K.-J. Hwang, S.-D. Yoon, J.-H. Lee, and I.-H. Lee, "Influence of glyoxal on preparation of poly (vinyl alcohol)/poly (acrylic acid) blend film," *Journal of nanoscience and nanotechnology*, vol. 15, no. 8, pp. 5955–5958, 2015.

[222] P. Davis and B. Tabor, "Kinetic study of the crosslinking of gelatin by formaldehyde and glyoxal," *Journal of Polymer Science Part A: General Papers*, vol. 1, no. 2, pp. 799–815, 1963.

[223] D. R. Sell, K. M. Biemel, O. Reihl, M. O. Lederer, C. M. Strauch, and V. M. Monnier, "Glucosepane is a major protein cross-link of the senescent human extracellular matrix relationship with diabetes," *Journal of Biological Chemistry*, vol. 280, no. 13, pp. 12310–12315, 2005.

[224] K. D. Yoon, K. Yamamoto, K. Ueda, J. Zhou, and J. R. Sparrow, "A novel source of methylglyoxal and glyoxal in retina: implications for age-related macular degeneration," *PloS one*, vol. 7, no. 7, p. e41309, 2012.

[225] A. R. Massensini, H. Ghuman, L. T. Saldin, C. J. Medberry, T. J. Keane, F. J. Nicholls, S. S. Velankar, S. F. Badylak, and M. Modo, "Concentration-dependent rheological properties of ecm hydrogel for intracerebral delivery to a stroke cavity," *Acta biomaterialia*, vol. 27, pp. 116–130, 2015.

[226] J. Banks, A. Muriel, and J. P. Smith, "Attrition and health in ageing studies: evidence from elsa and hrs," *Longitudinal and life course studies*, vol. 2, no. 2, 2011.

[227] Y. Shin, S. Han, J. S. Jeon, K. Yamamoto, I. K. Zervantonakis, R. Sudo, R. D. Kamm, and S. Chung, "Microfluidic assay for simultaneous culture of multiple cell types on surfaces or within hydrogels.," *Nature protocols*, vol. 7, no. 7, pp. 1247–59, 2012.

[228] Wikipedia, "Fibronectin — wikipedia, the free encyclopedia," 2016. [Online; accessed 27-January-2017].

[229] Wikipedia, "Laminin — wikipedia, the free encyclopedia," 2016. [Online; accessed 31-January-2017].

[230] P. D. Ngo, "Energy dispersive spectroscopy," in *Failure Analysis of Integrated Circuits*, pp. 205–215, Springer, 1999.

[231] B. Stuart, *Biological applications of infrared spectroscopy*. John Wiley & Sons, 2008.

[232] S. F. Badylak, D. O. Freytes, and T. W. Gilbert, "Extracellular matrix as a biological scaffold material : Structure and function," *Acta Biomaterialia*, vol. 5, no. 1, pp. 1–13, 2009.

[233] S. L. Voytik-Harbin, A. O. Brightman, M. R. Kraine, B. Waisner, and S. F. Badylak, "Identification of extractable growth factors from small intestinal submucosa," *Journal of cellular biochemistry*, vol. 67, no. 4, pp. 478–491, 1997.

[234] Y. L. Yu, Y. K. Shao, Y. Q. Ding, K. Z. Lin, B. Chen, H. Z. Zhang, L. N. Zhao, Z. B. Wang, J. S. Zhang, M. L. Tang, and J. Mei, "Decellularized kidney scaffold-mediated renal regeneration," *Biomaterials*, vol. 35, no. 25, pp. 6822–6828, 2014.

[235] B. Yang, Y. Zhang, L. Zhou, Z. Sun, J. Zheng, Y. Chen, and Y. Dai, "Development of a porcine bladder acellular matrix with well-preserved extracellular bioactive factors for tissue engineering," *Tissue Engineering Part C: Methods*, vol. 16, no. 5, pp. 1201–1211, 2010.

[236] S. Y. Chun, G. J. Lim, T. G. Kwon, E. K. Kwak, B. W. Kim, A. Atala, and J. J. Yoo, "Identification and characterization of bioactive factors in bladder submucosa matrix," *Biomaterials*, vol. 28, no. 29, pp. 4251–4256, 2007.

[237] S.-Y. Fu, X.-Q. Feng, B. Lauke, and Y.-W. Mai, "Effects of particle size, particle/matrix interface adhesion and particle loading on mechanical properties of particulate–polymer composites," *Composites Part B: Engineering*, vol. 39, no. 6, pp. 933–961, 2008.

[238] N. Chawla and Y.-L. Shen, "Mechanical behavior of particle reinforced metal matrix composites," *Advanced engineering materials*, vol. 3, no. 6, pp. 357–370, 2001.

[239] J. S. Bergstrom and M. C. Boyce, "Mechanical behavior of particle filled elastomers," *Rubber chemistry and technology*, vol. 72, no. 4, pp. 633–656, 1999.

[240] D. Lloyd, "Particle reinforced aluminium and magnesium matrix composites," *International Materials Reviews*, vol. 39, no. 1, pp. 1–23, 1994.

[241] H. S. Kim, "On the rule of mixtures for the hardness of particle reinforced composites," *Materials Science and Engineering: A*, vol. 289, no. 1, pp. 30–33, 2000.

[242] Y. Feng, E. Shamsaei, C. H. Davies, and H. Wang, "Inorganic particle enhanced polymer hollow fiber membranes with high mechanical properties," *Materials Chemistry and Physics*, vol. 167, pp. 209–218, 2015.

[243] D. J. Rosario, G. C. Reilly, E. Ali Salah, M. Glover, A. J. Bullock, and S. MacNeil, "Decellularization and sterilization of porcine urinary bladder matrix for tissue engineering in the lower urinary tract," 2008.

[244] W. A. Farhat, J. Chen, J. Haig, R. Antoon, J. Litman, C. Sherman, K. Derwin, and H. Yeger, "Porcine bladder acellular matrix (acm): protein expression, mechanical properties," *Biomedical Materials*, vol. 3, no. 2, p. 025015, 2008.

[245] M. Fialkowski, C. Campbell, I. Bensemann, and B. Grzybowski, "Absorption of water by thin, ionic films of gelatin," *Langmuir*, vol. 20, no. 9, pp. 3513–3516, 2004.

[246] L. A. Stevens, J. Coresh, T. Greene, and A. S. Levey, "Assessing kidney function—measured and estimated glomerular filtration rate," *New England Journal of Medicine*, vol. 354, no. 23, pp. 2473–2483, 2006.

[247] D. Fleury and J. M. Walker, *Kidney research, experimental protocols*, vol. 466.

[248] B. M. Brenner, T. W. Meyer, and T. H. Hostetter, "Dietary protein intake and the progressive nature of kidney disease: the role of hemodynamically mediated glomerular injury in the pathogenesis of progressive glomerular sclerosis in aging, renal ablation, and intrinsic renal disease," *New England Journal of Medicine*, vol. 307, no. 11, pp. 652–659, 1982.

[249] J. Churg and E. Grishman, "Ultrastructure of glomerular disease: a review.," *Kidney international*, 1975.

[250] E. L. Schiffrin, M. L. Lipman, and J. F. Mann, "Chronic kidney disease," *Circulation*, vol. 116, no. 1, pp. 85–97, 2007.

[251] S. Musah, A. Mammoto, T. C. Ferrante, S. S. Jeanty, M. Hirano-Kobayashi, T. Mammoto, K. Roberts, S. Chung, R. Novak, M. Ingram, *et al.*, "Mature induced-pluripotent-stem-cell-derived human podocytes reconstitute kidney glomerular-capillary-wall function on a chip," *Nature Biomedical Engineering*, vol. 1, p. 0069, 2017.

[252] L. Ni, M. Saleem, and P. W. Mathieson, "Podocyte culture: tricks of the trade," *Nephrology*, vol. 17, no. 6, pp. 525–531, 2012.

[253] S. C. Slater, V. Beachley, T. Hayes, D. Zhang, G. I. Welsh, M. A. Saleem, P. W. Mathieson, X. Wen, B. Su, and S. C. Satchell, "An in vitro model of the glomerular capillary wall using electrospun collagen nanofibres in a bioartificial composite basement membrane," *PloS one*, vol. 6, no. 6, p. e20802, 2011.

[254] D. Huh, B. D. Matthews, A. Mammoto, M. Montoya-Zavala, H. Y. Hsin, and D. E. Ingber, "Reconstituting organ-level lung functions on a chip," *Science*, vol. 328, no. 5986, pp. 1662–1668, 2010.

[255] Y. Imura, Y. Asano, and E. Yoshimura, "A microfluidic system to evaluate intestinal absorption," *Analytical Sciences*, vol. 25, no. 12, pp. 1403–1407, 2009.

[256] K.-J. Jang, H. S. Cho, W. G. Bae, T.-H. Kwon, K.-Y. Suh, *et al.*, "Fluid-shear-stress-induced translocation of aquaporin-2 and reorganization of actin cytoskeleton in renal tubular epithelial cells," *Integrative Biology*, vol. 3, no. 2, pp. 134–141, 2011.

[257] N. S. Bhise, J. Ribas, V. Manoharan, Y. S. Zhang, A. Polini, S. Massa, M. R. Dokmeci, and A. Khademhosseini, "Organ-on-a-chip platforms for studying drug delivery systems," *Journal of Controlled Release*, vol. 190, pp. 82–93, 2014.

[258] Corning, "Transwell ® Permeable Supports Selection and Use Guide," 2007.

[259] C. Grobstein, "Morphogenetic interaction between embryonic mouse tissues separated by a membrane filter," *Nature*, vol. 172, no. 4384, pp. 869–871, 1953.

[260] A. Peled, I. Petit, O. Kollet, M. Magid, T. Ponomaryov, T. Byk, A. Nagler, H. Ben-Hur, A. Many, L. Shultz, *et al.*, "Dependence of human stem cell engraftment and repopulation of nod/scid mice on cxcr4," *Science*, vol. 283, no. 5403, pp. 845–848, 1999.

[261] G. Giannelli, J. Falk-Marzillier, O. Schiraldi, W. G. Stetler-Stevenson, and V. Quaranta, "Induction of cell migration by matrix metalloprotease-2 cleavage of laminin-5," *Science*, vol. 277, no. 5323, pp. 225–228, 1997.

[262] R. N. Kaplan, R. D. Riba, S. Zacharoulis, A. H. Bramley, L. Vincent, C. Costa, D. D. MacDonald, D. K. Jin, K. Shido, S. A. Kerns, *et al.*, "Vegfr1-positive haematopoietic bone marrow progenitors initiate the pre-metastatic niche," *Nature*, vol. 438, no. 7069, pp. 820–827, 2005.

[263] J. Marshall, "Transwell® invasion assays," *Cell Migration: Developmental Methods and Protocols*, pp. 97–110, 2011.

[264] B. Trappmann, J. E. Gautrot, J. T. Connelly, D. G. Strange, Y. Li, M. L. Oyen, M. A. C. Stuart, H. Boehm, B. Li, V. Vogel, *et al.*, "Extracellular-matrix tethering regulates stem-cell fate," *Nature materials*, vol. 11, no. 7, pp. 642–649, 2012.

[265] R. Taylor, D. Falconnet, A. Niemistö, S. Ramsey, S. Prinz, I. Shmulevich, T. Galitski, and C. Hansen, "Dynamic analysis of mapk signaling using a high-throughput microfluidic single-cell imaging platform," *Proceedings of the National Academy of Sciences*, vol. 106, no. 10, pp. 3758–3763, 2009.

[266] T. Merkel, V. Bondar, K. Nagai, B. Freeman, and I. Pinnau, "Gas sorption, diffusion, and permeation in poly (dimethylsiloxane)," *Journal of Polymer Science Part B: Polymer Physics*, vol. 38, no. 3, pp. 415–434, 2000.

[267] P. Abgrall and A. Gue, "Lab-on-chip technologies: making a microfluidic network and coupling it into a complete microsystem—a review," *Journal of Micromechanics and Microengineering*, vol. 17, no. 5, p. R15, 2007.

[268] H. Matsumoto and A. Tanioka, "Functionality in electrospun nanofibrous membranes based on fiber's size, surface area, and molecular orientation," *Membranes*, vol. 1, no. 3, pp. 249–264, 2011.

[269] N. Wang, K. Burugapalli, W. Song, J. Halls, F. Moussy, Y. Zheng, Y. Ma, Z. Wu, and K. Li, "Tailored fibro-porous structure of electrospun polyurethane membranes, their size-dependent properties and trans-membrane glucose diffusion," *Journal of membrane science*, vol. 427, pp. 207–217, 2013.

[270] E. Paluch and C.-P. Heisenberg, "Biology and physics of cell shape changes in development," *Current Biology*, vol. 19, no. 17, pp. R790–R799, 2009.

[271] Invitrogen, "Cell Culture Basics Handbook," *ThermoFisher Scientific Inc.*, pp. 1–61, 2010.

[272] Amsbio, "Protocol Hip Tm Human Neural Stem Cell (Nsc) Culture," pp. 4–5, 2011.

[273] U. S. Eggert, T. J. Mitchison, and C. M. Field, "Animal cytokinesis: from parts list to mechanisms," *Annual Review of Biochemistry*, vol. 75, pp. 543–566, 2006.

[274] G. G. Borisy and T. M. Svitkina, "Actin machinery: pushing the envelope," *Current opinion in cell biology*, vol. 12, no. 1, pp. 104–112, 2000.

[275] J. Bereiter-Hahn, "Mechanics of crawling cells," *Medical engineering & physics*, vol. 27, no. 9, pp. 743–753, 2005.

[276] S.-Y. Tee, J. Fu, C. S. Chen, and P. A. Janmey, "Cell shape and substrate rigidity both regulate cell stiffness," *Biophysical journal*, vol. 100, no. 5, pp. L25–L27, 2011.

[277] T. Yeung, P. C. Georges, L. A. Flanagan, B. Marg, M. Ortiz, M. Funaki, N. Zahir, W. Ming, V. Weaver, and P. A. Janmey, "Effects of substrate stiffness on cell morphology, cytoskeletal structure, and adhesion," *Cell motility and the cytoskeleton*, vol. 60, no. 1, pp. 24–34, 2005.

[278] C. S. Chen, J. L. Alonso, E. Ostuni, G. M. Whitesides, and D. E. Ingber, "Cell shape provides global control of focal adhesion assembly," *Biochemical and biophysical research communications*, vol. 307, no. 2, pp. 355–361, 2003.

[279] R. Singhvi, A. Kumar, G. P. Lopez, G. N. Stephanopoulos, D. I. Wang, G. M. Whitesides, D. E. Ingber, *et al.*, "Engineering cell shape and function," *Science*, pp. 696–696, 1994.

[280] M. P. Lutolf, P. M. Gilbert, and H. M. Blau, "Designing materials to direct stem-cell fate," *Nature*, vol. 462, no. 7272, pp. 433–441, 2009.

[281] J. M. Curran, R. Chen, and J. A. Hunt, "The guidance of human mesenchymal stem cell differentiation in vitro by controlled modifications to the cell substrate," *Biomaterials*, vol. 27, no. 27, pp. 4783–4793, 2006.

[282] R. T. Justin and A. J. Engler, "Stiffness gradients mimicking in vivo tissue variation regulate mesenchymal stem cell fate," *PloS one*, vol. 6, no. 1, p. e15978, 2011.

[283] M. J. Dalby, N. Gadegaard, R. Tare, A. Andar, M. O. Riehle, P. Herzyk, C. D. Wilkinson, and R. O. Oreffo, "The control of human mesenchymal cell differentiation using nanoscale symmetry and disorder," *Nature materials*, vol. 6, no. 12, pp. 997–1003, 2007.

[284] B. Haraldsson, J. Nyström, and W. M. Deen, "Properties of the glomerular barrier and mechanisms of proteinuria," *Physiological reviews*, vol. 88, no. 2, pp. 451–487, 2008.

[285] S. Quaggin and J. Kreidberg, "Development of the renal glomerulus: good neighbors and good fences," *Development*, 2008.

[286] Wikibooks, "Human physiology — wikibooks, the free textbook project," 2017.

[287] C. Heckman, S. Kanagasundaram, M. Cayer, and J. Paige, "Preparation of cultured cells for scanning electron microscope," *Nature Protocols Network*, 2007.

[288] A. D. Doyle, F. W. Wang, K. Matsumoto, and K. M. Yamada, "One-dimensional topography underlies three-dimensional fibrillar cell migration," *The Journal of cell biology*, vol. 184, no. 4, pp. 481–490, 2009.

[289] A. D. Doyle, R. J. Petrie, M. L. Kutys, and K. M. Yamada, "Dimensions in cell migration," *Current opinion in cell biology*, vol. 25, no. 5, pp. 642–649, 2013.

[290] D. Kerjaschki, P. Ojha, M. Susani, R. Horvat, S. Binder, A. Hovorka, P. Hillemanns, and R. Pytela, "A beta 1-integrin receptor for fibronectin in human kidney glomeruli.," *The American journal of pathology*, vol. 134, no. 2, p. 481, 1989.

[291] P. J. Courtoy, R. Timpl, and M. G. Farquhar, "Comparative distribution of laminin, type iv collagen, and fibronectin in the rat glomerulus.," *Journal of Histochemistry & Cytochemistry*, vol. 30, no. 9, pp. 874–886, 1982.

[292] Y. Gorin, K. Block, J. Hernandez, B. Bhandari, B. Wagner, J. L. Barnes, and H. E. Abboud, "Nox4 nad (p) h oxidase mediates hypertrophy and fibronectin expression in the diabetic kidney," *Journal of Biological Chemistry*, vol. 280, no. 47, pp. 39616–39626, 2005.

[293] Y. Liu, "Epithelial to mesenchymal transition in renal fibrogenesis: pathologic significance, molecular mechanism, and therapeutic intervention," *Journal of the American Society of Nephrology*, vol. 15, no. 1, pp. 1–12, 2004.

[294] B. Song, A. M. Smink, C. V. Jones, J. M. Callaghan, S. D. Firth, C. A. Bernard, A. L. Laslett, P. G. Kerr, and S. D. Ricardo, "The directed differentiation of human ips cells into kidney podocytes," *PloS one*, vol. 7, no. 9, p. e46453, 2012.

[295] M. Angarano, S. Schulz, M. Fabritius, R. Vogt, T. Steinberg, P. Tomakidi, C. Friedrich, and R. Mülhaupt, "Layered gradient nonwovens of in situ crosslinked electrospun collagenous nanofibers used as modular scaffold systems for soft tissue regeneration," *Advanced Functional Materials*, vol. 23, no. 26, pp. 3277–3285, 2013.

Appendix A

Optimising gelatin solution for LEP

The original composition of gelatin solution was obtained from reference [142]. There were four chemical components in the solution: gelatin powder, distilled water, acetic acids and ethyl acetate. The initial composition attempted was 15 wt% gelatin, 25 wt% water, 36 wt% acetic acid and 24 wt% ethyl acetate. Although straight fibres were produced in the reference paper, this solution composition was not suitable in LEP. I could not obtain a large area of straight and uniform fibres.

Initially, I supposed this could because of solvent properties, such as conductivity and surface tension. Various solvent compositions were tested whilst keeping the gelatin concentration constant. However, systematically testing the combination of the three solvent components was complicated. The outcome was not satisfying as I still failed to pattern continuous fibres.

This led me to explore another potential cause: insufficient polymer entanglement. Hence the gelatin concentration was increased and other components were reduced accordingly. With higher gelatin concentration ($>$16 wt%), straight and uniform fibres were patterned. This shows that the polymer entanglement is a main criteria in LEP. This could apply to other polymer solutions, such as polyurethane–HFP. In addition, one should understand the purpose of each solvent, in order to effectively optimise the composition. For the gelatin solution, water defined the nature of an aqueous solution. Acetic acid was used to dissolve gelatin power. Ethyl acetate was used to lower the surface energy of the solution. When tuning the composition, acetic acid was firstly reduced because one only need sufficient amount to dissolve gelatin. Secondly, ethyl acetate was decreased and water was kept roughly at constant. It is also important to note that, different batches of gelatin may cause variation in the optimum solution composition. If further modification is required, the viscoelastic behaviour of the solution may be a suitable benchmark.

Appendix B

Crosslinker concentration of gelatin fibres

The concentration of glyoxal as a gelatin crosslinker was initially adopted from reference [295]. To preliminarily test the crosslinking condition, glyoxal concentrations of 1 wt%, 3 wt% and 10 wt%, with respect to gelatin mass, were added to G(19) solutions. The solutions were used to cast gelatin films on glass slides. There films were left to crosslink for 24 hours. Afterwards, they were immersed in water.

With 1 wt% glyoxal, the sample was not fully crosslinked as it showed no defined shapes in water. This sample fractured easily when attempted to pick up with a pair of tweezers. Both 3 wt% and 10 wt% glyoxal concentrations were sufficient to crosslink the gelatin film. Smooth films were formed and remained gel-like after immersed in water for 7 days. This could potentially be longer with extended testing period. With increasing glyoxal concentration, the rate of crosslinking increased. 1 mL of G(19) solution stopped flowing after 20 min of mixing with 10 wt% glyoxal, whereas it remained liquid-like after 2 hours with 3 wt% glyoxal. The slow crosslinking rate was preferred as it allowed longer processing time for LEP. In addition, the 10 wt% film appeared stiffer than the 3 wt%. Therefore, 3 wt% glyoxal was used to crosslink gelatin microfibres.